OXIDATIVE REACTIONS TO FORM ETHYL METHACRYLATE VIA A PHASE SPECIFIC IRON PHOSPHATE CATALYST

By

FAIZA BIBI KHAN

Submitted in fulfillment of the academic requirements for the degree of
Doctor of Philosophy
In the
School of Chemistry and Physics,
University of KwaZulu-Natal,
Durban,
South Africa
(June 2012)

As the candidate's supervisor, I have approved this thesis for submission.

Name: Prof. Holger B. Friedrich Signed: _________ Date: ________________

I would like to dedicate this thesis to:

My father (Yussuf), mother (Shaida), husband (Akram) and son (Muhammad Yaseen)

ABSTRACT

The importance of alkyl methacrylates has been firmly established within the chemical industry. For example, free radical polymers, which contain the methacrylate backbone are more rigid than acrylate polymers. Several methods have been reported for the production of alkyl methacrylates.

The aim of this project is focused on isolating a phase specific iron phosphate catalyst and thereafter testing its efficacy in oxidative reactions to form ethyl methacrylate in a one step process in the gas phase using a fixed bed continuous flow reactor.

The catalyst was characterized by using Inductively Coupled Plasma-Optical Emission Spectroscopy (ICP-OES), Brunauer-Emmett-Teller (BET) surface area measurements, Attenuated Total Reflection-Infrared (ATR-IR) Spectroscopy, Scanning Electron Microscopy (SEM), Temperature Programmed Reduction (TPR), Temperature Programmed Oxidation (TPO), Energy Dispersive X-ray (EDX) determination, Temperature Programmed Desorption (TPD), Room Temperature X-ray Diffraction (XRD), *In situ* X-ray Diffraction (*In situ* XRD), Thermogravimetric/Differential Thermal Analysis (TGA/DTA), Transmission Electron Microscopy (TEM), Mössbauer Spectroscopy and Raman Spectroscopy. A further venture included employing certain of the above techniques to characterize the cesium promoted iron phosphate catalyst as well as the spent catalysts.

The catalytic activity of the iron phosphate based catalyst synthesized was investigated for the oxidative dehydrogenation (ODH) of ethyl isobutyrate (EIB) to ethyl methacrylate (EMA). Reaction conditions which were considered included variation in the contact time, co-feeding water at varying contact times, co-feeding ethanol at varying ratios, as well as co-feeding both ethanol and water and catalyst lifetime and regeneration studies. The cesium promoted iron phosphate catalyst was tested at optimal reaction conditions.

The findings of the investigation showed that the tridymite-like $FePO_4$ phase was the most suitable precursor to allow for the formation of the active α-phase during catalytic testing. It was found that the catalyst performed optimally at a contact time of 0.8 seconds and the beneficial effect of co-feeding water and ethanol primarily on conversion and selectivity towards EMA respectively, was demonstrated. Optimal results were obtained at a EIB:EtOH ratio of 1:5 with a conversion of 57 % and a yield of 34 mol %. The lifetime and regeneration studies showed that water had a significant effect on the regeneration of the catalyst after a specific time on stream and a shorter time on stream (i.e. 25 hours) prior to regeneration, minimized rapid deactivation of the catalyst.

The characterization results obtained for the spent catalysts showed that under the reaction conditions considered with respect to co-feeds, the active α-phase and the $Fe_2P_2O_7$ phase dominated.

The cesium promoted iron phosphate catalyst was synthesized to favour stabilization of the tridymite-like structure. The results showed that a mixture of phases was observed for the synthesized promoted catalysts and there was an increase in EIB conversion as well as EMA selectivity with a decrease in cesium loading. However, the promoted catalyst with the lowest cesium loading (Cs/Fe = 0.10), showed a lower selectivity towards EMA relative to the unpromoted iron phosphate catalyst.

PREFACE

The experimental work described in this thesis was carried out at the University of KwaZulu-Natal, School of Chemistry and Physics at both the Howard College and Westville Campus under the supervision of Prof. Holger B. Friedrich.

These studies represent original work by the author and have not otherwise been submitted in any form for any degree or diploma to any tertiary institution. Where use has been made of the work of others, it is duly acknowledged in the text.

Author: Mrs. Faiza Bibi Khan Signed: __________________ Date: _________________

DECLARATION 1- Plagiarism

I, Mrs. Faiza Bibi Khan, declare that:

1. The research reported in this thesis, except where otherwise indicated, is my original research.
2. This thesis has not been submitted for any degree or examination at any other university.
3. This thesis does not contain other persons' data, pictures, graphs or other information, unless specifically acknowledged as being sourced from other persons.
4. This thesis does not contain other persons' writing unless specifically acknowledged as being sourced from other researchers. Where other written sources have been quoted, then:
    a. Their words have been re-written but the general information attributed to them has been referenced.
    b. Where their exact words have been used, then their writing has been placed in italics and inside quotation marks, and referenced.
5. This thesis does not contain text, graphics or tables copied and pasted from the Internet, unless specifically acknowledged, and the source being detailed in the thesis and in the References sections.

Signed:

……………………………………………………………………………………….

Declaration Plagiarism 22/05/08 FHDR Approved

DECLARATION 2 - Publications and conference contributions

Part of the work has been published and presented at conferences as detailed below:

Publication:

1. F.B. Khan, K. Bharuth-Ram, H.B. Friedrich, 'Phase transformations of the $FePO_4$ catalyst in the oxidative dehydrogenation to form an alkyl methacrylate', Hyperfine Interactions, 197 (2010) 317-323.

Conference contributions:

1. Oxidative Dehydrogenation of a Saturated Acid and Alkyl Alcohols to produce Alkyl Methacrylates, Poster presentation, Catalysis Conference of South Africa (CATSA), November, 2006.
2. Oxidative Dehydrogenation Reactions to form Alkyl Methacrylates using an Iron Phosphate Catalyst, Oral presentation, Catalysis Conference of South Africa (CATSA), November, 2007.
3. Formation of Alkyl Methacrylates using an Iron Phosphate Catalyst, Poster presentation, Catalysis Conference of South Africa (CATSA), November, 2009.
4. Phase transformations of the $FePO_4$ catalyst pre- and post-oxidative dehydrogenation reactions to form an Alkyl Methacrylate, Poster presentation, International Conference on Hyperfine Interactions and Nuclear Quadrupolar Interactions – HFI/NQI in CERN, September, 2010.
5. Quantitative determination of phase transformations of the Tridymite-like $FePO_4$ catalyst pre and post oxidative dehydrogenation reactions to form Alkyl Methacrylates, Oral presentation, Catalysis Conference of South Africa (CATSA), November, 2010.

Author: Mrs. Faiza Bibi Khan Signed: _________________ Date: ________________

ACKNOWLEDGEMENTS

I would like to convey a sincere thanks to my mother and father for their constant motivation and patience throughout my academic career. They have been my pillars of strength and a sense of guidance which I know has been my driving force during the last few years. To the rest of my family members, thank you for supporting me through this process. I am forever indebted to you all.

My husband, Muhammad Akram Akabor, has been extremely patient and understanding. I thank him for all the assistance he has contributed during the completion of the degree. His help has assisted me on several levels in achieving my goal.

I would also like to thank Dr. Avinash Harilal. The practical knowledge which I have gained under his supervision during the earlier years shall hold me in very good stead in the future.

The financial and academic contribution by SASOL is duly acknowledged. Of particular note, the assistance of Dr. Jonathan Chetty. I have had several mentors from SASOL during my postgraduate years, however, I must admit, he did a fantastic job!

I would like to also thank the technical staff of the University of KwaZulu-Natal, School of Chemistry who had assisted me with some aspect of my thesis during the years.

My sincere gratitude goes out to Dr. Martin Onani and Prof. Krish Bharuth-Ram who have offered their assistance with the HR-TEM and Mössbauer spectroscopy analyses respectively.

A special note of gratitude is directed to my supervisor, Prof. Holger B. Friedrich. His compassion for his students, his commitment to attending to their every needs, as well as his precious advice and motivation, has been the primary factor in my desire to succeed. Thank you for being patient and understanding during the several adversities I have endured during the completion of the thesis.

To my dear friend Venkata Dasireddy. I will never be able to repay you for all the help you have provided during the years. Thanks for the motivation and most importantly, thanks for being a friend when I needed someone the most.

Last but not least, to my little baby boy, Muhammad Yaseen. When you are able to read this, I would like you to know that I am grateful to have you and you have been a primary source of motivation during the completion of this thesis.

CONTENTS

This dissertation is written as a series of eight chapters

Chapter 1 gives an overall introduction to catalysis.

Chapter 2 provides a literature review which introduces alkyl methacrylates and iron phosphate catalysts as well as the motivation for this study.

Chapter 3 introduces the preparation and characterization techniques for the catalyst, the catalytic testing procedure and the analytical methods used to interpret the data.

Chapter 4 contains the characterization results for the unpromoted iron phosphate catalyst.

Chapter 5 contains the catalytic testing results for the unpromoted iron phosphate catalyst.

Chapter 6 contains the characterization for the spent unpromoted iron phosphate catalysts.

Chapter 7 contains the characterization and catalytic testing results for the cesium promoted iron phosphate catalysts.

Chapter 8 gives the overall summary and conclusion for the work carried out.

Appendices A-D

TABLE OF CONTENTS

CHAPTER 1

INTRODUCTION TO CATALYSIS

CHAPTER 2

ALKYL METHACRYLATES AND IRON PHOSPHATES

CHAPTER 3

EXPERIMENTAL

Page No.

CHAPTER 4

CHARACTERIZATION OF THE IRON PHOSPHATE CATALYST

Page No.

CHAPTER 5

CATALYTIC REACTIONS

CHAPTER 6

CHARACTERIZATION OF THE SPENT CATALYSTS

Page No.

CHAPTER 7

INVESTIGATION OF CESIUM PROMOTED IRON PHOSPHATE CATALYSTS

LIST OF FIGURES

Page No.

Page No.

Page No.

Page No.

LIST OF TABLES

Page No.

Page No.

LIST OF SCHEMES

CHAPTER 1

INTRODUCTION TO CATALYSIS

In chemistry and biology, catalysis has been described as the acceleration of the rate of a chemical reaction by a substance called a catalyst [1]. A catalyst is a substance which increases the rate of a reaction without being consumed during the process [2]. Essentially, the catalyst which is added at the start of the reaction is still present and chemically unchanged after the reaction has gone to completion. The diagram depicted below (Fig. 1.1) gives an indication of the effect of the catalyst on a reaction.

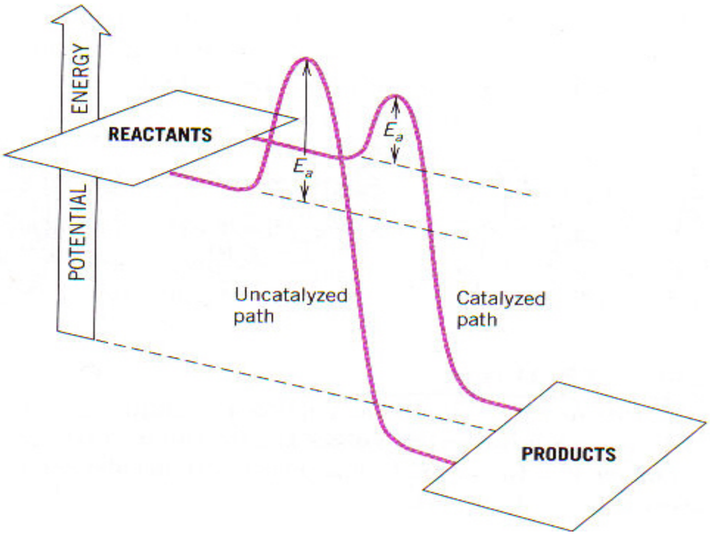

Figure 1.1 Effect of a catalyst on a reaction [2]

The catalyst provides an alternative, lower activation energy pathway than that of the uncatalyzed reaction, starting from the reactants and proceeding to the products. Since the activation energy depicted by the catalyzed route is significantly lower, a larger portion of the reactant molecules have the minimum energy required to react, thus facilitating the reaction to proceed at a greater rate [3].

Catalysts are used in industry, nature and on a laboratory scale and it is estimated that they contribute to one-sixth of the value of all goods manufactured in industrialized countries [3]. Their use has been gaining increasing importance in particular reference to the role of catalysis achieving cleaner environments, both through the destruction of pollutants *via* automotive catalytic exhaust converters, as well as the development of cleaner industrial processes with less abundant by-products [3].

Inorganic catalysts are primarily used for the production of major organic chemicals and petroleum products, such as fuels, petrochemicals and polyalkene plastic.

Table 1.1 shows that 13 of the top 20 synthetic chemicals are produced either directly or indirectly by catalysis [3].

Table 1.1 The top twenty synthetic chemicals [3]

Synthetic Chemical	Rank [#]	Catalytic Process
Sulphuric acid	1	SO_2 oxidation, heterogeneous
Ethylene	2	*a*
Ammonia	3	N_2 + H_2; heterogeneous
Calcium hydroxide	4	Not catalytic
Phosphoric acid	5	Not catalytic
Sodium hydroxide	6	Not catalytic
Propylene	7	*a*
Chlorine	8	Electrocatalysis, heterogeneous
Sodium carbonate	9	Not catalytic
Urea	10	*b*
Nitric acid	11	NH_3 + 0_2; heterogeneous
1,2-Dichloroethane	12	C_2H_4 + CI_2; homogeneous
Ammonium nitrate	13	*b*
Vinyl chloride	14	Chlorination of C_2H_4; heterogeneous
Benzene	15	Petroleum refining; heterogeneous
Ethylbenzene	16	Alkylation of benzene; homogeneous
Carbon dioxide	17	Not catalytic
Methyl tert-butyl ether	18	Heterogeneous
Styrene	19	Dehydrogenation of ethylbenzene;
Methanol	20	CO + H_2, heterogeneous

[#] Based on mass, from Chemical and Engineering News survey of US industrial chemicals April12, (1993), [a] Primarily used in a catalytic polymerization, [b] Synthesis based on starting materials produced by a catalytic process.

Promoter and supports

Impurities for example, poisons, hinder the effectiveness of the catalyst by coordinating strongly to the catalytically active sites. However, other additions such as promoters and supports can have a different effect. Promoters are substances which are not catalytically active, but allow the active phase to function at its maximum capacity [3]. It could also form a layer on the surface of the catalyst to prevent formation of a coat of coke on the surface or even aid in the removal of such material [4]. In addition, promoters can assist with the dispersion of the catalytic material or also bind to the reagent [4]. There are two types of promoters, namely:

Structural promoters: these types of promoters prevent sintering by separating the surface active atoms and thus increase surface area as well as the rate of the reaction.
Electronic promoters: these promoters make the catalyst more selective and active.

Supports can be classed into two categories as well, inorganic and organic. Their properties are tabulated below (Table 1.2):

Table 1.2 Properties of inorganic and organic supports

	Inorganic	**Organic**
Effect of temperature	Good	Poor
Heat transfer	Good	Poor
Chemical reactivity	Reasonable	Inert

Homogenous and heterogeneous catalysis

Catalysis is further classified according to two major categories [3]:

a) *Heterogeneous catalysis:* The catalyst is present in a different phase relative to the reagents.
b) *Homogenous catalysis:* The catalyst is present in the same phase as the reagents; this normally indicates that they are present as solutes in a liquid reaction mixture.

Homogenous catalysts have quite a few advantages over multiphase-heterogeneous catalysts**.** In a homogenous system, each metal centre of the catalyst is a potential site for catalytic activity, as opposed to a heterogeneous system where the reaction proceeds only *via* the surface of the catalyst. Since the homogenous catalyst has a definite stoichiometry and structural orientation as opposed to the heterogeneous catalyst, this results in it being essentially more reproducible. As a result of the type of ligand coordinating to the metal, the oxidation state of the metal and even the metal itself can be controlled, the efficiency and selectivity of homogenous catalysts can be enhanced.

Amidst these impressive advantages, homogenous catalysts have a severe weakness. Since the reaction proceeds in the same phase, it is extremely difficult to separate the products and catalysts on completion of the reaction. Efficient distillation systems are required for the separation of homogenous catalysts, but since the process is endothermic and losses of an expensive catalyst could occur during the process, this may make the separation unfeasible. In contrast, heterogeneous catalysts can easily be separated by filtration.

Heterogeneous catalysts act in a different phase in comparison to the reactant. Most of these catalysts are solid in nature, which act on substrates in a gaseous or liquid reaction mixture. The exact mechanistic route is dependent on the adsorption which takes place [5]. Generally, heterogeneous catalysts are supported, which entails the catalyst being dispersed on a secondary material, thus enhancing effectiveness and lowering the overall cost, although it has been noted that in certain instances the function of the support is to serve as a surface to spread the catalyst and thus increase the surface area [6]. The surface area plays an important role on the reaction rate.

The essence of catalysis is a cycle of reactions which entails the reactants being consumed, formation of products and regeneration of the catalytic species.

Developments related to the understanding of the mechanisms of catalytic reactions has shown a great degree of improvement as a result of advanced methods for determining reaction rates, improved spectroscopic and diffraction methods, as well as the availability of isotopically labelled molecules [3].

A proposed schematic for the determination of a catalytic mechanism is depicted in Figure 1.2.

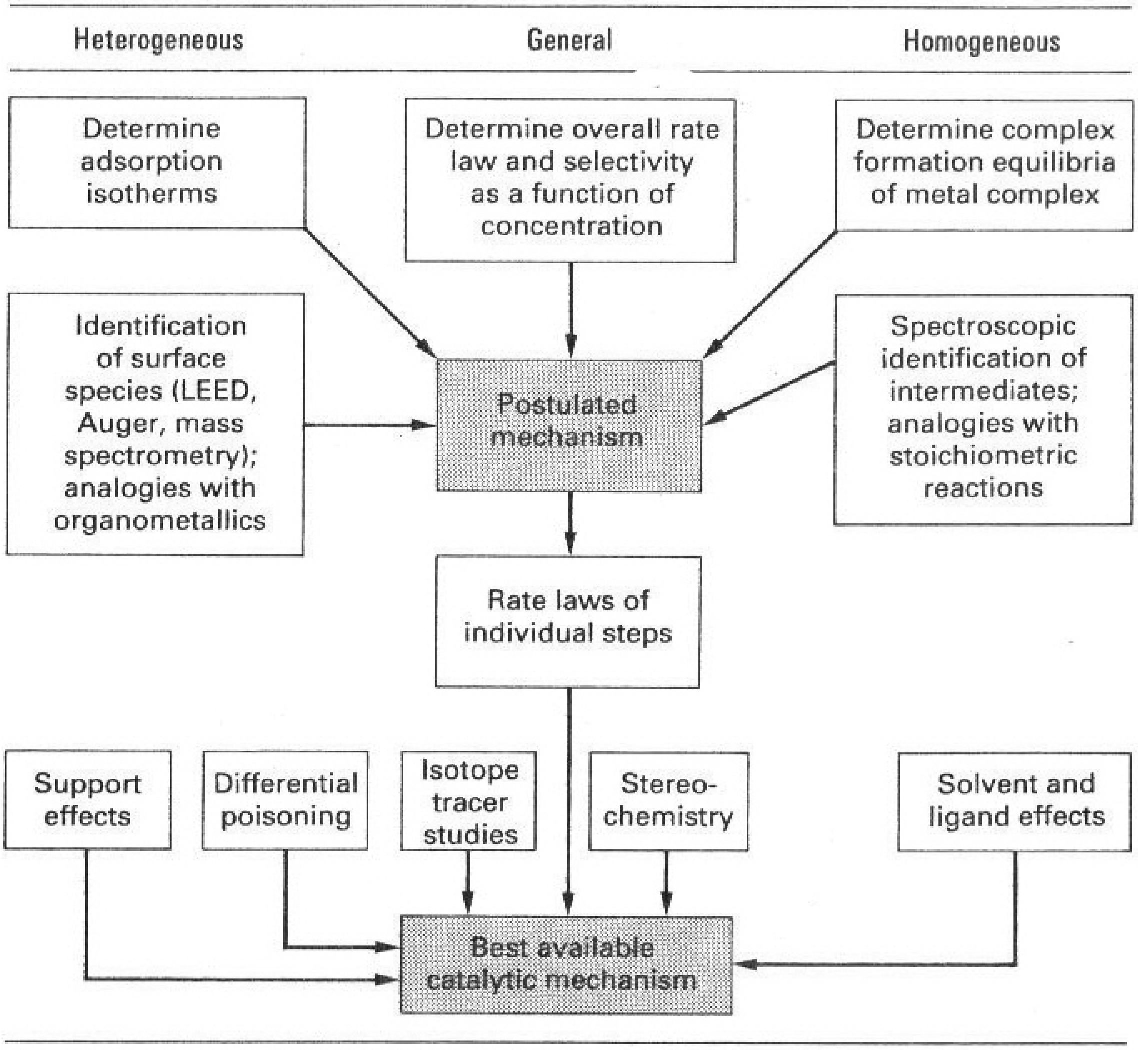

Figure 1.2 Steps for the determination of a catalytic mechanism [3] (Reprinted with permission from Oxford University Press, Oxford)

Although the general idea is depicted in Figure 1.2, the elucidation of catalytic mechanisms is generally complicated by the existence of several delicately balanced reactions, which often cannot be studied in isolation. Generally, heterogeneous catalysts are chosen for a particular reaction depending on conversion rates towards the desired products being considerably higher for the specific catalyst and also that the catalyst is able to remain active for prolonged periods while being subjected to a particular operating condition [7].

1.1 Catalyst deactivation

Catalyst deactivation has been described as an inevitable and slow phenomenon, however certain immediate measures may result in deactivation being partly avoided or even reversed [5]. Fundamental contributors towards catalyst deactivation have been identified as sintering, poisoning and coke formation or foulings where the effects of each of these factors occur separately or in combination, although the eventual outcome is related to the removal of active sites from the surface of the catalyst [5].

Deactivation of the catalyst may result from the adsorption of poisons such as sulphur on metals or alkali on stoichiometric acidic oxide catalysts. During this process, the surface of the catalyst changes and, as a result, the chemical rate constant is altered. However, the catalyst may also sinter and hence result in loss of surface area and a reduction in reaction rate [7].

Poisons are classed as selective seeing that the deactivation occurs by strong adsorption. Sulphur compounds, carbon monoxide and mercury are the most common poisons on metals, however, a range of other compounds, such as any gas which is very strongly adsorbed on metals, certain metal ions and certain compounds of the elements of Group VB and VIB, also result in the deactivation of metal sites [7].

The effect of a poison relative to a foulant is dependent on the chemical nature of both the species as well as the catalyst. The effect of a poison is due to strong adsorption on the surface of the catalyst which results in deactivation, while a foulant masks active sites *via* the deposition of large quantities of material on the surface [7].

The implications of catalyst deactivation impact the lifetime of the catalyst, cause loss of activity and selectivity and can cause process interruption industrially due to during catalyst replacement and regeneration procedures [4].

The formation of coke, as well as the deposition of any unreactive material on the surface of the catalyst, not only masks the surface and hence reduces the concentration of adsorbed species, but also results in the blockage of pores which leads to a reduction in surface area and increasing resistance to mass transfer [7].

1.2 Coking

Coking, which involves the deposition of carbonaceous materials on all types of catalysts, is the most common form of catalyst deactivation. In comparison to sintering, it is usually regarded as reversible by gasification of the carbon with oxygen, carbon oxides, steam or hydrogen [7]. Coke formation is postulated to occur *via* several mechanisms and identification of the particular source from the analysis of the products is difficult, seeing that the coke deposits are quite similar [7]. Coke may contain [7]:

1. Condensed high molecular weight aromatic compounds which may be a liquid or solid (tar).
2. Soot which is produced in the gas phase.
3. Ordered or disordered carbon which is produced on an inert surface (surface carbon).
4. Ordered or disordered carbon which is produced on a surface which catalyses the formation of carbon (catalytic carbon).

A relationship is known to exist between the various forms of coke [6]. All forms of coke deposition result in deactivation of the catalyst; however some are more effective than others.

1.3 Non-oxidative and oxidative dehydrogenation:

Non-oxidative dehydrogenation is a widely practised process; however it does suffer from significant disadvantages, namely [8, 9]:

1. Thermodynamic equilibrium limitations exist, seeing that it is an endothermic process and thus high temperatures are required in order to shift the equilibrium towards dehydrogenation products. This inevitably leads to the formation of cracked products which are considered as products of undesirable side reactions.
2. The occurrence of carbon deposition on the surface of the catalyst is not uncommon due to the lack of oxygen and the need for high operating temperatures. This eventually results in a decrease in catalyst activity and an increased frequency of catalyst regeneration.
3. In all commercial processes, higher operating conditions inevitably impact the economics of the overall process.

In comparison to the disadvantages of non-oxidative dehydrogenation, oxidative dehydrogenation (ODH) has several advantages [10]:

1. Lower operating temperatures are possible during this catalytic process seeing that no thermodynamic equilibrium limitations exist due to the fact that it is an exothermic reaction. Water is produced as a by-product during this reaction, as opposed to hydrogen in the case of the non-oxidative dehydrogenation; hence ODH can

contribute towards the energy requirements, thus making operation possible at lower temperatures.

2. Formation of significant quantities of cracked products is also minimised as a result of the lower temperatures.
3. Coke formation is minimised due to the presence of oxygen in the system and this would inevitably reduce the occurrence of catalyst deactivation.

Although ODH can be more beneficial, there are a few drawbacks which need to be considered and these include the formation of carbon oxides, which are more thermodynamically stable than the dehydrogenation products [10].

Heterogeneous catalysis is the basis for several technologies applicable to the petrochemical industry, bulk chemical production, as well as for pollution abatement [10]. A typical heterogeneous catalytic oxidation reaction occurring at the gas-solid interface involves a mixture of hydrocarbon and oxygen being passed at an elevated temperature through a catalyst bed. The five fundamental steps involving a gas mixture passed through a catalytic reactor are [10]:

1. Reactant diffusion to the active sites on the catalyst.
2. Adsorption of a minimum of one reactant molecule on the surface of the catalyst.
3. Surface reaction for product formation.
4. Product desorption.
5. Difussion from active site.

The rates for steps 1 and 5 are related to porosity as well as diffusion coefficients, while chemical phenomena occurring at the molecular level are the defining parameters for steps 2-4. It is possible that any of the steps listed above could represent the slow step for the process. Evaluations which are of importance to consider during the catalytic testing include conversion of the reactant/s as well as selectivity and yield of the target product.

1.4 Kinetics of oxidation reactions

Five basic kinetic rate laws exist which describe heterogenous oxidations [11]:

a) Eley-Rideal
b) Langmuir-Hinshelwood (uniform surface with one type of site)
c) Langmuir-Hinshelwood (uniform surface with two types of sites)

d) Power Rate Laws

e) Mars-Van Krevelen (surface oxido-reduction)

A further elaboration on each of these mechanisms is outlined below:

a) Eley-Rideal mechanism

This mechanism involves a simple reaction between an adsorbed species and a second species reacting without adsorbing [10]. Essentially, a gas phase reactant does not reside on the surface of the catalyst for a period longer than 10^{-13} seconds i.e. less than the time specified which defines a physisorbed state, and during this time a reaction occurs with the adsorbed species according to the mechanism [10]. The constraint of the mechanism is related to describing energetically and chemically uniform adsorption and reaction sites. An example of a reaction (eq.1) which follows this mechanism is shown below [12]:

$$CH_4 + O_2 \xrightarrow[Fe_2(MoO_4)_2, 968\ K]{} HCHO + H_2O \qquad (1)$$

b) Langmuir-Hinshelwood mechanism

In this mechanism it is highlighted that when considering the five steps characteristic of a catalysed reaction, the slowest step is the interaction between the two adsorbed species on a uniform catalyst surface. It is stated that adsorption can occur on a single type of surface site or each adsorbing species could adsorb on its own individual type of surface site. However, each adsorbing species is in a thermodynamically equilibrium state with its corresponding gas phase species [10]. Reactions proceeding *via* the Langmuir-Hinshelwood mechanism are shown below in Equations 2 and 3 [11, 13]:

$$C_4H_6 + 2.5\ O_2 \xrightarrow[VPO, 623\ K]{} HCHO + H_2O \quad \{uniform\ surface\ with\ one\ type\ of\ site\} \qquad (2)$$

$$C_2H_4 + 0.5\ O_2 \xrightarrow[Ag/Al_2O_3, 493\ K]{} HCHO + H_2O \quad \{uniform\ surface\ with\ two\ type\ of\ site\} \qquad (3)$$

c) Power Rate Laws

This kinetic expression has been classified as an oversimplified rate expression and generally interpretation becomes difficult when fractional exponents are considered. The following reaction can be described with a Power rate equation (eq.4) [14]:

$$CH_4 + N_2O \xrightarrow[Mo/SiO_2, 853\,K]{} HCHO + H_2O + N_2 \qquad (4)$$

d) Mars-Van Krevelen mechanism

The Mars-Van Krevelen mechanism, also referred to as the redox or regenerative mechanism, has been reported as the most common mechanism for heterogeneous oxidation catalysis [10, 15]. The defining feature of this mechanism is that during the process, some of the products formed leave the surface of the solid catalyst with either one or more constituents of the catalysts lattice [15].

The mechanistic process occurs such that the hydrocarbon removes lattice oxygen from the surface of the catalyst thus resulting in a reduced catalyst and during steady state operation; the extent of reduction of the catalyst varies, however this is not deemed as a major factor influencing the kinetics. A defining step of this mechanism is that gas phase oxygen replenishes the lattice oxygen in a reoxidation process [10]. An example of a reaction proceeding *via* the mechanism is shown in equation 5 [16]:

$$C_2H_4 + O_2 \xrightarrow[Pd/V_2O_5, 853\,K]{} CH_3COOH + H_2O + N_2 \qquad (5)$$

1.5 General requirements for oxidation catalysis

In general, catalysts applicable for use in fixed bed reactors are spheres or cylinders, while those considered for application in fluidized and moving bed reactors are powders with uniform particle size [10]. It is essential that the mechanical properties of the catalyst are sufficient during operating conditions such that they do not form ‘fines’ via degradation during the catalytic process [10]. Fines are classified as material which is less than 2/3 of the original size, but generally considered in practise to be less than a 1µm. They are also considered as part of the support or small particles of the supported phase which could have been separated from the original pellet. Fines negatively influence the flow characteristics of the reactor bed due to their effect of clogging interstitial spaces and valves [10].

The heating procedure for fresh catalysts is thus crucial with respect to structure stability. Essentially, the benefits of calcining the catalyst are:

1. Removal of water, impurities and volatile phases.
2. Formation of stable oxides which are not reactive from thermally unstable compounds.
3. Formation of new compounds from decomposition products.
4. Increase in crystallinity.
5. Change in the pore structure and mechanical strength of precipitated catalyst.

During the heating steps, a pressure build-up could result within the pellets due to the effect of steam generation and vaporization of the water [10]. This could lead to cracking of the pellets as well as the supported phases becoming detached because of either loss of adhesion as a result of varying rates of expansion or significant changes in molar volume due to the precursor to active phase transformation process [10].

Two kinds of oxidation reactions exist, namely, a) oxygen insertion reactions and b) ODH [17, 18]. In the case of metal oxides, it is well established that oxidation reactions proceed due to the redox cycle of the metal oxide and hence the oxidation activity is due to the reducibility and reoxidizability of the metal oxide [19]. Thus it has been proposed that when the reducibility of the metal oxide is moderate, the oxidation reaction proceeds selectively [20].

It has been proposed that two factors promote the oxidation reaction of a metal oxide catalyst namely: a) oxygen activation as a result of the redox cycle of the metal oxide and b) reactant molecule activation due to the acid base interaction between the reactant molecules and the metal oxide [19]. The latter factor implying that acidic molecules are activated on basic sites and *vice versa*. In addition, it has been mentioned that selectivity is enhanced when the oxidation reaction is governed by the latter factor [19].

Requirements specified for selective oxidation catalysts include a) possession of reducibility with a moderate strength and b) reactant molecule activation without activation of the target products [19]. It is important to note that these requirements become more complex seeing that selective oxidation reactions are classified into four types which are dependent on acid-base properties of the reactant as well as the product. The acid-base properties specified for metal oxides catalysts are shown in Table 1.3 [19].

Table 1.3 Acid-base properties required for oxidation catalysts [19]

Reaction Type	**Properties of**		**Properties required for metal oxide**
	Reactant	**Product**	
1	base	acid	acidic
2	base	base	Moderate in both acid and base
3	acid	base	basic
4	acid	acid	acidic

Reaction type 1 is termed as ‘acid formation’ while reaction type 2 is considered as ‘base formation’ [19]. Reactant molecules, such as hydrocarbons and aldehydes, form part of the basic (electron-donating) molecules.

In reaction type 1, possession of a strong acidic property is necessary [19]. Phosphates or oxides of vanadium and molybdenum suite the criteria for catalysts applicable to these types of reactions, because they serve as solid acid catalysts and posses moderate redox capability.

Reaction type 2 is characteristic of diene and unsaturated aldehyde formation [19]. Requirements for these types of reactions include moderate acidic and basic properties of the catalyst. Enhanced activity is favoured by the acidic character of the catalyst, however, when this property is considerably high, the reaction does not end at the step of the basic product. Formation of these specific catalysts is *via* the combination of acidic and basic oxides, e.g. Bi-Mo.

Type 3 reactions require catalysts with basic properties seeing that the reactant is acidic and the product is basic. Contrary to this, although type 4 reactions involve acidic reactants, the product is acidic and thus requires a catalyst of acidic nature similar to the type 1 reaction. An example of these types of catalysts include heteropoly acids and an examples of these type of reactions is the ODH of isobutyric acid (IBA) to methacrylic acid (MAA).

Iron phosphates posses both redox and acidic properties similar to that of the phosphates of vanadium and molybdenum and are therefore promising when considering reactions similar to those of type 1 and 4 [19, 21].

References

[1] http://encyclopedia.laborlawtalk.com/Catalysis, (Date accessed 10th January 2009).

[2] J.E. Brady, J.R. Holum, Chemistry: the study of matter and its changes, Wiley, 1993.

[3] D.F. Shriver, P.W. Atkins, C.H. Langford, Inorganic chemistry, Oxford University Press, 1994.

[4] http://www.fhi-erlin.mpg.de/manfred_baerns_catalystdeactivation_110121.pdf, (Date accessed 15th April 2009).

[5] http://herkules.oulu.fi/isbn9514269543/html/c476.html, (Date accessed 15th April 2009).

[6] http://en.wikipedia.org/wiki/Catalysis, (Date accessed 15th April 2009).

[7] J.L. Figueiredo, Progress in catalyst deactivation: proceedings of the NATO Advanced Study Institute on Catalyst Deactivation, Algarve, Portugal, May 18-29, 1981, Martinus Nijhoff Publishers, 1982.

[8] M.M. Bhasin, J.H. McCain, B.V. Vora, T. Imai, P.R. Pujadó, Appl. Catal., A. 221 (2001) 397-419.

[9] E.A. Mamedov, V. Cortés Corberán, Appl. Catal., A. 127 (1995) 1-40.

[10] B.K. Hodnett, Heterogeneous catalytic oxidation: fundamental and technological aspects of the selective and total oxidation of organic compounds, John Wiley, 2000.

[11] H. Mozzanega, J.M. Herrmann, P. Pichat, J. Phys. Chem. 83 (1979) 2251-2255.

[12] K. Otsuka, Y. Wang, I. Yamanaka, A. Morikawa, J. Chem. Soc., Faraday Trans. 89 (1993) 4225-4230.

[13] P.D. Klugherz, P. Harriott, AlChE J. 17 (1971) 856-866.

[14] H.F. Liu, R.S. Liu, K.Y. Liew, R.E. Johnson, J.H. Lunsford, J. Am. Chem. Soc. 106 (1984) 4117-4121.

[15] C. Doornkamp, V. Ponec, J. Mol. Catal. A: Chem. 162 (2000) 19-32.

[16] D. Brklc, F. Trifiro, Industrial & Engineering Chemistry Product Research and Development. 18 (1979) 333-339.

[17] M. Ai, K. Ohdan, in: S.T.O.A.M.G. R.K. Grasselli, J.E. Lyons (Eds.), Stud. Surf. Sci. Catal., Elsevier, 1997, pp. 527-534.

[18] M. Ai, Catal. Today. 52 (1999) 65-69.

[19] M. Ai, Kinet. Catal. 44 (2003) 198-201.

[20] Proceedings of the 3rd International Congress on Catalysis: Amsterdam 20-25 July 1964, North-Holland Publ. Co., 1965.

[21] M. Ai, Catal. Today. 85 (2003) 193-198.

CHAPTER 2

ALKYL METHACRYLATES AND IRON PHOSPHATES

2.1 Introduction to alkyl methacrylates

Alkyl methacrylates are α,β-unsaturated carbonyl compounds and are generally used as building blocks for commercial polymers. Due to the electron-donating effect and the steric hindrance of the α-methyl group of methacrylates, they are generally less reactive than their corresponding acrylates [1]. However, free radical polymers containing the methacrylate backbone are more rigid than acrylate polymers and copolymerisation of the respective methacrylates and acrylates results in hard but flexible polymers which serve important functions in paints, polishes and several other coatings [1]. In addition, methacrylates are able to undergo reactions such as Michael and Michael-type conjugate addition as well as various types of cycloaddition and related reactions [1].

Methacrylate polymers have both indoor as well as outdoor applications due to their clarity, colour compatibility, weatherability and ultraviolet light stability. The primary use of methacrylates are in moulding resins as well as acrylic sheets which have commercial application in signs, displays, glazing compounds, light fixtures, building panels, automotive components, plumbing fixtures and appliances. In addition, they are also used as impact modifiers in poly vinyl chloride (PVC) siding, film, sheet and plastic bottle manufacture [1].

The importance of acrylic and methacrylic monomers and hence the resulting polymers, were initially considered during the doctoral studies of Otto Röhm in 1901 [1]. Although research progressed within this field, it was not until the 1920’s that serious initiatives were carried out in developing commercial processes for producing methacrylate monomers. The initial commercial production of methacrylate monomers began in the 1930’s and was based on acetone cyanohydrins [1,2]. A drawback of this process was the significant quantities of sulphuric acid and ammonium bisulphate which were being produced as by-products and which were difficult to recycle [2]. As a result of the disadvantages of the acetone cyanohydrine process, the chemical industries were pushed into developing novel processes which were less environmentally detrimental.

2.1.1 Routes for the preparation of alkyl methacrylates

One of these processes involved the synthesis of isobutyric acid (IBA) *via* propene carbonylation, followed by oxidative dehydrogenation (ODH) over an iron-phosphate-based catalyst to yield methacrylic acid (MAA), which was further esterified to form methyl methacrylate (MMA) as shown below [2]:

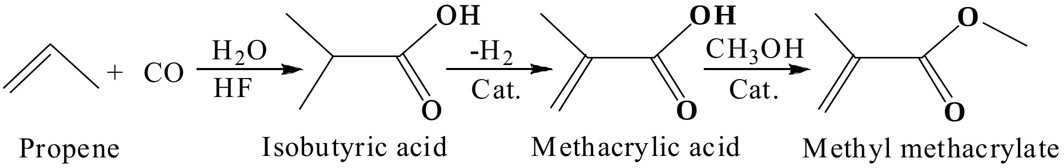

Figure 2.1 Formation of MMA from propene carbonylation

The large scale industrial methacrylate processes are predominantly focussed on the production of MMA or MAA. However, a slight modification of these processes, for example the addition of alkyl alcohols such as ethanol and propanol, as opposed to methanol, result in the formation of the higher alkyl methacylates. Generally, the routes adopted for the production of these higher methacrylates are either by direct esterification from MAA or *via* transesterification of MMA with the desired alcohol [1].

Direct esterification is carried out such that a mixture of water and MAA shifts the equilibrium towards the desired ester [1]. During the process an appropriate solvent is used which aids in removing water azeotropically and hence the reaction is carried out at moderate temperatures. The use of an alcohol for this reaction which has a lower boiling point than water necessitates specialised processing techniques. Direct esterification is favoured under heterogeneously catalysed vapour phase conditions. Primary alcohols are more reactive than secondary alcohols in direct esterification and esterification of tertiary alcohols, which is catalysed by an acid catalyst, is not successful due to elimination reactions resulting in olefins [1]. However, branched alkyl esters can also be prepared by the reaction of olefins with MAA, which is catalysed by a solid acid catalyst. Transesterification is an alternative route for the production of higher alkyl methacrylates as well as functional methacrylates [1]. This reaction is favoured by the use of excess MMA and by the removal of the MMA-methanol azeotrope.

2.1.2 Previous catalytic studies to produce alkyl methacrylates

Abraham P. Gelbeln had carried out catalytic testing in 1983 for the conversion of methyl isobutyrate (MIB) to its corresponding α, β-unsaturated ester, i.e. MMA *via* ODH. It had been shown that the process can occur without the formation of considerable amounts of saturated and α, β-unsaturated acids [3]. The saturated and α, β-unsaturated acids, i.e. IBA and MAA, are formed as a result of hydrolysis of both the feed as well as the target product respectively as shown below [3]:

$$H_3C\text{-}CH(COOCH_3)CH_3 + H_2O \rightarrow H_3C\text{-}CH(COOH)CH_3 + CH_3OH$$

MIB IBA (1)

$$H_2C{=}CH(COOCH_3)CH_3 + H_2O \rightarrow H_3C{=}CH(COOH)CH_3 + CH_3OH$$

MMA MAA (2)

Figure 2.2 Hydrolysis reaction of both MIB as well as MMA

IBA and MAA can be separated, however separation involves a high capital cost to effectuate this process, seeing that separating units need to be built, and expenditure on energy is necessary [3]. In addition, the acids need to be converted back to the corresponding esters and recycled into the process. Formation of the hydrolysis products can be controlled by co-feeding the corresponding alcohol into the system [3].

Generally the respective alcohol is added in molar excess in comparison to the carboxylic acid ester [3]. During the reaction process, the alcohol is preferably added downstream relative to the carboxylic acid ester entrance based on the motivation that it will interact with the feed post reaction between the oxygen and the carboxylic acid ester and thus reduce the occurrence of a reaction between the alcohol and oxygen and hence minimise alcohol loss. It is also noted that addition of the alcohol in combination with the primary feed is a viable option.

During the catalytic testing it was found that the addition of methanol, at a molar ratio greater than unity relative to the feed, hinders the formation of the unwanted hydrolysis products, and in addition methanol oxidation products were not observed. When considering exclusion of the methanol co-feed, the hydrolysis products were formed during this reaction. It was, however, noted that no mention of the additional products which formed during the reaction was made. The catalysts considered for this reaction included supported and unsupported heteropoly acid oxides, activated aluminas, silica alumina, iron phosphorous oxides and transition metal oxides. These various types of catalysts were chosen seeing that they aid in minimising acid formation [3].

Other catalytic testing which has been carried out towards the formation of alkyl methacrylates involves the reaction of alkyl saturated acids and an alkyl alcohol [4]. The investigation makes reference to heterogeneous ODH-esterification catalysts which are selective or dual functioning catalysts having sites for ODH of the α-β hydrogen atoms of the saturated acid and sites for esterification [4]. The catalysts considered included copper, iron and nickel with the acid anions such as arsenate, borate, tungstate, vanadate and phosphate.

In terms of oxidation reactions several catalysts have been considered, however, of particular note are the phosphates of molybdenum, vanadium and iron [5,6,7,8]. Certain molybdate type catalysts such as MoO_3, Bi_2MoO_6, $CoMoO_4$ and $Fe_2(MoO_4)_3$ have been found to be less selective and active than iron(III) phosphates ($FePO_4$) [2]. Although, contrary to this observation, phosphomolybdic heteropolyanions have been shown to be particularly active and selective catalysts for the ODH of IBA to MAA due to the fact that low water vapour pressure is required in the feed to keep the catalyst active. However, the catalyst lacks long-term stability, which makes iron phosphate-based catalysts the preferred option [2].

The phosphates of molybdenum, vanadium and iron were compared in a study by Ai and co-workers [8] involving partial oxidation reactions which were the vapour-phase contact oxidation of 1-butene, crotonaldehyde, methacrylaldehyde, propinaldehyde, butyraldehyde, isobutyraldehyde, propionic acid, butyric acid and isobutyric acid. These reactions contained several types of oxidation mechanisms, namely ODH, oxygen insertion and oxidative C-C bond fission. The C-C bond fission is generally an unwanted side-reaction.

2.2 The favourability of iron phosphates in oxidation reactions

Ai and co-workers [8] had shown that, based on the catalytic results, $FePO_4$ cannot promote oxygen insertion reactions such as in the case of the conversion of 1-butene to maleic anhydride. This could be explained when considering the redox properties of the metal ions. Vanadium and molybdenum phosphates possess oxygen atoms which are not linked to the phosphorous atom, in contrast to $FePO_4$ where each oxygen atom is directly linked with at least one phosphorous atom. The oxygen atoms in vanadium and molybdenum exist as double-bond oxygen [V=O and Mo=O]. As a result, the vanadium and molybdenum phosphates can liberate an oxygen atom by reduction of the metal ions, whilst in the case of $FePO_4$, reduction of the metal ion from a ferric to a ferrous state makes it difficult to liberate an oxygen atom, thus supporting the fact that $FePO_4$ cannot promote oxygen insertion reactions.

Also, iron phosphate catalysts are undesirable for the reactions involving the production of carboxylic acids from aldehydes. When the reactions involving the ODH and oxidation of an aldehyde to an acid take place in competition with one another, e.g. oxidation of butyraldehyde, the iron phosphate catalyst does not allow for acid formation [8].

During the reactions involving the oxidation of carboxylic acids, ODH and oxidative C-C fission take place in competition with each other [8]. It was found that when the carbon atom at the α-position is secondary, as in the case of IBA, the reaction favoured is ODH. However, in the case of propionic acid and butyric acid, the carbon at the α-position is primary and thus the reaction proceeds mainly towards C-C fission. This is due to the fact that the hydrogen at the secondary carbon is more reactive than the hydrogen at the primary carbon. Since the hydrogen-abstracting function of $FePO_4$ is weak relative to vanadium and molybdenum phosphates, this has an influence on the oxidation mechanism of IBA. As mentioned, the hydrogen is more reactive in the case of IBA and thus ODH is favoured when $FePO_4$ is used as the catalyst and less favourable when vanadium and molybdenum phosphates are used.

However, in certain ODH reactions such as the ODH of 1-butene, $FePO_4$ catalysts are not desirable, since the hydrogen-abstracting function of $FePO_4$ is so weak that side-reactions such as C-C fission occur in preference to ODH, due to the low reactivity of hydrogen in the respective reactant.

Thus, it was further elaborated by Ai [9,10] that iron phosphates showed lower oxidation activity as well as lower selectivity in certain partial oxidation reactions in comparison to vanadium and molybdenum phosphates, however, iron phosphates exhibit relatively higher selectivity for the products of the ODH reaction in which the reactants exhibit high reactivity.

Iron phosphates have been used for ODH reactions because the iron cations can easily be oxidized or reduced, resulting in a Fe^{3+}/Fe^{2+} redox couple [11,12]. In an effort to understand the mechanism of the catalytic process much attention must be drawn to the active sites and to the identification of the various active phases of $FePO_4$ which are formed from varying synthetic procedures.

2.3 Preparation of iron phosphate catalyst

There have been a few procedures reported for the synthesis of iron phosphate catalysts [2,13,14,15]:

2.3.1 Precipitation method

The precipitation method involves the mixing of ferric compounds, usually nitrates, dissolved in water with an aqueous solution of either phosphoric acid or ammonium phosphate. The water-soluble nitrate salts are preferred for synthetic procedures seeing that they have desirable solubility and are readily available as well. The mixture is thereafter evaporated, dried in an oven and calcined between 400 ºC and 500 ºC in a stream of air. Silica is usually added as the support [2]. The P/Fe ratio of catalysts prepared *via* the precipitation method is close to unity, based on the stoichiometry of the starting materials. Due to this fact and the temperature of calcination, one could assume the formation of the $FePO_4$ phase in the catalyst. This $FePO_4$ phase has been shown to crystallize with a quartz type structure similar to that of SiO_2. However, Millet and co-worker [16] observed an amorphous phase and a tridymite-like $FePO_4$ phase for these catalysts. It was also interesting to note that all of the catalysts prepared *via* this particular method contained only Fe^{3+}, based on the data obtained from Mössbauer spectroscopy [16].

It was reported by Ai *et al.* [17] that phase transformations occurring after calcination are not associated with any clear difference in mass and heat. Thus it was concluded that it could possibly be the result of agglomeration or sintering [17].

2.3.2 Ammonia gel method

An alternative method for the preparation of the $FePO_4$ catalyst was demonstrated by Ai *et al.* [2,13,17]. In this method an iron hydroxide gel is prepared from a dilute ammonia solution containing iron nitrate. In a heated atmosphere the gel is reacted with an aqueous solution of orthophosphoric acid. The resulting solid was calcined between 500 ºC and 550 ºC. Silica may also be added to the mixture as a support as in the case of the precipitation method. Phases which seemed to be quite predominant in the catalyst synthesised *via* the ammonia gel method were also the amorphous phase, tridymite-like $FePO_4$ phase and

$NH_4FeP_2O_7$ was also observed as a minor phase. In certain instances $FeH_2P_2O_7$ and $Fe(PO_3)_3$ were also observed [2]. The formation of the latter two phases mentioned is attributed to the decomposition of the $NH_4FeP_2O_7$, which formed in larger quantities at lower temperatures [2]:

$$NH_4FeP_2O_7.1.5H_2O \xrightarrow{450\ ^\circ C} NH_4FeP_2O_7 \xrightarrow{500\text{ -}550\ ^\circ C} FePO_4 + NH_3 + \text{polyphosphates}$$

In correlation with the precipitation method, the catalyst consists of only Fe^{3+} cations which were determined by redox titrations [18].

2.3.3 Vivianite method

This method involves reacting vivianite, $[Fe_3(PO_4)_2.8H_2O]$ and $H_4P_2O_7$ with a P/Fe ratio between 1.5 and 4.5 in acetone under reflux. After completion of the 15 hour reaction the solid is filtered, washed with acetone and dried at 100 ºC [14]. Characterisation of the catalyst obtained by the vivianite method showed that the prepared solid was completely amorphous, the $Fe^{3+}/(Fe^{3+}+ Fe^{2+})$ ratios were 0.8 as determined by Mössbauer spectroscopy and the P/Fe ratios determined *via* chemical analysis were between 1.8-2.3 [2,14].

2.3.4 Hydrothermal method

In this method, iron nitrate was reacted with an ammonium hydroxide solution to form an iron hydroxide gel. The gel was thereafter dissolved in orthophosphoric acid prior to the mixture being subjected to hydrothermal treatment for four hours at 175 °C in a Teflon lined autoclave. The resulting white powder was cooled, washed and dried at 100 °C [15]. Prior to calcination, the phase observed for the as prepared catalyst was $FePO_4.2H_2O$. Upon calcination the tridymite-like $FePO_4$ phase was observed from 150 °C, however, at elevated temperatures of 500 °C, a phase change occurred which entailed a transformation of the tridymite-like $FePO_4$ phase to the quartz type $FePO_4$ phase. The complete transformation occurred at 600 °C [15].

2.4 Phase transformations of the iron phosphate catalyst

Iron phosphates undergo various phase changes which are linked to the method of preparation and calcination, as well as the redox atmosphere they are subjected to during catalytic testing.

2.4.1 Effect of calcination

Iron phosphates exhibit varying structures and surface areas which are dependent on the different sources of starting iron(III) phosphates as well as the preparation techniques [13,19]. Freshly calcined $FePO_4$ (with P/Fe ratios of 1.0 ~ 1.3) may contain the amorphous phase, quartz type phase and/or the tridymite-like phase [20]. At present there exists no crystallographic information pertaining to the tridymite-like phase of $FePO_4$, thus identification was based on the $AlPO_4$ analogue of the tridymite-like phase [21,22].

Ai and co-workers [16] had initially observed that $FePO_4$ consisting of a P/Fe ratio of unity undergoes phase transformations during the calcination procedure as follows:

$$\text{Amorphous compound} \xrightarrow{500\ ^\circ\text{C}} \text{Tridymite-like } FePO_4 \text{ phase} \xrightarrow{550\ ^\circ\text{C}} \text{Quartz type } FePO_4 \text{ phase}$$

However, it was later reported that the tridymite-like $FePO_4$ phase was observed as an intermediate between the amorphous and the quartz type $FePO_4$ phase even if calcined until 400 °C [13]. At temperatures above 500 °C, the quartz type phase was formed *via* transformation of either the amorphous or tridymite-like phase [13].

Previous studies carried out had shown that ferric cations corresponding to the tridymite-like $FePO_4$ phase, as opposed to the low quartz type $FePO_4$ phase, render the catalyst precursor more active [11,16,23].

2.4.2 Effect of a redox atmosphere

Muneyama and co-workers [20] had observed that $FePO_4$ which contains an excess of phosphorous is reduced to $Fe_3(P_2O_7)_2$ and not to iron(II) pyrophosphate ($Fe_2P_2O_7$) under catalytic conditions. However, it was also noted that in an oxidising and reducing atmosphere (non-catalytic), catalysts with or without an excess of phosphorous are reduced to $Fe_2P_2O_7$, although in the case of the catalyst containing an excess of phosphorous, reduction occurs *via* the intermediate phase, $Fe_3(P_2O_7)_2$, which was also previously reported by Millet and co-workers [24].

Under oxidising conditions, the reduced $Fe_2P_2O_7$ phase was transformed into the α-$Fe_3(P_2O_7)_2$ phase (α-phase) [2,13,20,25]. The α-phase contains both ferrous and ferric species which makes it favourable in terms of being active and selective for ODH reactions [2,26]. When these cations are close to each other within the same structure, it allows for easier electron mobility and transfer during the catalytic cycle. The α-phase consists of clusters with three face sharing FeO_6 octahedra. This arrangement facilitates the intervalency between the redox couple and limits the electron hopping between the iron cations [27]. The efficiency of these active sites could be related to their limited size, allowing for the stereochemistry of the reactant molecule and that of the surface active site to fit and thereafter a localised electron transfer between them [2].

It has also been reported that catalysts which contain the tridymite-like $FePO_4$ phase, with both low surface area and low crystallinity, which are converted to the α-phase under catalytic conditions, had portrayed the best stability in terms of activity and specific activity [13]. However, catalysts containing the tridymite-like $FePO_4$ phase with high crystallinity and low surface area exhibited low specific activity [13]. Catalysts consisting of the amorphous phase with a high surface area were not stable, but these catalysts showed easy reduction and reoxidation relative to the catalysts consisting of the tridymite-like $FePO_4$ phase. However, catalysts consisting of the tridymite-like phase had shown enhanced activity upon reduction and reoxidation [13].

Based on these observations, it is evident that the tridymite-like $FePO_4$ phase is the most suitable precursor to allow for the formation of the α-phase under catalytic conditions, which is reported to be active and selective in ODH reactions. The previous characterization studies done on iron phosphate catalysts showed that the tridymite-like $FePO_4$ phase is formed in certain preparation methods which were discussed in Section 2.3 [2,13,15,19,28]. This phase was observed primarily post calcination in the precipitation method, ammonia gel method and the hydrothermal method. However, of importance were the phases present during the catalytic testing, and these were dependant on the preparation techniques. The phase transformations reported for iron phosphate catalysts prepared *via* different preparation methods are discussed for the ODH of IBA to MAA [2]:

2.4.2.1 *Precipitation method*

In the precipitation method, activation of the tridymite-like $FePO_4$ phase under catalytic conditions sees the formation of the low quartz type $FePO_4$ phase, $Fe_2P_2O_7$ and the active α-phase [2]. If the α-phase is always present, the quantities of the low quartz type phase and $Fe_2P_2O_7$ are largely dependent on the oxidative-reductive atmosphere during the catalytic testing. It was reported that oxidation of $Fe_2P_2O_7$ at a temperature range between

400 – 500 °C did not result in the formation of the $FePO_4$ phase but rather a combination of two phases, namely, the α-phase and α-Fe_2O_3 [2]. The two phases were reported to have formed in the following proportions [2]:

$$4\ Fe_2P_2O_7 \rightarrow \alpha\text{-}Fe_2O_3 + 2\ \alpha\text{-}Fe_3(P_2O_7)_2 \quad (3)$$

Formation of α-Fe_2O_3 is not desired based on the motivation that iron phosphates have lattice oxygen which is not as active in comparison to iron oxides. This results in iron phosphates being more selective for oxidative catalytic reactions in comparison to iron oxides [28]. In addition, analyses carried out on the activated catalyst showed that there was no homogenous distribution between the phosphorous and the iron. There seemed to have been a phosphorous enrichment on the surface [29]. This inconsistent distribution of phosphorous to iron was considered to limit the oxidation-reduction of the surface cations, as well as the separation of the active sites [30].

2.4.2.2 *Ammonia gel method*

Ai *et al.* have reported the identification of five phases after activation of $FePO_4$ catalysts synthesized *via* the ammonia gel method [17,20,31]. These were the low quartz type $FePO_4$ phase, $Fe_2P_2O_7$, β-$Fe_3(P_2O_7)_2$ (β-phase), α-phase, and a small amount of $NH_4FeP_2O_7$. It was reported that the β-phase was formed upon reduction of $FePO_4$ with an excess of phosphorous and transformation between the α-phase and $Fe_2P_2O_7$ took place reversibly depending on the reduction-oxidation conditions [20]. In addition, it was reported that the reduction of $FePO_4$ without an excess of phosphorous resulted in the formation of $Fe_2P_2O_7$ and no evidence of transformations between the α-phase and less active β-phase was observed under the conditions tested [20].

It has been reported that in comparison to the precipitation method, the ammonia gel method appears to be slightly more advantageous [2]. Activation of the primary phases mentioned previously under catalytic conditions did not result in the formation of the phases $NH_4FeP_2O_7$ or polyphosphates. This could be due to two possible reasons, either the prepared precursors were originally more homogenous or they lost all the ammonia upon heating. However, catalysts which were synthesized *via* this particular method contained the β-phase which is not very active

2.4.2.3 *Vivianite method*

After catalytic testing, the initial amorphous solid prepared *via* the vivianite method transforms into $Fe_2(PO_3OH)P_2O_7$, which is further superficially transformed into an amorphous-phase precursor, which could result in the formation of the α-phase [14]. However, the formation of the β-phase, which is not very active, is not completely avoided [2]. It was reported that the α-phase was formed when the catalysts were tested under low oxygen partial pressures, whereas β-phase formation was attributed to the presence of certain ferrous species in the amorphous precursor [26].

2.4.2.4 *Summary*

From the above consideration, it can be concluded that the ammonia gel method is the most preferable method for the preparation of the iron phosphate catalyst specific to this study. There is no evidence in literature for catalytic testing done on the catalyst prepared *via* the hydrothermal method; however, it was observed that the phases present in the catalyst prepared by the hydrothermal method are in correlation with the catalyst prepared from the ammonia gel method [15].

The use of a support was considered to allow for stabilisation of catalytically active phases during the catalytic reactions as well as other additional functions such as dispersion of active sites, enhancing mass and heat transfer etc. Previously it had been mentioned that silica was the most preferable option as a support for the $FePO_4$ catalyst synthesized *via* the ammonia gel method. Hence it was necessary to investigate the role of supports reported in literature.

2.5 Role of silica as a support

Studies have shown that the interaction between the active metal and the support has an influence on the reducibility as well as the dispersion of the active phase [32]. It has been reported that support materials such as silicas, aluminas, molecular sieves, titania and zirconia serve to either spread out the active sites on the catalyst, enhance mass and heat transfer and also may assist in promoting the catalytic activity of the active catalyst [33].

SiO_2, as well as alundum (aluminium oxide) have been reported to be acceptable supports for the iron phosphate-based catalysts [34]. Colloidal silica which is added to the starting material ensures good mechanical strength [35]. Silica relative to other supports has been shown as the most preferable option in certain oxidation reactions [36,37].

McCormick and Alptekin [38] had tested alumina, silica, zirconia and titania supported iron phosphate catalysts for the selective oxidation of methane. During this study it was shown that relative to each of the support materials tested, silica emerged as the most beneficial and, in addition, produced the highest yield towards oxygenates. This was attributed to the easily reducible iron which is in high coordination and isolated by surface phosphate groups when silica is used as the support.

It was found that for the oxidative bromination of methane, the silica supported iron phosphate catalyst showed a larger surface area as opposed to the unsupported catalyst, and in addition it showed a stable performance with time on stream for 70 hours with no loss in activity after an initial induction period of ~ 30 hrs [25].

As mentioned previously, during catalytic testing the tridymite-like $FePO_4$ phase is transformed into the α-phase and evidence of $Fe_2P_2O_7$ was also noted. It has been mentioned that transformations between the α-phase and $Fe_2P_2O_7$ took place reversibly depending on the reduction-oxidation conditions [20]. It was postulated that the α-phase was derived from the tridymite-like $FePO_4$ phase and $Fe_2P_2O_7$ was formed from $FePO_4$ interacting strongly with the SiO_2 support [25].

The α-phase which was formed by the oxidation of $Fe_2P_2O_7$ appears to be the active and selective phase in its hydrated and oxidised form [2].

$$2\alpha\text{-}Fe_3(P_2O_7)_2 + (x/2)O_2 + 4 - xH_2O \rightarrow 2Fe^{3+}{}_{2+x}\,Fe^{2+}{}_{1-x}\,(PO_3OH)_{4-x}(PO_4)_x \qquad (4)$$

Large quantities of water are necessary for stabilizing the hydroxylated form of the α-phase, which is in fact the actual active phase participating in the ODH reactions [39].

2.6 Effect of water on the iron phosphate catalyst

During ODH reactions, water forms as a by-product of the reaction and hence it should theoretically create a negative effect on the reaction [40]. However, it has been shown to influence the properties of iron phosphates seeing that it favours formation of the hydroxylated active form of the α-phase, acts as a heat transfer agent in ODH reactions, as well as aids in reducing combustion of the carboxylic acids to undesirable waste products [2,40,41].

Water plays a role by displacing the dehydroxylation equilibria of the α-phase to the left [2]:

$$2(PO_3OH)^{2-} \leftrightarrow (P_2O_7)^{4-} + H_2O \text{ for } \alpha\text{-}Fe_3(P_2O_7)_2 \qquad (5)$$

The dehydroxylation was found to occur in the same temperature range as the catalytic reaction involving the ODH of IBA to MAA studied by Millet *et al.* [2] and it was also observed that water prevents dehydration of the catalyst [39]. In the absence of water vapour, the α-phase was not completely deactivated, but rather underwent a slow deactivation as a result of it being hydroxylated on the surface as opposed to the bulk [2]. The use of water vapour during ODH reactions has been studied previously by several authors [39,40,42]. It was reported that water vapour aids in suppressing carbon deposition on the surface of the catalyst as well as the formation of phosphorous rich species, thus preventing degradation in catalytic activity as well as selectivity during the ODH reactions [2,42]. In addition, Muneyama *et al.* [42] proposed that catalyst pre-treatment with water vapour or the inclusion of water vapour with the reactants aids in restoring the activity and selectivity of the deactivated catalyst. Water vapour also aids in removing the oxygenated products from the surface of the catalyst [40,43].

Ernst *et al.* [44] reported that during the ODH of IBA to MAA, water inhibits the reaction by adsorbing on the surface of the catalyst and thus reducing the number of active sites available. It was thus concluded that an optimal value of water in the gaseous phase is necessary. Muneyama *et al.* [45] had later shown that during the ODH of IBA, large quantities of water are required for all iron phosphate-based catalysts to be active and selective. The reactions are generally carried out at optimal values of 10-12 water molecules per molecule of IBA [14,40]. Evidence supporting the benefit of including water during the ODH of IBA showed that a water vapour co-feed suppresses side reactions, such as the decomposition of IBA into propylene and carbon monoxide (CO), and in addition it had also been shown that water, when added to the gaseous feed, aids in the desorption of MAA [42,30].

Based on the above investigations, the use of water vapour as a co-feed was considered, seeing that it has an influence during the reaction, especially in terms of the active α-phase, and also has a positive effect on conversion in oxidation reactions.

Iron phosphates exist in the form of various crystalline phases post calcination and, based on this, it is imperative to determine which of these phases are catalytically active. It has been proposed that certain extrinsic metal components facilitate the formation of the active phase during the preparation stage, namely, alkali or alkaline earth metals [39]. Isolation of the tridymite-like phase of the $FePO_4$ catalyst is essential as a precursor to allow for the formation of the active α-phase. Thus, based on this finding, the use of a suitable promoter was selected on the principle of stabilising the structure of the tridymite-like phase, hence favouring the formation of the active α-phase.

2.7 Use of promoters

Studies involving the use of noble metals as promoters impregnated on iron phosphates have been considered due to the bifunctional behaviour which occurs as a result of the redox property of iron phosphates where the Fe cations can easily be reduced and reoxidised resulting in the Fe^{3+}/Fe^{2+} redox couple, and in addition, because of the activation of reactants over noble metal centres which are supported on the phosphate [12]. It was found that both bivalent as well as highly charged cations were able to stabilise iron phosphates [2].

The effect of various foreign ions as promoters of $FePO_4$ catalysts were evaluated based on the ODH of IBA to MAA. The $FePO_4$ catalyst was prepared via the ammonia gel method and the foreign ions were added prior to calcination [46]. It was found that the addition of Mo^{6+}, V^{5+} and Cr^{3+} as promoters resulted in a substantial decrease in the selectivity towards MAA. However, the addition of U^{6+}, Sb^{3+}, Sn^{2+}, Pb^{2+}, Co^{2+}, Ni^{2+}, Mn^{2+} and alkali metal ions improved the selectivity towards MAA. The most favourable selectivity obtained for MAA was observed for the addition of the Pb^{2+} ion [46].

2.7.1 Lead (Pb) as a promoter

The study involving the ODH of IBA to MAA favouring the use of Pb^{2+} as a promoter had indicated that the addition of Pb^{2+}, which resulted in the formation of an iron-lead-binary phosphate, increased the selectivity towards MAA [46]. It was shown that at the highest selectivity towards MAA, the P/Fe ratio increased as the Pb^{2+} content increased, seeing that a portion of the phosphoric acid was consumed by the formation of the lead phosphate.

Several reports in literature have documented the examples of Pb and Fe (+2 and +3) compounds with varying phosphate groups [47]. $PbFeP_2O_7$ [48], $PbFe_3(P_2O_7)_2$ [49] and $PbFe_2(P_2O_7)_2$ [50] phosphates consist of the $P_2O_7^{4-}$ group with iron cations in varying oxidation states. The Pb present in the iron-lead-binary phosphate was found to exist in the form of $Pb_2P_2O_7$ [46]. The ODH of IBA was carried out using only the $Pb_2P_2O_7$ phase and this had shown that this single phase was less active than iron phosphates [46].

A comparison of the iron-lead binary phosphate and the iron phosphate catalyst prepared with a P/Fe ratio of 1.2 excluding the promoter was carried out [46]. During the ODH of IBA including water as a co-feed, the iron-lead-binary phosphate was less active in terms of the decomposition of MAA relative to the iron phosphate catalyst and the decomposition of MAA via the iron-lead binary phosphate decreased as the water content within the feed increased. It was however also reported that the iron-lead binary phosphate had a lower activity for the ODH of IBA and a lower acidity than the single iron phosphate which may be due to the lower surface area of the iron-lead binary phosphate. Post catalytic testing, it was observed that the iron ions within the iron phosphate were more deeply reduced than those within the iron-lead binary phosphate [46].

The findings of the study indicated that the ODH reaction was favoured by the redox cycle between the ferrous and ferric species which was postulated previously and not due to the $Pb_2P_2O_7$ phase [6,51]. It was suggested that the role of the Pb promoter was in the suppression of the consecutive oxidation of MAA to COx [46].

The benefit of adopting a particular method of synthesis was also mentioned where it was shown that addition of Pb via the impregnation technique was more favourable than via the co-precipitation technique. The results obtained for the reaction had shown that the selectivity towards MAA was significantly lower in the case of the iron-lead binary phosphate synthesized via the co-precipitation technique and this was explained by considering that a homogenous mixture of iron and lead phosphates cannot be obtained, seeing that lead phosphates precipitate significantly faster than iron phosphates [46].

2.7.2 Rhodium (Rh) as promoter

Synthesis of Rh doped $FePO_4$ catalysts with a P/Fe ratio of 1:1 had also shown the effect due to varying methods of preparation [52]. It was found that the Rh doped catalysts prepared via the impregnation technique exhibited the same diffraction pattern as the $FePO_4$ catalyst without the Rh, which was the quartz type $FePO_4$ phase, due to the P/Fe ratio of 1:1.

Rh doped catalysts prepared from mixed aqueous solutions had shown a lower intensity for the most intense peak of the quartz type $FePO_4$ phase, although new reflections were reported which increased with an increase in Rh content. It was considered that these peaks could be due to the tridymite-like $FePO_4$ phase [52]. These findings suggest that Rh influences the crystalline structure of $FePO_4$. Samples which had shown the formation of the tridymite-like

$FePO_4$ phase with an increase in loading also showed a decrease in the temperature of $FePO_4$ reduction. The effect of acceleration of reduction of an oxide by the presence of a noble metal is a well known phenomenon, e.g. Pt/Fe_2O_3 [53], and it is believed that hydrogen is dissociatively chemisorbed on the noble metal and thereafter the H atoms spill over to the metal oxide to further enhance its reduction [54]. It was therefore considered that the Rh(III) species on the surface of the $FePO_4$ was reduced initially by hydrogen, thereafter the Rh^0 would have activated the hydrogen molecules to H atoms. It was concluded that since a single peak was observed for the reduction of the Rh doped $FePO_4$ catalysts, it was plausible that the H atoms were rapidly used for the $FePO_4$ reduction as a result of efficient spillover [52].

It was, however, noted that the peak temperature of reduction for the catalyst prepared by the impregnation technique was lower than for the catalyst prepared via the mixture of aqueous solutions. It was suggested that the Rh^{3+} ions were incorporated into the lattice of $FePO_4$ for the samples prepared via the mixture of aqueous solutions. Reduction by hydrogen of isolated Rh^{3+} ions within the lattice would be difficult compared to surface Rh(III) species hence resulting in high-temperature shifts and broadening. Also, diffusion of hydrogen molecules and not spillover of H atoms to the lattice may also cause broadening of the reduction peak [52].

The use of Pb and Rh promoters as examples has motivated the necessity for including promoters in the $FePO_4$ catalyst. In another study it was further suggested that iron phosphate catalysts which are prepared with alkaline elements (A) in large stoichiometric quantities crystallize in a tridymite-like $FePO_4$ structure prior to catalysis and post catalytic testing leads to the occurrence of three phases, namely, $Fe_2P_2O_7$, $AFeP_2O_7$ and the α-phase [2]. It has been mentioned that ODH catalysts containing alkaline elements such as K, Rb and Cs exhibit higher selectivities and activities towards ODH products [16].

2.7.3 Cesium (Cs) as a promoter

The use of $Fe_2P_2O_7$ and cesium/iron pyrophosphate ($CsFeP_2O_7$) has been reported for the ODH of IBA to MAA [16]. It was found that pure $CsFeP_2O_7$ exhibits poor catalytic selectivity for the ODH reaction and, in addition, no significant synergy effect was observed during this reaction when using mixed phases of $Fe_2P_2O_7$ and $CsFeP_2O_7$.

In the above study, three catalysts, $Fe_2P_2O_7$, $CsFeP_2O_7$ and an industrial type cesium promoted iron phosphate catalyst were compared for the ODH of IBA to MAA [16]. It was found that the $CsFeP_2O_7$ showed a higher selectivity for acetone and the lowest selectivity for MAA formation as compared to $Fe_2P_2O_7$ and the industrial type catalyst. Characterisation of the spent catalyst after the catalytic testing showed that $CsFeP_2O_7$ did not undergo any bulk transformations, while phase changes of the industrial type catalyst resulted in the formation of $Fe_2P_2O_7$, $CsFeP_2O_7$ and the active α-phase. The $Fe_2P_2O_7$ catalyst was partially transformed into the α-phase and its catalytic activity was proportional to the quantity of this phase present.

It was reported that intimate mixtures of different phases, e.g. molybdates, could exhibit better catalytic properties in comparison to individual components, although new phases were not found [55, 56]. This is known as the synergy effect. Seeing that the pure $Fe_2P_2O_7$ and $CsFeP_2O_7$ phases could not explain the catalytic properties of the industrial catalyst containing the three phases mentioned above, it was decided to observe the behaviour of intimate mixtures of the $Fe_2P_2O_7$ and $CsFeP_2O_7$ phases [16]. Since the $Fe_2P_2O_7$ phase was modified under catalytic reactions resulting in the formation of a mixture of the $Fe_2P_2O_7$ and α-phase, the study carried out would also show whether a synergy existed between $Fe_2P_2O_7$, $CsFeP_2O_7$ and the α-phase. It was found that the selectivity to MAA decreases with the presence of $CsFeP_2O_7$, although a small synergy effect was observed at low $CsFeP_2O_7$ contents. It was also found that the $CsFeP_2O_7$ phase individually does not affect the efficacy of the industrial catalyst for MAA formation.

It was found that in the presence of cesium, the tridymite-like $FePO_4$ phase could be stabilised in a 95 % pure form for a P/Fe ratio of 1.32, whilst other phases such as $CsFeP_2O_7$ formed only at higher ratios [16]. However, in the absence of cesium, preparation of the catalyst with a P/Fe ratio of 1.33 resulted in a significant amount of unidentified phases. The stabilization of the tridymite-like $FePO_4$ phase due to the excess phosphorous could be explained by the homopolyhedral linkages. Replacement of one $(PO_4)^{3-}$ and one Fe^{3+} by a single $(P_2O_7)^{4-}$ within the structure of the $FePO_4$ creates an excess of negative charges which could be compensated by cations within the channels of the tridymite structure which are large enough to accommodate monovalent cations such as cesium. This creates a solid solution with the following formulae [16]:

$$Fe_{1-x}A_x(PO_4)_{1-2x}(P_2O_7)_x \qquad \text{where} \qquad A=H, Ag, Cu, Na, K, Rb, Cs \text{ etc.}$$

The value of x was considered dependent on two factors which the temperature and nature of the monovalent cation [16].

The role of cesium is believed to neutralise the surface acidity of the catalyst [56, 57]. It could also play a role during catalyst preparation where an enrichment of the surface in active sites or phases could result, thus creating a surface dopant effect described previously [58]. It was found that cesium was not homogenously distributed all over the crystallites [16]. Also, the existence of cesium at the surface of the active and selective phases could either neutralise the Brønsted sites or increase the mobility of the bulk oxygen atoms [56, 57]. Acidity favours the decarboxylation of IBA resulting in the formation of propene [59]. The results had shown that there was a decrease in propene formation with cesium content increase, hence eliminating the presence of acid sites. The Mössbauer data for the ferric ions of the alkaline/iron phosphate type catalyst were similar to those of the pure iron phosphate type catalysts indicating that the alkaline element did not increase the iconicity of the Fe-O bond and hence the mobility of the oxygen ions. It could also be plausible that cesium modifies the hydration state of the surface of the α-phase which was found to be beneficial during catalytic testing [16].

The use of a cesium as a promoter for the $FePO_4$ catalyst in comparison to lead and rhodium is linked to several beneficial effects of cesium. This includes the fact that it exhibits higher selectivities and activities towards ODH products; it aids in the formation of the tridymite-like $FePO_4$ phase and thus favours the formation of the active α-phase under catalytic conditions [16].

2.8 Motivation for this study

The findings reported in this literature summary have shown the importance of alkyl methacrylates in the chemical industry. Major commercial applications of MAA and its esters arise from the free-radical polymerisation reactions [1]. Although extensive information is available for the applications of MMA, the use of higher alkyl methacrylates is also evident. Ethyl methacrylate (2-methyl-2-propenoic acid ethyl ester, ethyl α-methylacrylate) (EMA), is described as a reactive monomer which can be readily polymerized with itself or another monomer resulting in the formation of thermoplastic and thermosetting polymers [60]. Some of the other uses of EMA include [61,62]:

- resins and dispersions for paints, varnishes and inks.
- usage in solvents, oil additives, dental products.
- aqueous dispersions for textiles and leather.
- a chemical intermediate in organic synthesis.

- A co-monomer in polyvinylidene chloride, high impact polystyrene, polyvinyl chloride, polyethylene and polystyrene.
- synthetic rubbers and lattices.

The aim of this study is focussed on the synthesis of EMA via ODH of its corresponding carboxylic acid ester (EIB). The oxidative route chosen was based on previous studies involving the synthesis of MMA [3]. It was also necessary to choose a suitable catalyst which would favour the ODH reaction, seeing that literature had described several types of catalysts as possible candidates to favour ODH [4]. These included supported and unsupported heteropoly acid oxides, activated aluminas, silica alumina, iron phosphorous oxides and transition metal oxides, seeing that they aid in minimising acid formation.

Heteropoly compounds, such as 12-molybdophosphoric acid, have been used for several chemical reactions due to their tuneable acidic and redox properties [63]. However, a drawback of this compound is its structural complexity, low thermal stability and poor reproducibility of synthetic methods, e.g. apart from considering the calcination temperature, the rate at which the sample is treated also has an effect on the final structure [64].

A comparison between the phosphates of vanadium, iron and molybdenum for oxidation reactions with varying oxidation mechanisms such as ODH, oxygen insertion and oxidative C-C bond fission was made by Ai *et al.* [8]. This study allowed for clarity in terms of the specific applications of each of these catalysts. It was found that iron phosphates are more selective than vanadium and molybdenum phosphates for the ODH of isobutyraldehyde and isobutyric acid. This could be explained when considering ODH reactions for each of the phosphates. It was found that for vanadium and molybdenum phosphates, the hydrogen is abstracted by lattice oxygen:

$$\text{R-H} + \text{O} \rightarrow \text{R} + \text{OH} \qquad (6)$$

Whilst in the case of iron phosphates, which cannot liberate oxygen atoms, it is postulated that reduction of the ferrous ion occurs *via* the abstraction of a hydrogen atom from a hydrogen-donating compound [R-H], e.g. IBA:

$$\text{Fe}^{3+} + \text{R-H} \rightarrow \text{Fe}^{2+}\text{H}^{+} + \text{R} \qquad (7)$$

The Fe^{3+} ions are regenerated via reoxidation of hydrogen phosphate by molecular oxygen:

$$Fe^{2+}H^{+} + 0.25\ O \rightarrow Fe^{3+} + 0.5\ H_2O \qquad (8)$$

This explains why iron phosphates promote only ODH but not oxygen insertion reactions.

In certain ODH reactions, such as the ODH of 1-butene, iron phosphates are not desirable catalysts because the hydrogen-abstracting functions of iron phosphates are so weak that side-reactions such as C-C fission occur in preference to ODH, when the reactivity of hydrogen in the respective reactant is low. When considering the reactant being investigated in this study, EIB, the possibility of oxygen insertion reactions would be eliminated using an iron phosphate catalyst and, since the hydrogen is more reactive at the carbon atom at the α-position in the case of EIB, this in turn would favour the use of iron phosphate due to its weak hydrogen-abstracting function and hence ODH should occur as opposed to C-C fission.

These observations further strengthened the choice to use iron phosphates as the catalyst for the ODH reactions. Other challenges were the method of synthesis of the catalyst, the phases formed after calcinations, as well as the active phases necessary for the catalytic testing, more specifically the active phase necessary for ODH reactions.

Four synthetic procedures were reported, namely, the precipitation method, ammonia gel method, vivianite method and the hydrothermal method [2,13,14,15]. Prior to the selection of the synthetic procedure, it was necessary to determine the active phases which were selective for ODH reactions. Millet [2] reported that phases containing both ferrous and ferric species in large quantities, such as the α-phase, are very active and selective for ODH reactions. The α-phase has a thermodynamically possible redox couple relative to its reactants. It exists as a mixed-valence phase at steady state. It favours a limited electron transfer between metallic cations. It has bulk proton mobility, which should be maximum under the conditions of the catalytic reactions used generally [2]. Based on this, it was necessary to determine a suitable precursor to allow for the formation of the active α-phase. Three major phases were recorded for the iron phosphate catalysts synthesized via the four techniques. These were, amorphous $FePO_4$, low quartz type $FePO_4$, and tridymite-like $FePO_4$.

Reports had mentioned that ferric cations corresponding to the tridymite-like $FePO_4$ phase, as opposed to the low quartz type $FePO_4$ phase, render the catalyst precursor to be more active [11,16,23]. In addition, formation of the less active β-phase was due to the presence of an amorphous precursor [26]. Also, it was found that the tridymite-like $FePO_4$ phase under redox conditions resulted in the formation of the α-phase during ODH reactions [2,13,20,25].

Hence it was decided to adopt a synthetic route which would favour the formation of the tridymite-like $FePO_4$ phase.

This phase was reported after calcination in the precipitation method, ammonia gel method and the hydrothermal method. The selection of the preferential method was based on the fact that in comparison to the precipitation method, the ammonia gel method appears to be slightly more advantageous seeing that activation of the primary phases under catalytic conditions did not result in the formation of the phases $NH_4FeP_2O_7$ and polyphosphates, which was due to either the prepared precursors being originally more homogeneous or they lost all the ammonia upon heating [2]. For the hydrothermal method, there was no evidence in literature of catalytic testing done on the catalyst prepared via the hydrothermal method relative to ODH reactions; however, it was observed that the phases present in the catalyst prepared by the hydrothermal method were in correlation with those found for the catalyst prepared via the ammonia gel method. Interestingly, it was reported that a phase change occurred which involved the transformation of the tridymite-like $FePO_4$ phase to the quartz type $FePO_4$ phase at 500 °C [15].

The ammonia gel method was selected as the most preferable option to allow for isolation of the tridymite-like $FePO_4$ phase. Included in this method was the addition of a support, in particular, silica. Although several other options for iron phosphates have been reported, colloidal silica ensures good mechanical strength [31,33]. In addition, silica, relative to other supports, has been shown as the most preferable option for several oxidation reactions [34,35]. It was postulated that the α-phase was derived from the tridymite-like $FePO_4$ phase and $Fe_2P_2O_7$ was formed from $FePO_4$ interacting strongly with the SiO_2 support, thus motivating that silica allows for stabilisation of important precursors [25]. McCormick and Alptekin's investigation had shown that silica relative to alumina, zirconia and titania supported iron phosphate catalysts produced the highest yield towards oxygenates during the selective oxidation of methane [36]. In addition, the $FePO_4$ catalyst supported on silica showed a stable performance for time on stream (TOS) experiments with no loss in activity during the oxidative bromination of methane [25].

An important aspect which was taken into consideration was the effect of water. Although the effect of hydrolysis of the feed was considered, the beneficial properties of water appeared to outweigh this. The α-phase was shown to have all the requirements necessary to be an active and selective catalyst in its hydrated and oxidised form for the ODH of IBA to MAA [2]:

$$2\alpha\text{-}Fe_3(P_2O_7)_2 + (x/2)O_2 + 4 - xH_2O \rightarrow 2Fe^{3+}{}_{2+x}\,Fe^{2+}{}_{1-x}\,(PO_3OH)_{4-x}(PO_4)_x \qquad (9)$$

The α-phase was indeed reported as the true phase responsible for the ODH reaction. The catalyst surface was considered as a ‘breathing’ structure oscillating between oxidised, reduced or hydrated forms [2]. Hence the use of water would enhance the formation of the hydrated active form of the α-phase.

Water was reported to act as a heat transfer agent in ODH reactions as well as an aid in reducing combustion of the carboxylic acids to undesirable waste products [2,38,39]. In addition, water prevents carbon deposition on the catalyst surface; removes phosphorous species from the surface of the catalyst, restores the activity of a deactivated catalyst, removes oxygenated products from the surface of the catalyst, has a positive effect on conversion in oxidation reactions and prevents side reactions such as the decomposition of IBA into propylene and carbon monoxide (CO) during the ODH of IBA, and when water is added to the gaseous feed it aids in the desorption of MAA as well [2,33,38,40,41].

It was also mentioned in literature that the addition of alkali or alkaline earth metal promoters during the preparation stages of iron phosphates favours the formation of certain phases [39]. The aim of this study was to isolate the tridymite-like phase of the $FePO_4$ catalyst and suitable metals as promoters were investigated. Initial reports had shown Pb as being the preferred option for the ODH reaction involving the conversion of IBA to MAA [45]. However, it was found that the ODH reaction was favoured due to the redox cycle between the ferrous and ferric species which was postulated previously and not due to the $Pb_2P_2O_7$ phase [6,50]. The role of the Pb promoter was in the suppression of the consecutive oxidation of MAA to COx. The method of promoted catalyst synthesis was also considered in this study. It was found that addition of Pb *via* the impregnation technique was more favourable than *via* the co-precipitation technique. This was due to the selectivity towards the target product MAA being lower in the case of the iron-lead-binary phosphate synthesized *via* the latter technique. This was explained by considering that a homogenous mixture of iron and lead phosphates cannot be obtained, seeing that lead phosphates precipitate significantly faster than iron phosphates [45].

The importance of the method of preparation was further shown by the use of Rh as a promoter for $FePO_4$ [51]. $FePO_4$ catalysts prepared *via* the impregnation technique exhibited the same diffraction pattern as the $FePO_4$ catalyst without the Rh, which was the quartz type $FePO_4$ phase, due to the P/Fe ratio of 1:1 [51]. Catalysts prepared from mixed aqueous solutions had shown a lower intensity for the most intense peak of the quartz type $FePO_4$ phase, although new reflections were reported which increased with an increase in Rh content which were postulated to be due to the tridymite-like $FePO_4$ phase. This suggested that promoters may influence the crystalline structure of $FePO_4$.

Although the preparation technique which involved mixed aqueous solutions had shown a change in the $FePO_4$ structure from the quartz type $FePO_4$ phase to the tridymite-like $FePO_4$ phase with increase in Rh loading and in addition the temperature of $FePO_4$ reduction was significantly lowered, it was found that the peak temperature of reduction for the catalyst prepared by the impregnation technique was lower than the catalyst prepared *via* the mixture of aqueous solutions. It was suggested that the Rh^{3+} ions were incorporated into the lattice of $FePO_4$ and thus reduction by hydrogen of isolated Rh^{3+} ions within the lattice would be difficult compared to surface Rh^{3+} species.

The idea of phase stabilisation was considered based on the role of cesium. Cesium was found to favour the formation of the tridymite-like structure of $FePO_4$ in an almost pure (95 %) state by using a P/Fe ratio of approximately 1.3. Under catalytic activation, it favours the formation of the α-phase, which was found to be the most selective and active phase for MAA formation during the ODH of IBA, in its hydroxylated and partly oxidised form [16]. In addition, it has been reported that cesium is the most efficient promoter relative to the alkaline metals, silver (Ag) and Pb based on the findings that incorporation of cesium into the structure of the $FePO_4$ catalyst allows it to play a role during the ODH of IBA in increasing the activity and selectivity to MAA at the expense of acetone and CO_2 [2].

The motivation discussed above defines the scope of this study, which is as follows:

- The reaction will involve the ODH of EIB to form EMA.
- The catalyst selected as being the most beneficial, which was the iron phosphate type catalyst, will be synthesized *via* the ammonia gel method.
- The support used will be colloidal silica.
- The addition of a promoter during the synthetic procedure, as well as the addition of water, will be investigated during the catalytic testing amongst other additional variables, such as the addition of the primary alcohol, ethanol.

References

[1] R. Wilczynski, J. Jerrick Juliette, Kirk-Othmer Encyclopedia of Chemical Technology, John Wiley & Sons, Inc., (2000) 227-270.

[2] J.-M.M. Millet, Catal. Rev. Sci. Eng. 40 (1998) 1-38.

[3] A.P. Gelbeln, in: E. Patent (Ed.), CHEM SYSTEMS Inc., 1983.

[4] D. Chelliah, P.L. Brusky, in: A.O. Inc (Ed.), United Kingdom, 1982.

[5] O. Watzenberger, G. Emig, D.T. Lynch, J. Catal. 124 (1990) 247-258.

[6] M. Dekiouk, N. Boisdron, S. Pietrzyk, Y. Barbaux, J. Grimblot, Appl. Catal., A. 90 (1992) 61-72.

[7] I. Matsuura, Stud. Surf. Sci. Catal. 72 (1992) 247-254.

[8] M. Ai, E. Muneyama, A. Kunishige, K. Ohdan, Bull. Chem. Soc. Jpn. 67 (1994) 551-556.

[9] M. Ai, Catal. Today. 52 (1999) 65-69.

[10] M. Ai, Kinet. Catal. 44 (2003) 198-201.

[11] J. Mingzhi, C. Xianhao, X. Weiming, L. Milang, Hyperfine Interact. 41 (1988) 645-648.

[12] M.M. Gadgil, S.K. Kulshreshtha, J. Solid State Chem. 111 (1994) 357-364.

[13] M. Ai, K. Ohdan, Appl. Catal., A. 180 (1999) 47-52.

[14] P. Bonnet, J.M.M. Millet, C. Leclercq, J.C. Védrine, J. Catal. 158 (1996) 128-141.

[15] A.M. Beale, G. Sankar, J. Mater. Chem. 12 (2002) 3064-3072.

[16] J.-M.M. Millet, J.C. Vedrine, Appl. Catal. 76 (1991) 209-219.

[17] M. Ai, E. Muneyama, A. Kunishige, K. Ohdan, J. Catal. 144 (1993) 632-635.

[18] M. Ai, E. Muneyama, A. Kunishige, K. Ohdan, Catal. Lett. 24 (1994) 355-362.

[19] P. Nagaraju, C. Srilakshmi, N. Pasha, N. Lingaiah, I. Suryanarayana, P.S. Sai Prasad, Catal. Today. 131 (2008) 393-401.

[20] E. Muneyama, A. Kunishige, K. Ohdan, M. Ai, J. Catal. 158 (1996) 378-384.

[21] H. Graetsch, Acta Crystallogr., Sect. C: Cryst. Struct. Commun. 56 (2000) 401-403.

[22] H. Graetsch, Acta Crystallogr., Sect. C: Cryst. Struct. Commun. 57 (2001) 665-667.

[23] M.M. Gadgil, S.K. Kulshreshtha, J. Solid State Chem. 113 (1994) 15-20.

[24] J.-M.M. Millet, J.C. Vedrine, G. Hecquet, in: G. Centi, F. Trifiro (Eds.), Stud. Surf. Sci. Catal., Elsevier, 1990, pp. 833-841.

[25] R. Lin, Y. Ding, L. Gong, W. Dong, J. Wang, T. Zhang, J. Catal. 272 (2010) 65-73.

[26] P. Bonnet, J.M.M. Millet, J. Catal. 161 (1996) 198-205.

[27] J.C. Vedrine, G. Coudurier, J.-M.M. Millet, Catal. Today. 33 (1997) 3-13.

[28] D. Yu, C. Wu, Y. Kong, N. Xue, X. Guo, W. Ding, J. Phys. Chem. C. 111 (2007) 14394-14399.

[29] Y. Barbaux, M. Dekiouk, D. Le Maguer, L. Gengembre, D. Huchette, J. Grimblot, Appl. Catal. A, 90 (1992) 51-60.

[30] P.A. Agaskar, L. Caul, R.K. Grasselli, Catal. Lett. 23 (1994) 339-351.

[31] E. Muneyama, A. Kunishige, K. Ohdan, M. Ai, J. Mol. Catal. 89 (1994) 371-381.

[32] M.A. Banares, J.L.G. Fierro, J.B. Moffat, J. Catal. 142 (1993) 406-417.

[33] D. Chelliah, P. L. Brusky, in Ashland Oil, Inc, U.K. Patent, GB2092572, 1981.

[34] D. Chelliah, P. L. Brusky, in Ashland Oil, Inc, U.S. Patent, 4,331,813, 1982.

[35] H.H.I. Teng, N.J. Waldwick, E. Pedersen, in: S.O. Inc (Ed.), U.S. Patent, 4,473,707, 1984.

[36] A. Parmaliana, F. Arena, J. Catal. 167 (1997) 57-65.

[37] Q. Sun, J.-M. Jehng, H. Hu, R.G. Herman, I.E. Wachs, K. Klier, J. Catal. 165 (1997) 91-101.

[38] R.L. McCormick, G.O. Alptekin, Catal. Today. 55 (2000) 269-280.

[39] J.M.M. Milleta, M. Forissier, D. Rouzies, P. Bonnet, J.C. Vedrine, Stud. Surf. Sci. Catal., 101(1996) 1011-1020.

[40] D. Rouzies, J.M.M. Millet, D. Siew Hew Sam, J.C. Védrine, Appl. Catal., A. 124 (1995) 189-203.

[41] D. Chelliah, in Ashland Oil, Inc, U.S. Patent, 4,390,725, 1983.

[42] E. Muneyama, A. Kunishige, K. Ohdan, M. Ai, Catal. Lett. 31 (1995) 209-220.

[43] O. Watzenberger, G. Emig, Stud. Surf. Sci. Catal., Elsevier, 72 (1992) 71-80.

[44] V. Ernst, Y. Barbaux, P. Courtine, Catal. Today. 1 (1987) 167-180.

[45] E. Muneyama, A. Kunishige, K. Ohdan, M. Ai, Appl. Catal., A. 116 (1994) 165-177.

[46] M. Ai, E. Muneyama, A. Kunishige, K. Ohdan, Appl. Catal., A. 109 (1994) 135-146.

[47] A.P. Malakho, V.A. Morozov, K.V. Pokholok, B.I. Lazoryak, G. Van Tendeloo, Solid State Sci. 7 (2005) 397-404.

[48] E.L. Belkoneva, O.V. Dimitrova, A.A. Ruchkina, Russ. J. Inorg. Chem. 44 (1998) 1507-1512

[49] A. Elmarzouki, A. Boukhari, A. Berrada, E.M. Holt, Solid State Sci. 118 (1995) 202-205.

[50] A. Boutfessi, A. Boukhari, E.M. Holt, Acta Crystallogr., Sect. C: Cryst. Struct. Commun. 52 (1996) 1594-1597.

[51] C. Virely, M. Forissier, J.-M.M. Millet, J.C. Védrine, D. Huchette, J. Mol. Catal. 71 (1992) 199-213.

[52] Q. Yuan, Q. Zhang, Y. Wang, J. Catal. 233 (2005) 221-233.

[53] G. Frohlich, W. M. H. Sachtler, J. Chem. Soc., Faraday Trans. 94 (1998) 1339-1346.

[54] W.C. Conner, J.L. Falconer, Chem. Rev. 95 (1995) 759-788.

[55] D. Carson, G. Coudurier, M. Forissier, J.C. Vedrine, A. Laarif, F. Theobald, J. Chem. Soc., Faraday Trans. 1 F. 79 (1983) 1921-1929.

[56] P. Ruiz, B. Zhou, M. Remy, T. Machej, F. Aoun, B. Doumain, B. Delmon, Catal. Today. 1 (1987) 181-195.

[57] O. Watzenberger. G. Emig and D.T. Lynch, J. Catal., 114 (1990) 7-10.

[58] M. Houalla, F. Delannay, B. Delmon, J. Phys. Chem. 85 (1981) 1704-1709.

[59] W.D. Mross, Catal. Rev. 25 (1983) 591-637.

[60] M. Ai, J. Catal. 98 (1986) 401-410.

[61] http://ema.ecem.nl/, (Accessed on 10th February 2009).

[62] http://www.chemicalland21.com/arokorhi/industrialchem/functional%20Monomer/ETHYL%20METHACRYLATE.htm, (Accessed on 12th February 2009).

[63] http://cpf.jrc.it/smt/monomers/pm20890.html, (Accessed on 12th February 2009).

[64] N. Mizuno, M. Misono, Chem. Rev. 98 (1998) 199-218.

[65] C. Srilakshmi, N. Lingaiah, I. Suryanarayana, P.S.S. Prasad, K. Ramesh, B.G. Anderson, J.W. Niemantsverdriet, Appl. Catal., A. 296 (2005) 54-62.

CHAPTER 3

EXPERIMENTAL

3.1 Reagents used for synthesis and characterisation

1. Iron(III) nitrate-9-hydrate: $FeNO_3.9H_2O$, 96 %, MM = 404 g/mol, Batch No.: 1026562, Merck Chemicals (PTY) LTD.
2. Ammonium hydroxide: NH_4OH, 25 %, MM = 35.05 g/mol, Batch No.: 11122 A, Associated Chemical Enterprises.
3. Orthophosphoric acid: H_3PO_4, 98 %, MM = 98.00 g/mol, Batch No.: 4198, Rochelle Chemicals.
4. Ludox® AS-40 colloidal silica: SiO_2, 40 wt% suspension in water, FW = 60.09 g/mol, d = 1.295, Lot No.: 12905 EI, Aldrich Chemical Company.
5. Cesium nitrate: $CsNO_3$, 99 %, FW = 194.91 g/mol, Batch No.: 44996TJ, Aldrich.
6. Iron, phosphorous and cesium ICP standard solutions (in 0.5 N sulphuric acid), Polychem Supplies cc.
7. Aqua regia: a) Nitric Acid: HNO_3, 55 %, MM = 63.01 g/mol, Batch No.: 291104 NC, Rochelle Chemicals
   b) Hydrochloric Acid: HCl, 32 % extra pure, MM = 36.36 g/mol, Lot No.: 30920, Riedel-de-Haen

3.2 Synthesis of the unpromoted and promoted iron phosphate catalysts

3.2.1 Synthesis of the iron phosphate catalyst

The catalyst was synthesized *via* the method outlined by Ai *et al.* [1]. Since the established method focuses on the large scale production of the catalyst, the values indicated for the synthesis have been scaled down by a factor of 10. The procedure was carried out as follows.

A quantity of 12.2 g of iron(III) nitrate was dissolved in 500 mL of double distilled water. The mixture was magnetically stirred until a pale orange solution was observed. Thereafter dilute ammonia was added drop-wise to precipitate the iron hydroxide gel. The supernatant solution was thereafter left on the bench top for approximately 5 minutes to allow the iron hydroxide precipitate to settle. This was followed by the solution being decanted and the precipitate filtered using a Buchner funnel and flask.

The precipitate was then placed on a hotplate and magnetically stirred, while an amount of approximately 2 g colloidal silica and approximately 3 g of 85 % orthophosphoric acid were added successively to the iron hydroxide gel. The resulting solution was then heated at approximately 75 °C and stirred on a hotplate for a period between 1-2 hours.

This yielded a light brown paste which was immediately placed in an oven at 90 ºC for 10 hours. Once removed from the oven, the solid was ground gently into a powder using a mortar and pestle. The resulting powder was then pelletized and sieved using sieves which were within the range of 710 µm-1000 µm mesh size. Finally, the material was calcined in a stream of air at 500 ºC for 8 hours. The catalyst was then cooled to room temperature.

3.2.2 Synthesis of the cesium promoted iron phosphate catalyst

Synthesis of the cesium promoted iron phosphate catalyst was carried out similarly to the technique outlined in Section 3.1.2. Iron(III) nitrate (12.2 g) was dissolved in 500 mL of double distilled water. Magnetic stirring of the mixture yielded a pale orange solution. Thereafter dilute ammonia was added drop-wise to precipitate the iron hydroxide gel. The solution was thereafter left to settle, followed by the solution being decanted and then filtered.

An amount of approximately 2 g colloidal silica and the desired amounts of 85 % orthophosphoric acid were added successively to the iron hydroxide gel. After 1 hour of gentle magnetic stirring and heating at 75 °C, the cesium nitrate solution, consisting of the desired amounts of cesium nitrate dissolved in water, was added to the mixture. The quantities of orthophosphoric acid and cesium nitrate added were calculated based on P/Fe/Cs ratios of 1.2-1.3/1/0.05-0.30, which were found to be favourable ratios for ODH reactions. The resulting solution was then further heated and stirred for a period of 1-2 hours at 75 °C. This yielded a brownish white paste which was placed in an oven at 90 ºC for 10 hours. Once removed from the oven, the resultant solid was ground gently into a powder, pelletized and sieved using the same mesh size described in Section 3.1.2 above. Finally, it was calcined in a stream of air at 500 ºC for 8 hours. The promoted catalyst was then cooled to room temperature.

3.3 Catalysts characterization

The various properties of the catalysts were determined using several characterization techniques which are mentioned below.

3.3.1 Inductively Coupled Plasma–Optical Emission Spectroscopy (ICP-OES)

The composition of the elements present in the catalysts was obtained by Inductively Coupled Plasma–Optical Emission Spectroscopy (ICP-OES) using a Perkin Elmer, Optima 5300 DV, Optical Emission Spectrometer equipped with Winlab 32® software.

The accurately weighed catalyst sample was agitated while being heated in aqua regia using a suitable volumetric flask. Once the sample was completely dissolved, it was cooled and thereafter deionised water was added to make up the correct volume.

Multi-element standard solutions, having concentrations within the range of 10 ppm to 100 ppm, were prepared for the iron and phosphorous standards of the iron phosphate catalyst. In terms of the cesium promoted iron phosphate catalyst, a multi-element standard was also prepared with concentrations within the same range for the iron and phosphorous standards; however, the cesium standard was prepared within the range of 100 ppm to 200 ppm.

3.3.2 Brunauer-Emmett-Teller (BET) surface area and pore volume

BET surface area measurements (11 point average analysis) and total pore volume were determined *via* a Micromeritics Gemini 2375 instrument using nitrogen physisorption isotherms at 77 K. Prior to analysis, the powdered samples (0.04-0.05 g) were degassed in a stream of nitrogen with gradual temperature ramps up to a temperature of 200 °C over a period of 24 hours using a Micromeritics FlowPrep 060 instrument.

3.3.3 Infrared Spectroscopy (IR)

A Perkin Elmer Spectrum 100 FT-IR Spectrometer fitted with a Universal ATR (Attenuated Total Reflectance) sampling accessory and operated at room temperature was used to obtain the infrared spectra. The measurements were carried out by placing a small quantity of the sample on the surface of a plate directly above the ATR crystal and a pressure of about 118 Gauge (9.2 bar) was applied to allow for good sample contact.

3.3.4 Scanning Electron Microscopy (SEM) and Energy Dispersive X-ray Spectroscopy (EDX)

Initially, the samples were carbon coated using a JEOL JEE 4C vaccum evaporator and thereafter the SEM images and EDX data were obtained by using a JEOL JSM 6100

Scanning Electron Microscope equipped with a Bruker EDX Detector and Espirit 1.8 software.

3.3.5 Transmission Electron Microscopy (TEM) and Selected Area Diffraction Pattern (SADP)

TEM images and electron diffraction patterns were obtained using a JEOL JEM 1010 Transmission Electron Microscope which was operated at a voltage of 100 kV. Sample preparation was carried out by placing a small amount of the catalyst between two formvar coated copper grids and the images were captured using MegaView III Soft Imaging System. Particle size determination was carried out using iTEM software.

3.3.6 High Resolution-Transmission Electron Microscopy (HR-TEM)

High resolution-TEM images were obtained using a Tecnai F20 Field Emmision TEM equipped with EDAX. The samples were prepared by sonicating methanol suspensions of the sample powders for 15 minutes followed by depositing a drop of the suspension on a standard nickel grid coated with a holey carbon film. Each grid was then mounted onto a sample holder, which was introduced directly into the shaft of the microscope.

3.3.7 X-ray Diffraction (XRD)

Powder room temperature and *in situ* high temperature XRD analyses were carried out on the synthesized catalysts using a Bruker D8 Advance Diffractometer equipped with an Anton Paar XRK 900 reaction chamber and a TCU 750 temperature control unit. The instrument was operated at 40 kV and 40 mA, using a Cu Kα radiation source. The samples were scanned within a 2θ range of 10° to 90°, with a step size of 0.02° at a speed of 1°/min. The diffractograms for the *in situ* high temperature measurements were obtained from room temperature to 600 °C at 50 °C intervals.

Room temperature powder X-ray diffraction patterns of the spent, reduced and reoxidised catalyst samples were obtained using a Philips PW1050 Diffractometer operated at 40 kV and 40 mA, consisting of a graphite monochromator and a Co Kα radiation source. The samples were scanned within a 2θ range of 10° to 90° with a step size of 0.02° at a speed of 1 °/min. The data was captured using a Sietronics 122D automated micro-processor.

3.3.8 Temperature Programmed Analysis (TPR/TPO/TPD)

Temperature programmed analyses were carried out using a Micromeritics 2900 Autochem II Chemisorption Analyser coupled with a thermal conductivity detector. The catalyst samples were placed in a U-shaped quartz tube and the methods and gases used were dependent on the technique being carried out.

Temperature Programmed Reduction (TPR) experiments were carried out by initially doing a pre-treatment which required heating the catalyst under a stream of argon (30 mL/min) at 400 °C for a period of 1 hour. The sample was then cooled to 80 °C under the same gas. During the reduction process, a 5 % H_2 in argon mixture was used as the reducing gas over specific temperature ranges depending on the experiments being carried out, at a ramp rate of 10 °C/min. The ideal gas flow rate was found to be 30 mL/min and a similar sample mass was maintained for each experiment.

Temperature Programmed Oxidation (TPO) experiments were carried out after the reduction experiments using the procedure mentioned above. However, a 5 % O_2 in argon mixture was used as the oxidizing medium.

Phase identification using XRD was carried out for the catalyst at each reduction and oxidation step by making use of variable flow rate and variable temperature TPR and TPO experiments. The small quantity of sample removed at each step for XRD analysis required the use of a blank sample holder.

The NH_3-temperature programmed desorption experiments involved flushing the catalyst with helium at 400 °C at a flow rate of 30 mL/min for 1 hour. The sample was then cooled once again to 80 °C. Thereafter, a 4.1 % ammonia in helium mixture was passed (30 mL/min) over the catalyst for a period of 1 hour. Following this, excess ammonia was removed by flushing the system with helium (30 mL/min) for 30 min and then the adsorbed ammonia was removed from the surface of the catalyst by the same stream of helium (30 mL/min) while ramping the temperature to 900 °C at a rate of 10 °C/min. During this stage the desorption profiles were recorded.

3.3.9 Thermogravimetric Analysis (TGA) and Differential Scanning Calorimetry (DSC)

The thermal analysis techniques, TGA and DSC, were carried out using a SDT Q600 Thermal Analyser Instrument. Sample mass used was around 0.05 g. The samples were housed within an alumina crucible during the analyses. Measurements were carried out over a temperature range of 100 °C to 1000 °C at a ramp rate of 10 °C/min, and varying gas environments such as static air and nitrogen were used, depending on the sample being analysed.

3.3.10 Mössbauer Spectroscopy

^{57}Fe Mössbauer measurements were carried out at room temperature (RT) in conventional transmission geometry with a ^{57}Co<u>Rh</u> source. The data obtained was analysed with the code RECOIL.

3.3.11 Raman Spectroscopy

Raman spectroscopy was carried out using an Advantage 532 series Spectrometer (NIR Spectrometer) at a laser wavelength 532 nm, utilizing Nuspec software.

3.4 Catalytic testing

3.4.1 Reactor design and function

Figure 3.1 is representative of one of the two identical fixed-bed micro reactors which were utilized for the project with respect to the catalytic testing [2]. The actual images of the complete reactor setup are found in Appendix A, A1.

The reactor setup consisted primarily of stainless steel fittings and ¼ inch outer diameter stainless steel tubing (supplied by Swagelok®), however, the lines from the gas cylinders to the entry point preceding the rotameters were a ¼ inch copper tubing (supplied by Swagelok®). The setup has been categorised into four zones, namely, A, B, C and D. Each of these zones shall be discussed individually to allow for ease of explanation for the design shown above in Figure 3.1.

Zone A: The oxidant (air) and nitrogen were supplied to the system *via* cylinders. Each cylinder was fitted with a gas specific AFROX multi-stage pressure regulator.

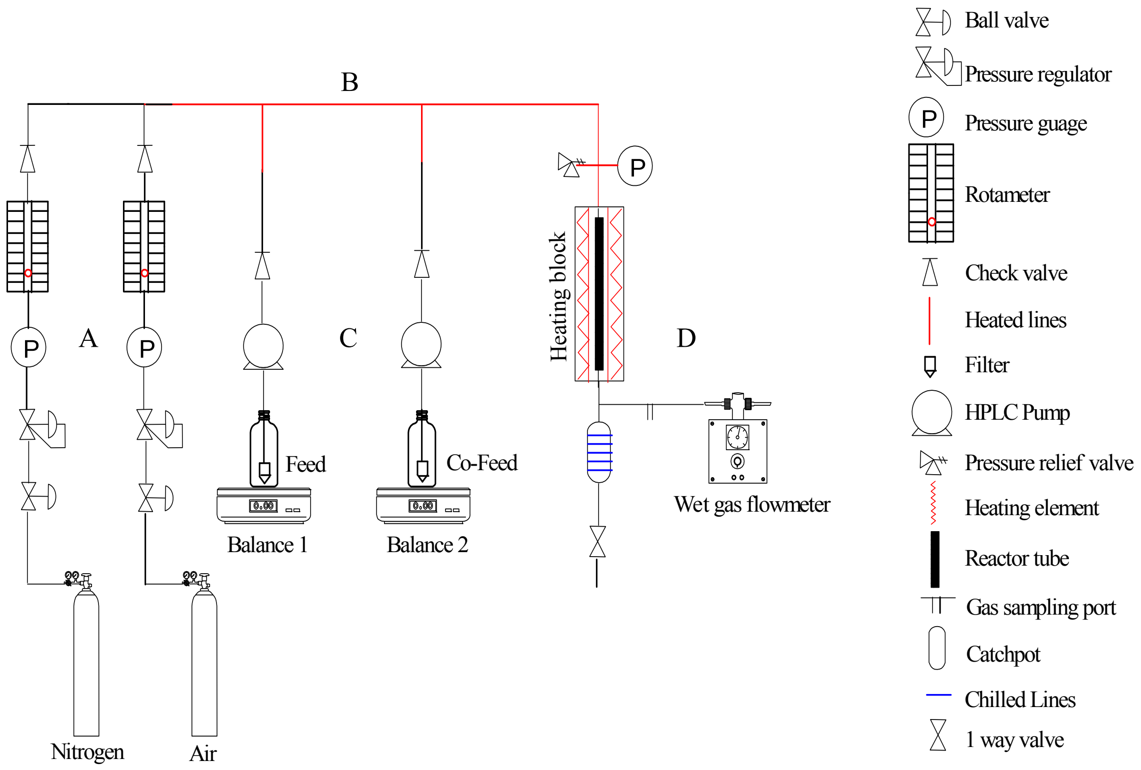

Figure 3.1 Reactor design

The gases were passed through ¼ inch copper tubing before reaching a one way brass ball valve, followed by a mini pressure regulator and pressure gauge. A gas specific rotameter, calibrated at 100 kPa, controlled the amount of gas entering the reactor. A check valve placed after the rotameter prevented any back flow of the exiting gas. All gases entering the system passed through ¼ inch stainless steel tubing before entering the heated region prior to the reactor tube.

Zone B: Liquid feed entering into the reactor was delievered by means of a LabAlliance Series II HPLC pump, which had a minimum flow rate of 0.01 mL/min and a maximum of 9.99 mL/min. A Teflon tube was used to withdraw the feed from the holding vessel which was positioned on the surface of a top loading weighing balance, used to accurately weigh the mass of feed entering into the system. The feed exiting the pump was passed *via* $^{1}/_{16}$ inch stainless steel tubing, which consisted of a stainless steel reducing union to allow for conversion of the line to a ¼ inch stainless steel tubing before entrance into the heated region prior to the reactor tube. A liquid check valve placed after the reducing union prevented any back flow of the liquid and gases into the pump.

Both the liquid and gas feeds were introduced into the heated region of the reactor setup *via* the ¼ inch stainless steel tubing and a union connected the gas lines and liquid feed lines. The feeds were heated at a temperature of 180 °C using RPG heating tape (400 W, 240 V). The temperature selected for this region was set using a temperature controller and monitored using a thermocouple.

After the heated region, the feed was passed into the reactor tube, using reducing unions, which were heated to the specific reaction temperature using a heating block equipped with a temperature controller and monitored using a thermocouple. The reactor tube was constructed from grade 316 stainless steel tube with a ½ inch (1.27 cm) outer diameter. The length of the reactor tube was 35 cm.

Within the reactor tube, 1 mL of catalyst was positioned in the isothermal zone of the reactor tube between two layers of glass wool and all void spaces were filled using inert 24-gritt carborundum (686 µm). The entrance and exit regions of the reactor tube were also packed with glass wool to prevent any leakage of the packing material. The temperature reading within the catalyst bed was monitored using a sliding thermocouple placed at the isothermal zone of the catalyst bed, which was determined from temperature profiling of the reactor tube.

Products formed during catalytic testing were found in two phases, the gaseous and liquid phase. The gaseous products exiting the reactor tube was passed into a chilled 150 mL stainless steel catchpot which was maintained at 2 °C using a chiller bath, allowing for condensation of the products. The liquid products were removed using a needle valve attached at the end of the catchpot, weighed and analysed using gas chromatography.

These products formed during the catalytic reaction existed in two layers i.e. the upper organic layer and the lower aqueous layer. After separation, both these layers were analysed for weight percent of water content using a Metrohm 870 KF Titrino plus Karl Fischer Titrator. The titrant used during the analysis was Riedel de Haën Hydranal-Composite 5. Initially a calibration was done with water and thereafter the samples were analysed in triplicate.

The uncondensed gaseous products were passed *via* ¼ inch stainless steel tubing, which contained a stainless steel union tee with a septum fitted at one end. The septum was used to withdraw gas samples with a gas tight 2.5 mL SGE syringe for analysis via gas chromatography.

In addition, the flows of the gaseous products exiting the system were monitored using a Ritter drum type gas flow meter, Type TG1-Model 5. This equipment was calibrated prior to usage and can measure up to 120 L/hr.

The spent catalyst was carefully removed after every reaction and characterized.

3.4.2 Gas chromotography (Product analysis)

A Perkin-Elmer Autosystem XL Gas Chromatograph equipped with two Flame Ionisation Detectors (FID) was used to analyse most of the products in both the gaseous and liquid phases. All cracked products were quantified on a CP-SIL 5CB column, while oxygenates where quantified on a PE WAX column. A Perkin-Elmer Clarus 600 Gas Chromatograph equipped with a Thermal Conductivity Detector (TCD) was used to analyse for carbon oxides after the catalytic testing. The software used on both of the instruments was TotalChrom®.

All the gaseous phase samples were injected with a 2.5 mL SGE gas tight syringe. The liquid phase samples were injected using 1μL liquid syringe. GC specifications for the systems mentioned above are found in Table 3.1.

For the first FID column, hydrogen was used as the carrier gas at a flow rate of 40.0 mL/min. The column was initially held at 36 °C for 3.0 min, and thereafter it was ramped at 45 °C/min until 200 °C, where it was further held for 2.0 min. The total run time was 7.64 min.

For the second FID column, hydrogen was also used as the carrier gas at a flow rate of 40.0 mL/min. The column was initially held at 50 °C for 3.0 min, and thereafter it was ramped at 35 °C/min until 200 °C, where it was further held for 2.0 min. The total run time was 9.29 min.

For the TCD column, helium was used as the carrier gas at a flow rate of 70.0 mL/min. The column was initially held at 36 °C for 1.5 min and thereafter it was ramped at 25 °C/min until 65 °C, where it was further held for 3.0 min. The total run time was 5.66 min.

Table 3.1 Specifications and experimental conditions related to the GC

	FID 1	FID 2	TCD
Column type	CP-Sil 5CB	PE wax	Carboxen 1006 Plot
Filament temperature (°C)	-	-	100
Filament thickness	0.25 μm	0.25 μm	1.50 μm
Column length	25 m	30 m	50 m
Column diameter	150 μm	320 μm	320 μm
Carrier gas	H_2	H_2	He
Flow rate of carrier gas	40 mL/min	40 mL/min	70 mL/min
Split flow (ratio)	30	150	20
Detector range	1	1	3
Detector time constant	50	200	200
Detector gas flows	Air : 400 mL/min H_2: 40 mL/min	Air : 400 mL/min H_2: 40 mL/min	He : 70 mL/min
Injector temperature (°C)	250	250	200
Detector temperature (°C)	300	300	100

3.4.3 Product quantification

The response factor (RF) for each of the liquid components was calculated. The response factor equals to the area of the spectral peak divided by the weight or volume of the substance injected. In determination of the response factors, pure compounds were used to make up the multi-component mixtures containing known amounts of the components and from these varying volumes were injected into the column attached to the FID and a chromatogram was obtained. The response factor was calculated as follows:

$$\text{Response factor (RF)} = \frac{\text{Peak area of component}}{\text{Weight of component injected}}$$

Relative response factors (RRF) were then calculated. They were calculated relative to a reference component (IBA) which was assigned a RF equal to one.

$$\text{Relative response factor (RRF)} = \frac{\text{Response factor of the reference component}}{\text{Response factor of the individual component}}$$

Finally, for the liquid phase the normalised peak area percentage of the individual component was used to calculate the moles of the component (Appendix A, A2).

For the gaseous products, it was necessary to obtain calibration curves in order to quantify them. The calibration curves were obtained by plotting the peak areas *vs.* number of moles of component injected. The quantity of each component in the gaseous phase was determined from the gradient of the calibration curve, the volume measured from the Ritter gas flow meter, as well as the volume injected during analyses (Appendix A, A2).

The moles of products formed from the gaseous and liquid phases were combined to calculate percentage conversion, yield and selectivity. A carbon balance of 100 % (±5 %) was used to confirm the accuracy of the quantification procedure; in addition data points were obtained in duplicate with a standard deviation of less than 1 %. Conversion, yield and selectivity which is in mol % carbon, were calculated using the following equations:

$$\text{Conversion (mol\%)} = \left(\frac{\text{Moles of EIB fed - Moles of EIB recovered}}{\text{Moles of EIB fed}} \right) \text{ x } 100$$

$$\text{Yield of a product (mol\%)} = \frac{\text{No. of carbons in product}}{\text{No. of carbons in feed}} \text{ x } \left(\frac{\text{Moles of specific product formed}}{\text{Moles of EIB fed}} \right) \text{ x } 100$$

$$\text{Selectivity of product (mol \%)} = \left(\frac{\text{Yield of a specific product}}{\text{Conversion}} \right) \text{ x } 100$$

3.4.4 Contact time

The contact time used for all the catalytic testing was calculated based on the volume of the catalyst used (mL) and the flow rate of the gaseous feed (mL/min).

$$\text{Contact time (seconds)} = \frac{\text{Volume of catalyst (mL)}}{\text{Flow rate of gaseous feed (mL/min)}}$$

References

[1] Ai, E. Muneyama, A. Kunishige, K. Ohdan, J. Catal. 144 (1993) 632-635.

[2] A. Harilal, Ph.D Thesis, University of KwaZulu-Natal, 2007.

CHAPTER 4

CHARACTERIZATION OF THE IRON PHOSPHATE CATALYST

During the experimental process several catalysts were synthesized, however, to illustrate the characterization techniques used, a single catalyst has been chosen as a representative catalyst. The primary objective was to isolate the tridymite-like $FePO_4$ phase, or to obtain it as the major phase, and to obtain a ratio of P/Fe of approximately 1.2 for all the catalysts. Ideally, the phase changes, surface area, surface morphology etc. would prove quite beneficial in allowing for a complete understanding of the catalysts synthesized.

4.1 Inductively Coupled Plasma-Optical Emission Spectroscopy (ICP-OES)

To show the accuracy of the experimental technique, the ICP results for two synthesized catalysts are tabulated below (Table 4.1):

Table 4.1 P/Fe molar ratios of two identical calcined catalysts

	Theoretical	Catalyst A	Catalyst B
P/Fe	1.05-1.2	1.15	1.14

The P/Fe ratio obtained for the two samples were within the expected range of 1.05-1.2 [1]. The reason for the slight variation in the ratios has been considered to be the result of leaching of ions during the synthesis of the catalyst.

4.2 Brunauer-Emmett-Teller (BET) surface area and pore volume

The BET results show that the catalysts had surface areas within the range of 10-13 m^2/g and pore volumes within the range of 0.048-0.053 cm^3/g (Table 4. 2).

Table 4.2 BET surface areas and pore volumes of two identical calcined catalysts

	Catalyst A	Catalyst B
Surface Area (m^2/g)	11.9	10.7
Pore Volume (cm^3/g)	0.052	0.049

Reports state that catalysts prepared with P/Fe ratios slightly lower than 1.2, calcined at a temperature below 500°C, possess surface areas between 10-13 m^2/g [1].

4.3 Infrared Spectroscopy (IR)

The IR spectra obtained for the uncalcined and calcined catalyst are shown below (Fig. 4.1-4.2):

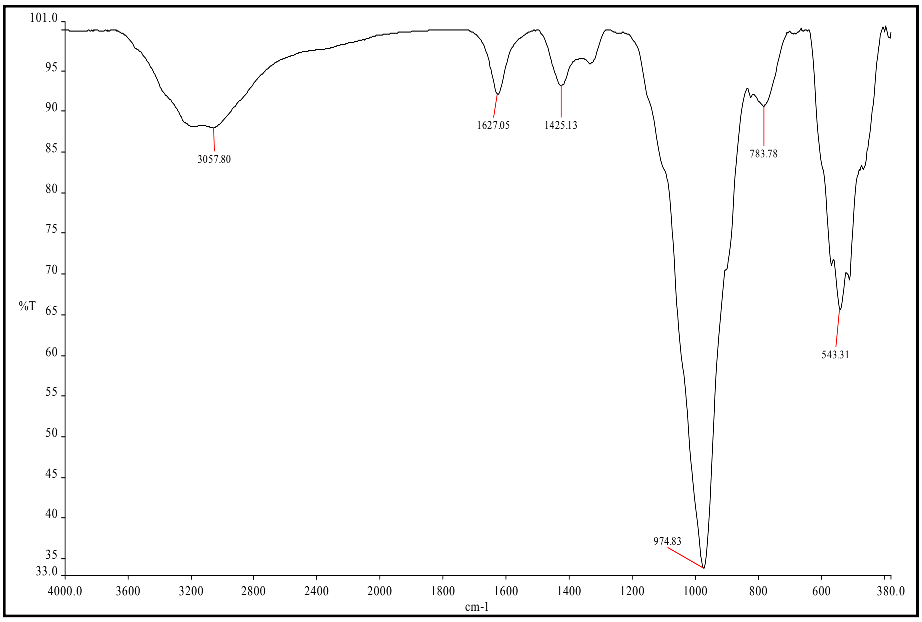

Figure 4.1 IR spectrum of uncalcined catalyst A

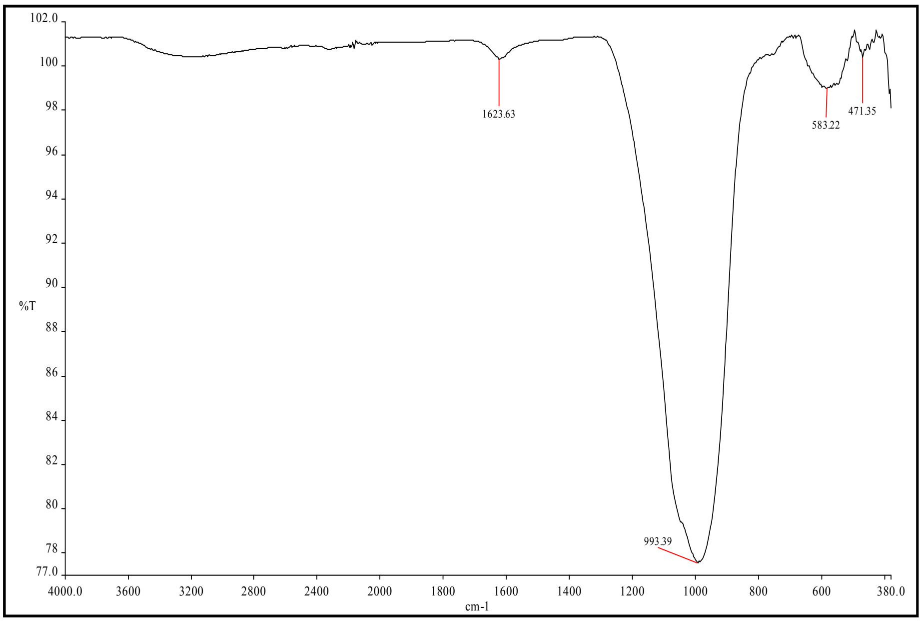

Figure 4.2 IR spectrum of calcined catalyst A

The uncalcined $FePO_4$ catalyst shows the major infrared peaks assigned and listed in Table 4.3 [2,3].

Table 4.3 Major IR peaks for a typical uncalcined $FePO_4$ catalyst

$FePO_4$	**Interpretation of peaks**
Strong, wide band with maximum at 3400 cm^{-1}	Due to the presence of the hydroxyl group from water molecules
Medium intensity band at 1630 cm^{-1}	Due to the water bending vibrations
Strong, very narrow band at 1380 cm^{-1}	Due to the bending vibrations of the O-H-O bond
Strong, wide band at 1030 cm^{-1} Medium band with maximum at 530 cm^{-1} overlapping with a small peak at 600 cm^{-1}	PO_4^{3-} (orthophosphate) shows medium intensity bands which are often doublets between 540-650 cm^{-1} as well as a strong peak between 940-1120 cm^{-1}

It was also reported that the region between 1200 and 550 cm^{-1} corresponds to the symmetrical and asymmetrical vibrations of the phosphate groups [2]. A comparison between the prepared uncalcined catalyst A and the typical uncalcined $FePO_4$ catalyst noted in literature is tabulated in Table 4.4.

Observing the material after calcination there is a substantial change in three peaks, namely, the peaks at 3000 cm^{-1}, 1630 cm^{-1} and 1380 cm^{-1}. Since the catalyst was calcined, it would be logical to expect a reduction in the intensity of these peaks or complete disappearance because all three peaks are linked to the presence of water or a hydroxyl group. It was also reported that the common frequencies for the phosphate ion, PO_4^{3-} (orthophosphate), are usually a strong peak between 940-1120 cm^{-1} and medium intensity peaks, often occurring as doublets, between 540-650 cm^{-1} [2]. Furthermore, the infrared spectrum of a calcined $FePO_4$ can be linked to a particular phase depending on the temperature of calcination and the P/Fe atomic ratio [4].

Table 4.4 Comparison between uncalcined catalyst A and a typical uncalcined $FePO_4$ catalyst reported in literature

Typical uncalcined $FePO_4$ [2]	**Uncalcined catalyst A**
Strong, wide band with maximum at 3400 cm^{-1}	Strong and wide band with maximum at ~ 3100 cm^{-1}
Medium intensity band at 1630 cm^{-1}	Medium intensity band at ~1600 cm^{-1}
Strong, very narrow band at 1380 cm^{-1}	Weak, narrow band at ~ 1400 cm^{-1}
Strong, wide band at 1030 cm^{-1}	Strong, wide band at ~ 980 cm^{-1}
Medium band with maximum at 530 cm^{-1} overlapping with a small peak at 600 cm^{-1}	Medium band with maximum at ~ 540 cm^{-1}

4.4 Scanning Electron Microscopy (SEM)

Consistency between the SEM images of the calcined and uncalcined catalyst A was the occurrence of bead-like structures (Fig. 4.3-4.4).

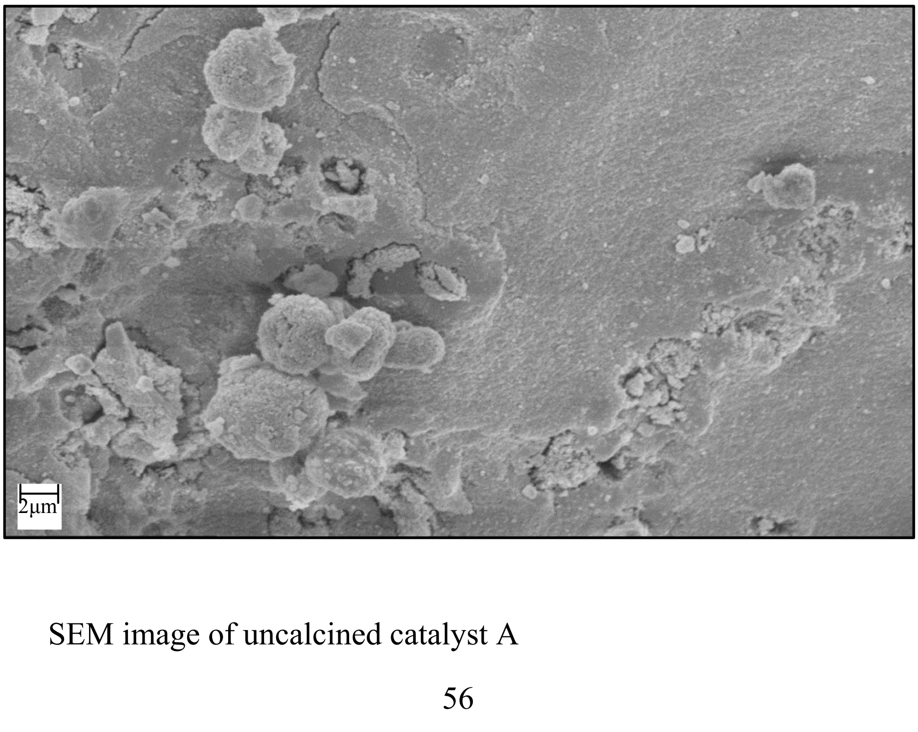

Figure 4.3 SEM image of uncalcined catalyst A

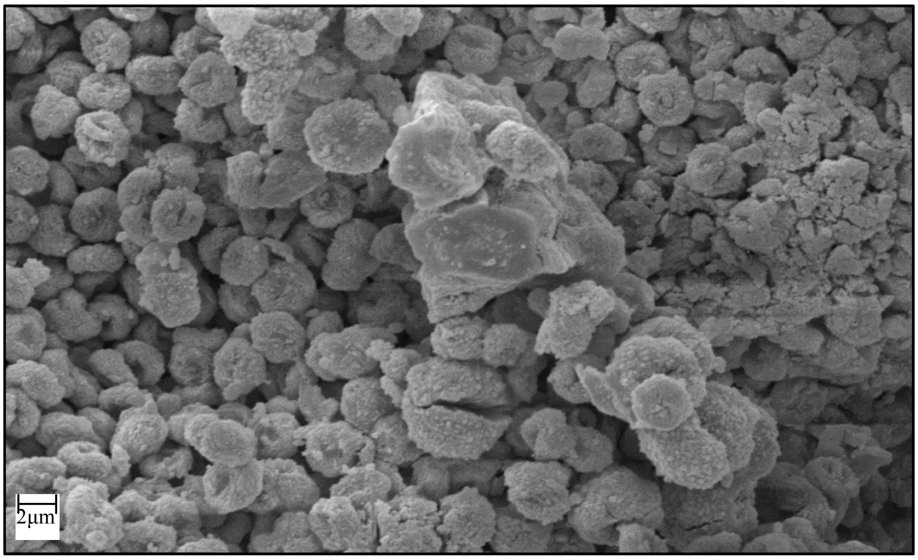

Figure 4.4 SEM image of calcined catalyst A

The uncalcined catalyst A (Fig. 4.3) showed an image of sheets with agglomerations on the surface. The sheets were possibly silica, which serves as the support to provide mechanical strength to the catalyst, and the agglomeration on the surface was the $FePO_4$ coating [5]. Upon calcination the iron phosphate coating was more evenly distributed.

4.5 Room temperature X-ray Diffraction (XRD)

It has been reported that freshly prepared iron phosphate catalysts with P/Fe ratios between 1.02-1.2 contain the quartz type phase, tridymite-like phase and a small amount of $NH_4FeP_2O_7$ [6]. Crystallographic information regarding the tridymite-like $FePO_4$ phase is not available; hence identification of this phase was carried out relative to the isotypic $AlPO_4$ analogue of the tridymite-like phase as mentioned previously (Chapter 2, Section 2.4.1). The X-ray diffractograms obtained for two uncalcined and calcined catalysts (A and B) are shown in Figure 4.5 and Figure 4.6 respectively.

The reflections observed for the uncalcined catalyst show a strong correlation with the diffractogram of the $FePO_4.2H_2O$ mineral type phase, metastrengite [7]. The additional reflections in the sample indicate the existence of a minor phase or phases. Upon calcination there was a reduction in the number of peaks present, which was expected since calcination stabilizes active phases and removes volatile phases. The calcined catalysts showed major reflections at $2\theta = 19.9^o$, 20.9^o, 22.5^o, 29.1^o and 34.8° which correlated with the results reported in literature where it was noted that the major reflections attributed to the tridymite-like phase of the $FePO_4$ catalyst where at 2θ = 20º, 20.95º, 22.6º, 29.35º and 35.5° [4,5]. Certain unidentified reflections were also observed, however it was interesting to note that the major reflection attributed to the quartz type phase, found at 2θ = 25.8º, was not evident.

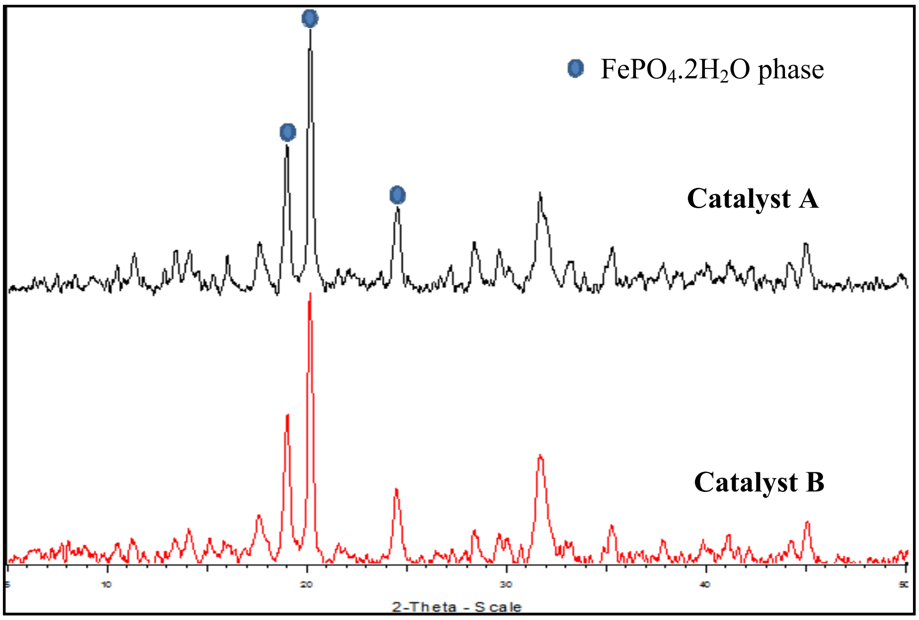

Figure 4.5 X-ray diffractograms of uncalcined catalyst A and uncalcined catalyst B

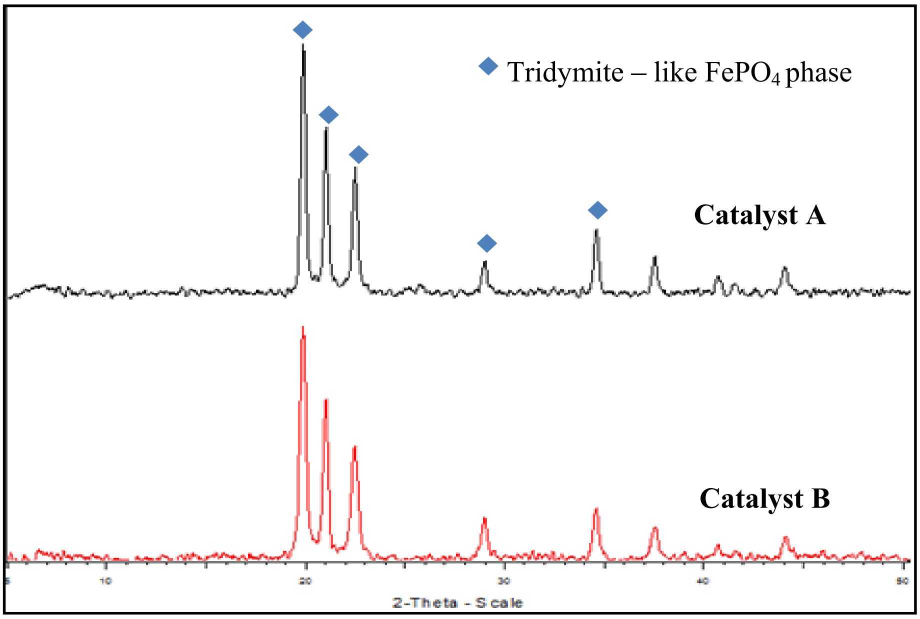

Figure 4.6 X-ray diffractograms of calcined catalyst A and calcined catalyst B

4.6 Temperature programmed reduction (TPR)

The TPR technique permits the determination of the most efficient reduction conditions [8]. In this technique, an oxidized catalyst precursor is subjected to a programmed temperature rise, whilst a reducing gas mixture is passed over it (usually hydrogen diluted in an inert gas like argon) [8]. Figure 4.7 shows the reduction pathway of the tridymite-like $FePO_4$ phase. Literature has shown that catalysts prepared by the ammonia gel method are reduced to iron(II) pyrophosphate ($Fe_2P_2O_7$) [9]. Also, $FePO_4$ with a P/Fe ratio ~ 1.2 is reduced via $Fe_3(P_2O_7)_2$ to $Fe_2P_2O_7$, which has 2θ angles of 39.4° and 30.3° in its XRD pattern (JCPDS card no. 76-1762) [10].

The TPR trace (Fig. 4.8) of the synthesized $FePO_4$ catalyst shows two peaks which are evidence of two reduction steps occurring and hence correlates with the premise that the tridymite-like $FePO_4$ phase is reduced via an intermediate phase, $Fe_3(P_2O_7)_2$, to form the $Fe_2P_2O_7$. The X-ray diffractogram (Fig. 4.9) for the reduced catalyst showed that the tridymite-like $FePO_4$ phase had been reduced to $Fe_2P_2O_7$ having 2θ angles of 34.4° and 35.8° (JCPDS card no. 76-1762). It is important to note that all diffractograms obtained for samples from the temperature programmed experiments were acquired using a Co Kα radiation source, hence a shift in reflections relative to diffractograms obtained with a Cu Kα radiation source is expected.

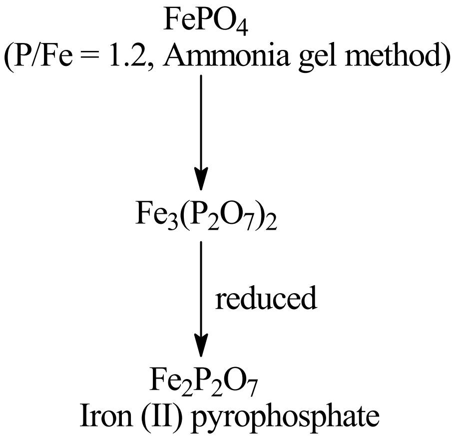

Figure 4.7 Reduction pathway of the tridymite-like $FePO_4$ catalyst

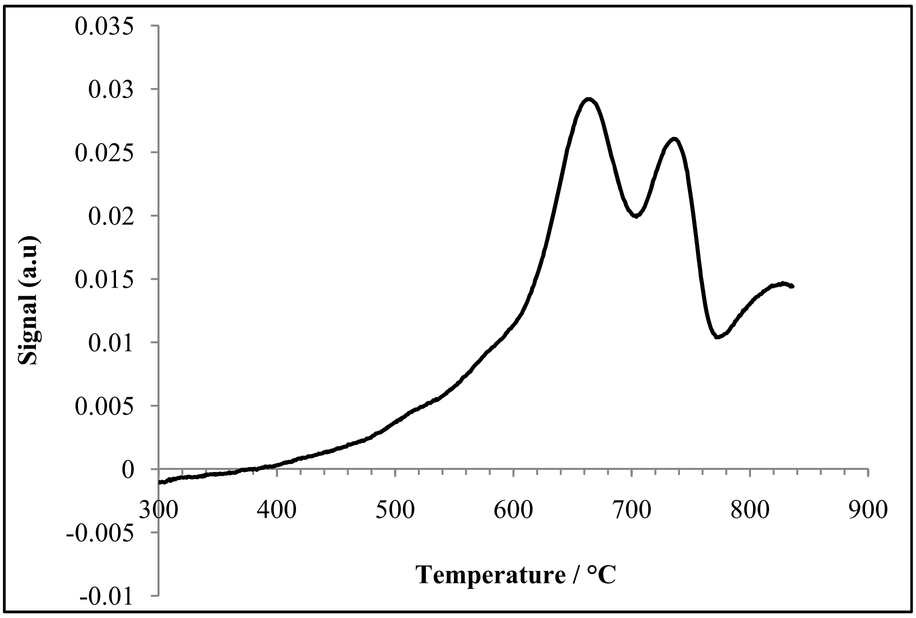

Figure 4.8 TPR profile of calcined catalyst A

These preliminary TPR data based on the TPR profile shape (Fig. 4.8), suggested the possibility of several overlapping peaks and although the diffractogram of the reduced catalyst (Fig. 4.9) showed the formation of only $Fe_2P_2O_7$, it was deemed necessary to carry out further experiments to determine a more accurate TPR profile for the catalyst.

It is important to note that prior to this investigation, it has been reported that factors such as the sample size, hydrogen concentration and heating rate were all critical aspects to consider during these TPR experiments. Arbitrary modifications of these parameters lead to distorted profiles and hence loss of resolution of the curves during the reduction process [11]. It was also observed that variation in sample weights resulted in a decrease in the resolution of the curve for Fe_2O_3 [12, 13].

The initial step was to vary the flow rate. The temperatures of four samples of similar mass were ramped up to 900 °C at 10 °C/min increments in a 5 % H_2 in argon reducing gas mixture. The flow rate was varied between 20 and 50 mL/min. The results obtained are shown in Figure 4.10.

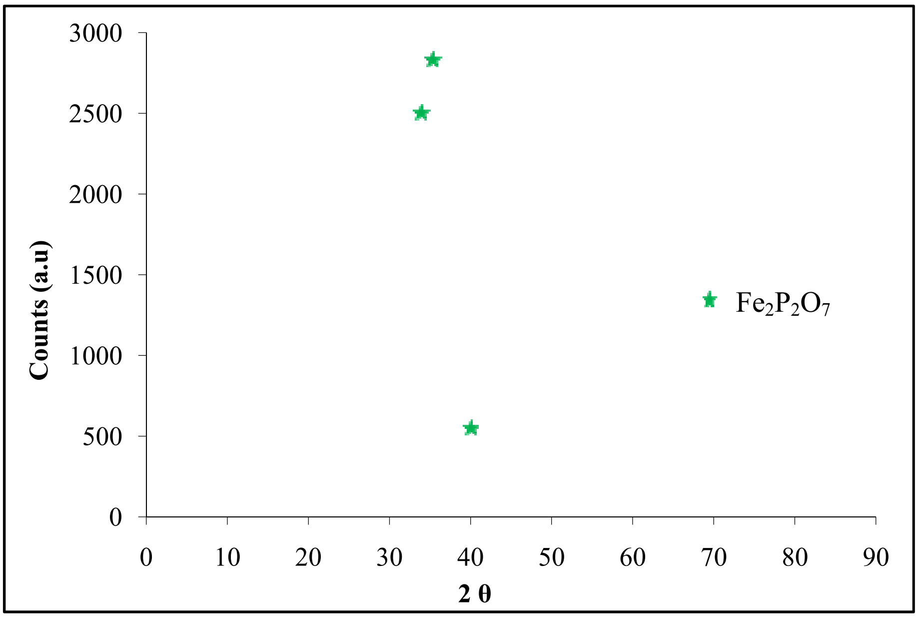

Figure 4.9 Diffractogram of reduced catalyst A

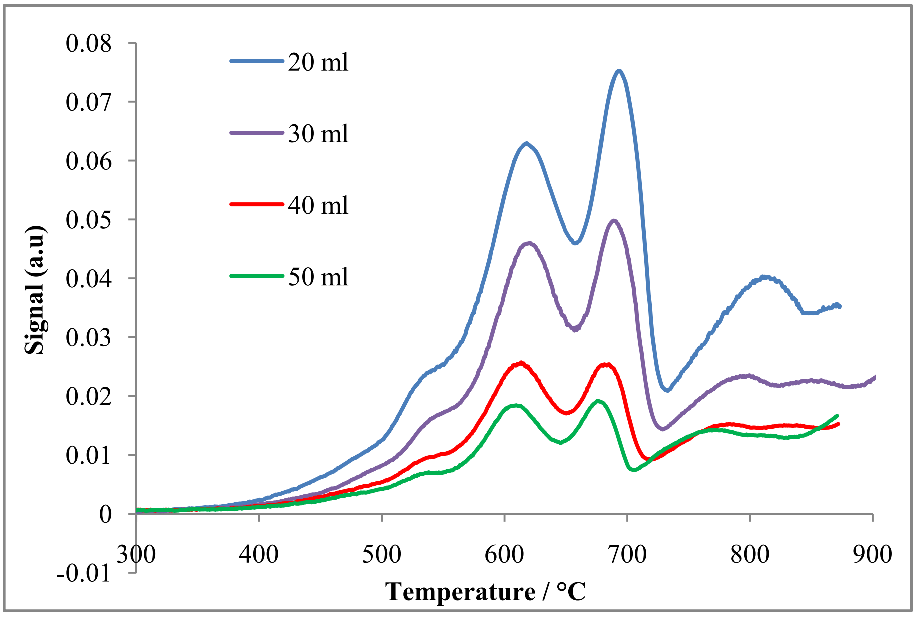

Figure 4.10 TPR profile of calcined catalyst A using varying flow rates

It is evident that variation in flow rate has an effect on the process in terms of peak resolution. The appearance of six peaks at a flow rate of 30 mL/min as opposed to four at 50 mL/min is a good example. However, it is noted that flow rate variation has an insignificant effect on the temperatures at which each reduction step occurs. Seeing that the 30 mL/min curve provided the optimal peak resolution, it was decided to carry out experiments to isolate the phases formed during the reduction process. This would enable the identification of the phases at each reduction step, as well as a determination of the oxidation state at each step. All the parameters used previously were maintained; however, the reduction was stopped at each of the six separate temperatures at which a reduction was observed, as shown in the plot in Figure 4.11. The material was removed and the X-ray diffractogram of each sample was recorded.

The diffractograms and the calculated oxidation states are shown in Figure 4.12 and Table 4.5 respectively. It is evident from the results that within the temperature range of 500-550 °C, the material is predominantly in a +3 oxidation state. This is verified by the existence of the tridymite-like $FePO_4$ phase within this temperature range (Fig. 4.12). However, with an increase in temperature to 660 °C the reduced phase, $Fe_2P_2O_7$, appears as does the intermediate phase i.e. $Fe_3(P_2O_7)_2$.

A further increase in temperature resulted in a complete transformation to $Fe_2P_2O_7$ as seen from the XRD data and supported by the calculated oxidation state.

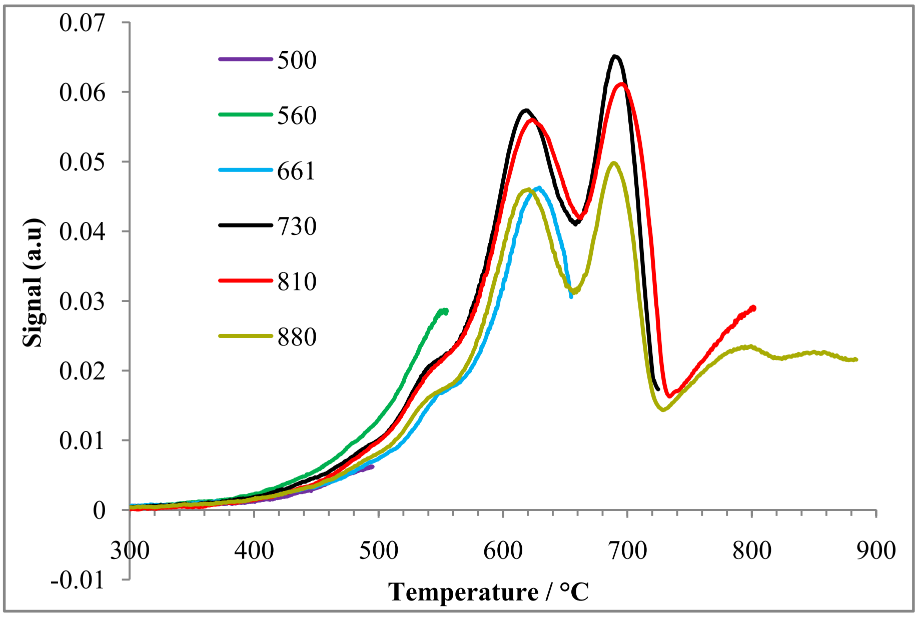

Figure 4.11 TPR profile of calcined catalyst A using varying temperatures

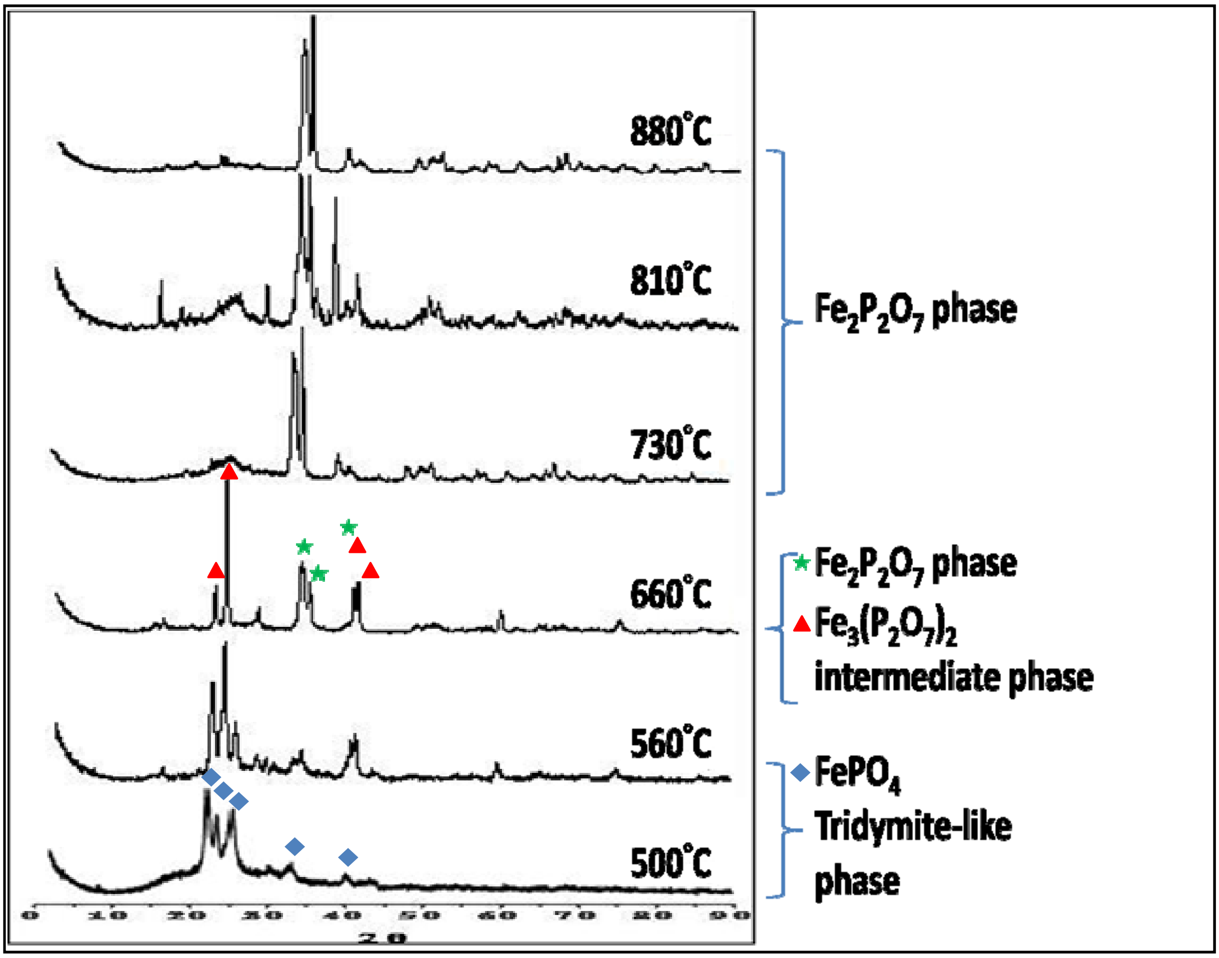

Figure 4.12 Diffractograms of calcined catalyst A at varying temperatures under reducing conditions

Table 4.5 Oxidation state at each reduction step

Temperature (°C)	Average oxidation state
500	2.9
560	2.9
661	2.4
730	1.7
810	1.7
880	1.8

The IR spectra were also obtained for the catalyst after each of these reduction steps to further verify the phases assigned from the diffractograms obtained above (Fig. 4.12). These IR spectra are shown in Figure 4.13.

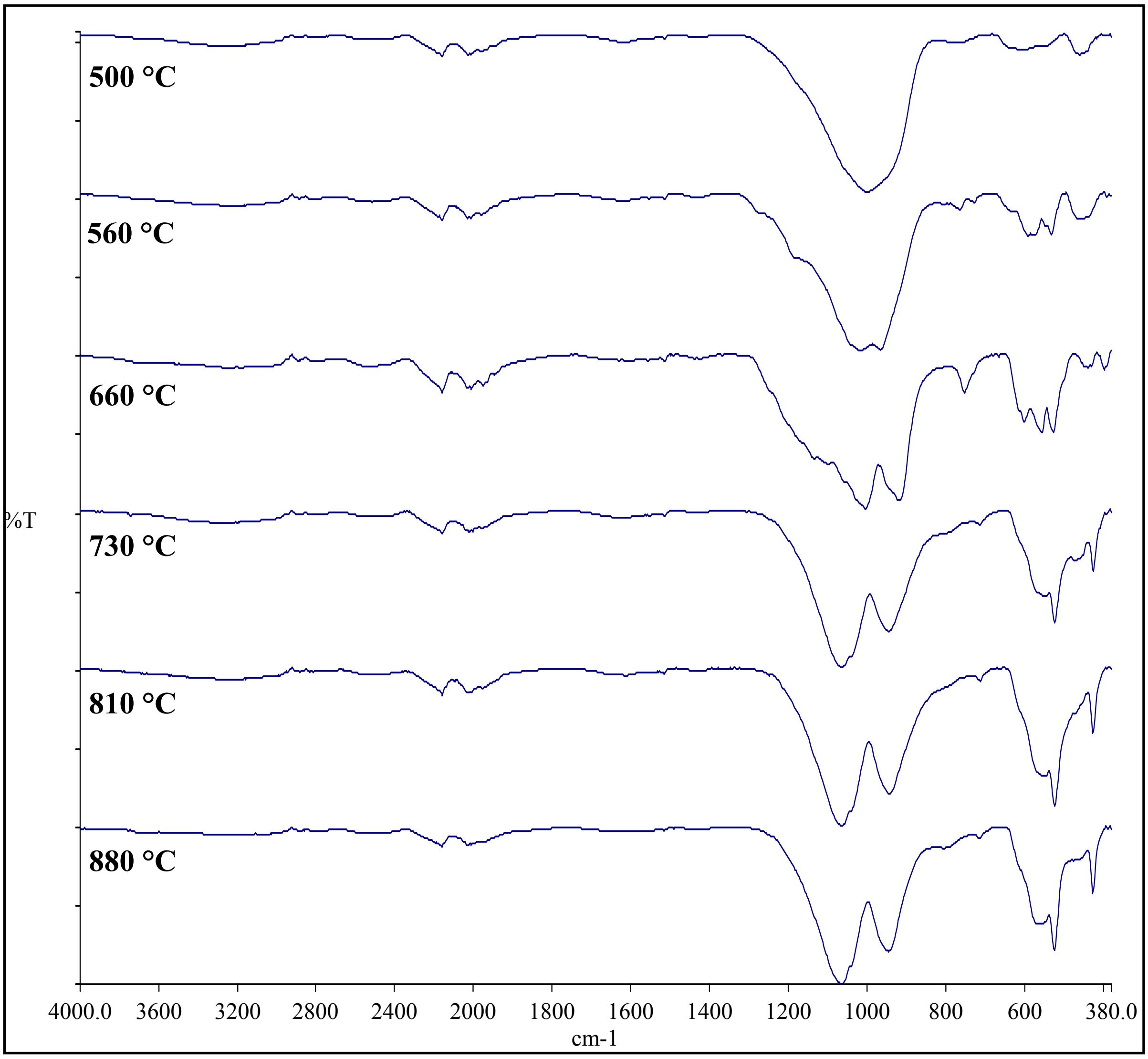

Figure 4.13 IR spectra of catalyst A after each reduction step

The comparative spectra clearly showed the transformation of the tridymite-like $FePO_4$ phase to $Fe_2P_2O_7$. Thus the spectrum after the last reduction temperature shows peaks which are characteristic of the pyrophosphate group, $(P_2O_7)^{2-}$. These are usually characterized by a strong peak between 1100-1200 cm^{-1}, a weak to medium peak between 960-1060 cm^{-1}, a medium peak between 850-980 cm^{-1}, a weak peak at around 705-770 cm^{-1} and a strong multiple peak between 545-580 cm^{-1} [14]. These peaks are visible in the spectrum shown in Figure 4.13 from 660 °C.

4.7 Temperature programmed oxidation (TPO)

The flow and temperature ramp conditions used for the TPR experiment discussed above were also used for the TPO experiment (Fig. 4.14).

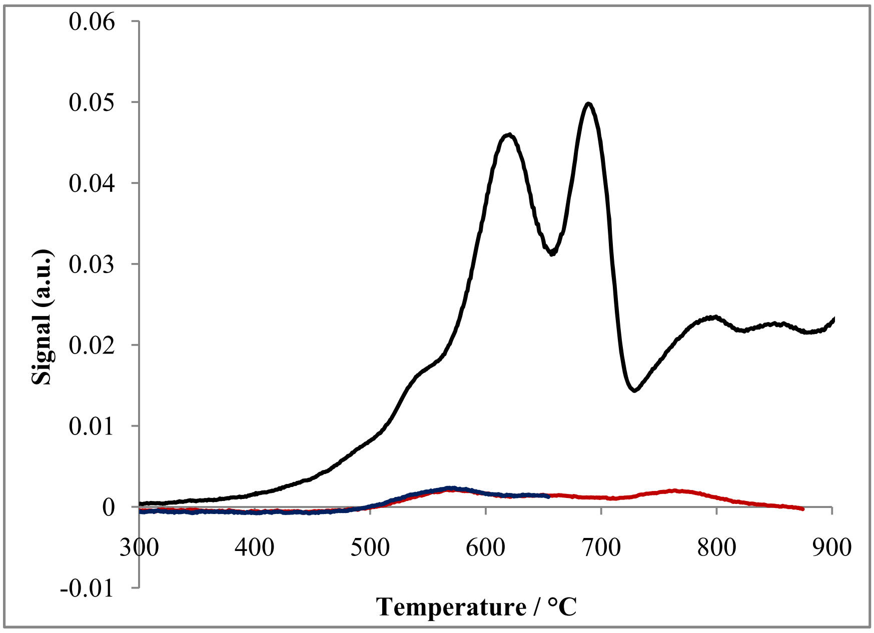

Figure 4.14 Combined TPR/TPO profile of calcined catalyst A at 30 mL/min

Initially, the catalyst was reduced and thereafter reoxidized in a stream of 5 % O_2 in argon. The results (Fig. 4.14) showed that two oxidation steps occurred during this process. The initial step was at an onset temperature of 510 °C and the latter at 715 °C. In an effort to understand the phase changes it was necessary to obtain the X-ray diffractograms of the samples after each of these steps.

The diffractogram for the sample after the initial oxidation step, (Fig. 4.15) showed the formation of the α-$Fe_3(P_2O_7)_2$ phase (α-phase), which is a mixed ferrous and ferric pyrophosphate phase, and this is the active phase under catalytic conditions **[6]**. However, the diffractogram observed for the sample after the elevated temperature oxidation step showed the formation of the quartz type $FePO_4$ phase (JCPDS card no. 84-0875) (Fig. 4.16).

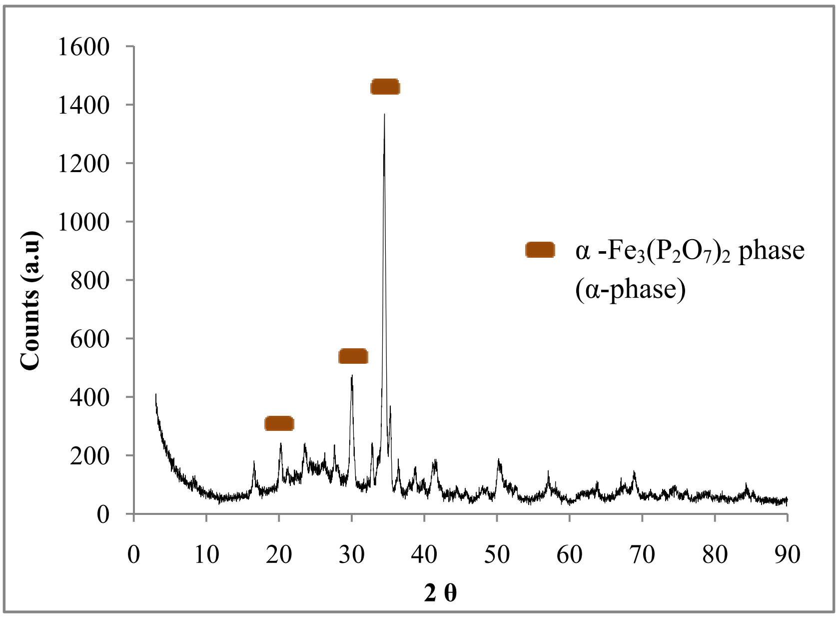

Figure 4.15 Diffractogram of the sample oxidized at 510 °C

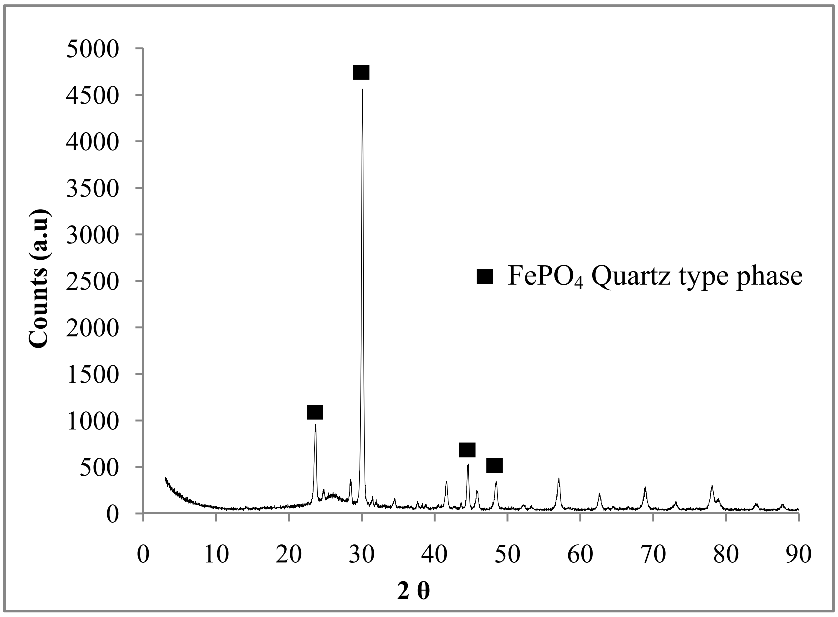

Figure 4.16 Diffractogram of the sample oxidized at 715 °C

The formation of the quartz type phase has been reported in the literature; however, it was formed at an elevated temperature of 1000 °C [6]. It was also observed that the transformation between the α-phase and $Fe_2P_2O_7$ is reversible [6]. The phase transformations of catalyst A, which occurred in the TPR and TPO experiments, are depicted in Figure 4.17.

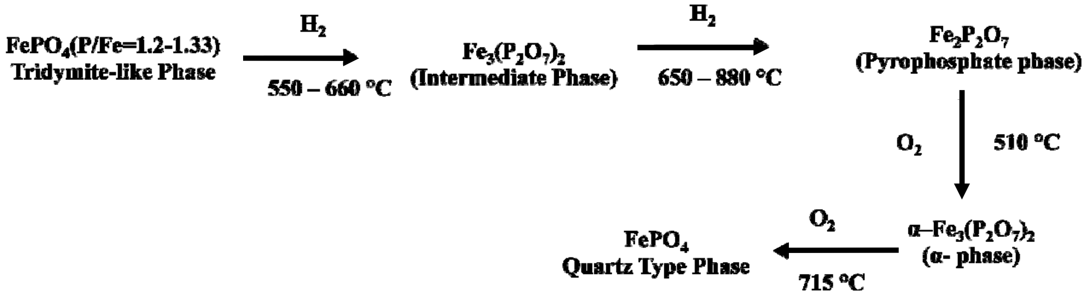

Figure 4.17 Phase transformation of catalyst A under the conditions of TPR and TPO

The infrared spectra of the α-phase (Fig. 4.18) and the quartz type $FePO_4$ phase (Fig. 4.19) were recorded and compared with literature [4]. The results show a significant correlation.

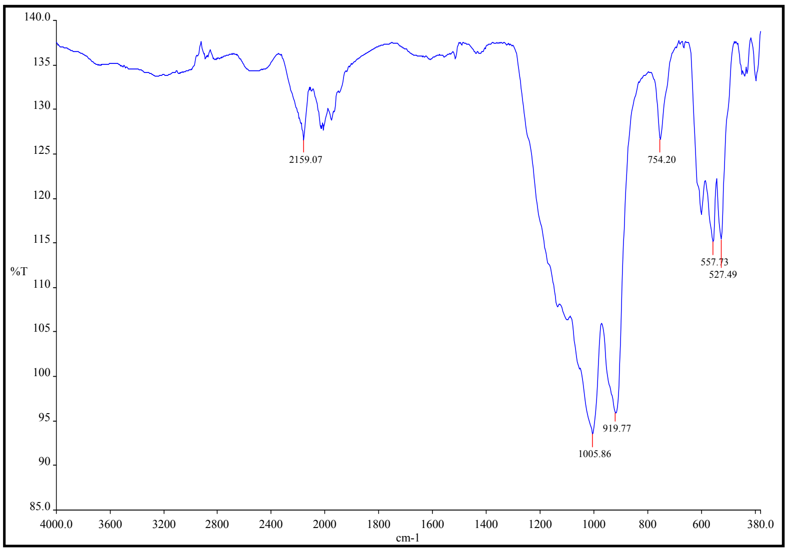

Figure 4.18 IR spectrum of the α-phase

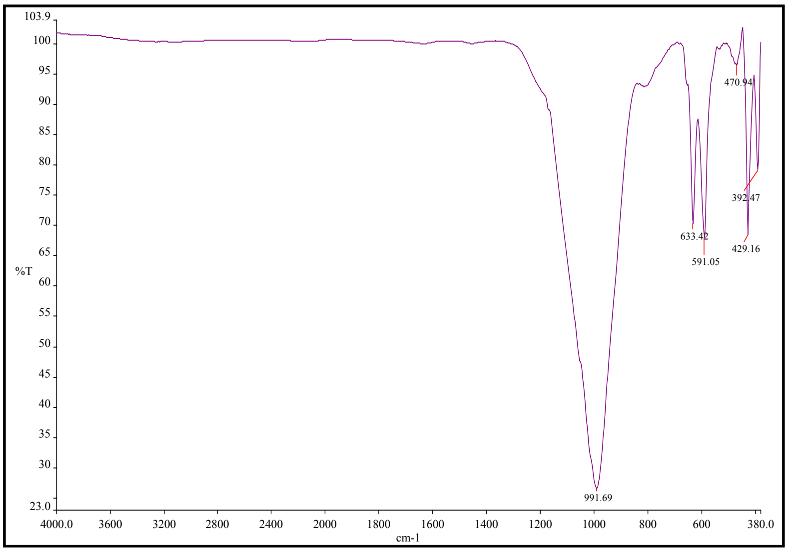

Figure 4.19 IR spectrum of the quartz type $FePO_4$ phase

4.8 SEM and Energy Dispersive X-Ray Spectroscopy (EDX) data of reduced and reoxidised catalyst A

The surface morphology of the catalyst which had been subjected to reduction and reoxidation provides a qualitative understanding of dispersion of metals on the surface of the catalyst after exposure to heat in a gaseous environment. Previously, the SEM images of the uncalcined and calcined catalyst showed that upon heating there exists an even distribution of the phosphorous and iron over the surface (Fig. 4.3-44). However, the effect of reduction and reoxidation shows an agglomeration or sintering effect (Fig. 4.20).

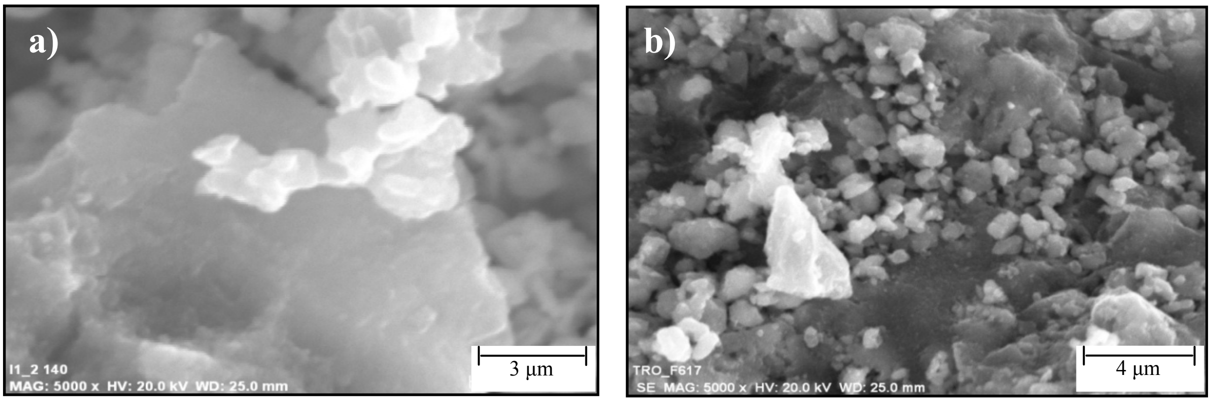

Figure 4.20 SEM images of the reduced catalyst (a) and reoxidised catalyst (b)

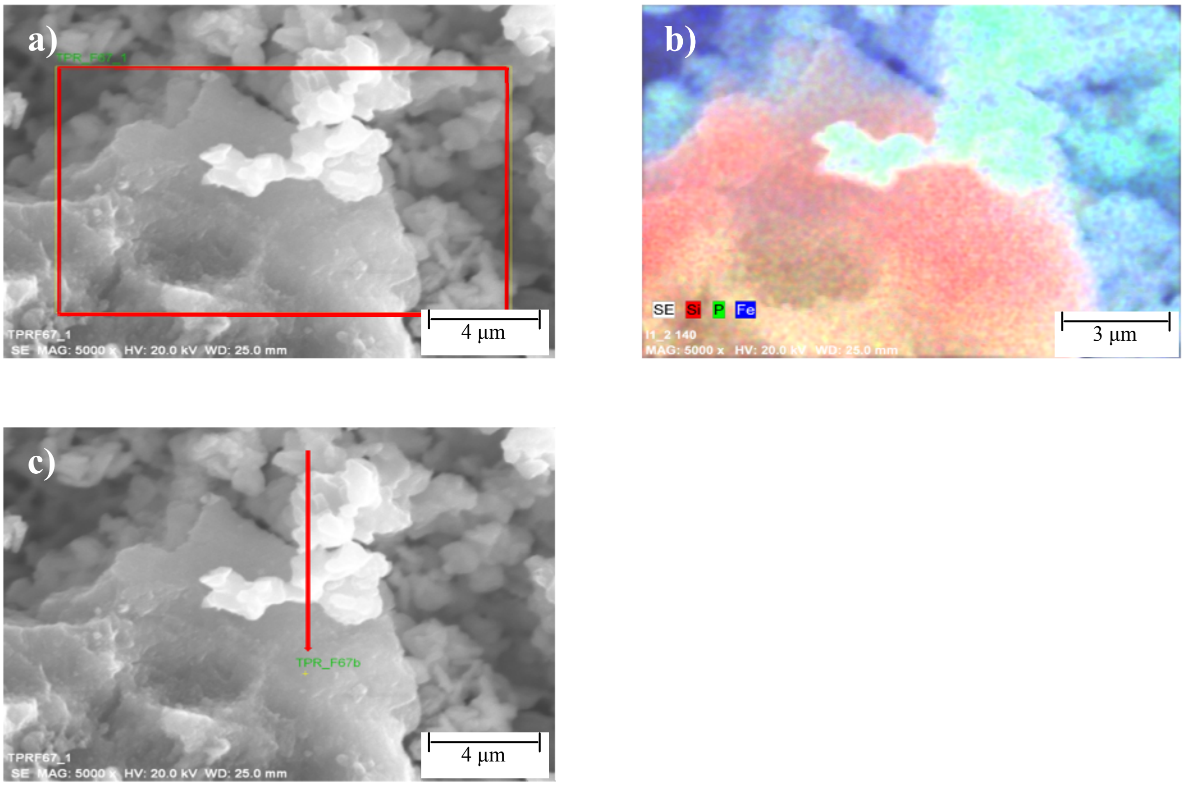

Figure 4.21 Area analysis (a), EDX mapping (b) and spot analysis (c) of reduced catalyst A

This is confirmed by the EDX data (mapping and spot analysis) which showed the distribution of phosphorous and iron over the silica support after the temperature programmed reduction and oxidation treatments of the calcined catalyst. Although EDX data does not provide a quantitative assessment of metal distribution, it does allow for differentiation in terms of metal distribution, as shown in Fig. 4.21 and Table 4.6. The EDX data obtained is in close correlation with the ICP elemental analysis results mentioned previously (Table 4.1).

Table 4.6 EDX elemental composition results

Element	**Silica (Si K)**	**Phosphorus (P K)**	**Iron (Fe K)**
Wt %	58.55	21.29	20.07

4.9 Temperature Programmed Desorption (TPD) and acidic site determination

In ODH reactions, product formation occurs *via* the consecutive homolytic abstraction of hydrogen from the adsorbed reactant intermediate [15]. Lewis acid sites facilitate the abstraction of the hydrogen [16]. Therefore, it is of interest to study the nature and strength of different types of acidic sites present on the surface of the $FePO_4$ catalyst.

The desorption profile was obtained by passing a stream of 4 % ammonia in helium over the catalyst. Prior and post ammonia treatment, the sample was flushed with helium. The flow rate was maintained at 30 mL/min at a ramp rate of 10 °C/min until 900 °C. The desorption profile is shown in Figure 4.22.

A study investigating the number and nature of the acidic sites obtained from ammonia adsorption-desorption experiments carried out for iron phosphate catalysts calcined at different temperatures showed the presence of both Brønsted and Lewis acid sites for the catalysts [16]. Upon calcination at a temperature of ~ 600 °C, there was a loss of Brønsted acid sites and therefore the concentration of acidic sites decreased [16]. The profile for the catalyst showed a peak at 580 °C which was due to presence of acidic sites. Catalysts generally comprise of three types of acidic sites namely, at ~ 350 °C (weak acid sites), 550 °C (moderate acid sites) and 650 °C (strong acid sites). The acidity determination of the two catalysts A and B prepared in different batches are depicted in Table 4.7.

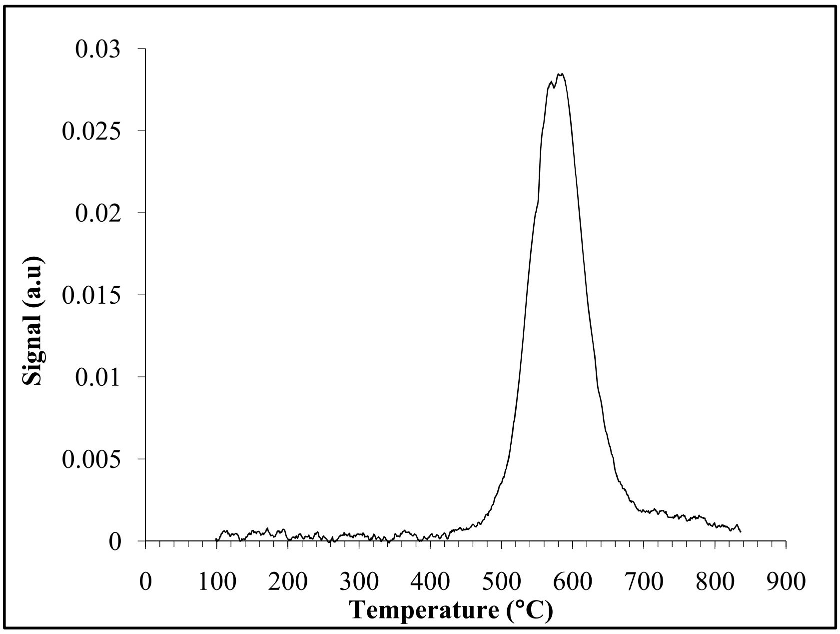

Figure 4.22 Desorption profile of calcined catalyst A

Table 4.7 Acidity of two similar catalysts

Catalyst	Total acidity (mmol/g)
Catalyst A	0.999
Catalyst B	0.953

Potentiometric titrations have been carried out to determine the strength of the acidic sites of the iron phosphate catalyst. The results showed that these types of catalysts contain very strong acidic sites. It was reported that the acidic strength of the catalyst increased proportionally with the P/Fe ratio until an optimal ratio of 1.2, after which there was a decline in acidity with an increase in P/Fe ratio [17].

4.10 *In situ* XRD of calcined catalyst A under varying atmospheres

Variable temperature XRD studies of calcined catalyst A under different atmospheres, i.e. air, nitrogen and hydrogen were carried out in order to obtain further information about possible phase changes which may occur whilst the catalyst is under catalytic conditions, as well as information concerning the calcination process for uncalcined catalyst A.

Initially the XRD pattern of the uncalcined catalyst was obtained under an oxidizing atmosphere from room temperature to 550 °C. The stacked diffractograms (Fig. 4.23) show the phase changes which occurred.

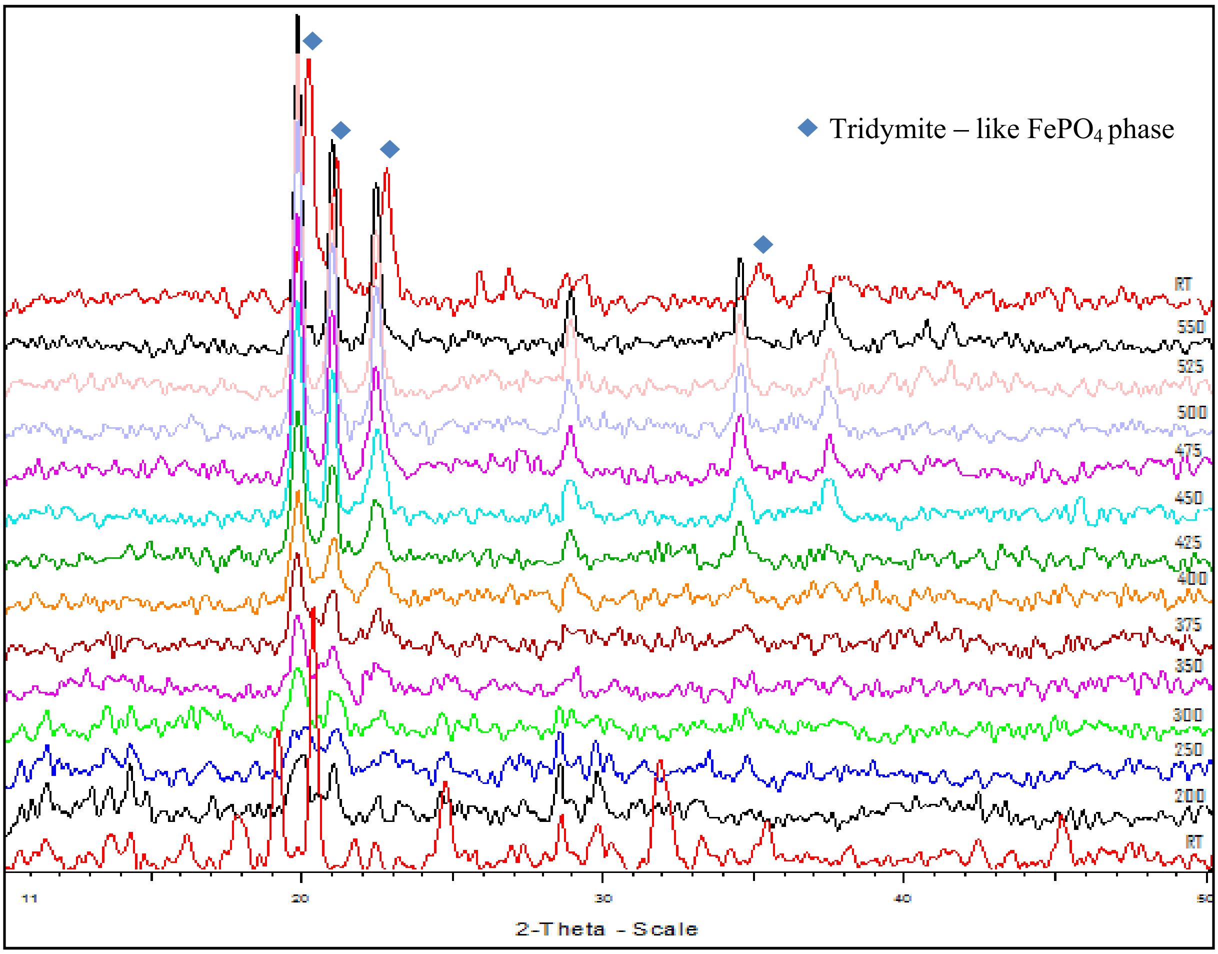

Figure 4.23 *In situ* diffractograms of uncalcined catalyst A in an oxidizing atmosphere

It was clearly evident that during the calcination process the four major reflections of the tridymite-like FePO$_4$ phase dominate from 300 °C and no evidence of reflections due to the unwanted quartz type FePO$_4$ phase was observed at the higher temperatures (550 °C). A plot of the variation in the FWHM *vs.* temperature (Fig. 4.24) for the reflection at $2\theta = 22.6°$, which belongs to the tridymite-like FePO$_4$ phase, suggests the growth of particles upon calcination with elevation in temperature. Using the Scherrer equation, the crystallite size was determined and it was estimated that the particle size was within the range of 4 nm to 11 nm.

The small crystallite size correlates with the low intensity of the peaks obtained for the tridymite-like $FePO_4$ phase. Also, the decrease in the FWHM values is a good indication of an increase in the crystallinity of the sample.

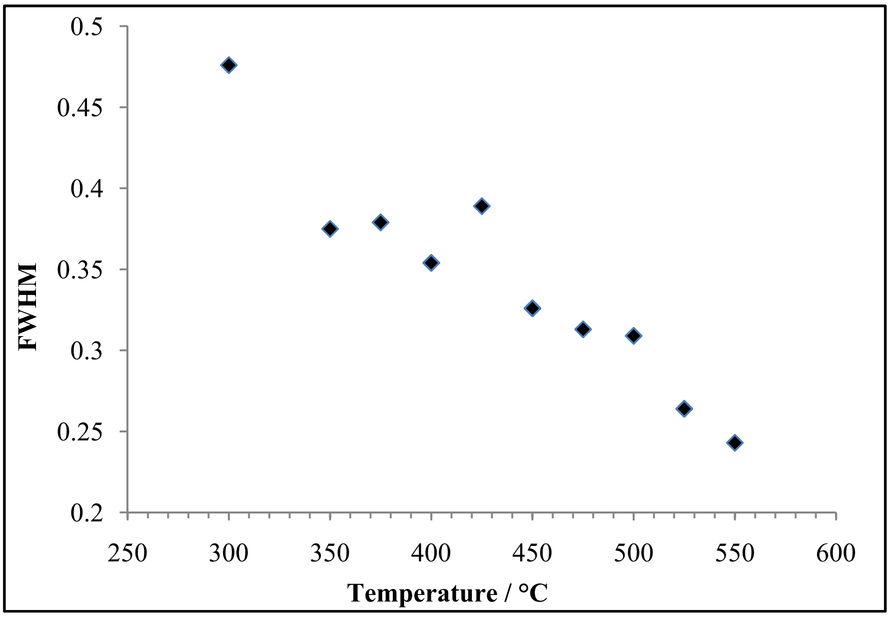

Figure 4.24 Change in FWHM for catalyst A

The effect of high temperature calcination was considered as well. The calcined catalyst A was subjected to a longer period of heating at each temperature interval under the oxidizing atmosphere (Fig. 4.25) which was in actual fact twice the time used at each temperature interval during the initial calcination process (Fig. 4.23). Contrary to what was observed previously (Fig. 4.23), reflections due to the quartz type $FePO_4$ phase were observed from the onset temperature of 548 °C (Fig. 4.25). These results indicate that at temperatures higher than 500°C, the longer exposure of the catalyst to heat at each temperature interval influences phase transformation.

The aim of the following *in situ* XRD experiments was to determine whether the initial formation of the tridymite-like $FePO_4$ phase as the major phase allows for the subsequent formation of the α-phase, which is reported to be a very selective and active catalyst for ODH reactions [6]. Hence it was decided to carry out *in situ* reduction and reoxidation of the tridymite-like precursor to observe the phase changes occurring during these processes. Initially *in situ* experiments for calcined catalyst A under nitrogen (as inert gas) were carried out from 30 °C to 550 °C. The data (Fig. 4.26) clearly indicate that there were no phase changes for calcined catalyst A up to the temperature of 550 °C.

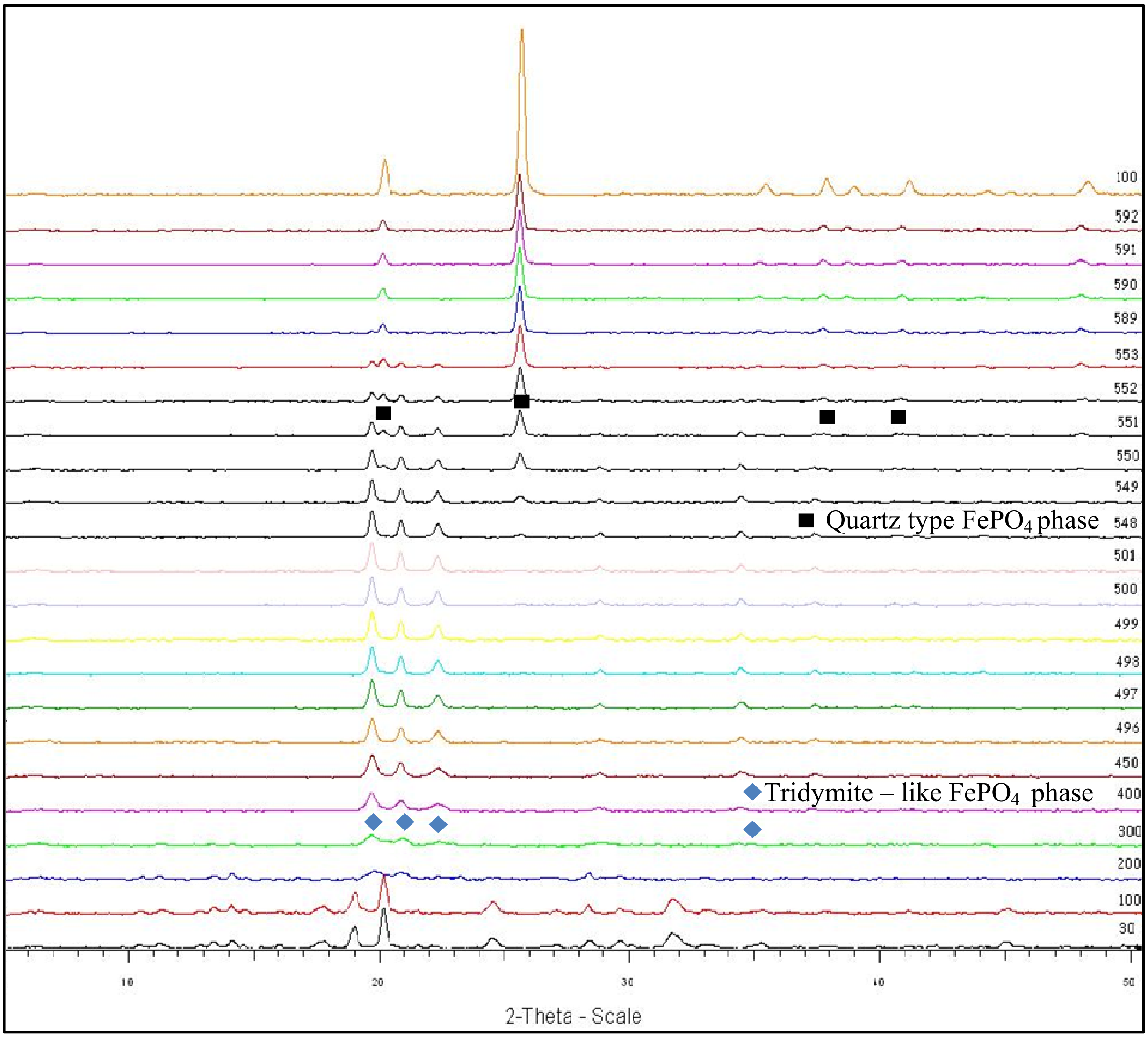

Figure 4.25 *In situ* diffractograms of uncalcined catalyst A in an oxidizing atmosphere over a longer heating period at elevated temperatures

The next step was to observe the phase changes occurring during the reduction process. The reducing gas used initially was a 5% H_2 in argon mixture and the flow rate used was also 30 mL/min, which was in correlation with the parameters used for the TPR experiments. The results obtained showed the negative effect when argon is used as the inert gas (Fig. 4.27). The evidence of incomplete reduction includes the appearance of both the $Fe_3(P_2O_7)_2$ (intermediate reduced phase), as well as $Fe_2P_2O_7$, at temperatures above 500 °C. The reoxidation process (Fig. 4.28) showed the formation of the α-phase, however, the intermediate reduced phase, which does not change under reoxidation conditions, was still present.

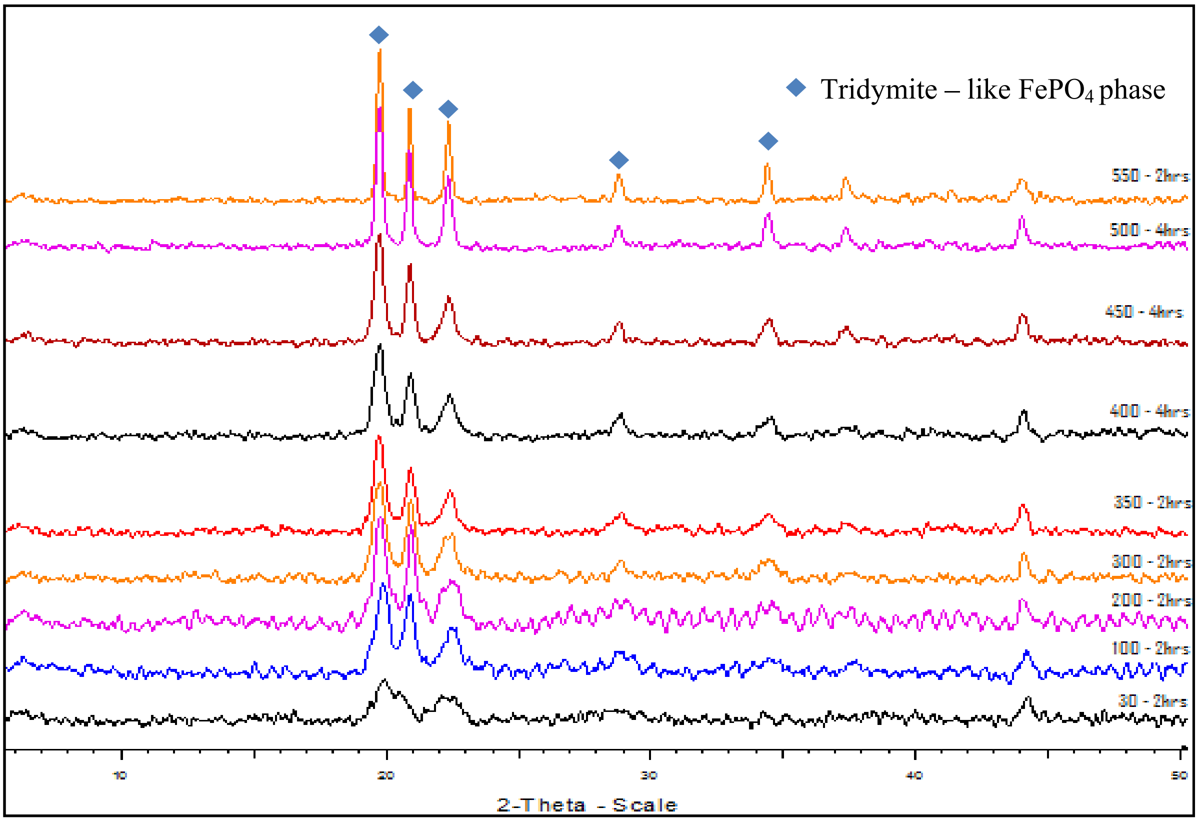

Figure 4.26 *In situ* diffractograms of calcined catalyst A in an inert (N_2) atmosphere

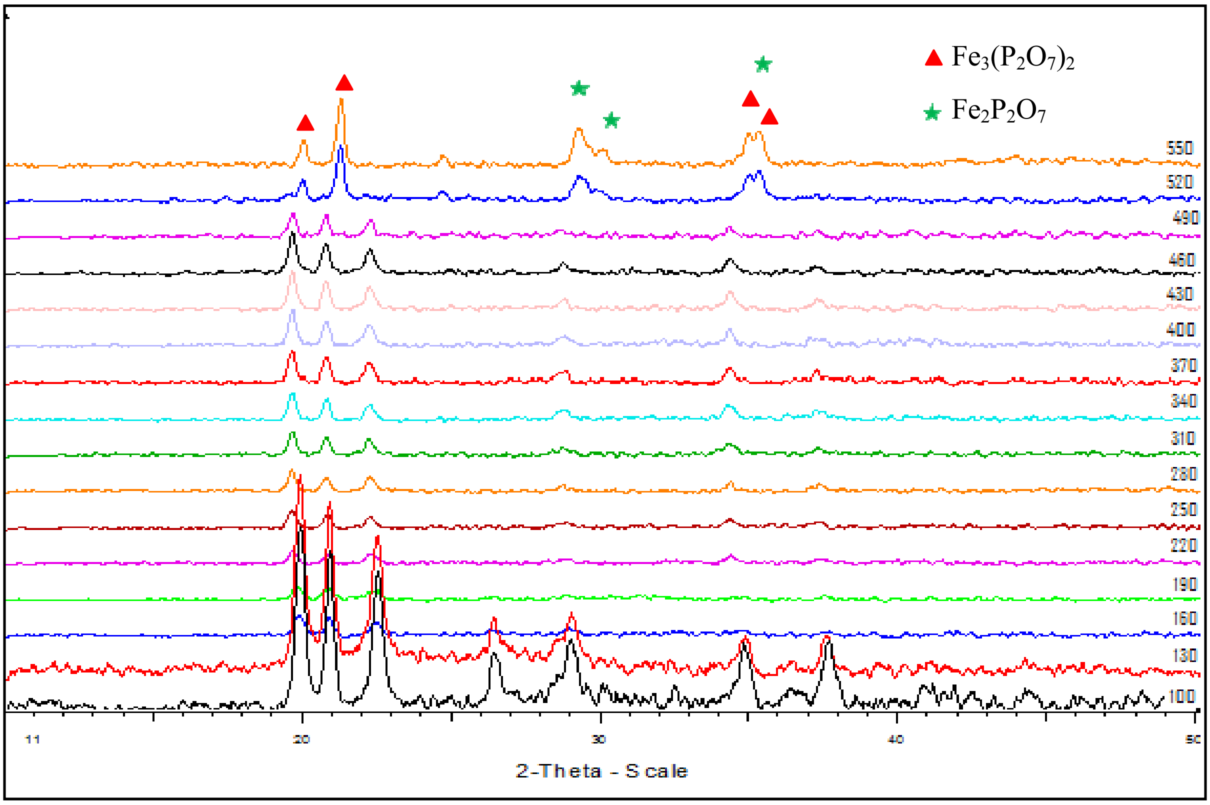

Figure 4.27 *In situ* diffractograms of calcined catalyst A in a reducing atmosphere, using a 5 % H_2 in argon mixture – incomplete reduction

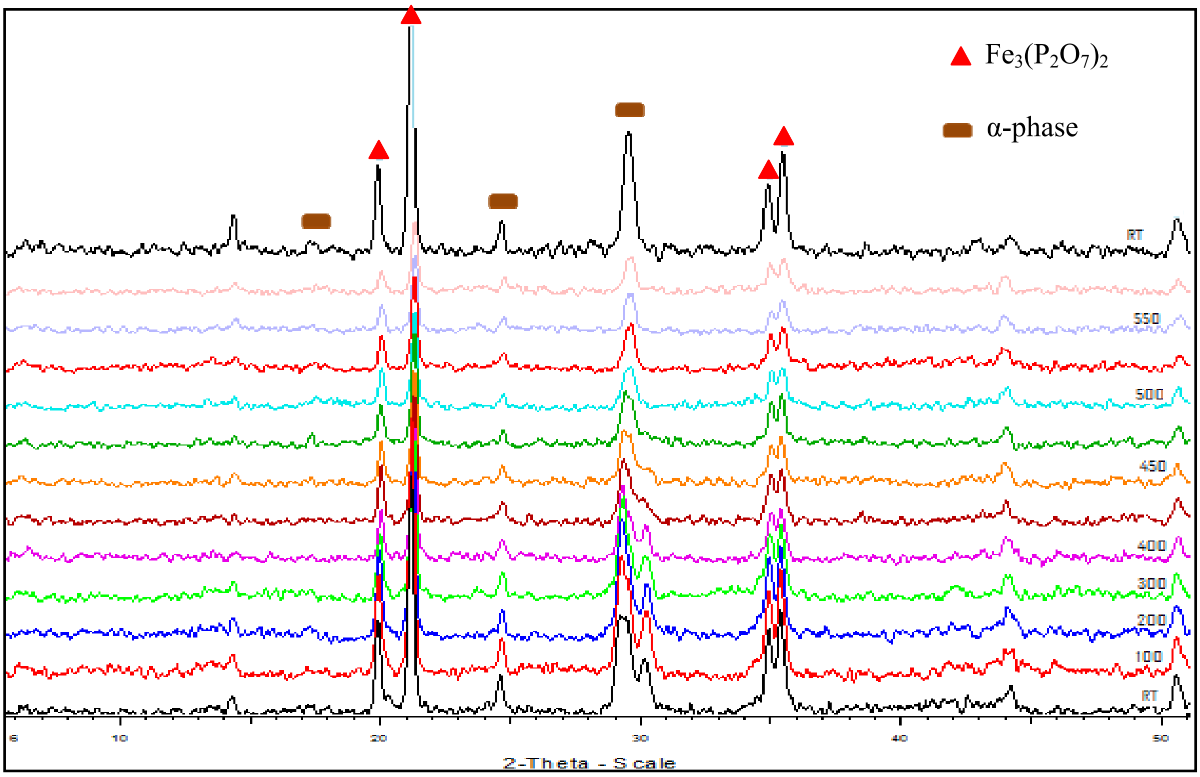

Figure 4.28 *In situ* diffractograms of the incompletely reduced catalyst A in an oxidising atmosphere, using a 5 % O_2 in nitrogen mixture - after incomplete reduction

Consequently, a 5% H_2 in nitrogen mixture was used to study the complete reduction process. The reduction and reoxidation results (Fig. 4.29 and Fig. 4.30) clearly showed the formation of $Fe_2P_2O_7$ with no evidence of the intermediate phase after the reduction process and its complete conversion to the α-phase during the reoxidation process. Figure 4.31 provides and overall summary of the phases formed after calcination, complete reduction and complete reoxidation shown in Figures 4.23, 4.29 and 4.30 respectively. It is evident that after isolation of the phase post calcination, reduction using the 5 % H_2 in nitrogen mixture allows for transformation to $Fe_2P_2O_7$, with no evidence of the intermediate phase and during the reoxidation process the α-phase is isolated.

The phase intensity *vs*. temperature plots (Fig. 4.32 and Fig. 4.33) provide a concise understanding of the phase changes occurring at the various temperatures during the reduction and reoxidation processes mentioned previously (Fig. 4.29 and Fig 4.30). A correlation could be drawn between the onset temperature for the formation of the active α-phase and that of the optimal operational conditions within the reactor bed found experimentally.

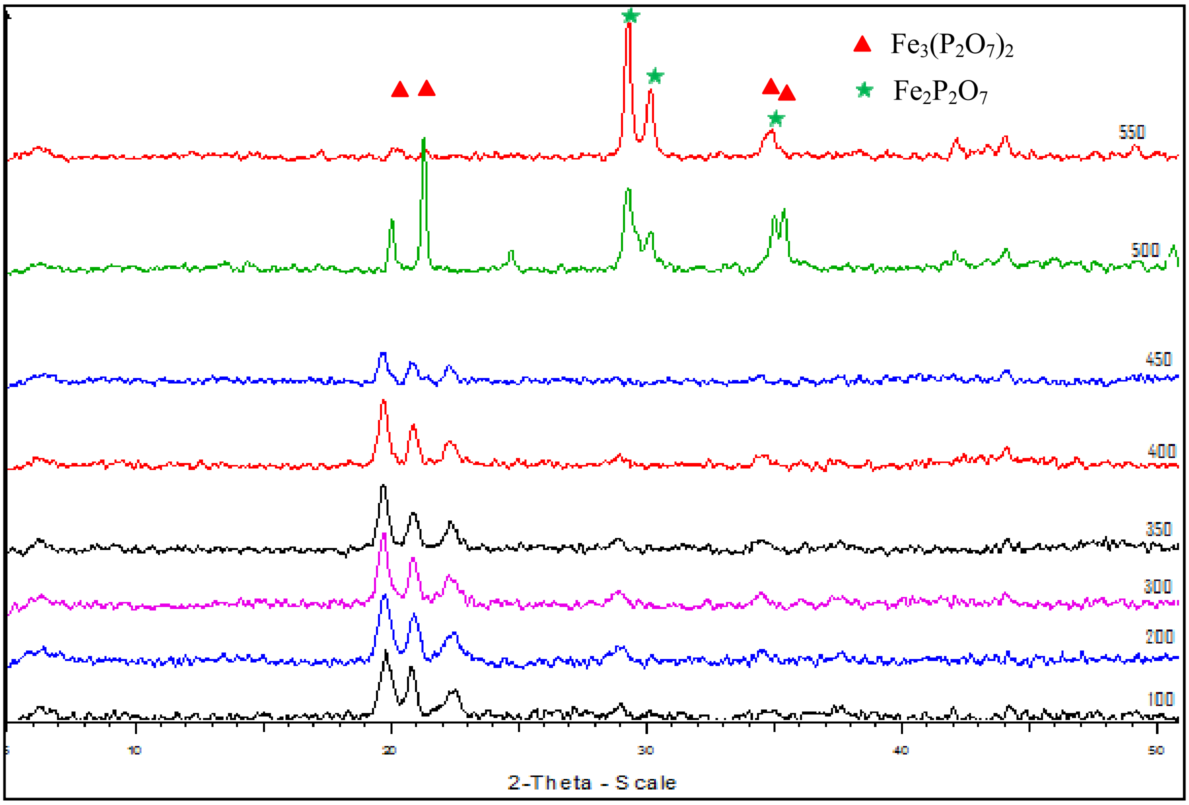

Figure 4.29 *In situ* diffractograms of calcined catalyst A in a reducing atmosphere, using a 5 % H_2 in nitrogen mixture - complete reduction

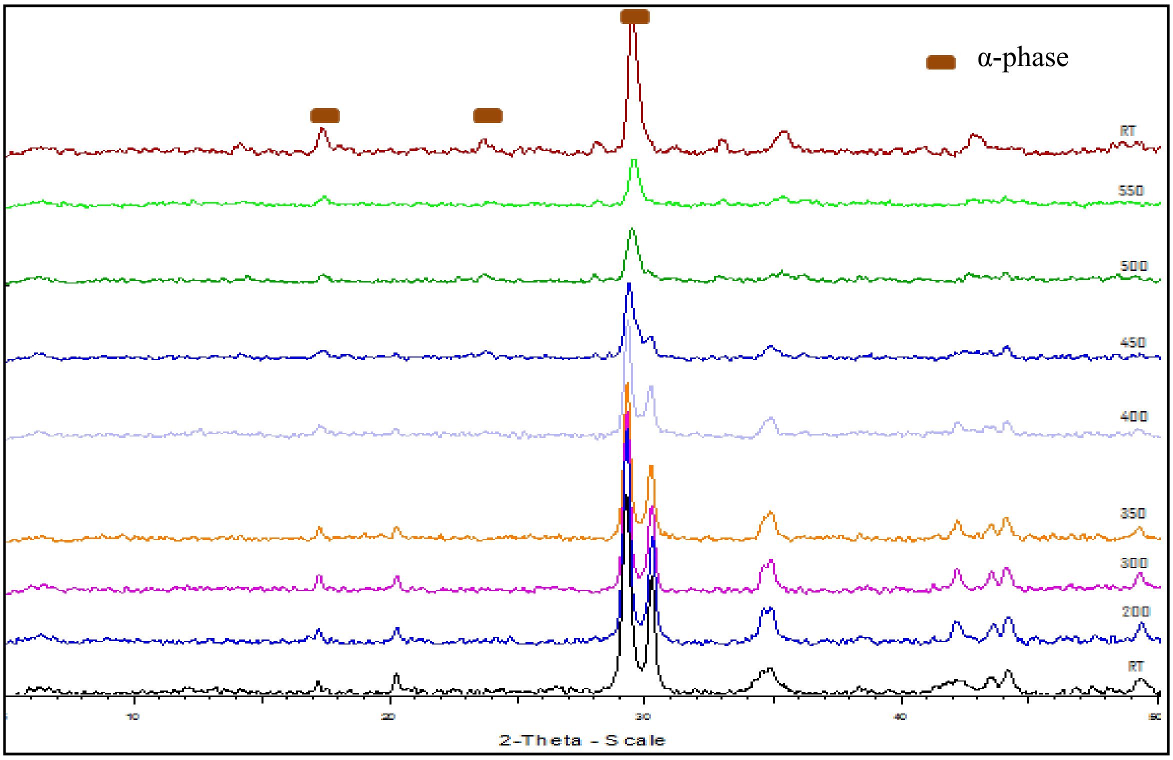

Figure 4.30 *In situ* diffractograms of the completely reduced catalyst A in an oxidising atmosphere, using a 5 % O_2 in nitrogen mixture - after complete reduction

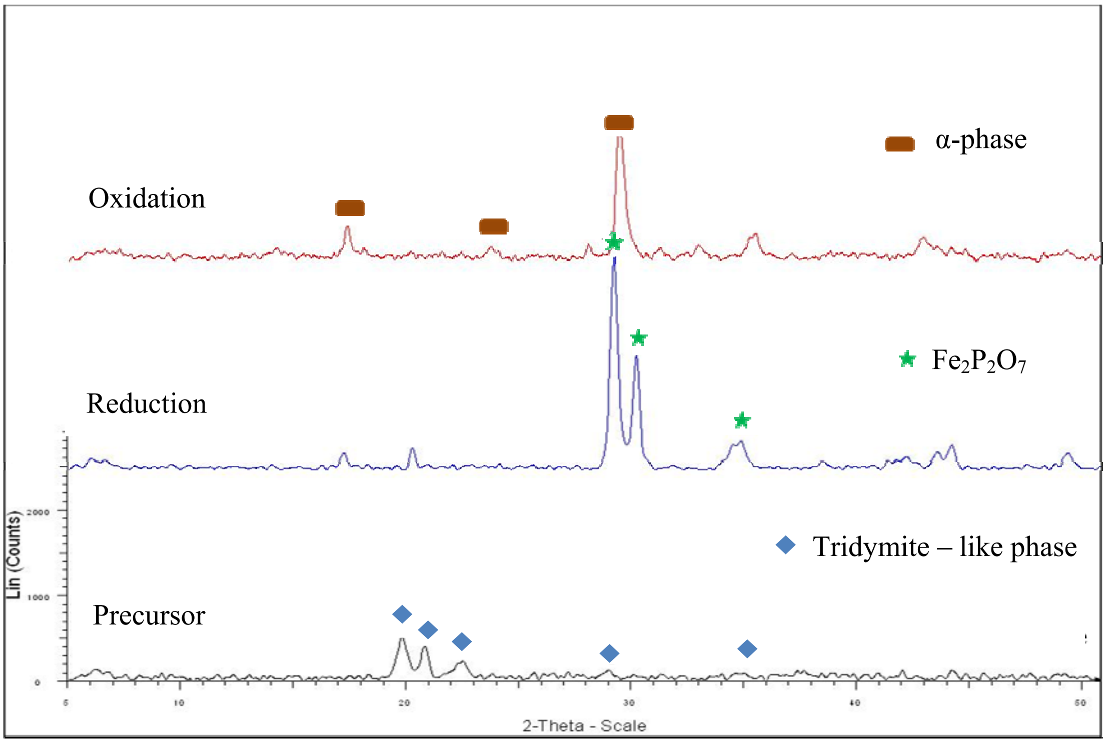

Figure 4.31 Phases formed for catalyst A after calcination, complete reduction and complete reoxidation

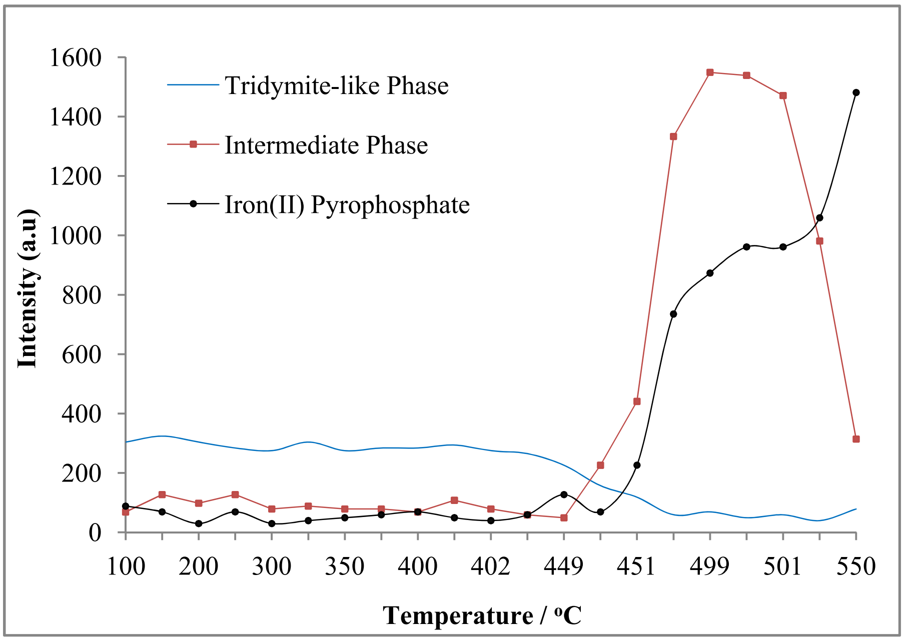

Figure 4.32 Summary of the phase changes occurring during the reduction cycle – starting with the tridymite-like $FePO_4$ phase of catalyst A

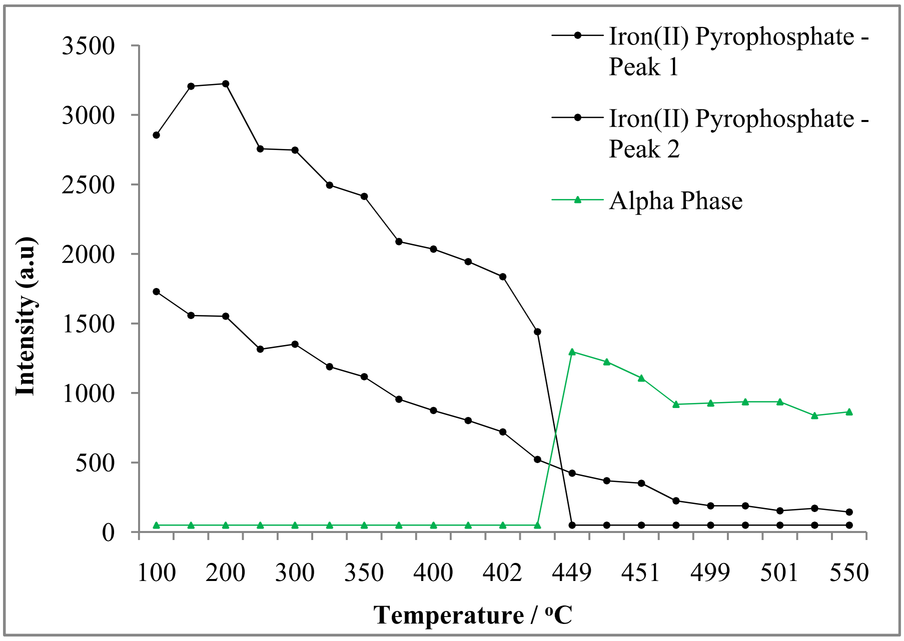

Figure 4.33 Summary of the phase changes occurring during the reoxidation cycle – starting with the $Fe_2P_2O_7$ reduced phase

Previous results showed that the quartz type $FePO_4$ phase formed at higher temperatures after calcination of catalyst A for longer periods at each temperature interval (Fig. 4.25). The room temperature XRD scan of the calcined catalyst (Fig. 4.34) clearly showed the formation of the quartz type $FePO_4$ phase as the major phase with peaks found at a 2θ values of 20.4°, 25.9°, 38.1° and 41.4°.

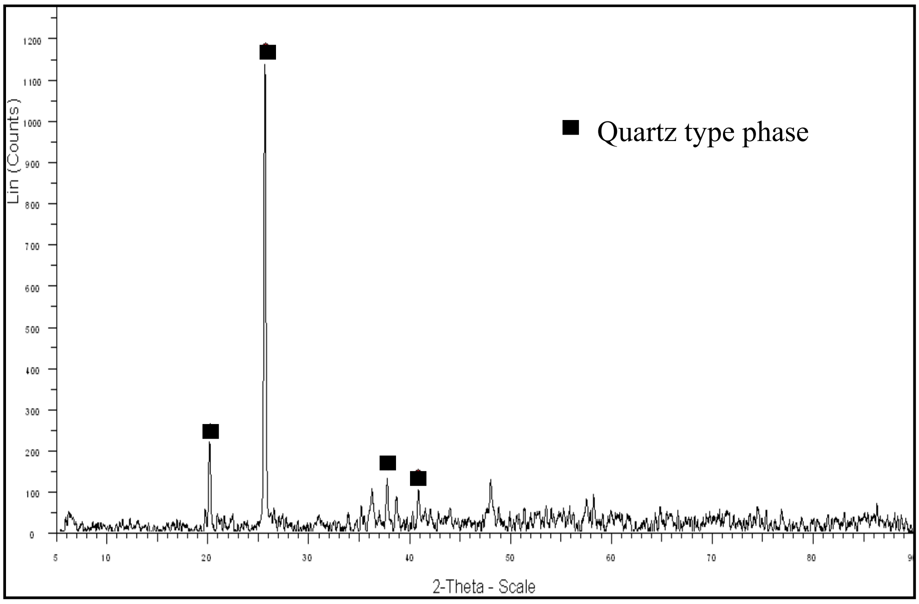

Figure 4.34 Room temperature scan of the quartz type $FePO_4$ phase of catalyst A after calcination at longer periods at each temperature interval

The identical conditions used for the complete reduction and reoxidation processes for the tridymite-like $FePO_4$ phase of calcined catalyst A were employed for the material consisting of the quartz type $FePO_4$ phase. A summary of the reduction and reoxidation process is shown in the diffractograms given in Figure 4.35.

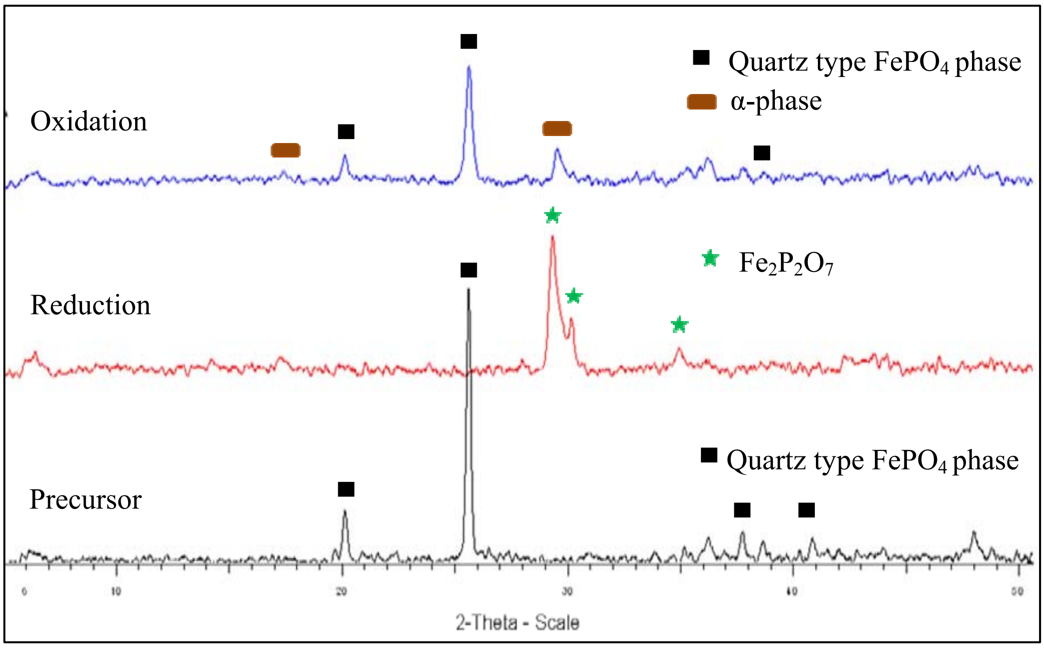

Figure 4.35 Summary of the phase changes of the quartz type phase of catalyst A after calcination for longer periods at each temperature interval, reduction and reoxidation

The complete reduction and reoxidation results for the quartz type $FePO_4$ phase can be found in Appendix B. The results shown in Figure 4.35 clearly revealed that a catalyst consisting of the pure quartz type $FePO_4$ phase was transformed to $Fe_2P_2O_7$ upon reduction and reoxidation showed the formation of the α-phase as well as the quartz type $FePO_4$ phase. This indicated that calcination at higher temperatures hinders the complete formation of the α-phase during the redox cycle.

The phase intensity *vs.* temperature plots for the phase transformations of the quartz type $FePO_4$ phase from 400 °C onwards are shown in Figures 4.36-4.38. The plot for the reoxidation process (Fig. 4.38) was very interesting, because it showed that when calcined catalyst A consisted of the quartz type $FePO_4$ phase as a precursor, it did not lead to the formation of the α-phase as the 'major phase' upon reoxidation. An increase in temperature during the reoxidation process decreases the concentration of the α-phase and initiation of the phase transformations occurs at a higher temperature. A schematic comparison of the phase transformations of catalyst A under varying conditions is depicted in Figure 4.39.

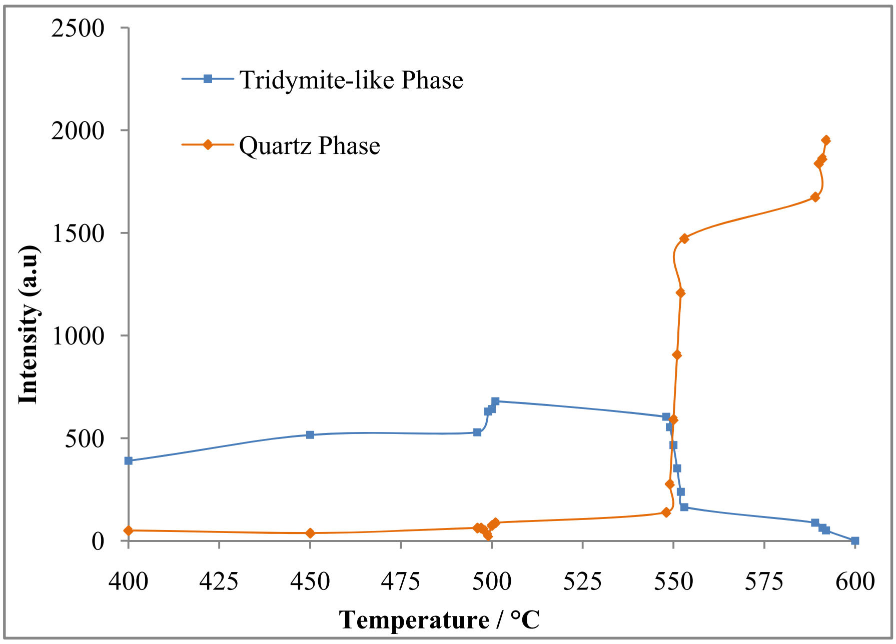

Figure 4.36 Summary of the phase changes occurring in catalyst A during calcination for longer periods at each temperature interval – formation of quartz type phase

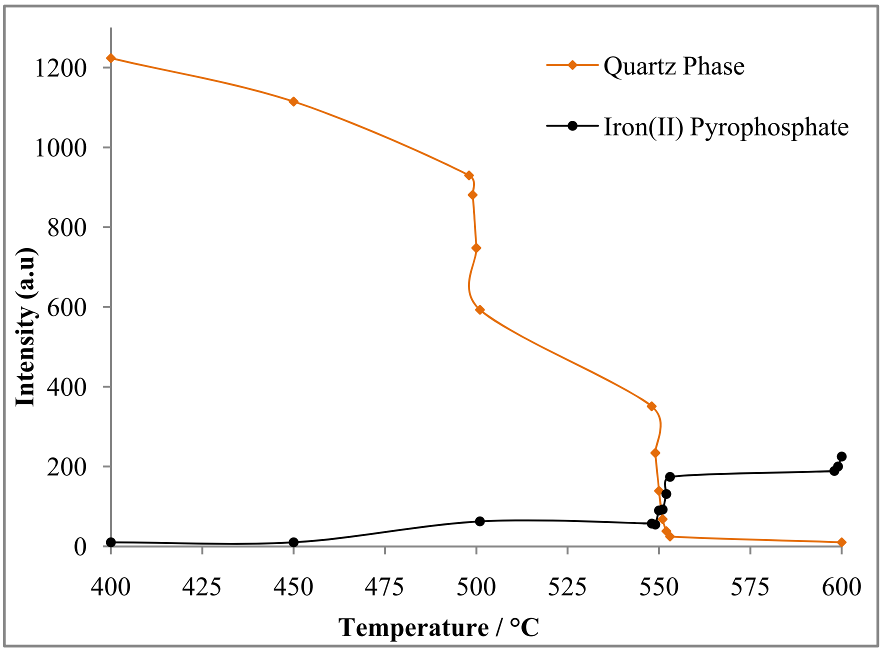

Figure 4.37 Summary of the phase changes occurring during the reduction cycle – starting with the quartz type $FePO_4$ phase of catalyst A

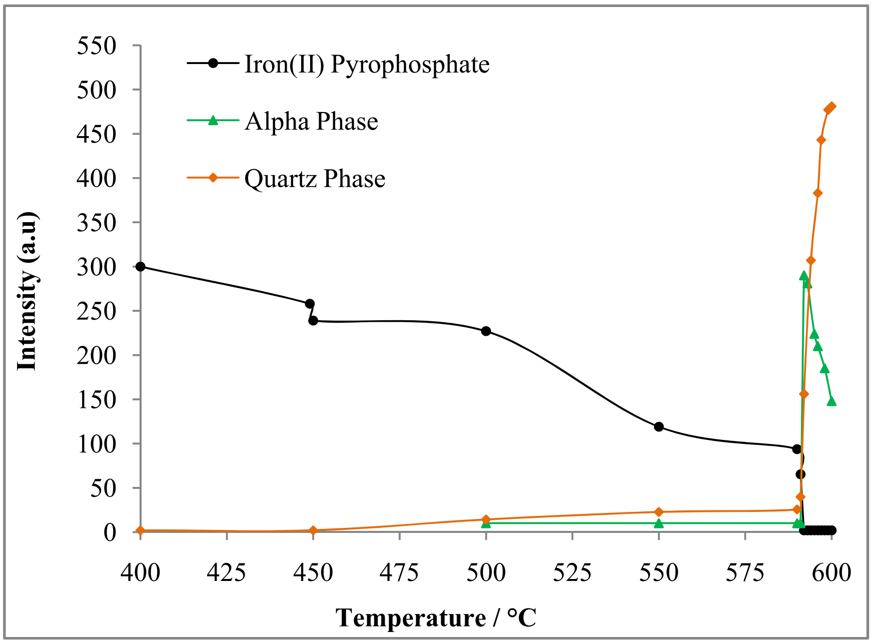

Figure 4.38 Summary of the phase changes occurring during the reoxidation cycle – starting with the $Fe_2P_2O_7$

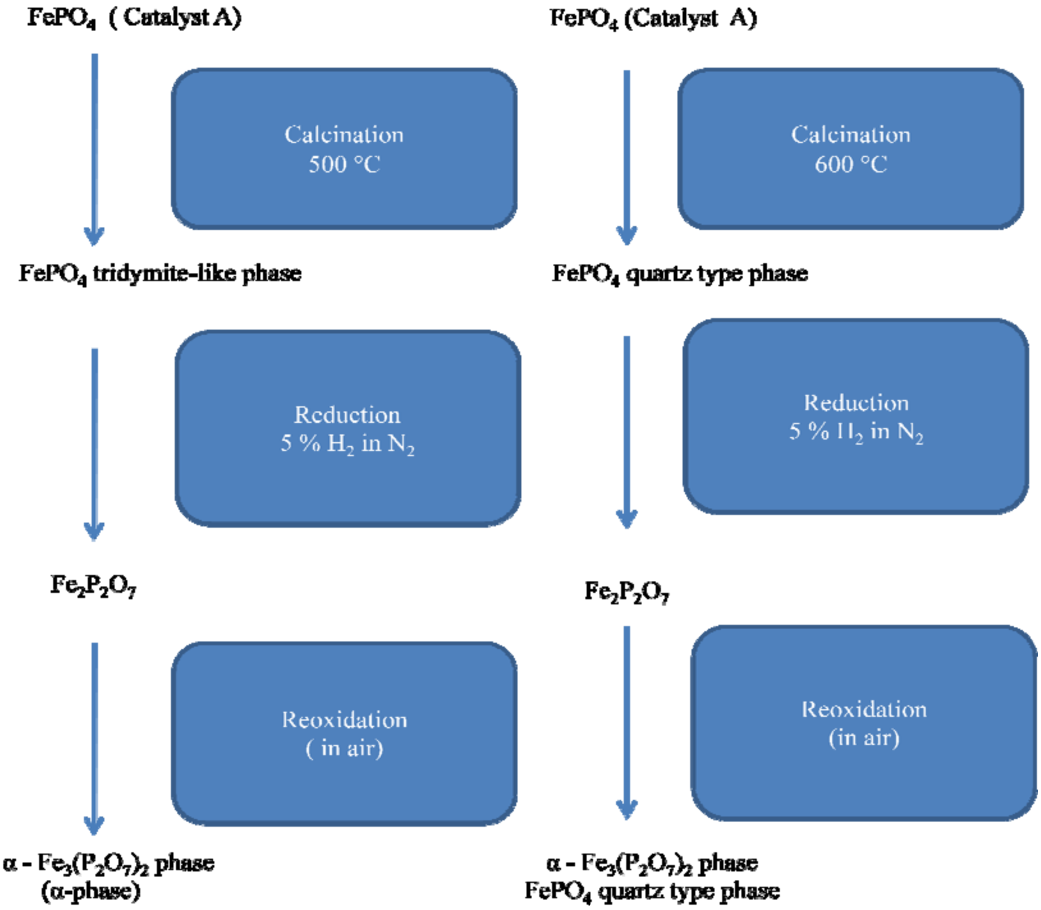

Figure 4.39 Phase transformations of catalyst A calcined at different temperatures

It must be noted that formation of the quartz type $FePO_4$ phase was due to a higher temperature of calcination as well as subjecting the catalyst to a longer period of time at each temperature interval during the calcination process.

4.11 Thermogravimetric Analysis/Differential Scanning Calorimetry (TGA/DSC) plots for uncalcined catalyst A

In an effort to determine the nature of loosely bound species present within the catalyst, a thermogravimetric analysis on uncalcined catalyst A was carried out in static air. The weight loss seems to have occurred via two steps (Fig. 4.40). The initial major weight loss was observed between the temperature range of 100-200 °C and the latter, minor weight loss was observed at around 300 °C. The TGA profile correlates with data reported in literature, where it was reported that the weight loss at the intial temperature range could be attributed to the loss of water molecules either physically adsorbed or from the loss of crystalline water [7, 17]. It is important to note that the diffractogram for the uncalcined catalyst A had shown a correlation to the $FePO_4.2H_2O$ type phase as mentioned previously.

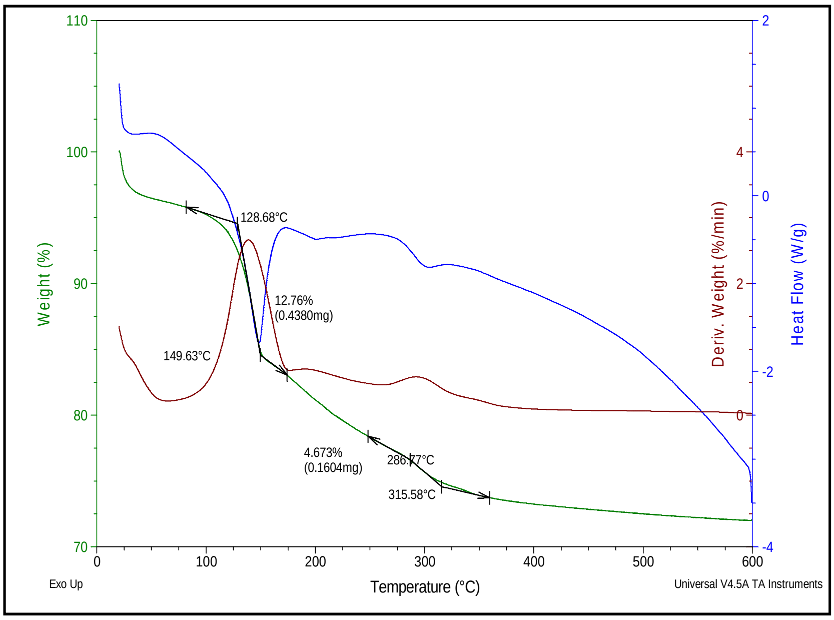

Figure 4.40 TGA-DSC profile of the uncalcined catalyst

Reports have shown that weight loss could also be attributed to the transition of $FePO_4$ to the tridymite-like $FePO_4$ phase and in addition there has been evidence of weight loss being observed due to the decomposition of $NH_4FeP_2O_7$, depending on the synthetic procedure [17]. In correlation, it was observed during the *in situ* experiments that formation of the tridymite-like $FePO_4$ phase occurs from the onset temperature of 300 °C and a weight loss of

~ 13 % was seen in the TGA profile. Thus based on these reports, the initial weight loss could be due to the loss of water either physically adsorbed or from the loss of crystalline water and the latter weight loss could be the result of phase transition.

4.12 Transmission Electron Microscopy (TEM), Selected Area Diffraction Pattern (SADP) and particle size analysis

TEM analyses determined the particle sizes of individual particles and the results are number averaged. The initial TEM results obtained for the calcined catalyst A are shown in Figure 4.41. It was observed that the catalyst consists of discrete round, stacked particles with particle size within the range of 30-35 nm. These particle sizes do not correlate with the values obtained from the XRD data. One of the reasons could be, as mentioned, that particles could be formed from several crystallite grains. In addition, the stacking of the particles enhances the particle size as observed for the 41 nm particle size in the micrograph shown below (Fig. 4.41). It was consequently decided to further investigate the sample.

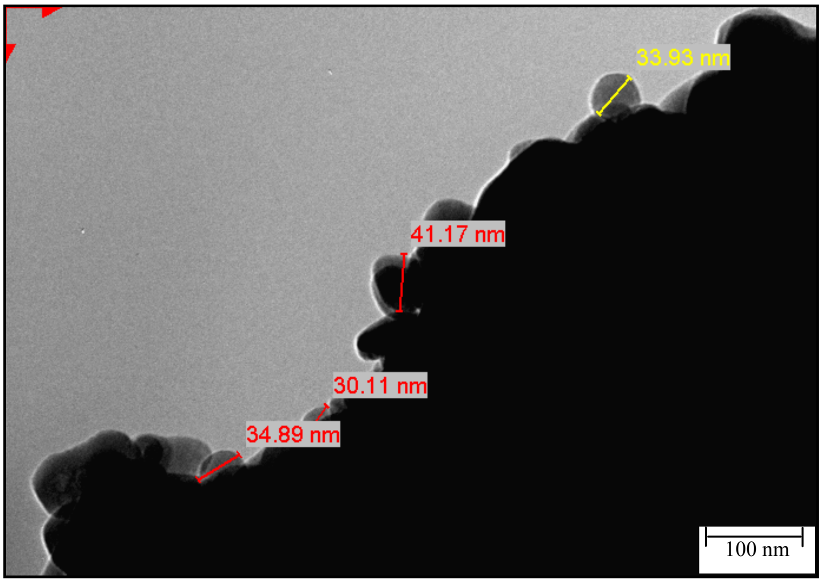

Figure 4.41 Initial TEM micrograph (scale = 100 nm) of the calcined catalyst A

Initially images of pure silica were obtained which was used as a support during synthesis. The results are shown in Figure 4.42. The micrograph showed that the large particle size seen in Figure 4.41 was actually due to the silica support. Hence further images were taken to determine the actual particle size of the $FePO_4$ particles. This is shown in Figure 4.43. The particle size was measured to be within the range of 7-11 nm, which is in good correlation with the crystallite size obtained from the XRD data.

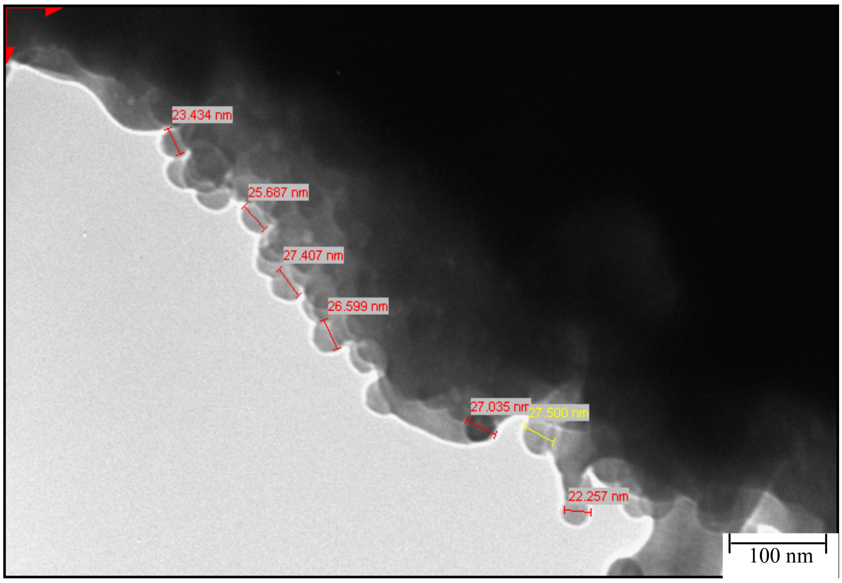

Figure 4.42 TEM micrograph (scale = 100 nm) of the pure silica support

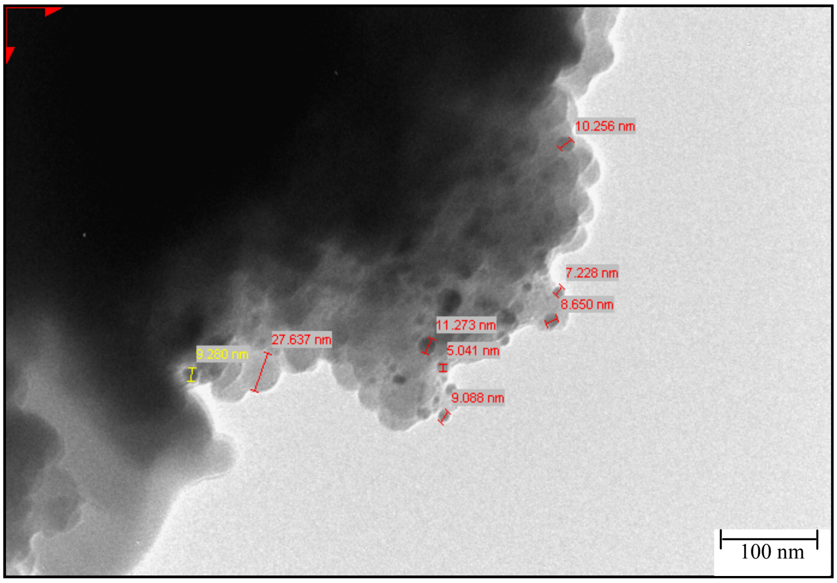

Figure 4.43 TEM micrograph (scale = 100 nm) of the $FePO_4$ particles on the silica support for calcined catalyst A

It is important to note that the behaviour of this catalyst is influenced by external factors such as moisture and the intense electron beam from the instrument. It seems that when the catalyst is not dried completely, it forms plate-like structures when in contact with the electron beam as shown in the micrographs shown in Figure 4.44.

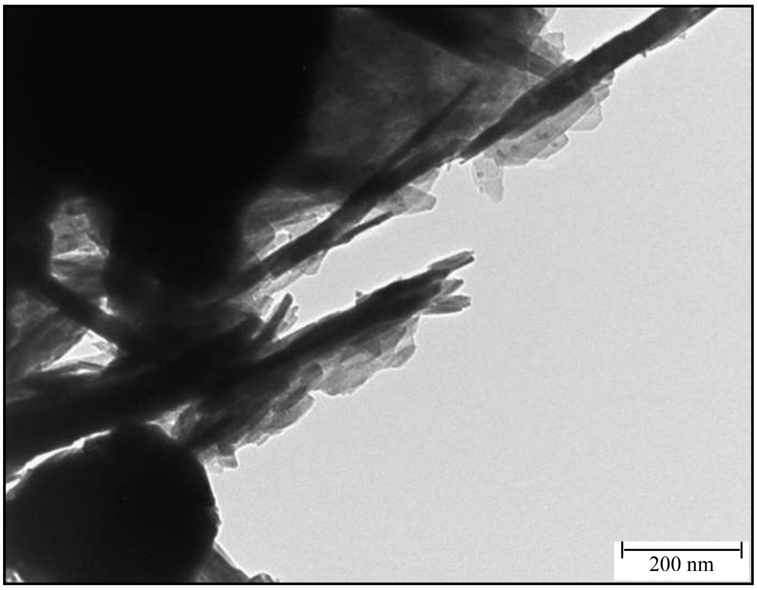

Figure 4.44 The effect of water on the TEM micrograph (scale = 200 nm) of calcined catalyst A

The selected area diffraction pattern (SADP) for calcined catalyst A was also recorded (Fig. 4.45). The appearance of the spots and the halo on the image is an indication of the catalyst containing both crystalline and amorphous regions; hence the catalyst is described as polycrystalline.

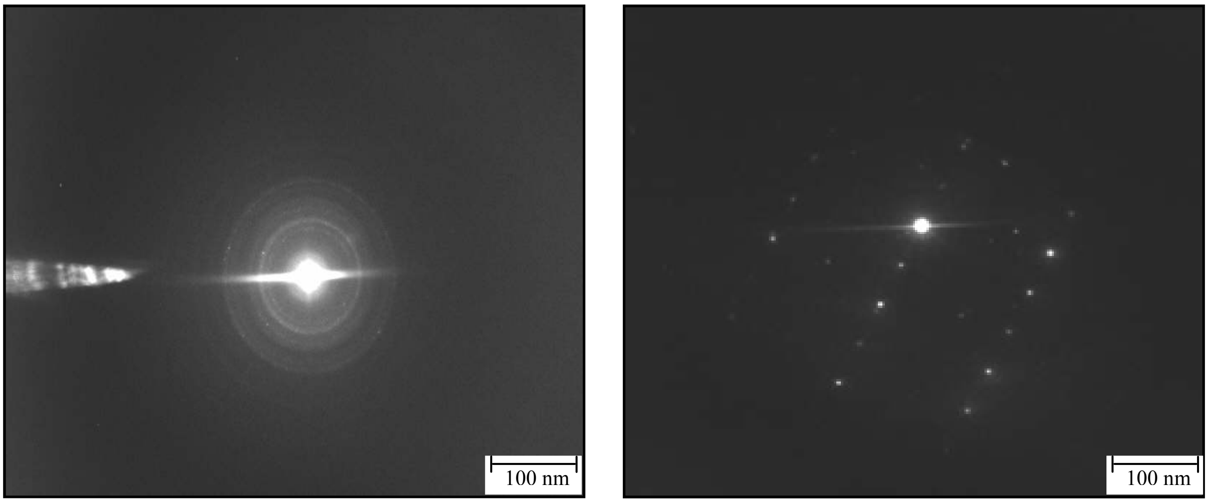

Figure 4.45 SADP (scale = 100 nm) of calcined catalyst A

Indexing of the electron diffraction pattern (Fig. 4.45) can be used to determine the actual crystalline planes which are present and these results can be correlated with the diffractogram of calcined catalyst A. However, there seems to be evidence of superimposed spots on the pattern which could be due to the beam being focused on more than one crystal particle. This is not due to the silica support because the diffractogram of silica used during the synthesis shows an amorphous pattern and no electron diffraction pattern was observed (Fig. 4.46).

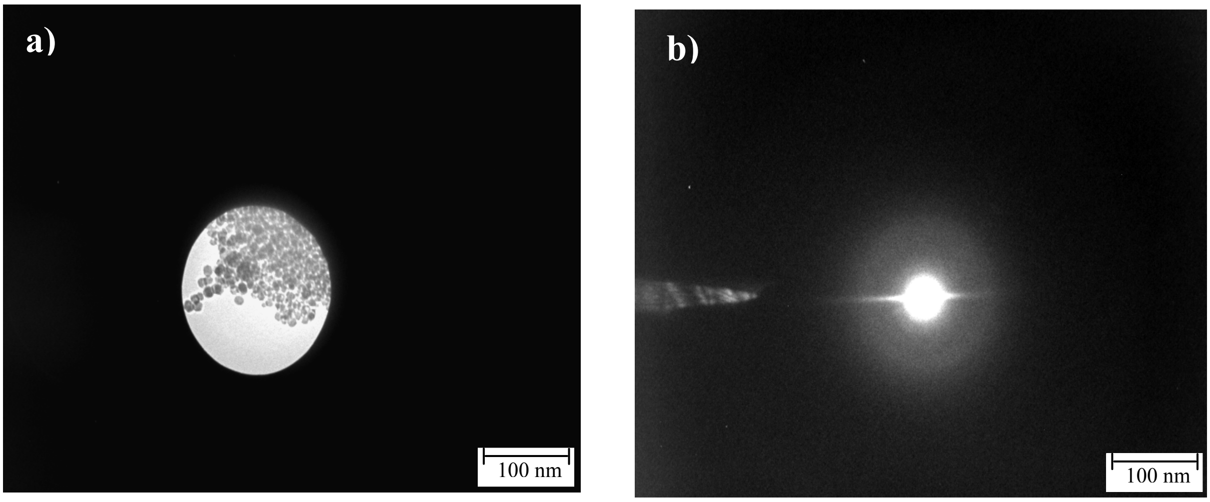

Area being analysed

Electron Diffraction pattern

Figure 4.46 Area being analysed in TEM (a) and SADP (scale = 100 nm) of silica (b)

4.13 HR-TEM, SADP and EDX of calcined catalyst A

HR-TEM was used as an additional technique to support the evidence found in Section 4.12. The image obtained (Fig. 4.47), did not allow for complete identification of the catalyst seeing that the actual silica support and $FePO_4$ particles could not be isolated. It appeared as a mass consisting of particles overlapping each other.

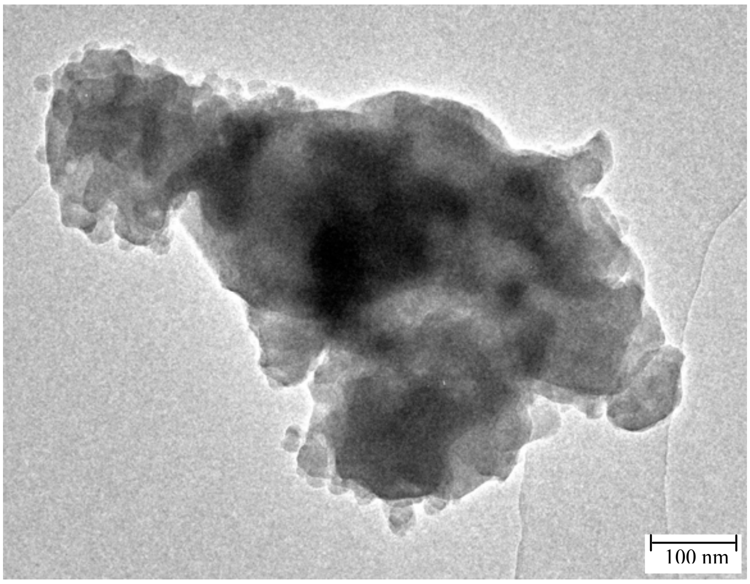

Figure 4.47 TEM micrograph (scale = 100 nm) of calcined catalyst A

The SADP and the EDX data were more useful as supporting evidence for the $FePO_4$ particles as well as the silica support (Fig. 4.48-4.49).

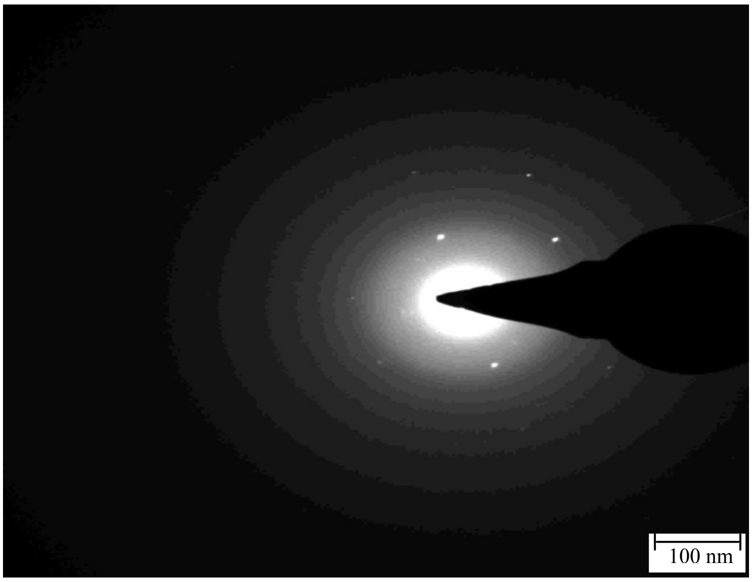

Figure 4.48 SADP (scale = 100 nm) of calcined catalyst A

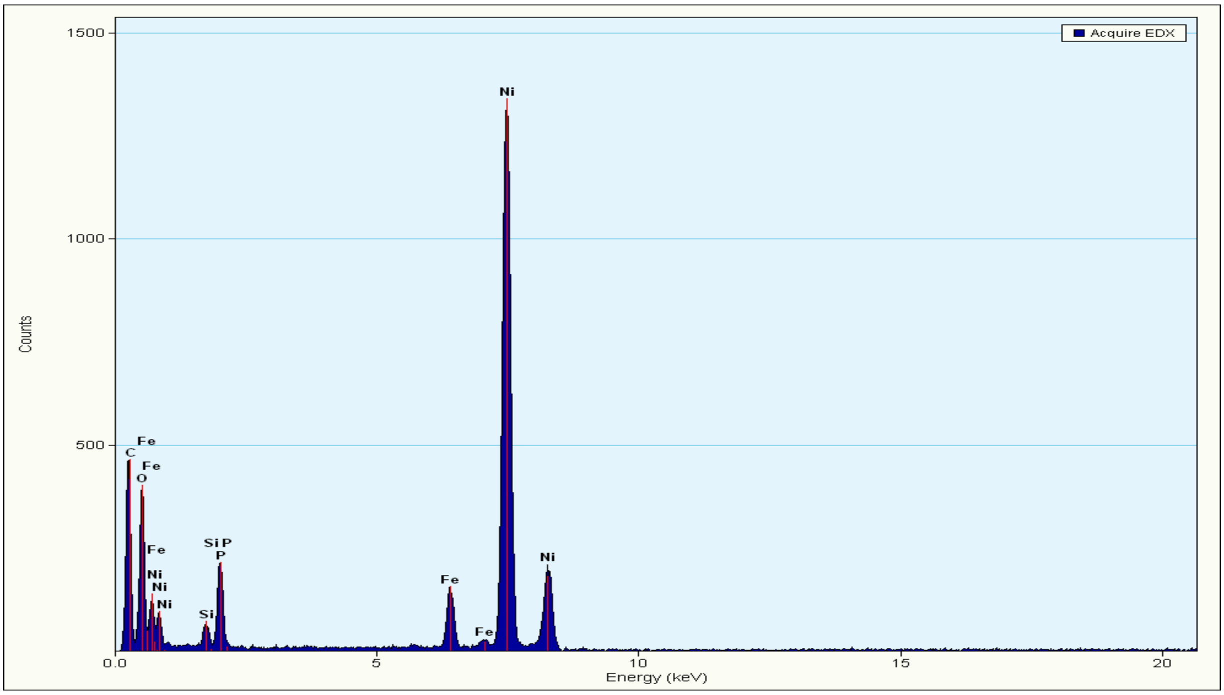

Figure 4.49 EDX data for calcined catalyst A obtained from HR TEM image

The appearance of the halo as well as the spots on the SADP pattern confirms the occurrence of a crystalline phase. The EDX data showed that iron, phosphorous, as well as silica were present in the sample. Although the results obtained from HR-TEM were not as conclusive as the TEM results discussed previously (Section 4.12), they did confirm that the catalyst was crystalline and iron, phosphorous and silica were present in the catalyst.

4.14 Mössbauer Spectroscopy

The Mössbauer spectra of the a) calcined (tridymite-like $FePO_4$ phase) catalyst A, b) reduced catalyst A and c)-d) oxidised catalyst A are shown in Figure 4.50, and the isomer shifts (IS), quadrupole splitting (QS), site fractions (*f*) and phase assignments are collected in Table 4.8 where the isomer shifts are given relative to α-Fe at room temperature.

The spectral parameters of calcined catalyst A (a) confirm the occurrence of the $FePO_4$ tridymite-like phase which has 100 % Fe^{3+} species and is in agreement with the experimental route used [9].

The formation of the reduced phase for catalyst A (b) is observed by the occurrence of Fe^{2+} species with IS and QS values of 1.23(2) mm/s and 1.22(2) mm/s, and 2.37(2) mm/s and 2.58(2) mm/s respectively, which are attributed to $Fe_2P_2O_7$ reported in literature as having similar parameters [5]. The spectrum also showed a small contribution (27 %) from a component with IS and QS values of 0.39(3) mm/s and 0.36(2) mm/s respectively, which is most likely the result of the tridymite-like $FePO_4$ phase of the calcined precursor catalyst which was not completely reduced during the process [5].

The Mössbauer spectra for the oxidised catalyst in Figure 4.50 (c) and (d), show the effect of temperature on phase formation. The spectrum obtained after oxidation at a temperature range below 500 °C (Fig. 4.50 (c)) showed a 50 % Fe^{3+} component with IS value of 0.45(2) mm/s and QS value of 0.70(4) mm/s, and a weaker Fe^{2+} component with IS of 1.22(2) mm/s and QS of 2.81(4) mm/s. These values are in accordance with the values of Fe^{3+} and Fe^{2+} components in the α-phase [5]. There were also contributions from Fe^{2+} species with IS and QS values consistent with those of $Fe_2P_2O_7$, which is not unexpected since this sample was previously in the reduced state. Fit to the spectrum required a very small (3(2) %) unidentified component with IS and QS values of 0.50(4) and 2.65(4) mm/s, respectively.

Table 4.8. Mössbauer parameters, isomer shift (IS), electric quadrupole splitting (QS) site fractions (*f*), phase assignments and the attributed phases, determined from the spectra of catalyst A after a) calcination, b) reduction, and oxidation c) ≤500 °C, and d) ≥550 °C. The isomer shifts are expressed relative to α-Fe at room temperature.

Sample	**IS (mm/s)**	**QS (mm/s)**	***f***	**Relative Intensity (%)**	**Attributed phase**
(a) Calcined $FePO_4$	0.42(2)	0.36(2)	Fe^{3+}	100(2)	$FePO_4$-tdm[a]
(b) Reduced catalyst	1.23(2)	2.37(2)	Fe^{2+}	36(3)	$Fe_2P_2O_7$
	1.22(2)	2.58(2)	Fe^{2+}	38(3)	$Fe_2P_2O_7$
	0.39(3)	0.36(2)	Fe^{3+}	27(2)	$FePO_4$ –tdm
(c) Low temperature oxidation (≤ 500 °C)	0.45(2)	0.70(4)	Fe^{3+}	50(4)	α-$Fe_3(P_2O_7)_2$
	1.22(2)	2.81(4)	Fe^{2+}	16(3)	α-$Fe_3(P_2O_7)_2$
	1.21(2)	2.46(4)	Fe^{2+}	32(3)	$Fe_2P_2O_7$
	0.50(4)	2.65(4)	Fe	3(2)	X*
(d) High temperature oxidation (≥550°C)	0.29(2)	0.59(2)	Fe^{3+}	79(2)	$FePO_4$ –quartz
	0.38(2)	1.14(5)	Fe	21(3)	X*

[a]*tridymite-like $FePO_4$ phase, *unidentified phases- (possible ferric compound)*

As the oxidation temperature was increased to 600 °C, a 79 % Fe^{3+} species is observed with the IS and QS values of 0.29(2) and 0.59(2) respectively, which are in accordance with the values for the $FePO_4$ quartz type phase [5]. The α-phase has been found to transform at higher temperatures to the quartz type $FePO_4$ phase, however these transformations were reported to occur at around a 1000 °C [6]. In addition, an unidentified phase was also evident.

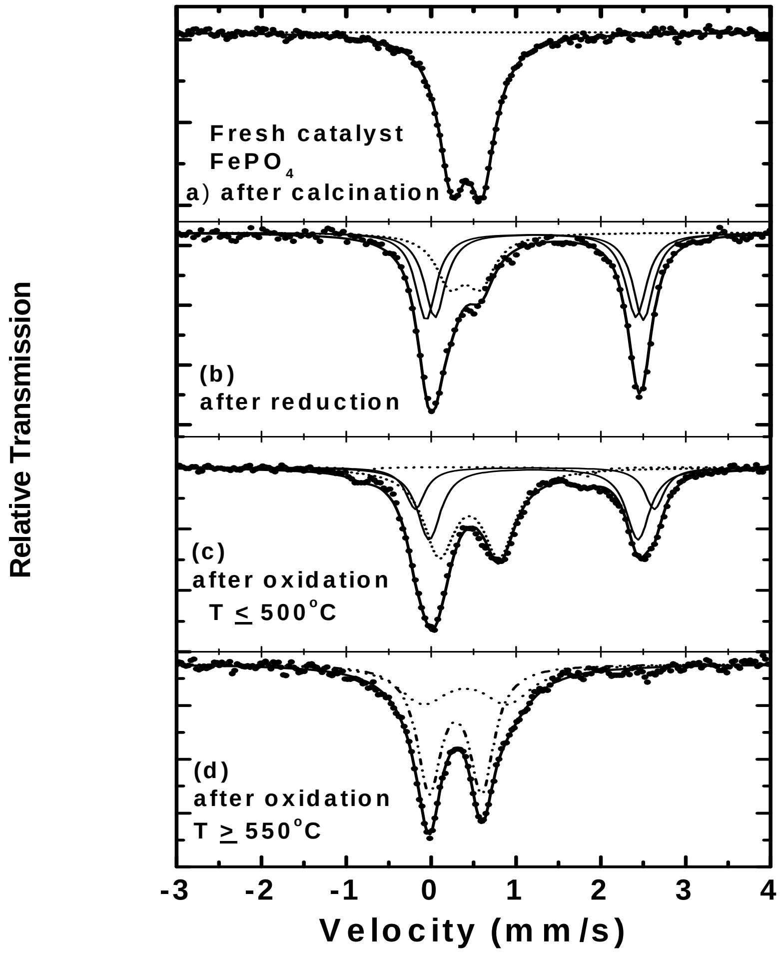

Figure 4.50 Mössbauer spectra, together with fitted components (a) the calcined $FePO_4$ catalyst A, (b) reduced catalyst A, (c) catalyst A after oxidation (≤ 500 °C), (d) catalyst A after oxidation (≥ 500 °C)

4.15 Raman Spectroscopy

The use of Raman spectroscopy serves as a complimentary technique to infrared methodologies, since certain infrared-inactive vibrational modes are Raman-active. Reports have shown that the Raman spectra of calcium phosphates are usually characterized by a strong band at ~ 960 cm^{-1}, which is a result of the symmetric stretching mode of the phosphate group. In addition, other Raman–active bands were reported at ~ 1075 cm^{-1}, ~ 590 cm^{-1} and ~ 435 cm^{-1} [18]. The position of the phosphate anion is dependent on the system it is in. The bands in an aqueous medium have been determined, yet within a solid the band position is dependent on the chemical environment. It was reported that the mineral phases of calcium phosphate can be distinguished based on the shape and position of these Raman bands [18].

It was of interest to correlate the changes in peak position and shape relative to the phases of catalyst A observed during calcination as well as the redox process. The Raman spectra were obtained for both uncalcined and calcined catalyst A (Fig. 4.51 and Fig. 4.52).

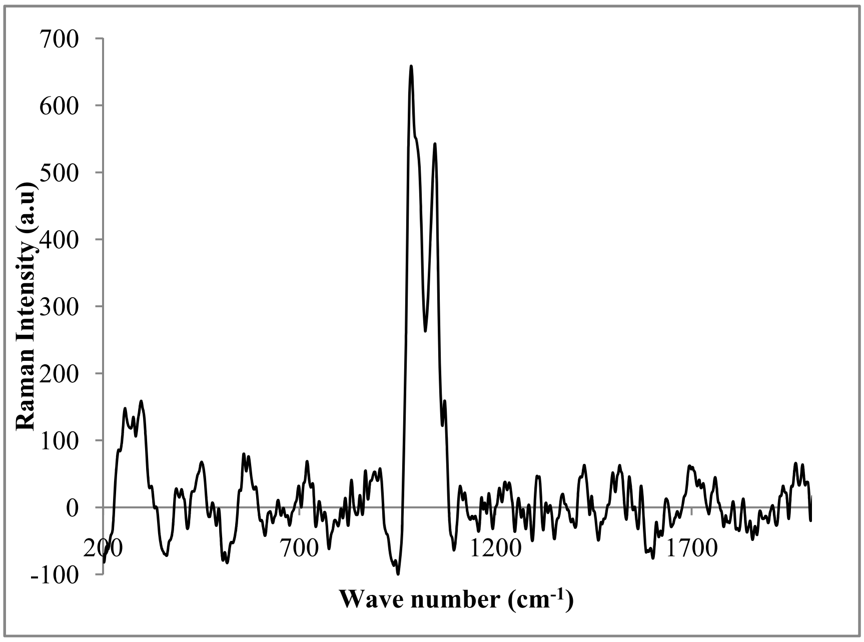

Figure 4.51 Raman spectrum of uncalcined catalyst A

The uncalcined catalyst A exhibits two intense peaks at ~ 985 cm^{-1} and ~ 1046 cm^{-1}. These two bands are attributed to the tetrahedral PO_4 and FeO_4 groups which are alternatively connected [19]. Since this catalyst exhibits a diffraction pattern similar to that of a hydrated ferrous orthophosphate, this assignment is justified. Upon calcination, the two bands seem to overlap into a single broad band at ~ 1015 cm^{-1}. The calcined catalyst A was characterized as a ferrous orthophosphate consisting of the tridymite-like phase. Calcination changes the structure of the catalyst as shown by the XRD data, hence the change in the Raman spectrum due to the orthophosphate group being subjected to a different chemical environment.

The phase change observed for catalyst A after complete reduction was discussed previously (Fig. 4.12, Fig. 4.13 and Fig. 4.31) and was characterized as $Fe_2P_2O_7$. The Raman spectrum was also obtained for this catalyst (Fig. 4.53). The reduced catalyst shows three characteristic peaks. A low intensity peak at ~ 719 cm^{-1}, an intense peak at ~ 1044 cm^{-1} and a shoulder at ~

1091 cm^{-1}. These peaks are not completely characteristic of the orthophosphate anion and this could be the result of the formation of the pyrophosphate anion in the reduced catalyst. It seems that there is a shift to higher wavenumbers with the reduction of the catalyst.

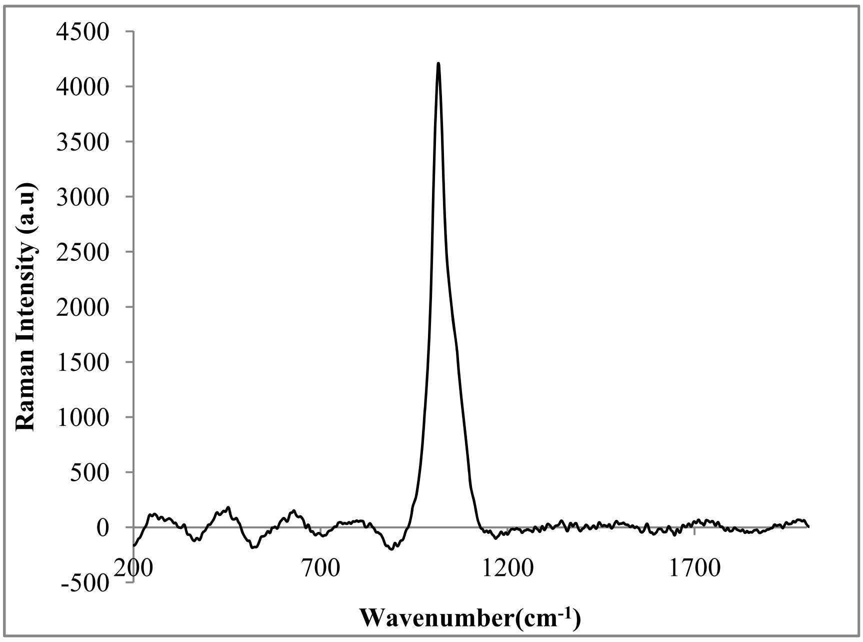

Figure 4.52 Raman spectrum of calcined catalyst A

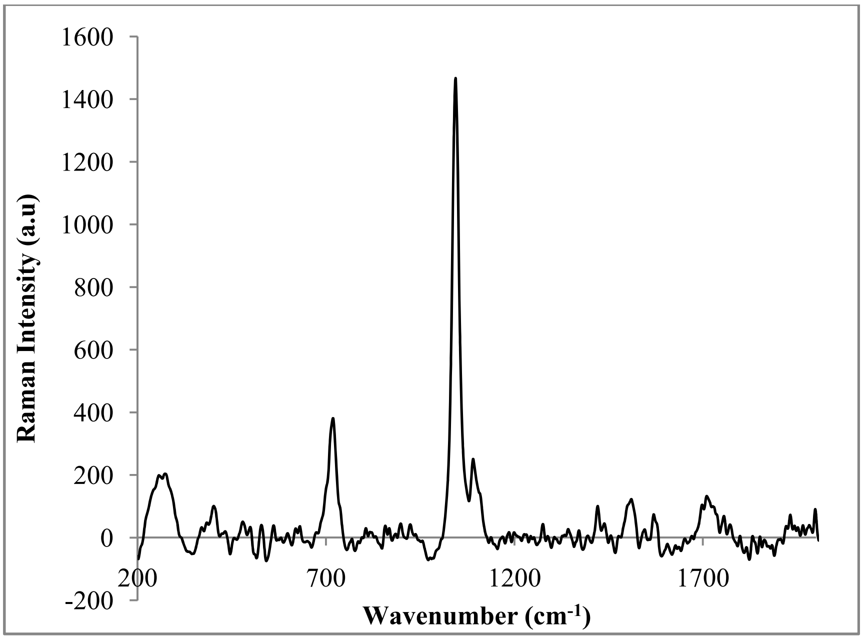

Figure 4.53 Raman spectrum of reduced catalyst A consisting of $Fe_2P_2O_7$

The reoxidised catalyst was also considered. Taking note of results reported previously, the reduced catalyst, $Fe_2P_2O_7$, can be reoxidised to the α-phase (Fig. 4.15) at lower temperatures and to the quartz type $FePO_4$ phase at higher temperatures (Fig. 4.16). The Raman spectrum of reoxidised catalyst A consisting of the α-phase is shown in Figure. 4.54.

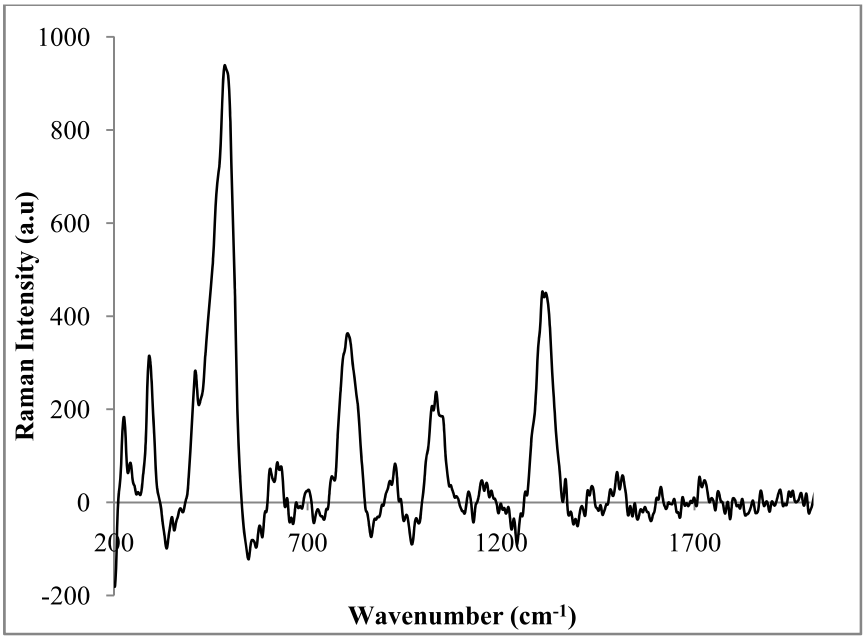

Figure 4.54 Raman spectrum of reoxidised catalyst A consisting of the α-phase

The bands observed for the reoxidised catalyst consisting of the α-phase were a low intensity band at ~ 410 cm^{-1}, a high intensity band at ~ 480 cm^{-1} and three medium intensity bands at ~ 804 cm^{-1}, ~ 1033 cm^{-1} and ~ 1307 cm^{-1} respectively. The Mössbauer results showed the presence of $Fe_2P_2O_7$ for the reoxidised catalyst due to incomplete oxidation, thus the bands at ~ 804 cm^{-1} and ~ 1033 cm^{-1} could be due to $Fe_2P_2O_7$ and the remaining bands at ~ 410 cm^{-1}, ~ 480 cm^{-1} and ~ 1307 cm^{-1} due to the α-phase. Based on these results it was decided to compare the spectrum with a sample consisting of both the α-phase and the quartz type $FePO_4$ phase. This sample was obtained when a catalyst was calcined over longer periods at each temperature interval to obtain the quartz type phase as the precursor (Fig. 4.25). Thereafter the sample was reduced and reoxidised, yielding both the α-phase and the quartz-type $FePO_4$ phase (Fig. 4.35). The spectrum is depicted in Figure 4.55.

Bands observed for this reoxidised sample are a medium intensity band at ~ 488 cm^{-1}, low intensity bands at ~ 809 cm^{-1} and ~ 1316 cm^{-1} and a very strong intense band at ~ 1012 cm^{-1}. The medium and low intensity bands can be assigned to the α-phase, as discussed above (Fig. 4.54), and the intense band at ~ 1012 cm^{-1} is due to the orthophosphate anion, which is similar to the band obtained for the $FePO_4$ catalyst consisting of the tridymite-like $FePO_4$ phase (Fig. 4.52).

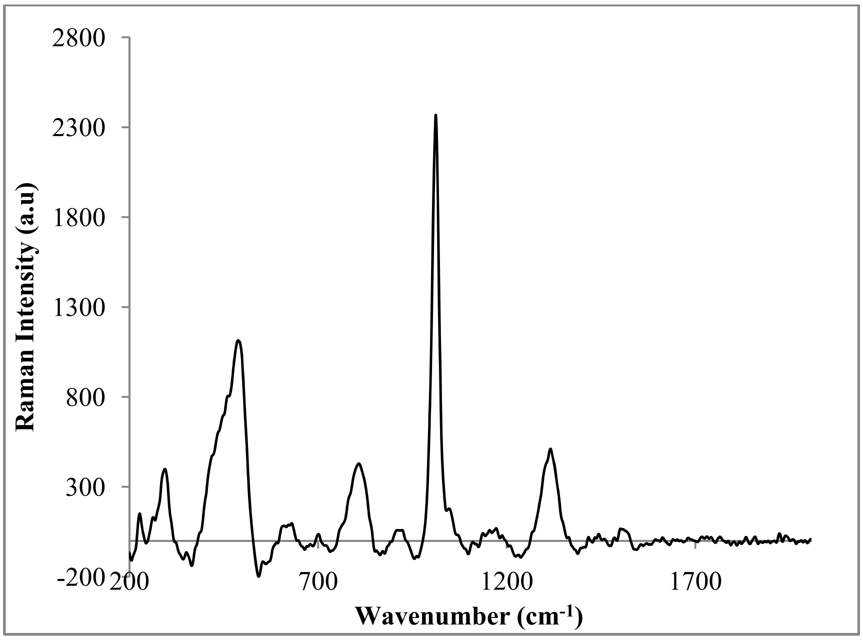

Figure 4.55 Raman spectrum of the catalyst containing of the α-phase and quartz type $FePO_4$ phase

4.16 Summary

The characterisation results of the synthesized iron phosphate catalyst showed isolation of the tridymite-like $FePO_4$ phase. During the synthetic procedure, it was necessary to maintain a specific P/Fe ratio (of ca. 1.05-1.2) in order for this phase to dominate during the calcination process. The ICP results confirmed that the correct ratio was obtained and the BET surface area of the catalyst was consistent with the respective ratio.

Infrared spectra showed the presence of water prior to calcination based on the occurrence of the strong band within the region of 3400 cm^{-1}, which was due to the hydroxyl groups of the water molecule. The bands between 600-1050 cm^{-1}, which served as evidence of the orthophosphate group, were prevalent in the samples pre and post calcination. Since the P/Fe ratio of the catalyst was confirmed as well as the presence of the orthophosphate group, room temperature XRD was carried out to determine the phases present in the calcined catalyst. Two catalysts were chosen as representative samples to identify the phases present in the $FePO_4$ catalyst after calcination. It was clearly evident that the tridymite-like $FePO_4$ phase was isolated as the major phase and reflections which are consistent with the quartz type $FePO_4$ phase, which is generally characterised by a major reflection at $2\theta = 25.8°$, were not evident.

The correlation between the TPR/TPO profile, room temperature XRD obtained for the sample at each reduction and oxidation step respectively, as well as the infrared spectra, allowed for complete phase assignment with variation in temperature during the reduction and oxidation process. The effect of variation in flow rate was also investigated. It was seen that the tridymite-like $FePO_4$ phase was reduced via an intermediate phase, $Fe_3(P_2O_7)_2$, to form $Fe_2P_2O_7$. During the oxidation process of the reduced catalyst two peaks were observed, which were attributed to the active α-phase at the lower temperature and formation of the quartz-type $FePO_4$ phase at the higher temperature.

The surface morphology of the reduced and reoxidised catalyst was compared to that of the initial uncalcined and calcined catalysts. The SEM image of the calcined catalyst showed that after calcination there was an even distribution of phosphorous and iron over the surface. However, in the case of the reduced and reoxidised catalyst there was evidence of agglomeration or sintering, which was further seen in the EDX map of the surface of the reduced catalyst.

The TPD experiments determined the number and strength of acidic sites. It was evident that the catalyst contains medium to strong acidic sites seeing that a major peak was observed in the region of 580 °C. It was found in literature that the results obtained from potentiometric titrations had shown that iron phosphate catalysts generally have strong acidic sites.

In situ variable temperature XRD data showed the effect of temperature and varying atmospheres on phase formation. Initially, the phase transformations which had occurred during the calcination process were studied via the *in situ* experiment. It was seen that the reflections of the tridymite-like $FePO_4$ phase appeared from 300 °C and up to the elevated temperature of 550 °C no evidence of the unwanted quartz type $FePO_4$ phase was found, thus showing isolation of the tridymite-like $FePO_4$ phase up to 550 °C. Calculation of the crystallite size had shown particle size from 4 nm to 11 nm. Calcination for longer periods at each temperature interval resulted in the emergence of the quartz type $FePO_4$ phase from 548 °C, which was contrary to what was observed previously, thus indicating that longer exposure of the catalyst at each temperature increment had a significant influence on phase formation. Exposure of the calcined catalyst to an inert atmosphere resulted in no phase change from room temperature to 550 °C. In terms of the reducing atmosphere, the effect of varying reducing gas mixtures was considered. The use of a 5 % H_2/argon mixture as the reducing gas showed evidence of both the intermediate phase as well $Fe_2P_2O_7$ at 550 °C, and upon reoxidation the intermediate phase was still observed in the diffractograms at 550 °C. However, when a 5 % H_2/nitrogen mixture was used as the reducing gas no evidence of the intermediate phase was observed at elevated temperatures during reduction and during reoxidation only the active α-phase was observed.

As a comparative study, the phase transformations which would occur if the quartz type $FePO_4$ phase was subjected to reduction and reoxidation were observed. The results obtained showed that during reduction, formation of $Fe_2P_2O_7$ occurs, however, upon reoxidation formation of the α-phase shifted to higher onset temperatures and the quartz type $FePO_4$ phase reappeared. This hindered α-phase isolation upon reoxidation, unlike the case of the tridymite-like $FePO_4$ phase where the α-phase was isolated upon reoxidation. It was seen from the results obtained from Mössbauer spectroscopy that there was a direct correlation with the XRD data as well as the TPR/TPO results in terms of the phase changes and oxidation state of the calcined, uncalcined, reduced and reoxidised catalyst. Mössbauer spectroscopy also allowed for a percentage allocation of the phases present.

The Raman data obtained supported the assignment of the phase changes of the uncalcined catalyst, as well as the phase changes of the calcined catalyst found during reduction and reoxidation using *in situ* XRD and TPR/TPO.

The TGA-DSC profile for the uncalcined catalyst showed weight loss within the temperature range of 100-300 °C. The initial weight loss was attributed to the loss of water either physically adsorbed or due to the loss of crystalline water and it was postulated that the weight loss which had occurred at the higher temperature was linked to phase change, more specifically the onset of the formation of the tridymite-like $FePO_4$ phase.

TEM particle size analysis had allowed for differentiation of the silica particles and the iron phosphate particles. It was concluded that the particles within the range of 30-35 nm were the silica support and the iron phosphate particles were within the range of 7-11 nm. The SADP pattern of the calcined catalyst suggested that the catalysts were polycrystalline. Although the results obtained from the HR-TEM analysis did not provide conclusive information in terms of isolation of the support as well as the $FePO_4$ particles, evidence of crystallinity as well as the presence of iron and phosphorous was confirmed from the SADP pattern and the EDX data respectively.

References

[1] M. Ai, K. Ohdan, J. Mol. Catal. A: Chem. 159 (2000) 19-24.

[2] P. Bonnet, J.M.M. Millet, C. Leclercq, J.C. Védrine, J. Catal. 158 (1996) 128-141.

[3] S. Scaccia, M. Carewska, A.D. Bartolomeo, P.P. Prosini, Thermochim. Acta. 383 (2002) 145-152.

[4] E. Muneyama, A. Kunishige, K. Ohdan, M. Ai, J. Catal. 158 (1996) 378-384.

[5] J.-M.M. Millet, Cat. Rev. - Sci. Eng. 40 (1998) 1-38.

[6] E. Muneyama, A. Kunishige, K. Ohdan, M. Ai, Bull. Chem. Soc. Jpn. 69 (1996) 509-513.

[7] A.M. Beale, G. Sankar, J. Mater. Chem. 12 (2002) 3064-3072.

[8] http://www.ceinstruments.co.uk/tprtpo.htmL.(Date accessed 20th February 2009)

[9] M. Ai, E. Muneyama, A. Kunishige, K. Ohdan, J. Catal. 144 (1993) 632-635.

[10] M. Ai, K. Ohdan, Appl. Catal., A. 180 (1999) 47-52.

[11] P. Malet, A. Caballero, J. Chem. Soc., Faraday Trans. 84 (1988) 2369-2375.

[12] H. Bosch, B.J. Kip, J.G. van Ommen, P.J. Gellings, J. Chem. Soc., Faraday Trans. 80 (1984) 2479-2488.

[13] O.J. Wimmers, P. Arnoldy, J.A. Moulijn, J. Phys. Chem. 90 (1986) 1331-1337.

[14] Richard A. Nyquist, R.O. Kagel, Infrared spectra of Inorganic Compounds Academic press, New York and London, 1971.

[15] O. Watzenberger, G. Emig, D.T. Lynch, J. Catal. 124 (1990) 247-258.

[16] M.M. Gadgil, S.K. Kulshreshtha, J. Solid State Chem. 111 (1994) 357-364.

[17] P. Nagaraju, C. Srilakshmi, N. Pasha, N. Lingaiah, I. Suryanarayana, P.S.S. Prasad, Appl. Catal., A. 334 (2008) 10-19.

[18] G.R. Sauer, W.B. Zunic, J.R. Durig, R.E. Wuthier, Calcified Tissue International. 54 (1994) 414-420.

[19] Y. Wang, X. Wang, Z. Su, Q. Guo, Q. Tang, Q. Zhang, H. Wan, Catal. Today. 93-95 (2004) 155-161.

CHAPTER 5

CATALYTIC REACTIONS

Characterization of the iron phosphate catalyst provided a clear understanding of several properties of the catalyst such as phase transformations, surface areas and morphologies, thermal properties etc. The phase specific tridymite-like $FePO_4$ catalyst was used to study the oxidative dehydrogenation (ODH) of ethyl isobutyrate (EIB) to ethyl methacrylate (EMA). Some of the factors which were investigated included varying contact times, additional feeds to enhance target product selectivity and yield, regeneration studies, as well as the use of a promoter.

5.1 Non-catalytic reactions: ethyl isobutyrate and ethanol

Initially, EIB and ethanol were fed into an empty and then a carborundum packed reactor (no catalyst). The conditions used for the testing were maintained at a fuel (EIB):O_2 ratio of 1:0.7-0.8 over a temperature range of 300-500 °C (Appendix C, C1). This ratio was used in all four tests. The results obtained for the EIB feed only are depicted below in Figure 5.1.

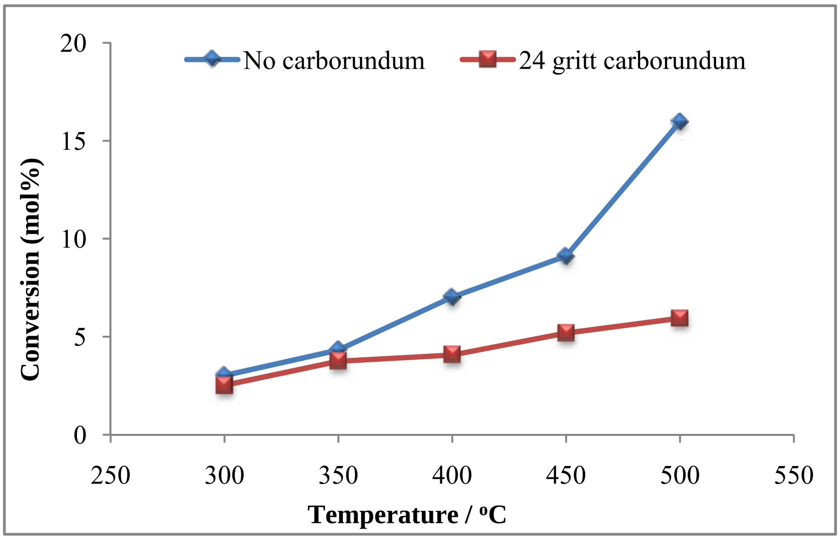

Figure 5.1 Conversion of EIB in the empty and carborundum packed reactor

In the empty reactor tube the conversion of EIB with an increase in temperature was much greater than in the carborundum packed reactor, hence indicating that carborundum quenches free radical reactions [1]. The conversion of EIB in the carborundum packed reactor at 500 °C was ~ 6 % as opposed to in the empty reactor which showed a conversion of ~ 16 %.

The major products formed at lower temperatures included acetone, acetaldehyde, ethyl acetate, ethanol, isobutyric acid (IBA) and carbon oxides (COx). However, at increasing temperatures COx dominated in the product profile and at temperatures of 450 ºC and 500 ºC, CO_2 was observed as the major product. This suggests that the oxygenates formed proceed to total oxidation at higher temperatures, also at the higher temperatures CO_2 is the result of combustion reactions.

The results obtained for ethanol fed into an empty and then a carborundum packed reactor are depicted in Figure 5.2. These also showed the effect of carborundum quenching free radical reactions. It was observed that in the empty reactor, the maximum conversion at 500 °C was ~ 19 % and when including the carborundum, the conversion at the same temperature had decreased to ~ 5 %. In correlation with the product profile obtained for the EIB feed, COx was the dominant product with a large amount of CO_2 forming at the higher temperatures. Minor products which formed at the lower temperatures included acetaldehyde and ethyl acetate.

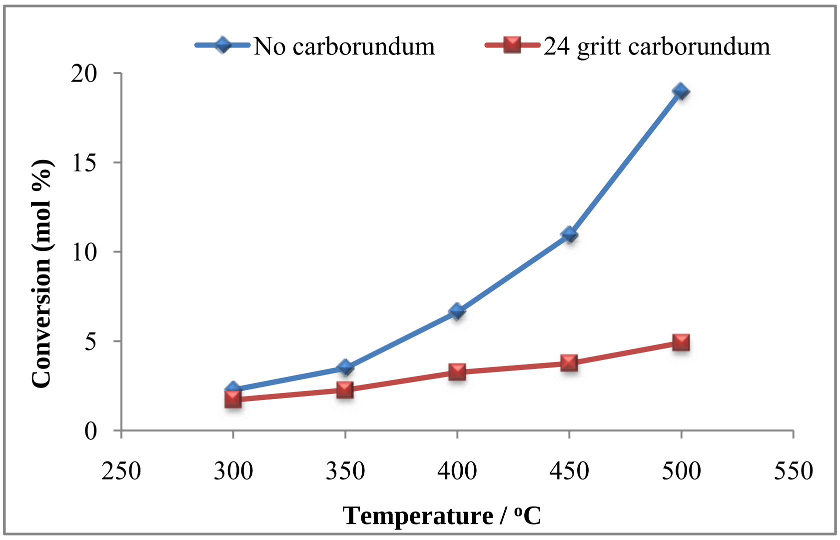

Figure 5.2 Conversion of ethanol in the empty and carborundum packed reactor

5.2 Catalytic reactions

After the carborundum blank and empty reactor testing, the catalyst was tested using the EIB feed. Ai and co workers reported, for the ODH of IBA to methacrylic acid (MAA) using a mixed phase iron phosphate catalyst, that optimal results were obtained at a contact time of 0.8 seconds with a fuel:O_2 ratio of 1:0.7-0.8 and a fuel:water ratio of 1:15 [2]. A similar fuel:O_2 ratio was used for the purpose of the tests carried out in this work, the volume of catalyst was maintained at 1 mL and nitrogen, which served as the diluent, was used to obtain the necessary contact times. Conditions maintained for this series of reactions, the scheme for product formation and abbreviations can be found in Appendix C, C2.

5.2.1 Ethyl isobutyrate in air at varying contact times

Initially, the EIB feed was tested over the tridymite-like $FePO_4$ phase catalyst in the presence of an oxidizing atmosphere at varying contact times, which were 1.2, 1.0, 0.8, 0.6 and 0.4 seconds respectively. Results obtained for these reactions can be found in Appendix C, C3.

Figure 5.3 shows the change in conversion over the varying contact times with increase in temperature. It was found that for all the contact times tested, the conversion increased with an increase in temperature up to an optimal temperature of 450 °C, where the highest conversion was observed. A further increase in temperature to 500 °C showed a uniform decrease in conversion for each of the contact times. The temperature of optimal conversion coincides with the results mentioned previously (Chapter 4, Fig. 4.32 and Fig. 4.33) namely, that during the redox process the tridymite-like $FePO_4$ phase is converted to $Fe_2P_2O_7$ upon reduction and during the reoxidation process, $Fe_2P_2O_7$ is converted to the α-phase.

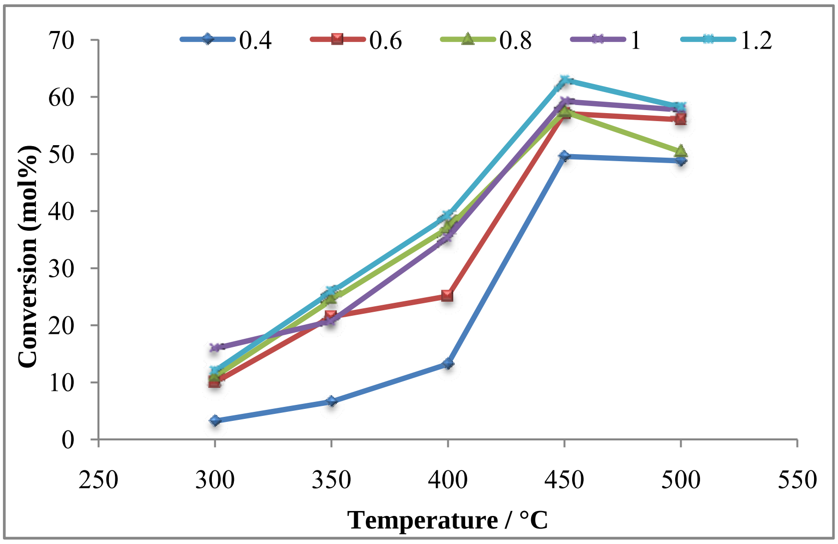

Figure 5.3 Effect of contact time on the conversion of EIB between 300-500 °C over varying contact times

The two transformations occur within the temperature range of ~ 450 °C. Seeing that the α-phase is the active phase under catalytic conditions [3] and transformations between the reduced and α-phase take place reversibly, this could explain the highest conversion within this temperature range. At temperatures above 450 °C i.e. 500 °C, a slight decrease in conversion was observed. The product profile at this temperature range showed a decrease in the selectivity towards EMA and an increase in the COx formation.

The selectivity and yield data for the target product EMA at 450 °C was plotted over the varying contact times (Fig. 5.4). The results obtained show that the contact time of 0.8 seconds produced the best selectivity and yield towards EMA, followed by the contact times of 0.6, 1.0, 1.2 and 0.4 seconds, respectively. A similar trend was observed at the lower temperature of 400 °C (Fig. 5.5) where optimal results were recorded at the contact time of 0.8 seconds.

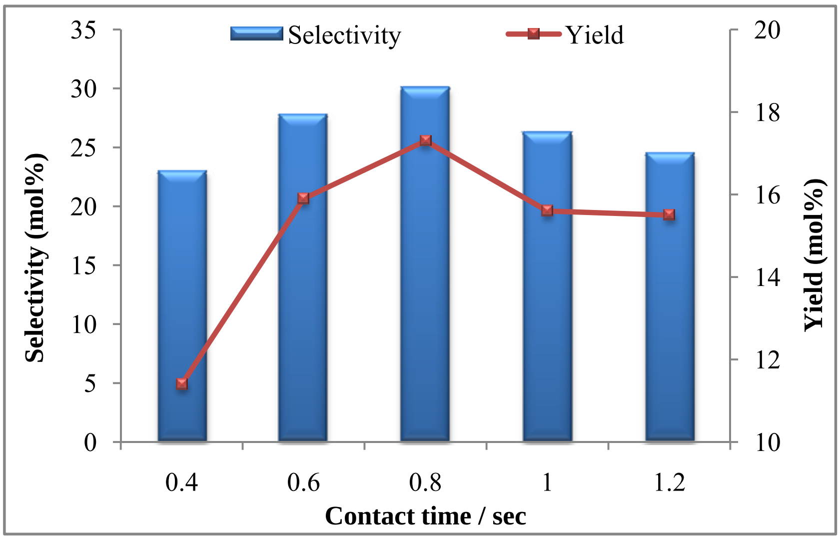

Figure 5.4 Selectivity and yield of EMA at 450 °C over the varying contact times

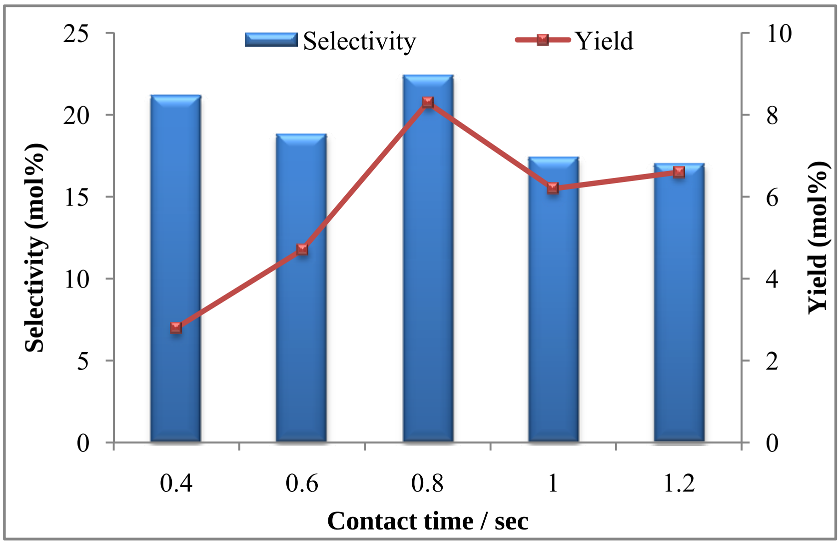

Figure 5.5 Selectivity and yield of EMA at 400 °C over the varying contact times

Figures 5.4 and 5.5 showed optimal results towards EMA selectivity and yield at the contact time of 0.8 seconds, however looking at the conversion results in Figure 5.3 it was observed that the contact time of 1.2 seconds shows higher conversion values across the temperature range. Comparing the results obtained for the two contact times at the optimal conversion temperature of 450 °C (Fig. 5.6), it was evident that although a higher conversion was observed for the longer contact time, there was an increased selectivity towards the products IBA, MAA and COx in the product profile relative to EMA. IBA is formed through the hydrolysis of EIB, and MAA is formed as a result of the hydrolysis of EMA or the ODH of IBA. This indicates that the longer contact time favours, to a certain extent, the formation of the hydrolysis products and especially the combustion products, seeing that the COx selectivity is greater across the temperature range for the longer contact time (Fig. 5.7). A list of the 'other products' in Figure 5.6 is found in Appendix C, C2.

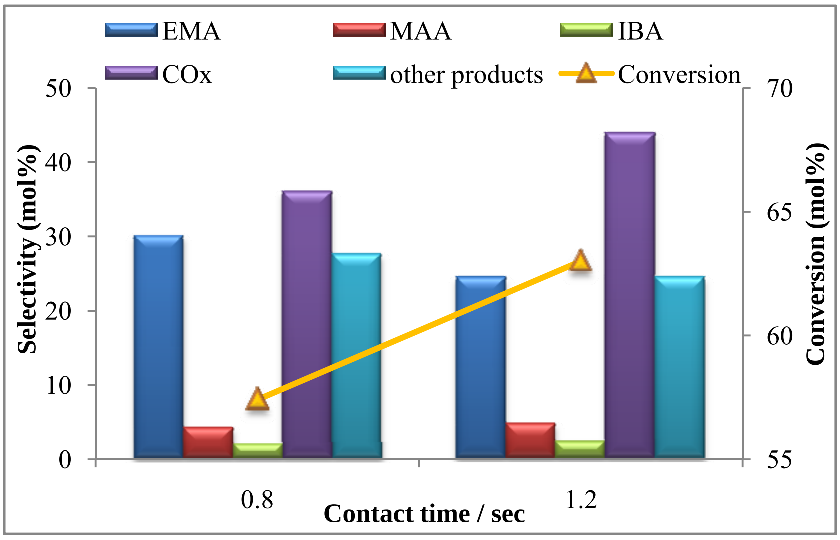

Figure 5.6 Comparison at 450 °C between the conversion and selectivity data for the contact times of 1.2 and 0.8 seconds

The product profile over the catalyst at the contact time of 0.8 seconds was plotted against temperature (Fig. 5.8). The results show that the selectivity towards EMA increases with an increase in temperature until an optimal temperature of 450 °C, as mentioned previously. It has been reported that an ester is hydrolyzed to its parent acid and alcohol when it is heated together with a stoichiometric excess of water and an acid catalyst [4]. It seems likely, even in the case of a reaction which excluded water as a co-feed, that both the feed and target product would easily be hydrolyzed during the catalytic reaction, because water forms from the combustion of the hydrocarbons and the ODH reaction. In line with the idea of hydrolysis, it was also observed that there was a decrease in IBA formation with an increase in EMA selectivity, thus indicating that hydrolysis of the feed is reduced with an increase in temperature, hence favoring EMA formation. It was, however, noted that the selectivity towards MAA increases with increase in EMA selectivity, which could lead to a reduction in the actual selectivity towards EMA, seeing that MAA is the hydrolysis product of EMA.

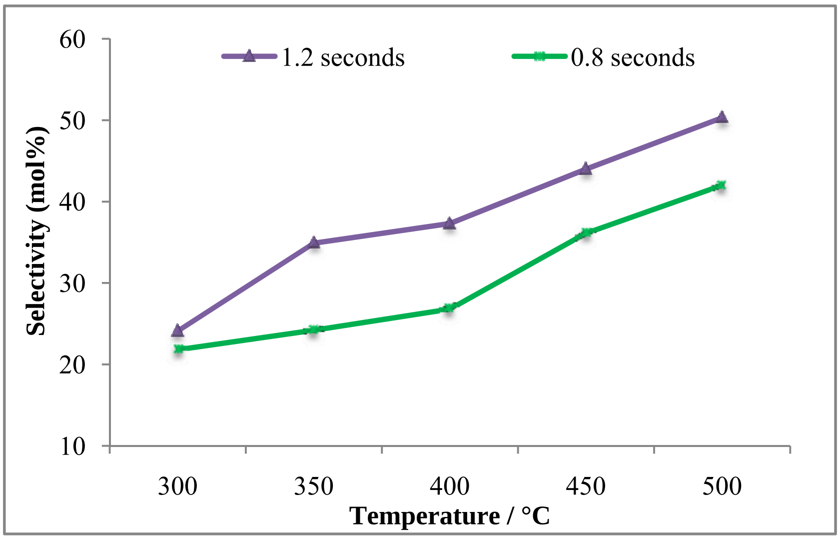

Figure 5.7 Comparison of COx selectivity from 300-500 °C at the contact times of 1.2 and 0.8 seconds

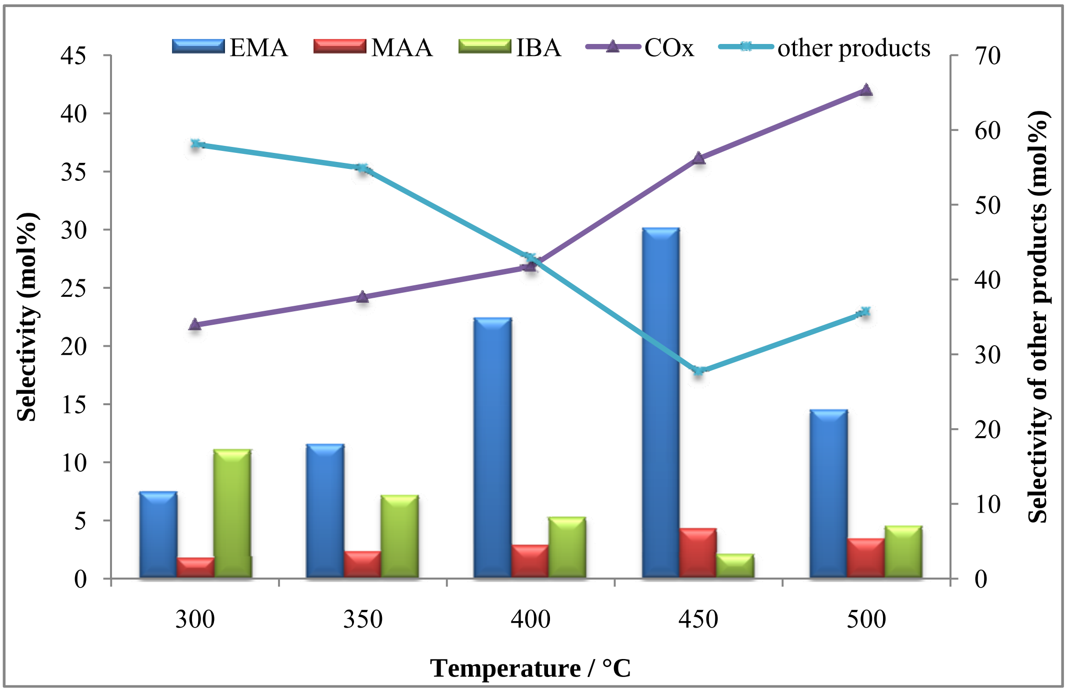

Figure 5.8 Complete product profile for the EIB feed only at the contact time of 0.8 seconds over the varying temperatures

MAA is also formed during the ODH of IBA; hence the increase in selectivity towards MAA could also be attributed to the latter reaction, since the selectivity towards IBA decreases as well. The selectivity towards ethanol also decreases with an increase in temperature (Fig. 5.9), and this could be linked to the decrease in selectivity of IBA, seeing that hydrolysis of the feed does favour the formation of IBA and ethanol. The COx selectivity increased with an increase in temperature, while the overall selectivity towards the other products decreased with the increase in temperature (Fig. 5.8 and Fig. 5.9).

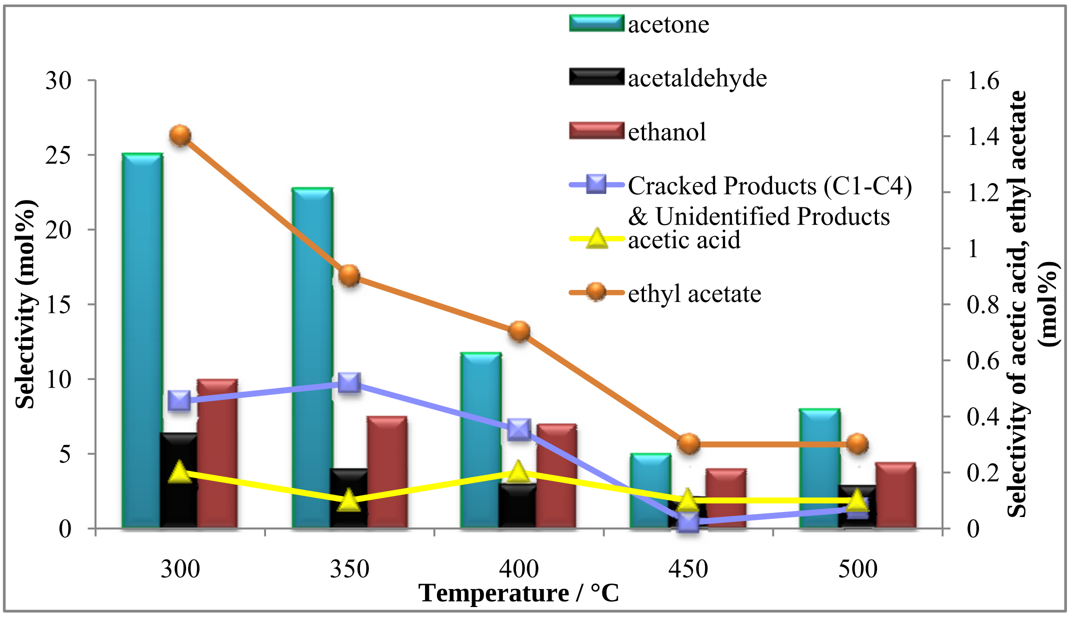

Figure 5.9 'Other products' profile at the contact time of 0.8 seconds at different temperatures

The selectivity towards EMA was considered as probably being lowered as a result of hydrolysis of the feed, EIB and the target product EMA itself. The plot of the selectivity of these hydrolysis products, MAA and IBA, over varying contact times were considered at two temperatures, namely, 400 °C and 450 °C. The conversion of EIB at 450 °C was higher than the conversion at 400 °C at the contact time of 0.8 seconds. However, it was observed that there was a lower selectivity towards MAA and IBA at 450 °C (Fig. 5.10) in comparison to the data at the temperature of 400 °C (Fig. 5.11). It was shown previously that formation of the reduced phase, $Fe_2P_2O_7$ and the active α-phase occurs within the temperature range of ~ 450 °C (Chapter 4, Section 4.10, Figure 4.32 and Figure 4.33). Hence, it was expected that hydrolysis would be reduced and ODH would dominate at 450 °C as a result of the active phase forming, thus favouring the formation of EMA.

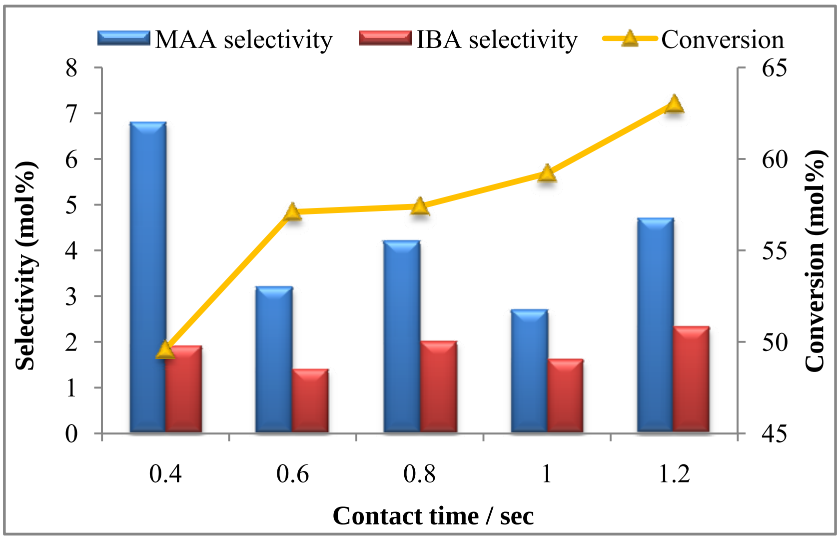

Figure 5.10 Selectivity of products MAA and IBA and the conversion at 450 °C over varying contact

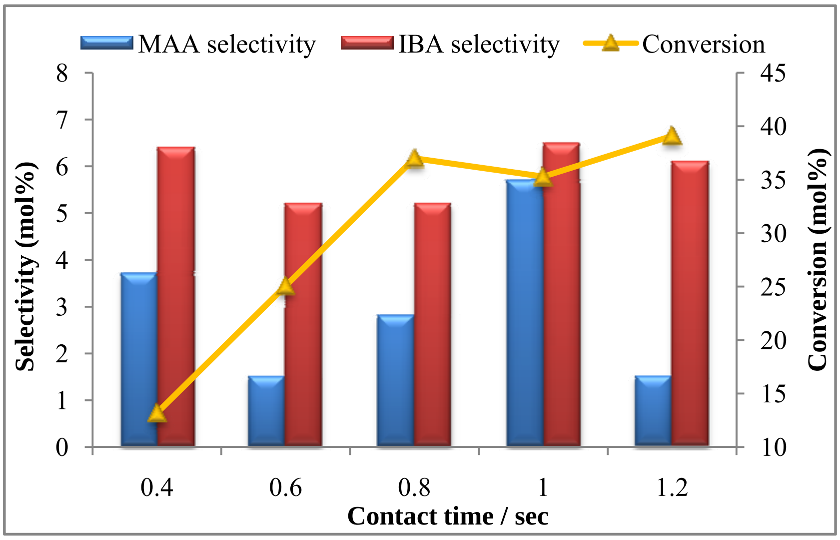

Figure 5.11 Selectivity of products MAA and IBA and the conversion at 400 °C over varying contact times

It was observed previously (Chapter 4, Section 4.10, Fig. 4.25), that under conditions of higher temperatures of calcination, the tridymite-like $FePO_4$ phase converts to the quartz type $FePO_4$ phase, starting from ~ 548 °C. The study of phase transformations of this iron phosphate phase had shown that under conditions of reduction, the pure quartz type $FePO_4$ phase is transformed to $Fe_2P_2O_7$ at temperatures greater than 500 °C (Chapter 4, Section 4.10, Fig. 4.37), and reoxidation had shown the formation of the α-phase as well as the quartz type

$FePO_4$ phase at a temperature greater than 500 °C (Chapter 4, Section 4.10, Fig. 4.38). Hence, it was decided to investigate the catalytic activity of the pure quartz type $FePO_4$ catalyst at the contact time of 0.8 seconds.

The product profile (Fig. 5.12) of the quartz type $FePO_4$ phase showed a similar trend to the tridymite-like $FePO_4$ phase i.e. the optimal selectivity towards EMA was observed at the temperature of 450 °C. With an increase in temperature, the COx selectivity increased and the selectivity towards the other products decreased. Also the trend towards the hydrolysis products was similar to the profile obtained using the tridymite-like $FePO_4$ phase.

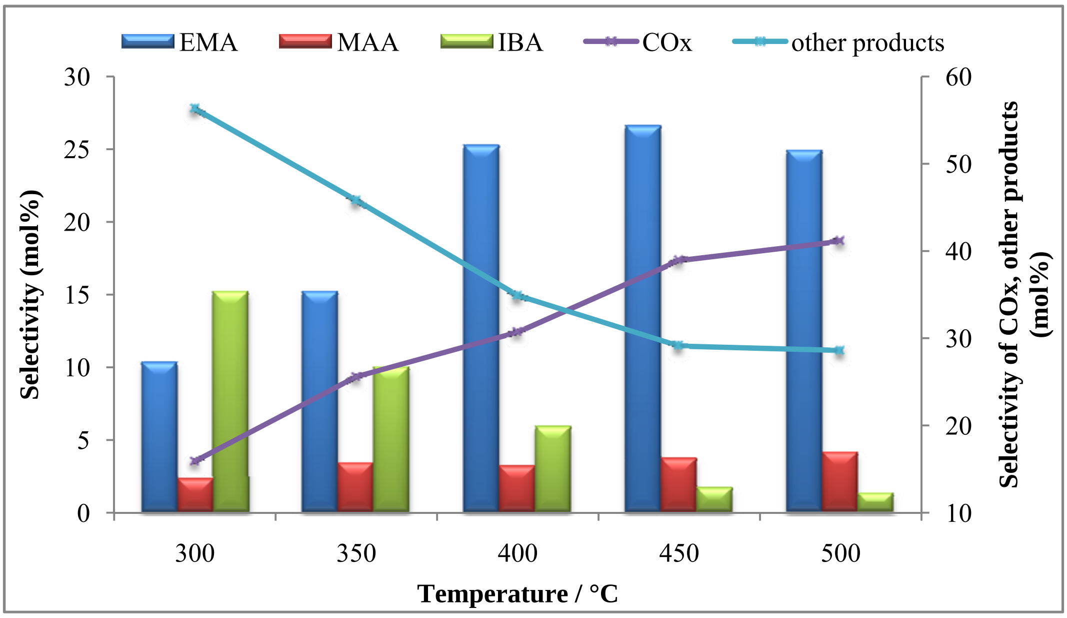

Figure 5.12 Product profile at a contact time of 0.8 seconds at varying temperatures over the quartz type $FePO_4$ catalyst

Seeing that the α-phase was formed at a higher temperature from the quartz type $FePO_4$ phase precursor than from the tridymite-like $FePO_4$ phase, a comparative graph was plotted between the quartz type phase and tridymite-like phase at a contact time of 0.8 seconds at temperatures greater than 400 °C, to observe the effect of phase formation on EMA selectivity at higher temperatures (Fig. 5.13). In terms of the tridymite-like $FePO_4$ phase, the highest selectivity towards EMA was found at 450 °C. With an increase in temperature a relative decrease in conversion was observed. The quartz type $FePO_4$ phase showed an increase in conversion from 450 °C to 500 °C and this can be attributed to the transformation of the quartz type $FePO_4$ phase to the α-phase which occurs within this temperature range

(Appendix B). Also, the selectivity towards EMA was lower than found at 450 °C. This is the result of secondary combustion of the ODH products at higher temperatures.

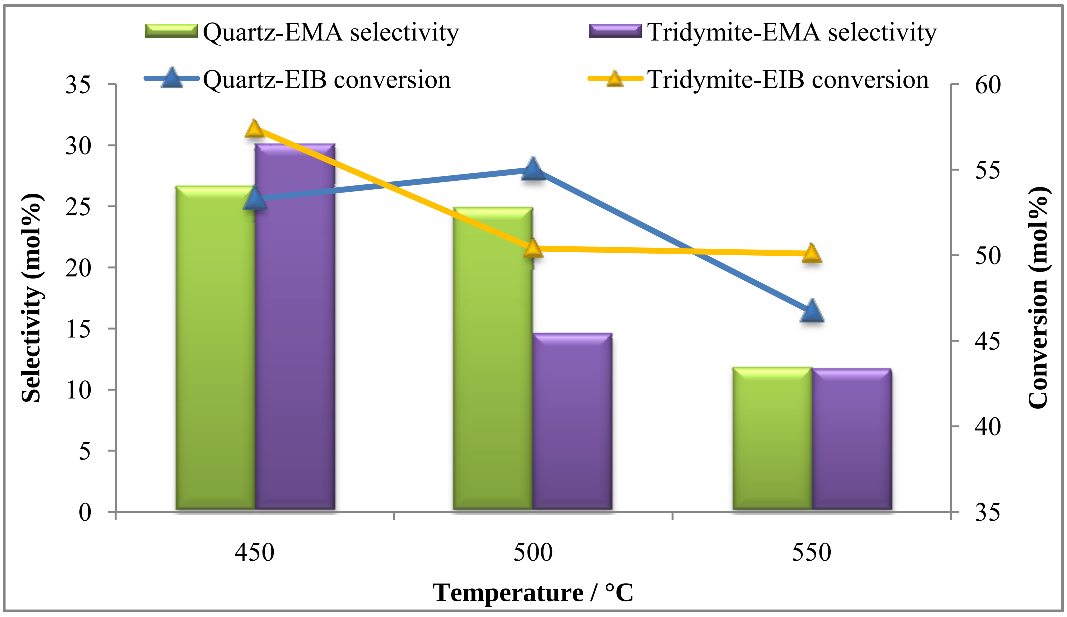

Figure 5.13 Conversion of EIB and selectivity to EMA over quartz *vs.* tridymite-like phases of the $FePO_4$ catalyst at a contact time of 0.8 seconds

5.2.2 Ethyl isobutyrate and water co-feed in air at varying contact times

The results showed that the selectivity and yield to EMA was the greatest at the contact time of 0.8 seconds and the probable yield towards EMA was higher when one takes into account the hydrolysis products which formed. These results show a correlation with the literature data where Ai and co-workers reported an optimal contact time of 0.8 seconds for the ODH of IBA using an iron phosphate catalyst [2]. They also stated that iron phosphates are largely dependent on water in the ODH of IBA to MAA [2, 5]. Water is believed to act as a thermal diluent and contributes to the desorption of the products from the surface of the catalyst. It also plays a role in stabilizing the hydroxylated form of the active α-phase in the iron phosphate catalyst [3]. Reports have shown that the temperature of optimal efficiency of the catalytic reaction coincides systematically with the beginning of the dehydroxylation of the active phase. It was found that at this specific temperature the mobility of the protons and electrons in the solid are enhanced. The water has a role in maintaining the catalyst in a metastable state where a steady state is obtained between the hydrogenation/reduction of the solid (dehydrogenation of EIB) and its combined dehydroxylation-oxidation [3].

Hence, water was included as a co-feed and its effects were examined at varying contact times using a fuel:water ratio of 1:15 over the temperature range of 300-500 °C. Results obtained for these reactions at a fuel:ratio of 1:15 can be found in Appendix C, C4.

The selectivity towards EMA at varying contact times over the temperature range of 300 ºC to 500 ºC is shown in Figure 5.14. The results showed optimal selectivity towards EMA at 400 ºC over the varying contact times tested. Based on these results a product profile was plotted showing, at 400 ºC, conversion as well as EMA and hydrolysis product selectivity over the varying contact times (Fig. 5.15).

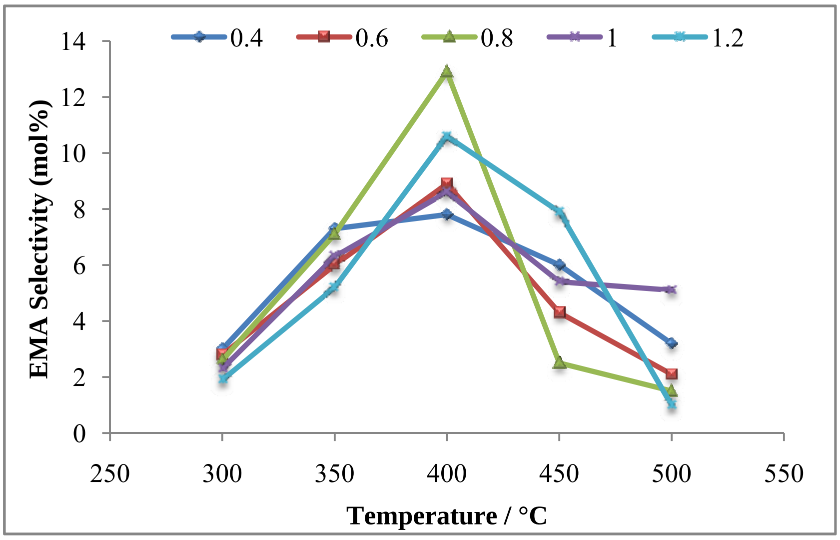

Figure 5.14 Selectivity towards EMA at varying contact times between 300-500 °C over $FePO_4$ (tridymite-like phase) and a fuel:water ratio of 1:15

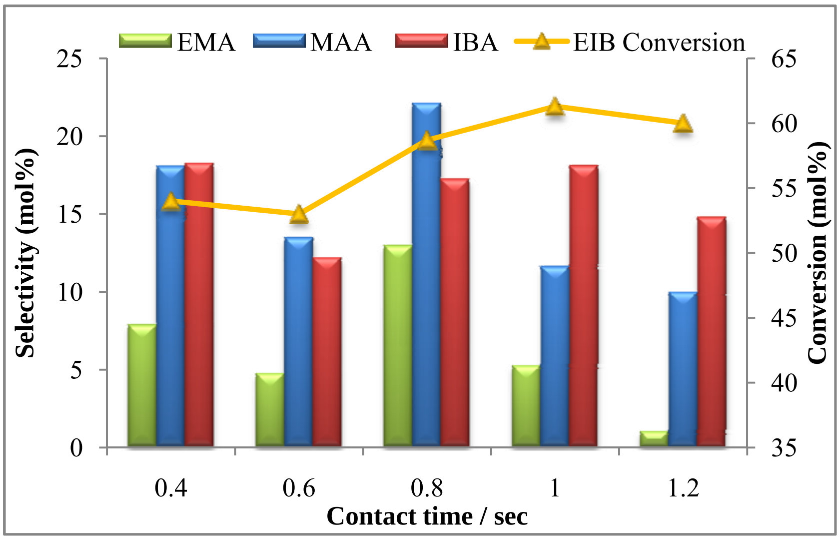

Figure 5.15 Selectivity towards EMA, MAA and IBA, and EIB conversion at 400 °C over varying contact times including water co-feed (fuel:water = 1:15)

The product profile at 400 °C showed that EIB conversion increased with an increase in contact time and the optimal selectivity towards EMA and MAA was found at the 0.8 seconds contact time. The selectivity towards MAA is greater at 0.8 seconds relative to the other contact times. This could be the result of the presence of water which enhances the hydrolysis reaction, seeing that the largest selectivity towards EMA is also obtained at this contact time.

The results for the reactions including the water co-feed showed that the conversion of EIB was higher than for the reactions excluding the water co-feed, although the selectivity towards EMA was lower (Fig. 5.16). Also, for the reaction including the water co-feed, it was observed that optimal selectivity towards EMA occurred at 400 °C as opposed to 450 °C as found for the reaction excluding the water co-feed. This could be the result of water stabilizing the hydroxylated form of the active α-phase at the lower temperature of 400 °C.

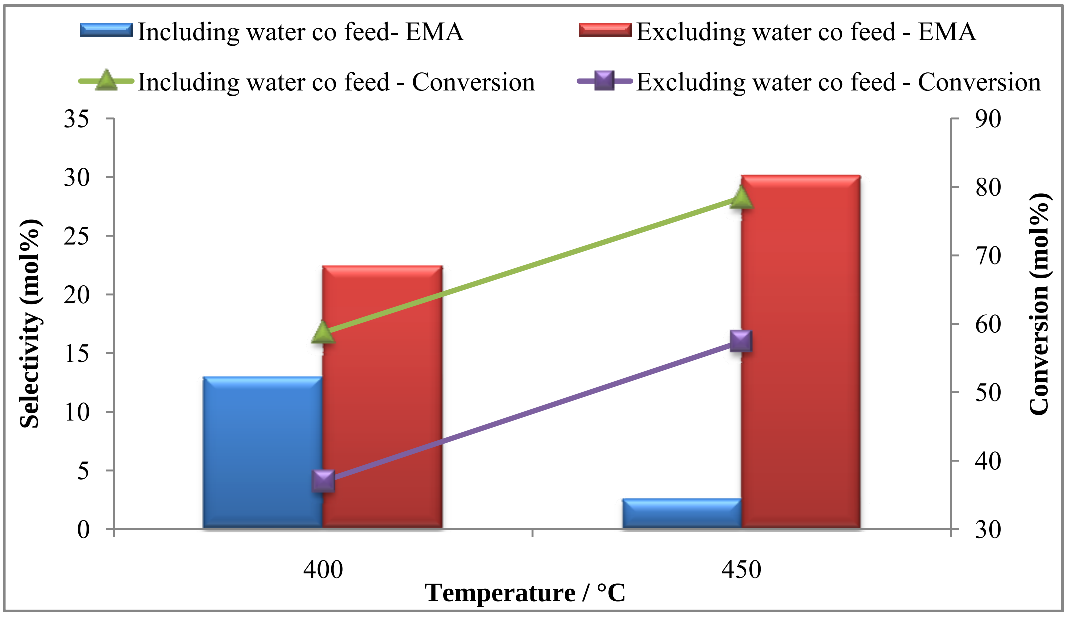

Figure 5.16 Conversion of EIB and selectivity towards EMA at a contact time of 0.8 seconds including and excluding the water co-feed at 400 °C and 450 °C

The COx selectivity decreases in the presence of the water co-feed, and this was also reported in literature for the ODH of IBA to MAA [3]. It was reported that reactions excluding a water co-feed had shown a decrease in the selectivity towards MAA and an increase in COx formation. A similar trend was also observed for the reactions carried out in this work which excluded a water co-feed at the contact time of 0.8 seconds (Fig. 5.17). For the reaction including the water co-feed a slight increase in selectivity towards COx was observed with an increase in temperature up to 400 °C. However, at the temperatures above 400 °C there is a significant increase in COx selectivity. This could be due to the combustion of the hydrolysis products at elevated temperatures, seeing that the selectivity towards MAA decreases sharply in this temperature range.

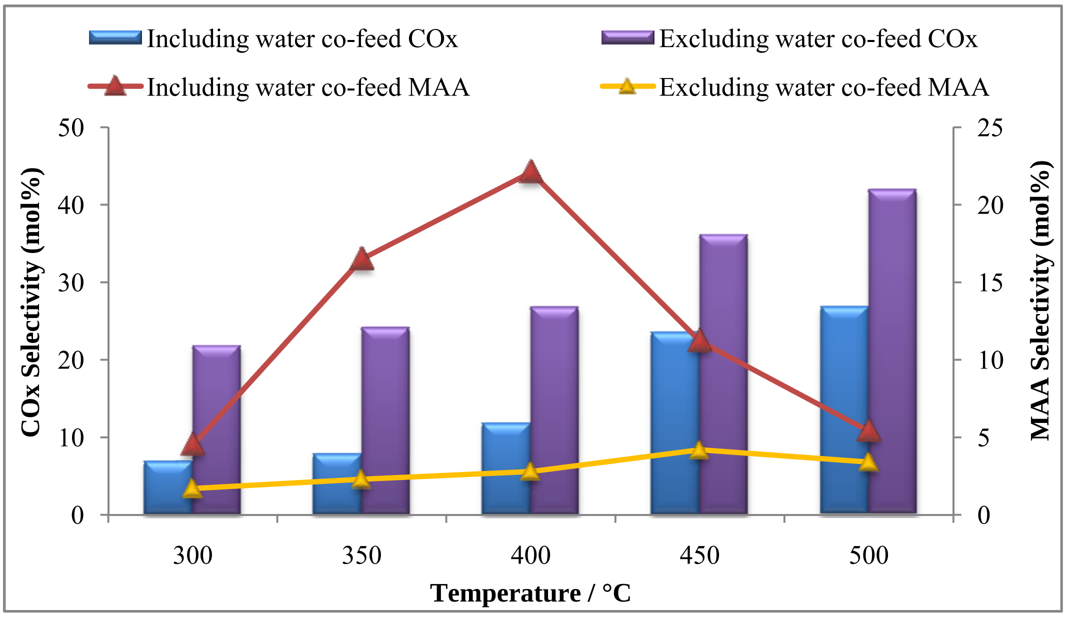

Figure 5.17 MAA and COx selectivity between 300-500 °C at a contact time of 0.8 seconds including and excluding the water co-feed

5.3 Ethyl isobutyrate and ethanol co-feed in air at varying ratios

The reactions including the water co-feed showed an increase in conversion, however, the selectivity towards the target product decreased. It was also observed that there was an increase in the selectivity towards the hydrolysis products, MAA and IBA.

A report has suggested that the selectivity to the ester could be improved by adding a stoichiometric excess of the alcohol formed from the hydrolysis of the feed [6]. Thus similar reactions were carried out in an attempt to reduce hydrolysis and increase the selectivity and yield of EMA. The optimal contact time of 0.8 seconds was maintained and ethanol was introduced as a co-feed at varying ratios, initially with no water co-feed. It was decided not to reduce the ratio to less than unity, since reports based on related work have stated that the molar ratio should be between the range of 1 and 20 moles of alcohol per mole of ester, preferably within the range of 1 and 10 [7]. A fuel:EtOH ratio between the range of 1:1-1:10

was used during the catalytic testing. Results obtained for these reactions can be found in Appendix C, C5.

The results obtained for the varying fuel:EtOH ratios showed that conversion increased with an increase in temperature (Fig. 5.18). In comparison, the conversion results were lower than the results obtained for the reaction of EIB including the water co-feed (Fig. 5.15). Optimal conversion was obtained at 450°C and the fuel:EtOH ratios of 1:5, 1:7 and 1:10 showed comparable conversion at this temperature (Fig. 5.18).

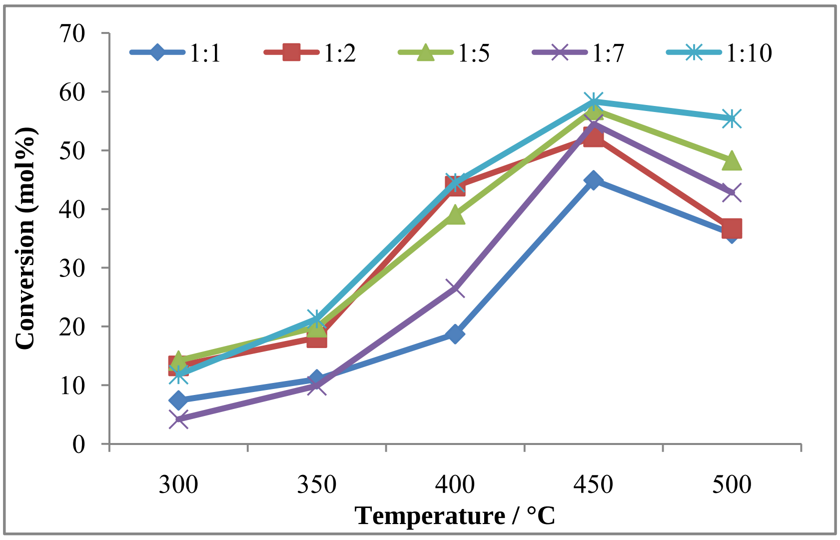

Figure 5.18 EIB conversion over the temperature range of 300-500 °C at a contact time of 0.8 seconds for the varying fuel:EtOH ratios

A plot of the product profile obtained for the reactions of the varying fuel:EtOH ratios at 450 °C is depicted in Figure 5.19. It showed that the addition of the ethanol co-feed reduced the formation of hydrolysis products and enhanced the selectivity to the target product EMA. The selectivity towards COx for each of the fuel:EtOH ratios at 450 °C was lower than the selectivity obtained for the reaction involving the EIB feed excluding water at 450 °C. This was due to the increase in selectivity towards EMA and hence secondary combustion of other products is hindered. For the quantification of the products formed for this particular set of reactions, it was important to note that ethanol was both a co-feed as well as a product of the reaction. The selectivity towards EMA was found to be optimal at the fuel:EtOH ratio of 1:5 and a further increase in the fuel:EtOH ratio showed a decrease in the selectivity towards EMA.

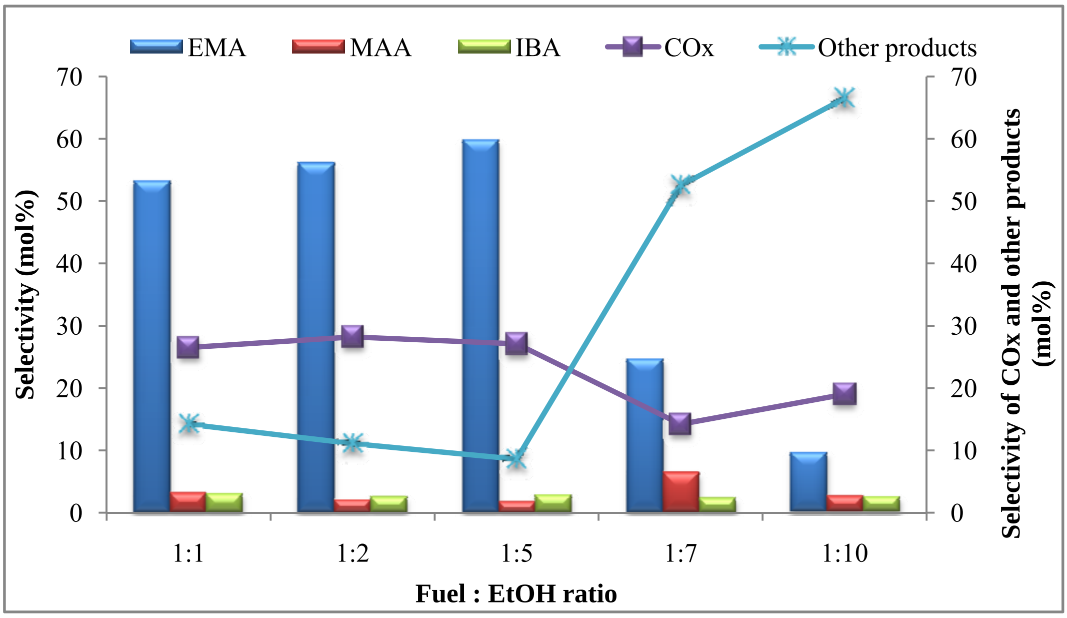

Figure 5.19 Selectivity to products at 450 °C with varying fuel:EtOH ratios

Figure 5.20 shows the product profile at the fuel:EtOH ratio of 1:5 over the temperature range of 300-500 °C. The EMA selectivity increased with an increase in temperature until an optimum of 450 °C. However, with a further increase in temperature there is a decrease in selectivity towards EMA, and an increase in COx formation, which is attributed to the combustion of the ODH product at elevated temperatures. Selectivity towards other products was found to be greater at lower temperatures and decreased with increase in temperature.

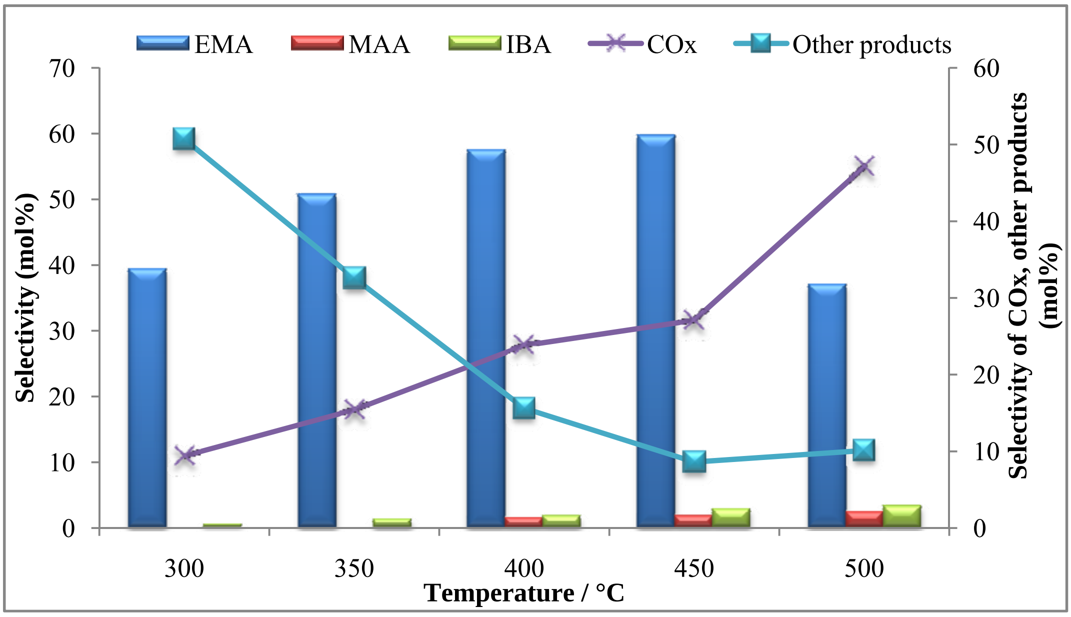

Figure 5.20 Product profile of the reaction with a fuel:EtOH ratio of 1:5 between 300-500 °C at a contact time of 0.8 seconds

5.4 Ethyl isobutyrate with ethanol and water co-feeds in air at varying ratios

The reactions involving the use of ethanol as co-feed (Section 5.3) showed that there was a substantial decrease in the selectivity towards the hydrolysis products and an increase in the selectivity towards EMA. However, the conversion obtained was lower than the conversion obtained for the reactions involving the water co-feed (Section 5.2). Hence it was decided to include a water co-feed for the reactions involving EIB and the ethanol co-feed. The aim was to increase the conversion and thus further increase EMA selectivity. Results obtained for these reactions can be found in Appendix C, C6.

Figure 5.21 shows the selectivity towards EMA of the varying fuel:EtOH:water reactions over the temperature range of 300-500 °C. The EIB:water ratios were kept constant and the ethanol ratios were varied to see the effect of ethanol on the reaction in the presence of water. The results obtained showed that the fuel:EtOH:water ratio of 1:5:15 produced the optimal selectivity towards EMA at a temperature of 400 °C relative to the other ratios. The temperature of optimal selectivity coincides with the reactions involving the use of EIB and water as co-feed (Fig. 5.16), where it was found that optimal selectivity towards the target product was at 400 °C, compared to the reactions excluding the water co-feed, and it was postulated that this had occurred due to water stabilizing the hydroxylated form of the active α-phase at a lower temperature.

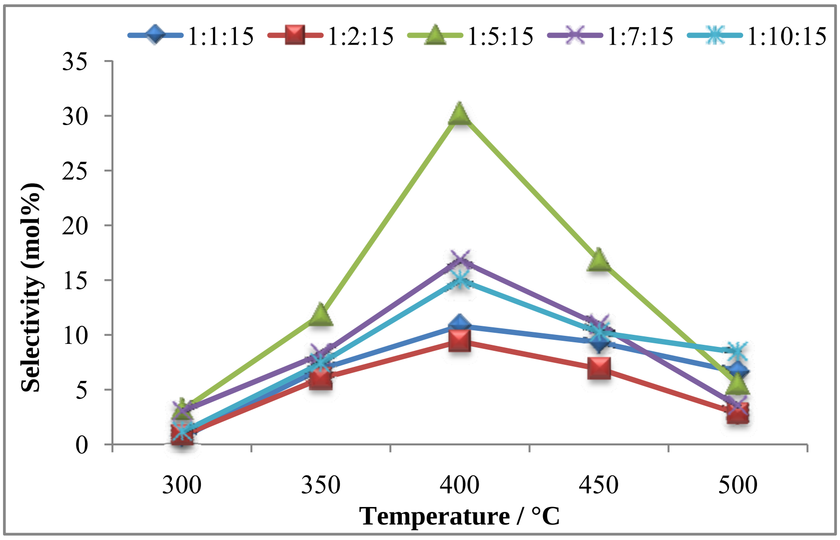

Figure 5.21 Selectivity towards EMA at varying fuel:EtOH:water ratios over the temperature range of 300-500 °C at a contact time of 0.8 seconds

The product profiles for the reaction of fuel:EtOH:water in the ratio of 1:5:15 was plotted across the temperature range of 300-500 °C and is shown in Figure 5.22. As mentioned previously, the greatest selectivity towards EMA was found at 400 °C and the selectivity towards MAA and COx increased with an increase in temperature. This suggests that the addition of water enhances the formation of MAA, and the formation of COx could be attributed to the secondary combustion of EMA at higher temperatures. The selectivity towards the other products decreases with an increase in temperature. Although, the selectivity towards other products is higher at 500 °C as compared to 450 °C which could be due to the formation of COx as a result of combustion of ODH products at the higher temperatures.

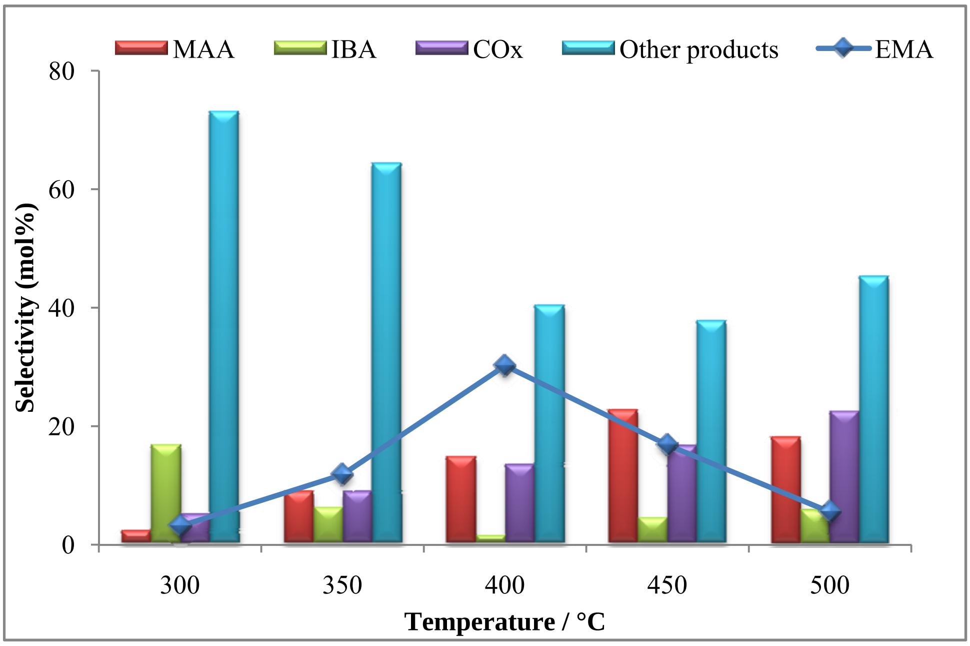

Figure 5.22 Product profile of the reaction with fuel:EtOH:water ratio of 1:5:15 between 300-500 °C at a contact time of 0.8 seconds

5.5 Mechanistic pathway for the reactions

Although a scheme for product formation is shown in Appendix C, C2, it was necessary to gain insight into the mechanistic pathways to certain products, in particular, EMA, MAA and IBA. The iron phosphate catalyst, which was synthesized with the tridymite-like $FePO_4$ phase as the major phase, was postulated to undergo the following reaction pathway [8]:

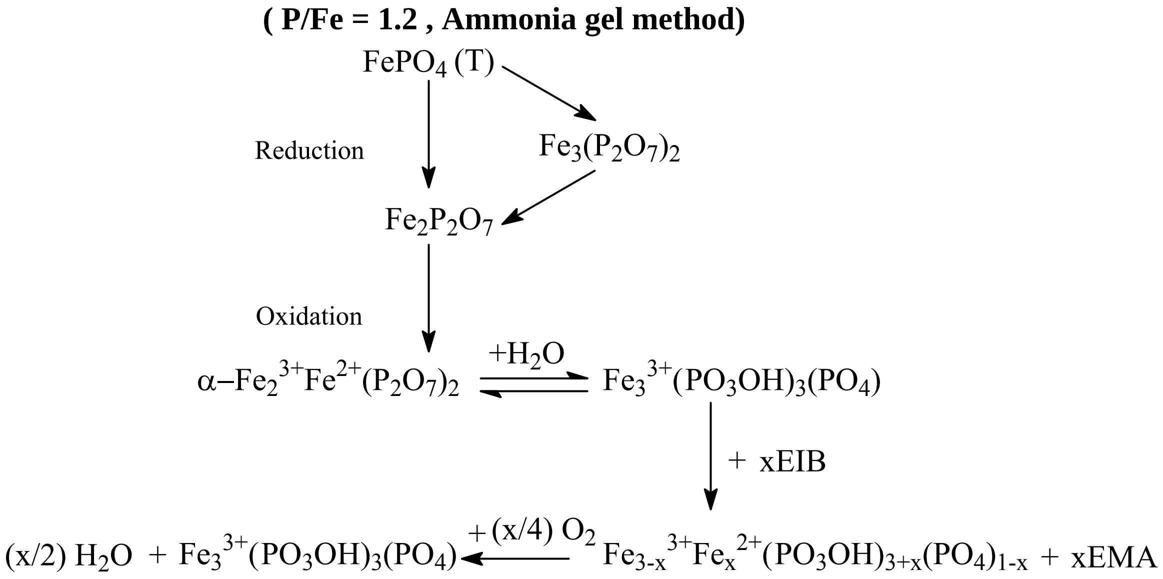

Scheme 1: Reaction of the hydroxylated and oxidized α-phase with EIB

It was considered that the tridymite-like $FePO_4$ phase is reduced under catalytic conditions in the temperature range of ~ 450 ^oC *via* an intermediate to form $Fe_2P_2O_7$. It is then reoxidized to the active mixed Fe(II) and Fe(III) α-phase. The hydroxylated and oxidised form of the α-phase reacts with the feed and the catalyst is reduced again. Since the catalyst is within a redox atmosphere, it is reoxidized and the water generated is used within the catalytic system. It is evident that the Fe^{3+}/Fe^{2+} redox couple is involved in the Mars and van Krevelen mechanism which occurs here.

The proposed mechanisms for the formation of EMA as well as the hydrolysis of EIB and EMA which results in the formation of IBA and MAA respectively, are found in Appendix C, C7.

5.6 Lifetime and regeneration studies

Once these reactions had been completed, it was decided to carry out lifetime and regeneration studies on the catalyst at the optimal temperature of 450 °C. The reaction was carried out at a contact time of 0.8 seconds. The lifetime of the catalyst was monitored based on the consistency of the conversion of the feed and the yield of EMA over time. Once the conversion was observed to decrease significantly, the feed was paused and the catalyst was treated with water in an oxidising atmosphere for 2 hours. The regeneration process was then stopped, and the feed flow resumed. Once again the conversion and yield were monitored.

The regeneration process was carried out twice, in order to observe if the activity of the catalyst could be maintained. Figure 5.23 and Figure 5.24 showed the results obtained for the fresh catalyst and after the two regeneration procedures. Initially the fresh catalyst maintained its activity for approximately 32 hours on stream and thereafter there was a decrease in conversion. After 76 hours, when the conversion had dropped to 17 %, it was decided to start the first regeneration process. After the first regeneration process, the conversion data resembled the results obtained for the fresh catalyst at the start of the experiment. However, with time on stream, the catalyst showed a decrease in conversion to 12 % after 63 hours. It was evident that the conversion data for the catalyst after the initial regeneration showed a significant decrease after ~ 23 hours on stream and thereafter a lower conversion was obtained relative to the fresh catalyst with time on stream.

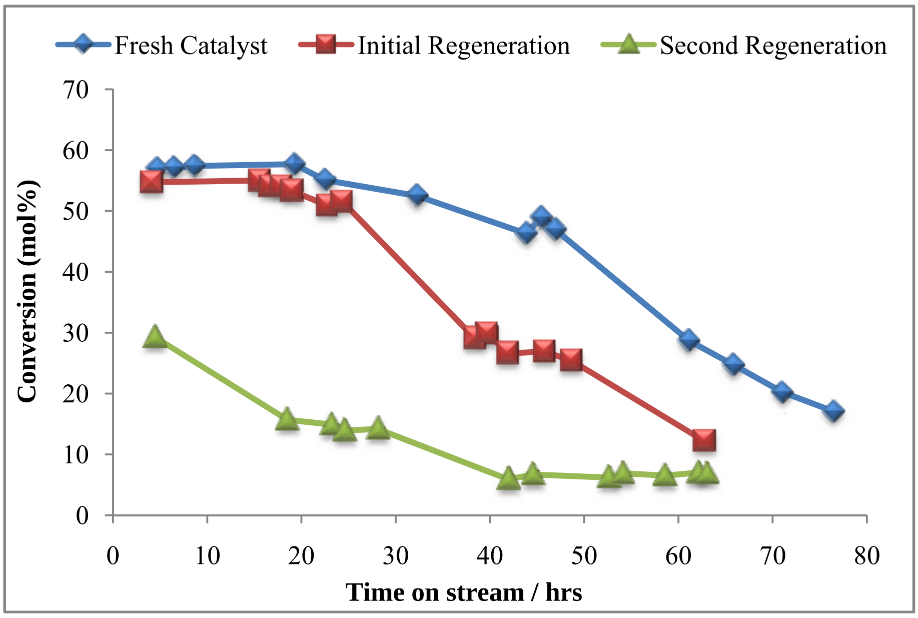

Figure 5.23 Conversion - longer time on stream study using an EIB feed

Once the catalyst was partially deactivated (~ 12 % conversion), the second regeneration was carried out. On completion of this process, it was observed that the efficacy of the catalyst had drastically reduced after the second regeneration, since the conversion data when the feed was resumed was now around 29 %. The reaction was ended after monitoring the conversion until catalyst deactivation was evident (63 hours).

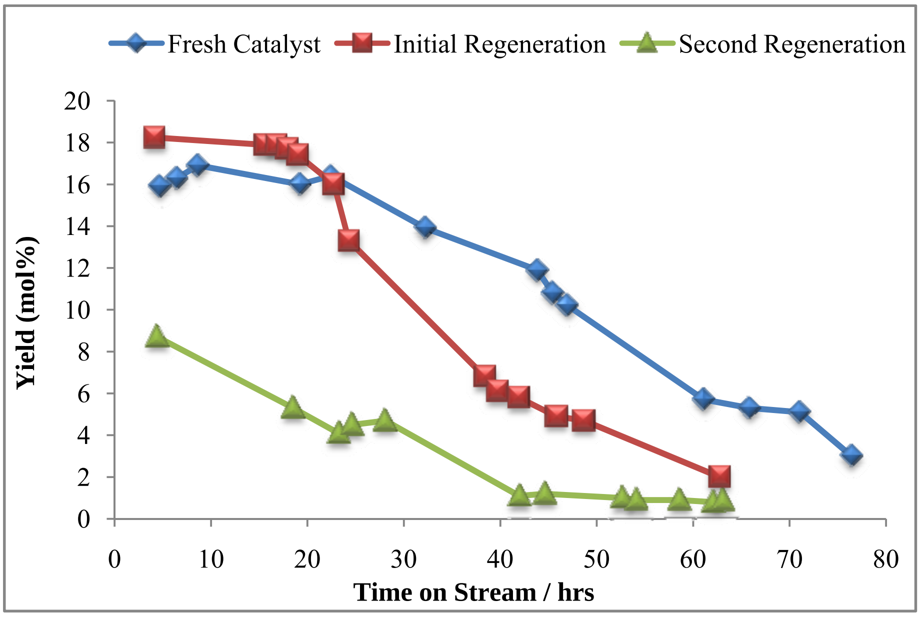

Figure 5.24 Yield - longer time on stream study using an EIB feed

Interestingly, the yield of EMA obtained after the first regeneration was slightly higher than the yield of EMA for the fresh catalyst, pre-regeneration. The higher yield of between 17-18 mol % was observed directly after the first treatment and this activity was maintained for 23 hours on stream, although the yield of EMA decreased thereafter (Fig. 5.24). The trend in the graph could be attributed to the reported beneficial effects of water. Reports have shown that water increases the lifetime and activity of the catalyst, seeing that water aids in the removal of non-volatile species from the surface of the catalyst [3, 9]**.** In addition, it plays a role in stabilizing the hydroxylated form of the active α-phase in the iron phosphate catalyst, which is very important since it facilitates the ODH process. Also, the temperature of optimal efficiency of the catalytic reaction coincides with the beginning of the dehydroxylation of the active α-phase [3]**.** Hence, after the regeneration process one could deduce that the addition of water facilitated the formation of the active α-phase thus allowing the catalyst to be hydroxylated in the bulk as opposed to the surface, therefore favouring slightly greater yields relative to the fresh catalyst. Also, after the partial deactivation of the fresh catalyst, which could be the result of coking, the use of water could be responsible for the removal of coke, therefore allowing for the catalyst to work optimally. It was considered that the slow deactivation of the fresh catalyst could be explained by the report stating that in the absence of water vapour the α-phase was not completely deactivated, but rather underwent a slow deactivation as a result of it being hydroxylated on the surface as opposed to the bulk [8]. Although the catalyst performed optimally after the initial regeneration, it underwent a slightly quicker deactivation after 23 hours and this may be the degradation of the physical properties of the catalyst, seeing that the active sites could be compromised as a result of the almost complete deactivation in the intial run and the absence of water during the testing facilitates this process. This idea is further supported by the decreased activity of the catalyst after the second regeneration process.

The results (Fig. 5.23 and Fig. 5.24) showed that the catalyst maintained its efficacy for 23 hours on stream and the addition of water as a regeneration medium showed that the yield obtained for the first 23 hours on stream was greater than the yield obtained for the fresh catalyst. However, the second regeneration was not as beneficial as the first treatment which could be the result of degradation of the catalyst properties with the extended time on stream. Based on this it was decided to carry out an additional study which involved a shorter time on stream prior to the regeneration process, hence not allowing the catalyst to undergo a considerable degree of deactivation prior to regeneration. During this investigation, the catalytic results were monitored over a 25 hour period on stream and thereafter the feed was paused and the catalyst was treated with water in an oxidizing atmosphere for 2 hours per regeneration period (Fig.5.25- Fig. 5.26).

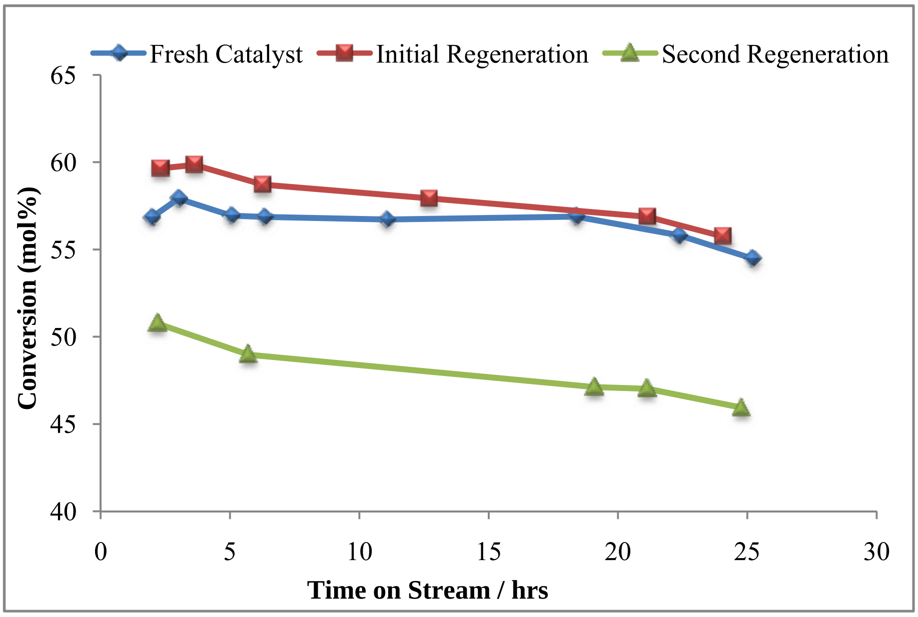

Figure 5.25 Conversion - shorter time on stream study using an EIB feed

During this experiment the fresh catalyst maintained its efficacy for 18 hours on stream with a negligible decrease in conversion after 18 hours.

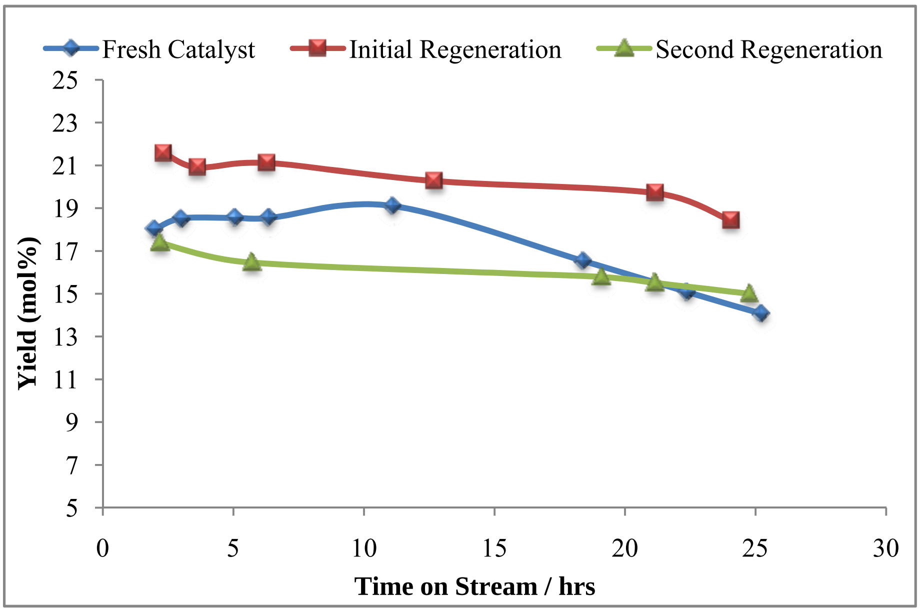

Figure 5.26 Yield - shorter regeneration study using an EIB feed

The yield towards EMA was an average of ~ 18-19 mol %, which was in close correlation with the initial investigation over the longer time on stream experiment for the fresh catalyst (Fig. 5.23 and Fig. 5.24). After the 25 hours on stream, the first regeneration process was carried out. The results showed that the catalyst activity was significantly greater than the results for the fresh catalyst with conversion and yield peaking at values of ~ 60 % and 21 mol % respectively. In addition, these values were greater than the conversion and yield data obtained for the longer time on stream experiment after the initial regeneration which had conversion and yield data of ~ 55 % and ~ 18 mol % respectively. These results evidenced the improved activity of the catalyst after the regeneration process due to the fact that the efficacy of the catalyst was not compromised by time on stream deactivation. After the second regeneration procedure, the conversion and yield after the feed was resumed, resembled the activity of the fresh catalyst initially, however with time on stream the catalyst showed stable results over the 25 hour period. The results obtained after the second regeneration relative to the results after the second regeneration during the longer time on stream experiment were significantly different. The onset conversion in the case of the former was ~ 50 % with a ~ 17 mol % yield, however, in the case of the latter, a conversion of ~ 29 % with a yield of ~ 9 mol % was observed. The investigation supported the benefit of the use of water as an effective regeneration medium and showed the success of the shorter time on stream regeneration technique.

It was reported that the $FePO_4$ catalyst is deactivated at low temperatures as a result of the deposition of non-volatile components on the surface of the catalyst. Further investigation had found that catalytic activity was totally regenerated after calcination in air at a temperature of 400 °C [9]. It was decided to investigate the effect of increasing the temperature above operating conditions during the regeneration process with the intent of 'burning' of the carbonaceous material in the presence of steam, while facilitating the formation of the α-phase with the addition of water. The temperature ramp involved an increase in the temperature to 500 °C during the initial and second regeneration step.

The fresh catalyst maintained a constant conversion of ~ 56 % with time on stream over the 25 hour period, as was observed in the previous regeneration study (Fig. 5.25 and Fig. 5.26). After the first regeneration process, there was a significant increase in conversion to ~ 62 % with an EMA yield of ~ 23 mol % and during the course of the reaction (~ 6 hours) a minor decrease in conversion to ~ 58 % with a corresponding yield of ~ 21 mol % was observed. These results outlined the significance of the removal of coke at elevated temperatures with the addition of water.

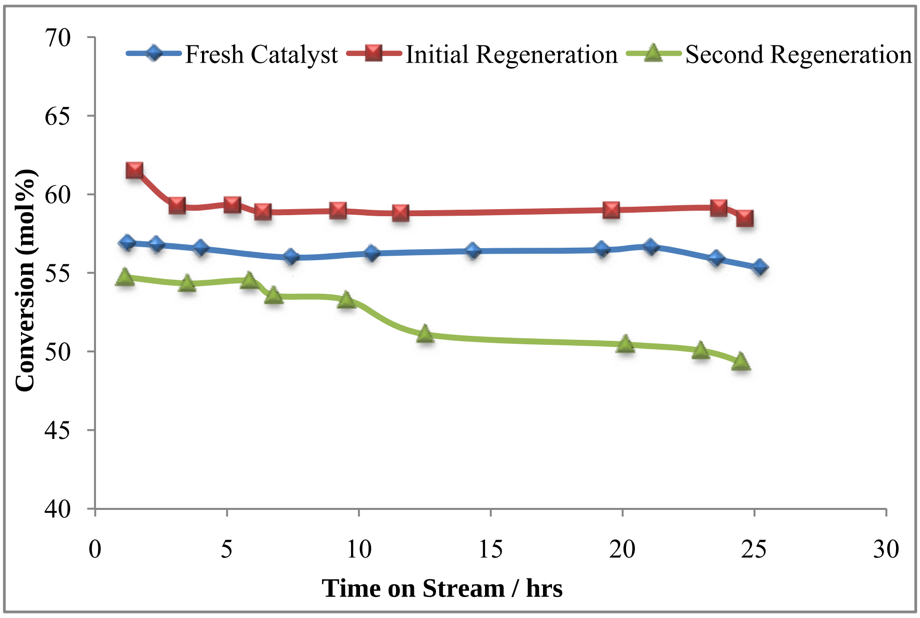

Figure 5.27 Conversion obtained during the shorter regeneration study – steam treatment at 500 °C

During the second regeneration process, the conversion when the feed was resumed was ~ 54 % with a corresponding yield of ~ 18 mol % showing favourable performance. However, with time on stream the conversion decreased to ~ 49 %, showing a degree of catalyst deactivation. This was considered to be the result of hard coke formation which cannot easily be removed by the regeneration temperature, thus blocking the active sites of the active α-phase.

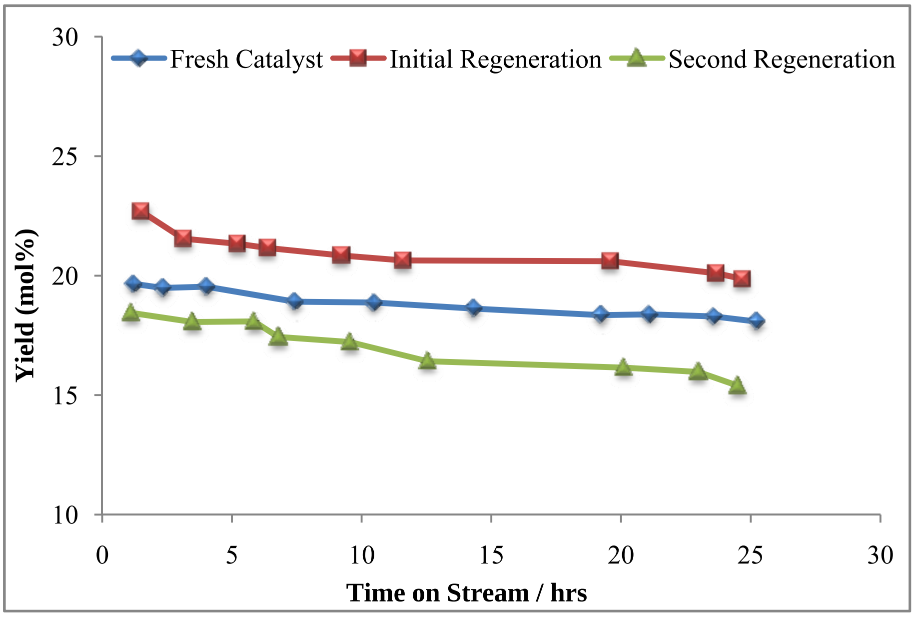

Figure 5.28 Yield obtained during the shorter regeneration study – steam treatment at 500 °C

5.7 Summary

The catalytic testing carried out demonstrated the effect of various reaction conditions on the performance of the tridymite-like $FePO_4$ catalyst precursor for the formation of the target product EMA. Initial testing involved the use of the EIB feed only in the presence of an oxidizing atmosphere at varying contact times of 1.2-0.4 seconds in increments of 0.2 seconds respectively. During this investigation it was observed that the optimal conversion was obtained at a temperature of 450 °C at each of the contact times which coincided with the redox procedure showing the formation of the active α-phase at a similar onset temperature. At a temperature above 450 °C i.e. 500 °C, it was found that there was a slight decrease in conversion and in addition the product profile within this temperature range showed a decrease in selectivity towards EMA and an increase in COx formation. The selectivity and yield data for EMA at the optimal operating temperature over the varying contact times showed that the contact time of 0.8 seconds produced the greatest yield of EMA, which was ~ 17 mol % with a ~ 30 % selectivity.

To confirm the assumption made in choosing a suitable catalyst precursor, which was that the tridymite-like $FePO_4$ catalyst was better than the quartz type $FePO_4$ catalyst for ODH reactions, the quartz type phase was tested at the optimal contact time of 0.8 seconds. Results were compared to those of the tridymite-like phase under the same reaction conditions. It was observed that with respect to quartz type phase optimal results were obtained at a similar temperature of 450 °C with a maximum EMA yield of ~ 14 mol % and a selectivity of ~ 27 %. With an increase in temperature, i.e. 500 °C, the conversion increased over the quartz type phase although the selectivity towards EMA decreased. This was attributed to secondary combustion occurring at the elevated temperature. These results were consistent with the XRD characterization data showing that formation of the active α-phase occurs at higher temperatures in the case of the quartz type phase precursor and at temperatures above 500 °C, reflections of the quartz type phase reemerge with a subsequent decrease in reflections characteristic of the α-phase.

At higher temperatures, over both the tridymite-like and quartz type phase, a decrease in conversion was observed. It was considered that the deposition of non-volatile products on the surface of the catalyst resulted in the decrease. Based on this it was decided to include water as a co-feed during the catalytic testing. The investigations including a water co-feed over the varying contact times also showed optimal results at 0.8 seconds; however the temperature of optimal efficiency shifted to a lower temperature of 400 °C, which was postulated to be related to the effect of water in favoring the formation of the hydroxylated form of the active α-phase, which was in fact the actual phase participating in the reaction. The presence of water during the catalytic testing showed an increase in the conversion of EIB relative to the reactions excluding the water co-feed, however, the selectivity towards EMA was lower, whilst that of hydrolysis products increased. In addition, the selectivity towards carbon oxides also decreased in the presence of the water co-feed which correlated with the reports in literature for the ODH of IBA; however there was a significant increase at elevated temperatures in carbon oxides selectivity due to the secondary combustion of ODH products.

Although the conversion was found to increase with the addition of the water co-feed, the effect of hydrolysis reduced the selectivity towards EMA. The use of ethanol was considered during the catalytic testing to shift the equilibrium towards EMA, however, initial testing involved the exclusion of the water co-feed to eliminate the effect of hydrolysis. The reactions were carried out at varying ratios, all of which exceeded a 1:1 ratio of fuel:EtOH, at a contact time of 0.8 seconds. Optimal conversion was obtained at 450 °C, which was similar to the reaction involving the EIB feed only, although the conversion was lower in comparison to the reaction including the water co-feed. It was found that the higher ratios, namely, 1:5, 1:7 and 1:10 fuel:EtOH showed similar conversion at the optimal temperature. In the product profile at 450 °C for the varying fuel:EtOH ratios it was evident that the addition of the alcohol reduced hydrolysis and enhanced selectivity towards EMA. Also, the carbon oxides selectivity was lower in comparison to the reaction involving the EIB feed only. At a ratio of 1:5 fuel:EtOH, a yield of ~ 34 mol % EMA was obtained at a conversion of ~ 57 %.

The beneficial effect of water was considered during the investigation involving the use of the ethanol co-feed. It was considered that, since the addition of ethanol enhances EMA selectivity and reduces the formation of hydrolysis products, the addition of water would benefit this study by influencing the conversion. The catalytic tests were carried out at varying fuel:EtOH ratios, which were in line with the reactions excluding the water co-feed and the fuel:water ratio was maintained at 1:15. The reaction with the fuel:EtOH:water ratio of 1:5:15 showed the optimal selectivity (31 %) at 400 °C towards EMA relative to the other fuel:EtOH:water ratios at a conversion of 70 %. The effect of water in enhancing the conversion and shifting the optimal temperature of the reaction was observed. The hydrolysis products formed during the reaction were greater than those from the reaction including the ethanol co-feed only, but lower than those of the reaction including the water co-feed at the contact time of 0.8 seconds.

The various reactions which were carried out, irrespective of reaction parameters, were the reactions including the EIB feed only, EIB and ethanol co-feed, EIB and water co-feed, as well as the EIB, ethanol and water co-feed. Comparisons of the results obtained at optimal operating conditions are shown in Figure 5.27 and Figure 5.28 and the results for EIB conversion and yield of EMA obtained at a contact time of 0.8 seconds are plotted. The results are plotted at 400 °C and 450 °C, respectively, due to the effect of water in favouring hydroxylation at a lower temperature. It was evident that the addition of water increases the conversion significantly relative to the reactions excluding the water co-feed. At 400 °C the yield of EMA was optimal for the reaction including the ethanol co-feed with a value of ~ 23 mol % relative to the other variations tested. However, the reaction including the ethanol and water co-feed showed a yield towards EMA of ~ 21 mol % and the yield of the hydrolysis product MAA was ~ 11 mol %, hence, considering that the hydrolysis product formed primarily from the EMA, one could assume that the yield towards EMA could be ~ 32 mol %.

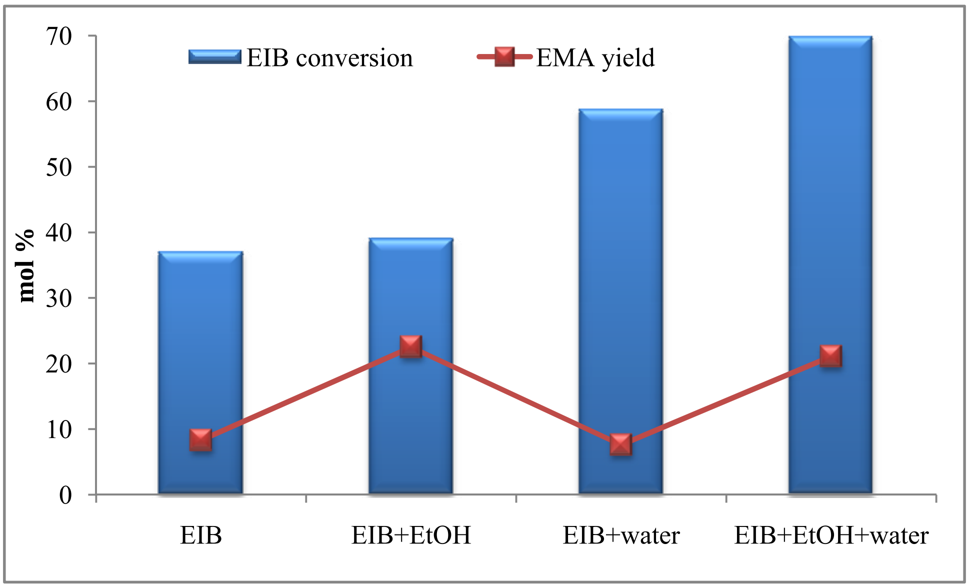

Figure 5.29 Yield and conversion at 400 °C

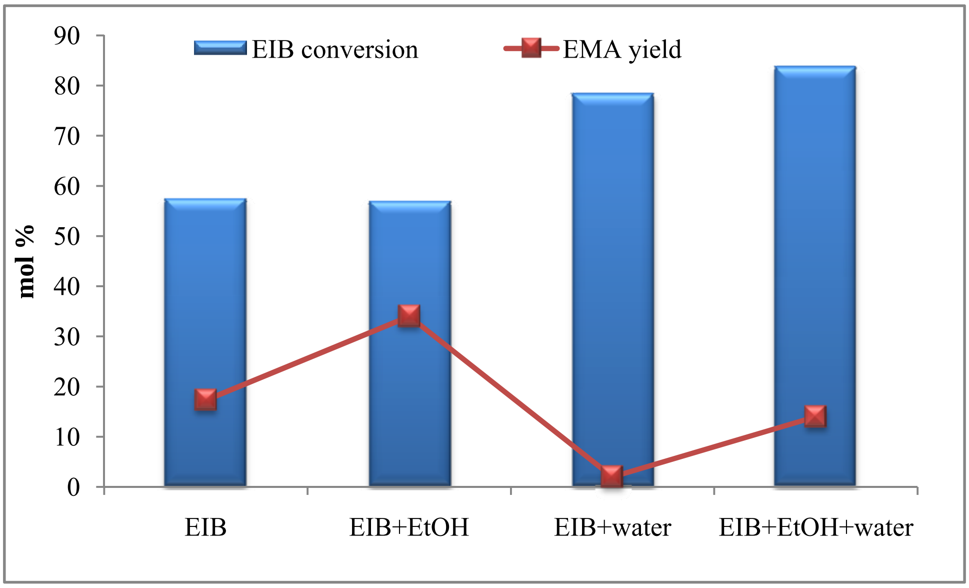

Figure 5.30 Yield and conversion at 450 °C

As mentioned previously, when water was excluded as a co-feed, optimal results were obtained at 450 °C, possibly because the exclusion of water does not allow for the hydroxylation/dehydroxylation process to occur at a lower temperature. Hence, a similar plot as that shown in Figure 5.29 was obtained for EIB conversion and EMA yield at 450 °C (Fig. 5.30). These results showed that the yield towards EMA at this temperature was significantly greater for the reactions which excluded the water co-feed. The reaction including the ethanol co-feed only, showed that at a conversion of ~ 57 % a yield of ~ 34 mol % was obtained. In addition, a higher conversion was obtained for the reactions including the water co-feed; however, the yield was lower as compared to the results obtained at 400 °C.

The lifetime and regeneration studies were carried out to observe the efficacy of the catalyst with time on stream and whether water served as an effective regeneration medium during this process. The initial investigation involved a longer time on stream and almost complete deactivation of the catalyst prior to regeneration. It was observed that the catalyst remained active initially for a period of 32 hours on stream and thereafter underwent a slow deactivation, which was evident by the decrease in conversion from ~ 57 % to 29 % after 61 hours. After the first regeneration process the results showed that the catalyst gave a better yield of EMA of ~ 18 mol %, however, the activity of the catalyst decreased after to 23 hours on stream following a rapid deactivation evidenced by the decrease in conversion from ~ 55 % to 29 % after 38 hours. After the second regeneration, the initial activity was not restored.

An additional investigation was carried out with the same parameters as the first lifetime and regeneration study, however, a shorter time on stream (25 hours) prior to regeneration was considered to prevent complete deactivation of the catalyst, hence minimizing rapid deactivation after the initial regeneration process. The conversion was almost consistent throughout the 25 hour period with a negligible decrease in conversion after 18 hrs. After the initial regeneration process, the conversion increased to a maximum ~ 60 % with a yield of ~ 21 mol % and the change in conversion with time on stream was ~ 5 % over the 25 hours. After the second regeneration procedure, the conversion and yield data after the feed was resumed were similar to those of the fresh catalyst, although lower relative to the catalyst after the initial regeneration. It seemed that with time on stream the catalyst showed almost constant results over the 25 hour period.

In light of the beneficial effects of the shorter lifetime and regeneration study, it was decided to combine the effect of water as a suitable regeneration medium and include an elevated heating step in the presence of steam to remove the carbonaceous material.

The optium yield of 23 mol % was observed after the first regeneration step and relative to the previous shorter regeneration procedure this technique showed better results. After the second regeneration step, a marginal decrease in the conversion was observed.

The use of the varying regeneration techniques showed that the tridymite-like $FePO_4$ catalyst was significantly more active over a 25 hour period on stream and the use of heat and steam enhanced the conversion and selectivity towards the target product EMA.

References

[1] H.B. Friedrich, N. Govender, M.R. Mathebula, Appl. Catal., A. 297 (2006) 81-89.

[2] M. Ai, E. Muneyama, A. Kunishige, K. Ohdan, Appl. Catal., A. 109 (1994) 135-146.

[3] J.M.M. Milleta, M. Forissier, D. Rouzies, P. Bonnet, J.C. Vedrine, in: W.N.D.E.I. Joe W. Hightower, T.B. Alexis (Eds.), Stud. Surf. Sci. Catal., Elsevier, 1996, pp. 1011-1020.

[4] J.L. Figueiredo, Progress in catalyst deactivation: proceedings of the NATO Advanced Study Institute on Catalyst Deactivation, Algarve, Portugal, May 18-29, 1981, Martinus Nijhoff Publishers, 1982.

[5] E. Muneyama, A. Kunishige, K. Ohdan, M. Ai, Catal. Lett. 31 (1995) 209-220.

[6] J.E. Brady, F. Senese, Chemistry: The Study of Matter and Its Changes, John Wiley & Sons, London, 2009.

[7] A.P. Gelbeln, Chem. Systems Inc., EP 0 088 615 A1.

[8] J.-M.M. Millet, Catalysis Reviews. 40 (1998) 1-38.

[9] M. Ai, K. Ohdan, J. Mol. Cat. A: Chemical, 159 (2000) 19-24.

CHAPTER 6

CHARACTERIZATION OF THE SPENT CATALYSTS

The activity of catalysts in oxidation or oxidative dehydrogenation is based on the presence of cations in the active phase which are susceptible to changing their valence in the course of the catalytic reaction [1]. Ai and co-workers [2-4] have reported on the presumed phase formations after activation of $FePO_4$ catalysts synthesized via the ammonia gel method. Five phases were identified, which were the quartz type $FePO_4$ phase, $Fe_2P_2O_7$, β-$Fe_3(P_2O_7)_2$, α-$Fe_3(P_2O_7)_2$ and a small amount of $NH_4FeP_2O_7$. As mentioned previously, the β-phase formed upon reduction of the $FePO_4$ with an excess of phosphorous and the transformation between the α-phase and $Fe_2P_2O_7$ took place reversibly depending on reduction-oxidation conditions [3]. In addition, it was reported that the reduction of $FePO_4$ without an excess of phosphorous resulted in the formation of $Fe_2P_2O_7$ [3].

The results obtained for the spent catalyst characterization from the work presented in this thesis have been divided into three sections reflecting the varying reaction conditions, namely, reactions including an organic (ethanol) co-feed (excluding water), reactions including a water co-feed and reactions including a combined ethanol (EtOH) and water co-feed. The results obtained have been averaged for each of the reaction conditions.

6.1 Inductively Couple Plasma-Optical Emission Spectroscopy

ICP analysis was carried out on the spent catalysts and the average P/Fe ratio obtained was within the range of 1.13-1.14.

6.2 Brunauer-Emmet-Teller surface areas and pore volumes

Previous results showed that the surface area for the fresh calcined catalyst was within the range of approximately 10-12 m^2/g (Chapter 4, Section 4.2). The surface area results obtained were compared for the spent catalysts from the reactions including and excluding the water co-feed as well as the reaction including the EtOH and water co-feed (Fig. 6.1). It was found that for the reactions including the water co-feed, the surface area (and pore volume) of the spent catalyst was within the region of the fresh calcined catalyst. This could be attributed to the fact that water suppresses the formation of carbon deposits on the surface of the catalyst and in addition it was reported that water assists in the desorption of products from the surface of the catalyst [5,6]. The surface area (and the pore volume) of the spent catalyst for the reactions excluding the water co-feed showed a slight decrease, and this could be a direct relation to the effect of coking. In comparison to these results, it was observed that for the reaction including both water as well as the ethanol co-feed, there was a slight decrease in surface area relative to the fresh catalyst and the catalyst after the reaction including the water co-feed. This was anticipated and the surface area was greater than the surface area obtained for the reactions which excluded the water co-feed, since although ethanol is included, the use of water as an additional co-feed is beneficial once again in suppressing carbon deposition and assists in the desorption of products from the surface of the catalyst.

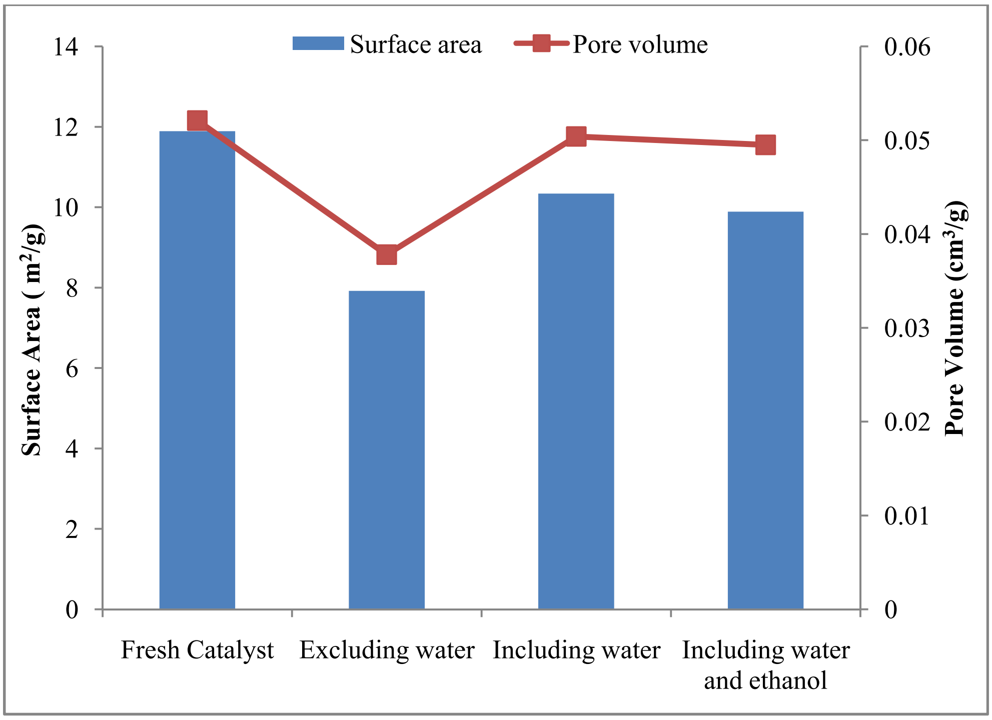

Figure 6.1. Effect of reaction conditions on surface area and pore volume

6.3 X-ray Diffraction and Mössbauer spectra of the spent catalysts

The use of X-ray diffraction as well as Mössbauer spectroscopy was considered for the reactions including varying co-feeds. Initially the spent catalyst for the ethyl isobutyrate (EIB) only reaction was considered and quite significant during the interpretation of the result was a single intense peak within the region of $2\theta = 34.4°$ (Fig. 6.2). This peak was attributed to the presence of the active α-phase. Based on these results it was decided to observe the variation in phase formation with change in reaction conditions using XRD, which was supported by phase assignments from Mössbauer spectroscopy.

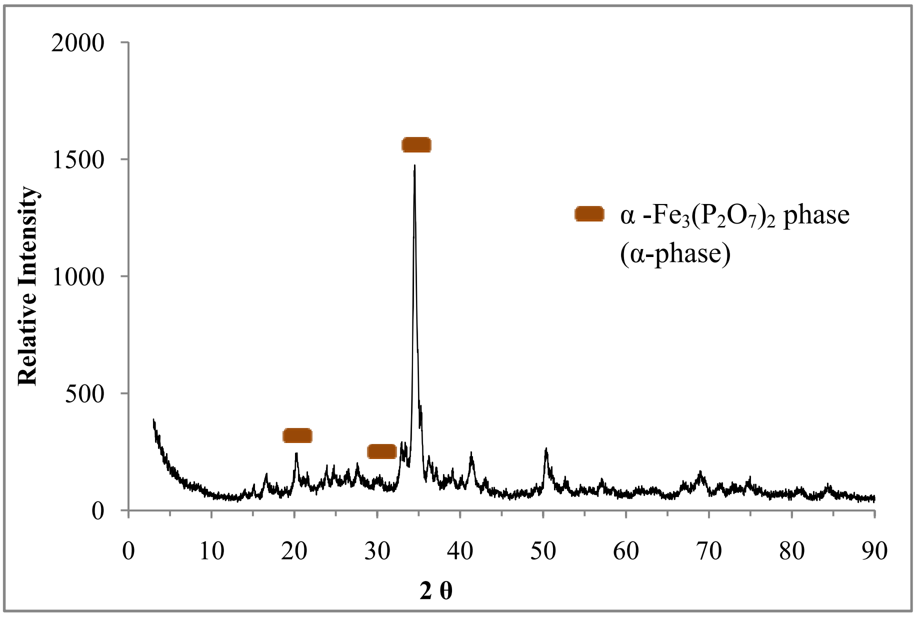

Figure 6.2. X-ray diffraction trace of the spent catalyst after the EIB only reaction

Figure 6.3 represents the X-ray diffractograms obtained for the spent catalyst after the three different reaction conditions, namely, (a) EIB and EtOH co-feed, (b) EIB and water co-feed and (c) EIB, EtOH co-feed and water co-feed. Their corresponding Mössbauer spectra and fit parameters, including assignments, are shown in Figure 6.4 and Table 6.1, respectively.

In the diffractogram shown in Figure. 6.3a (EIB and EtOH co-feed), two major peaks are evident at $2\theta = 34.3°$ and 35.2° respectively; in addition there are several minor peaks within the range of 2θ = 24–25°, 40–41° and 50–51°. The two major peaks are attributable to $Fe_2P_2O_7$, but this region also coincides with an overlap of the most intense peak of the α-phase [7]. Also, the peaks within the regions of 2θ = 24–25° and 40–41° are characteristic of the β-$Fe_3(P_2O_7)_2$ phase (β-phase) [1].

The Mössbauer data, Figure 6.4a, are dominated (74 %) by a Fe^{2+} spectral component which has IS and QS values (Table 6.1) which allow it to be attributed to $Fe_2P_2O_7$. The emergence of the β-phase is also evident, by the IS and QS values of ferric and ferrous species, each contributing towards an 8 % total site fraction [8]. The spectrum also shows a 17 % contribution from an Fe^{3+} component with IS and QS values of 0.44(3) and 0.62(4) mm/s respectively, which are consistent with the parameters of the α-phase and the hydrated form of the α-phase, $Fe_3(PO_3OH)_4.4H_2O$ [1]. The mixture of phases could be due to transformation between the α-phase and the $Fe_2P_2O_7$ phase taking place reversibly, depending on reduction-oxidation conditions [7].

The Mössbauer data for the spent catalyst after the water co-feed, Figure 6.4b, shows IS and QS values for a 35 % Fe^{3+} species and 21 % Fe^{2+} species with parameters which are consistent with the α-phase and a 19 % Fe^{2+} species with IS and QS values which again allow them to be attributed to $Fe_2P_2O_7$. Importantly, there is no evidence of the β-phase, although the emergence of the $Fe_7(PO_4)_6$ phase with IS and QS values of 0.32(3) and 0.65(3) mm/s having a 14 % site fraction of Fe^{3+} species and an unidentified phase, with IS and QS values not typical of a ferrous or ferric species, with a 10 % site fraction is observed. The results show an increase in site allocation towards the α-phase after the water co-feed treatment, which is further verified by the diffractogram in Figure 6.3b which has an intense peak within the region of $2\theta = 34.5°$ and a minor peak within the region of $2\theta = 27.9°$, both of which are characteristic of the α-phase.

The absence of evidence of the β-phase is an important result, given that it has been reported to be a poor catalyst, as it does not undergo oxidation even superficially due to the Fe^{2+} species occurring in a trigonal prismatic coordination [9]. It has been reported previously that the β-phase was not observed during the oxidative dehydrogenation (ODH) of isobutyric acid (IBA) with the addition of a water co-feed [8].

Formation of the $Fe_7(PO_4)_6$ phase could be the result of transformation of a certain percentage of the tridymite-like $FePO_4$ phase to the quartz type $FePO_4$ phase in the presence of water during the catalytic testing. Although results mentioned previously (Chapter 4, Section 4.10, Fig. 4.25) showed that this transformation can only occur during the calcination process at temperatures above 550 °C, it has been reported that this transformation is possible at lower temperatures with the addition of water [10]. Hence, assuming a certain quantity of the quartz type $FePO_4$ phase formed during the catalytic testing, it has been reported that this phase undergoes transformation during a catalytic reaction involving the ODH of IBA to form $Fe_7(PO_4)_6$ and the α-phase [11].

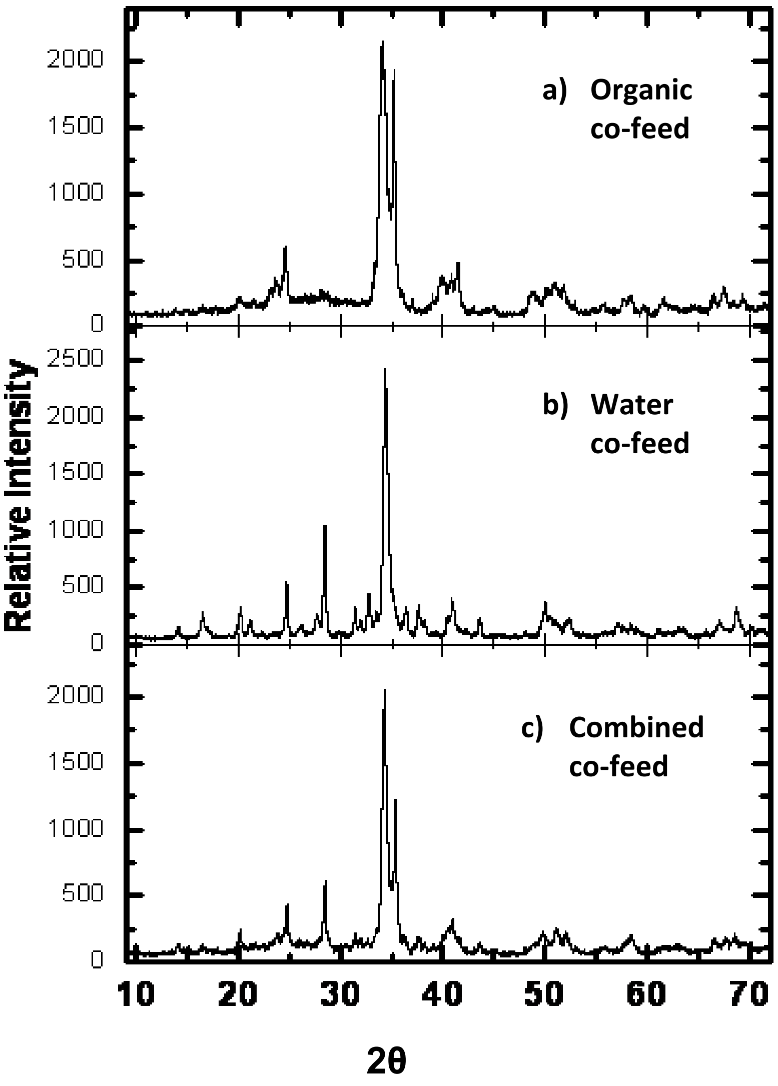

Figure 6.3. X-ray diffraction traces of the spent catalyst after a) EtOH co-feed, b) water co-feed, and c) after combined EtOH and water co-feed

The diffractogram of the spent catalyst using the combined co-feeds, Figure 6.3c, correlates with the spent catalyst described in Figure 6.3a, where the phase assignment was attributed to a mixture of both the $Fe_2P_2O_7$ and the α-phase. However, there is less intensity in the second component. The Mössbauer spectrum obtained after the EtOH and water co-feeds, Figure. 6.4c, shows Fe^{2+} components with IS values of 1.23(2) and 1.16(2) mm/s and corresponding QS values of 2.37(3) and 2.62(3) mm/s with a combined 68 % intensity, which were assigned to $Fe_2P_2O_7$. The spectrum also shows the occurrence of the Fe^{3+} species with a 32 % site fraction. The respective IS and QS values of 0.47(2) and 0.57(3) mm/s of this ferric species showed correlation with the Fe^{3+} species in the three phases, namely (1) the α-phase, (2) the hydrated form of the α-phase with IS and QS values of 0.42 and 0.58 mm/s respectively, and (3) the $Fe_2(PO_3OH)P_2O_7$ phase which has IS and QS values of 0.43 and 0.55 mm/s and shows similar properties to that of the α-phase [8,9]. Intimate mixtures of each of these phases could exist within the system. There is no evidence of the β-phase. It is interesting to observe that the addition of the water co-feed blocks the formation of the less selective β-phase. It has been reported that formation of the β-phase is dependent on the structure and reduction levels of the precursors [9]. Evidently, water plays a role in avoiding high reduction levels.

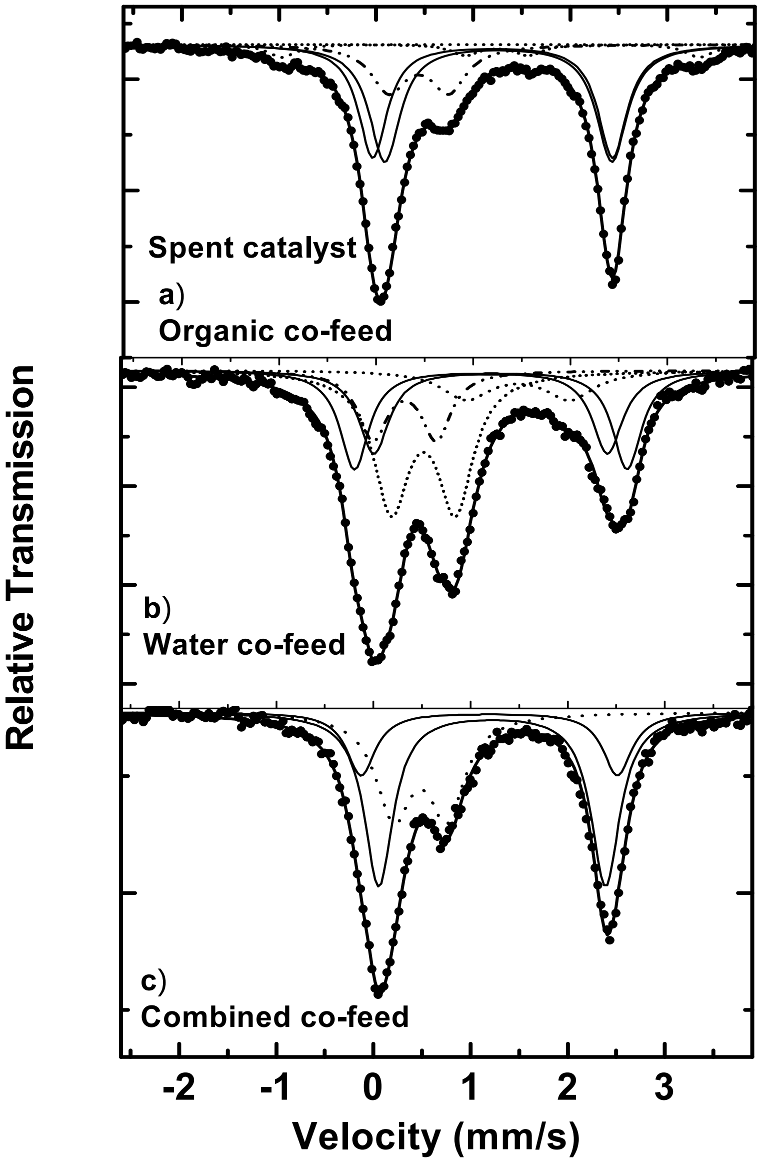

Figure 6.4. Mössbauer spectra, together with fitted components, of the spent catalyst after a) EtOH co-feed, b) water co-feed, and c) after combined EtOH and water co-feed.

Table 6.1. Mössbauer parameters, isomer shift (IS), electric quadrupole splitting (QS) site fractions (*f*) and phase assignments, determined from the spectra of the spent catalyst after a) EtOH co-feed, b) water co-feed and c) combined EtOH and water co-feed. The isomer shifts are expressed relative to α-Fe at room temperature

Sample	**IS (mm/s)**	**QS (mm/s)**	***f***	**Relative Intensity (%)**	**Attributed Phase**
a) Organic co-feed	1.26(3)	2.34(4)	Fe^{2+}	39(4)	$Fe_2P_2O_7$
	1.20(4)	2.47(4)	Fe^{2+}	35(4)	$Fe_2P_2O_7$
	0.44(3)	0.62(4)	Fe^{3+}	17(2)	α-$Fe_3(P_2O_7)_2$/ $Fe_3(PO_3OH)_4.4H_2O$
	1.18(3)	4.30(6)	Fe^{2+}	4(2)	β-$Fe_3(P_2O_7)_2$
	0.46(3)	0.27(3)	Fe^{3+}	4(2)	β-$Fe_3(P_2O_7)_2$
b) Water co-feed	1.21(4)	2.40(3)	Fe^{2+}	19(2)	$Fe_2P_2O_7$
	1.22(2)	2.81(4)	Fe^{2+}	21(2)	α-$Fe_3(P_2O_7)_2$
	0.52(3)	0.66(3)	Fe^{3+}	35(3)	α-$Fe_3(P_2O_7)_2$
	0.32(3)	0.65(3)	Fe^{3+}	14(3)	$Fe_7(PO_4)_6$
	1.49(5)	1.07(3)	Fe	10(2)	X*
c) Combined organic and water co-feed	1.23(2)	2.37(3)	Fe^{2+}(2)	60(4)	$Fe_2P_2O_7$
	1.16(2)	2.62(3)	Fe^{2+}(1)	8(3)	$Fe_2P_2O_7$
	0.47(2)	0.57(3)	Fe^{3+}	32(4)	α- $Fe_2P_2O_7$/ $Fe_3PO_3OH)_4.4H_2O$/ $Fe_2(PO_3OH)P_2O_7$

* *Unidentified species*

6.4 Infrared Spectroscopy

The IR spectra for the spent catalyst obtained from the varying reaction conditions were recorded. The spectra are represented in Figures 6.5–6.7. The results presented in this study for XRD and Mössbauer spectroscopy showed that for each of the reaction conditions, $Fe_2P_2O_7$ and the α-phase exist as the major phases. The spectra obtained for the catalyst after varying reaction conditions showed a close match to the spectra reported in literature for both $Fe_2P_2O_7$ and the α-phase [3]. The pyrophosphate group, $(P_2O_7)^{2-}$, which is present in both of these phases is characterised by a strong peak between 1100-1200 cm^{-1} and a weak to medium peak between 960-1060 cm^{-1}. These peaks were evident in all three cases [12].

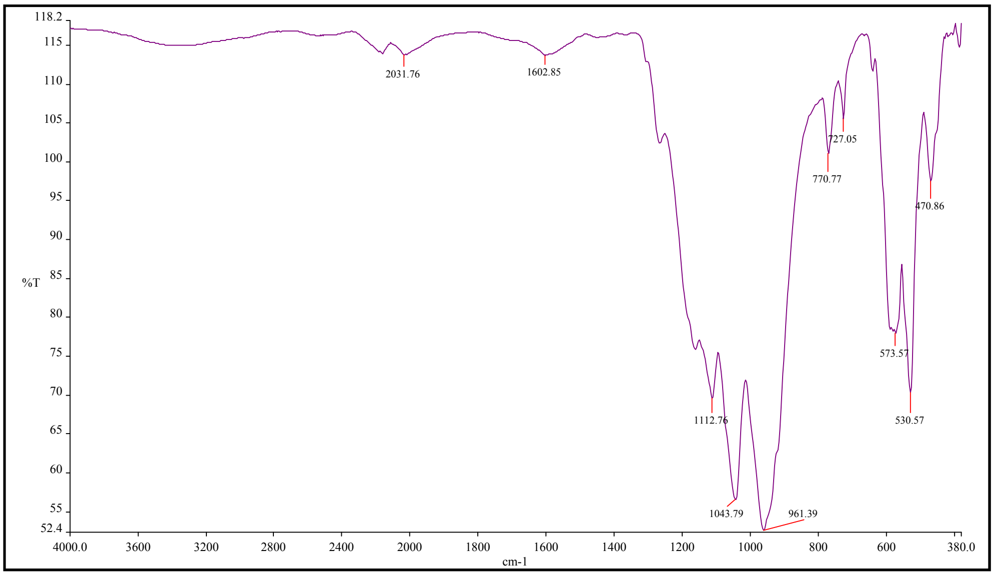

Figure 6.5. IR spectrum of the spent catalyst from the reaction including the EtOH co-feed (excluding water)

The use of water has been mentioned previously to prevent carbon deposition and in addition it assists in the desorption of products from the surface of the catalyst [5,6]. It was observed that the spectra for the reactions including a water co-feed (Fig. 6.6-6.7), showed no evidence of the IR band within the region of approximately 1590 cm^{-1} which is generally characteristic of polyaromatic coke on acidic sites [13,14]. A very small signal was, however, evident in Figure 6.5, the catalyst after the reaction excluding a water co-feed; suggesting some coking or it could be attributed to the presence of adsorbed organic products on the surface of the catalyst seeing that the reaction did exclude a water co-feed. Coke formation could explain the significant decrease in conversion as well as EMA selectivity with the increase in temperature above the optimal operating conditions. In correlation, the BET surface areas for the catalysts after the reactions excluding a water co-feed showed a decrease in surface area and pore volume relative to the reactions including a water co-feed which could be assigned to coke formation or adsorbed organic products.

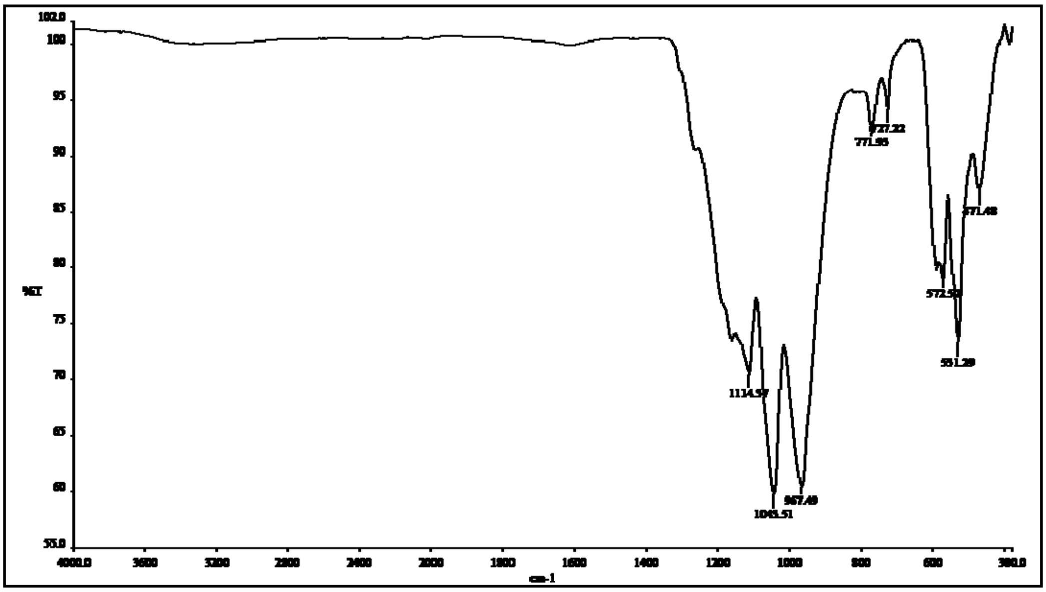

Figure 6.6. IR spectrum of the spent catalyst from the reaction including a water co-feed (excluding EtOH)

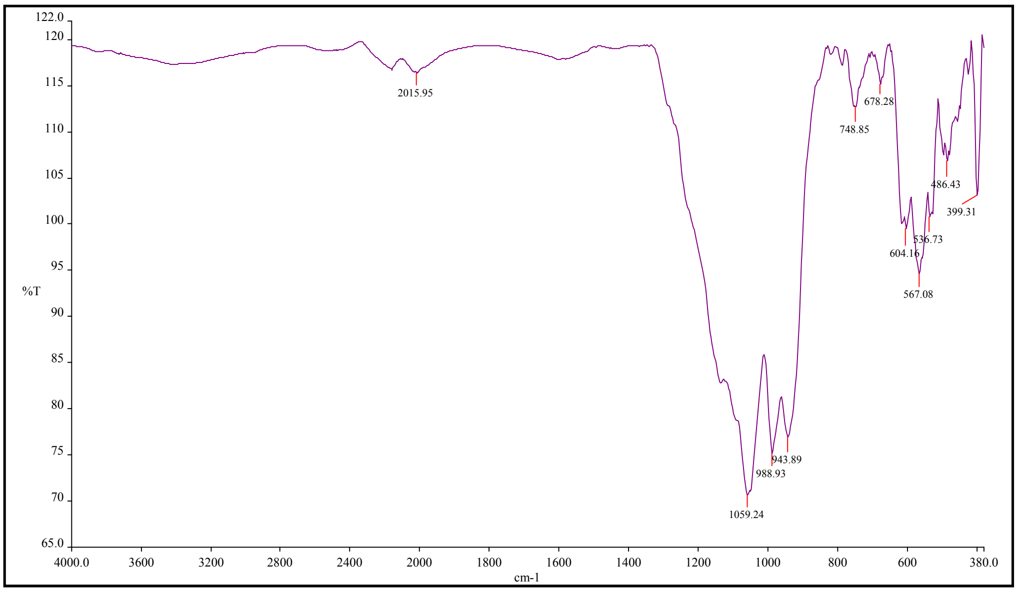

Figure 6.7. IR spectrum of the spent catalyst from the reaction including the combined EtOH and water co-feed

6.5 Scanning Electron Microscopy

The SEM images (Fig. 6.8) of the spent catalyst after each of the reaction conditions discussed above were similar to those of catalyst A in its reduced state (Chapter 4, Figure 4.21). The images do not show the even distribution of iron phosphate particles on the surface of the silica support. It seems that under all the reaction conditions the iron phosphate particles agglomerate on the surface of the support, as was observed in the case of the reduced catalyst.

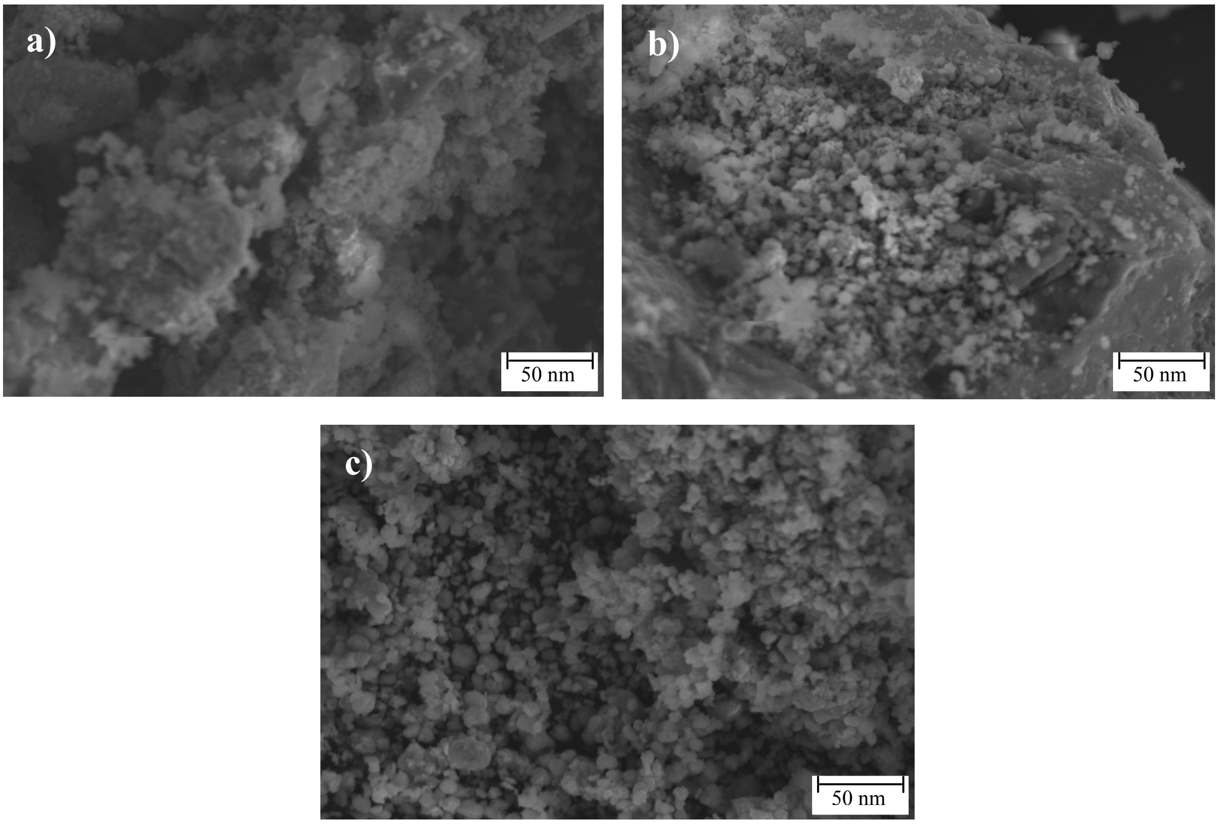

Figure 6.8. SEM images (scale = 50 nm) of the spent catalyst after the EtOH co-feed (a), water co-feed (b) and combined EtOH and water co-feed (c)

6.6 Transmission Electron Microscopy, Selected Area Diffraction Pattern and particle size analysis

The TEM images obtained for the spent catalyst samples under the varying reaction conditions did not allow for much identification in terms of particle size isolation for both the silica support as well as the iron phosphate particles. The results obtained for each of the reaction conditions (Figures 6.9 (a)-(c)) showed a distribution of silica particles which were within the range of 25-33 nm. As discussed previously, (Chapter 4, Section 4.12), the silica particle size was within the range of 30-35 nm, hence indicating that post catalytic testing, a significant variation in support particle size was not observed. It was also seen that for certain reaction conditions, Figure 6.9 (c), particle stacking hindered particle isolation, thus making analysis of the sample difficult. The SADP results of the spent catalyst samples (Fig. 6.10) did not show an ordered pattern as in the case of the tridymite-like $FePO_4$ precursor discussed previously (Chapter 4, Fig. 4.45). There seems to be several superimposed spots on the pattern which could be explained by the additional crystalline phases which were indentified from the Mössbauer results mentioned previously (Fig. 6.4, Table 6.1).

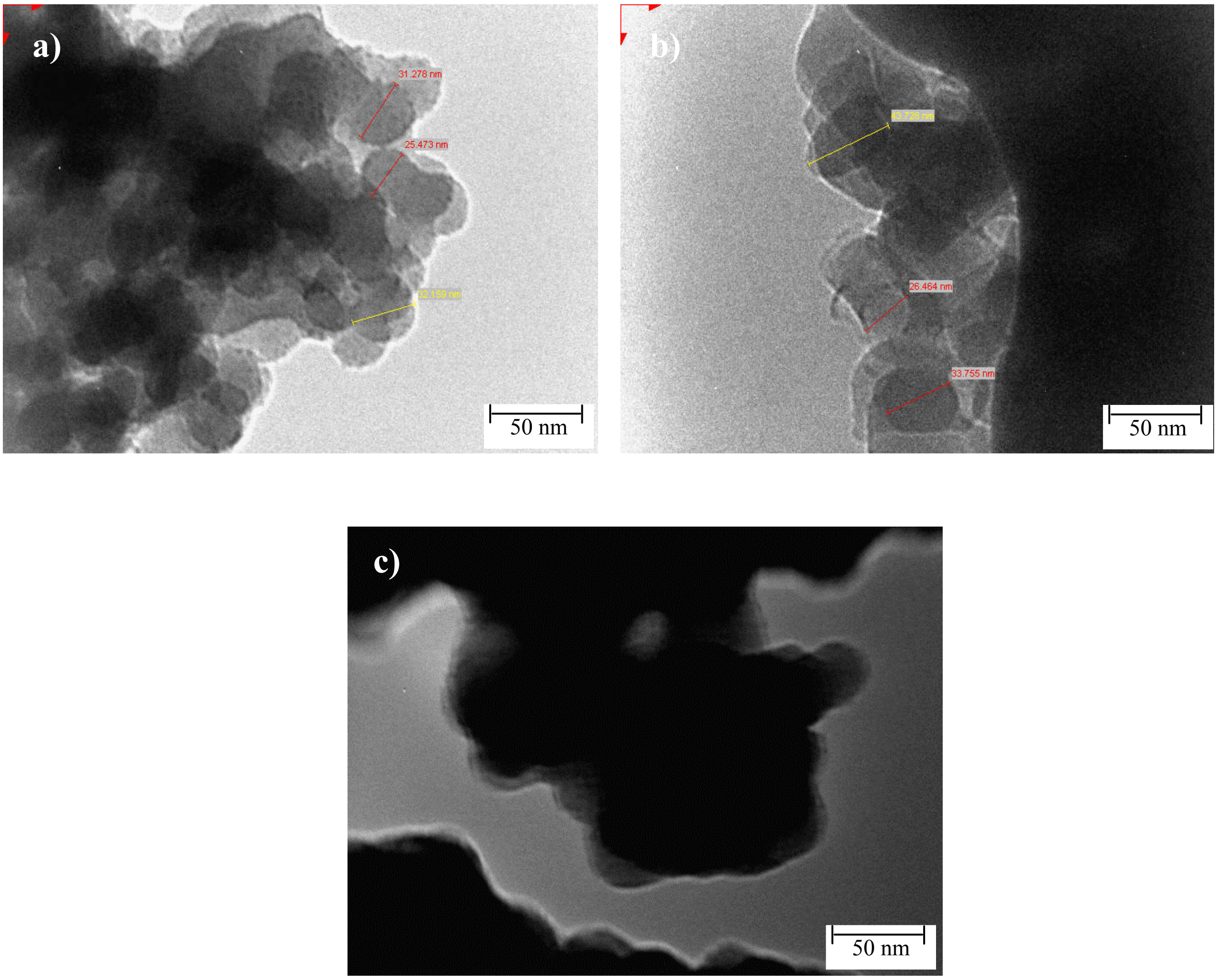

Figure 6.9. TEM micrograph (scale = 50 nm) of the spent catalyst after the EtOH co-feed (a), water co-feed (b) and combined EtOH and water co-feed (c)

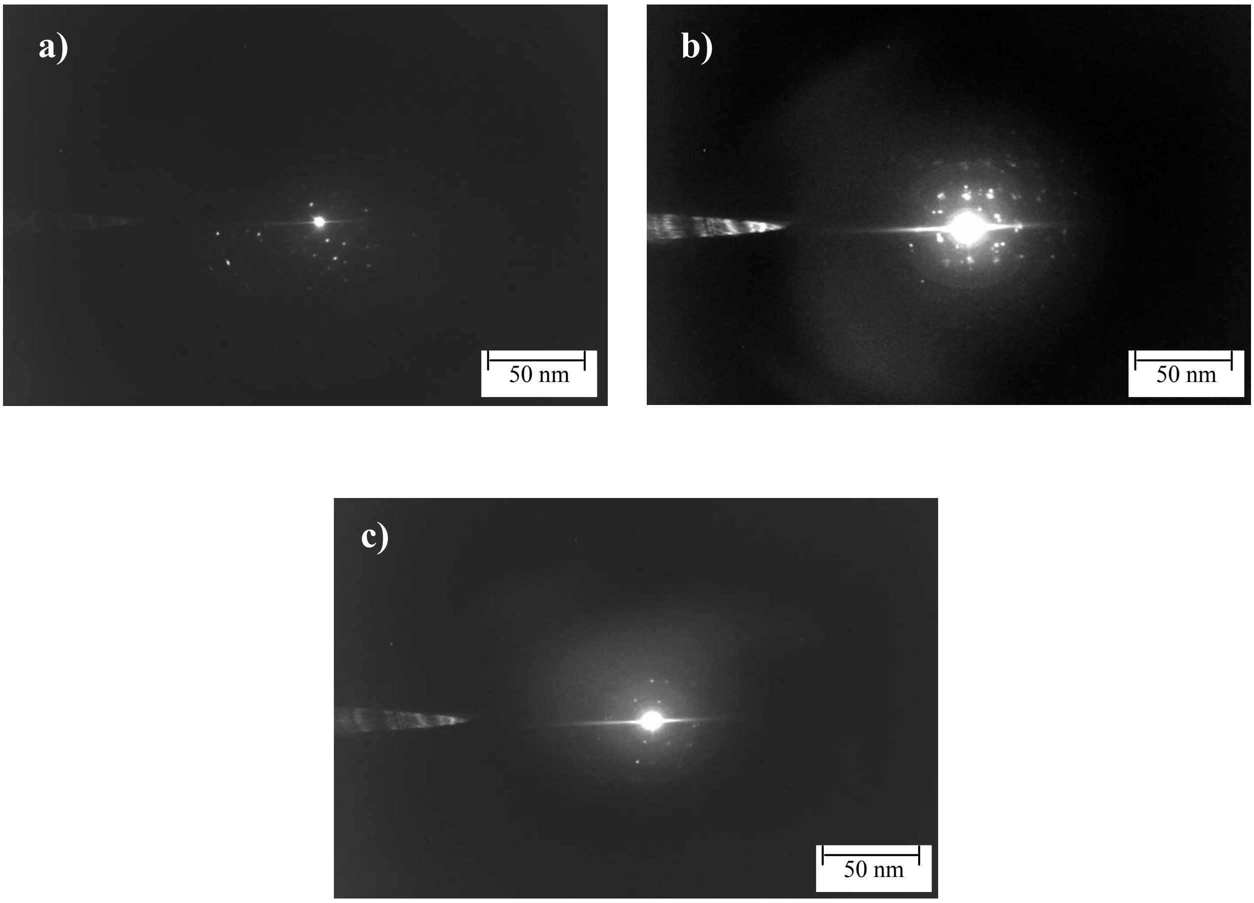

Figure 6.10. SADP (scale = 50 nm) of the spent catalyst after the EtOH co-feed (a), water co-feed (b) and combined EtOH and water co-feed (c)

6.7 Raman spectroscopy

The results shown in Figure 6.4 and Table 6.1 for the spent catalysts showed the existence of the α-phase as well as the reduced phase, $Fe_2P_2O_7$, as the major phases. Based on this observation, it was decided to compare the Raman spectrum obtained for a single spent catalyst (Fig. 6.11), which was representative of the reaction including the EtOH co-feed, to the Raman spectrum of the reoxidized catalyst (Chapter 4, Fig. 4.54) consisting of the α-phase as the major phase with the occurrence of the reduced $Fe_2P_2O_7$.

The bands as mentioned previously for the reoxidized catalyst (Chapter 4, Fig. 4.54) were a low intensity band at ~410 cm^{-1}, a high intensity band at ~480 cm^{-1} and three medium intensity bands thereafter at ~804 cm^{-1}, ~1033 cm^{-1} and ~1307 cm^{-1}, respectively. It was concluded that the bands at ~804 cm^{-1} and ~1033 cm^{-1} could be due to $Fe_2P_2O_7$ and the remaining bands at ~410 cm^{-1}, ~480 cm^{-1} and ~1307 cm^{-1} due to the α-phase. The spent catalyst showed a high intensity band at ~493 cm^{-1}, two medium intensity bands at ~812 cm^{-1} and ~1041 cm^{-1} and a weak band at ~1603 cm^{-1}. It seems that the high intensity band at ~493 cm^{-1} and the medium intensity band at 1041 cm^{-1} are characteristic of the α-phase, which is consistent with the results of the reoxidized catalyst. The medium intensity band at ~812 cm^{-1} is due to $Fe_2P_2O_7$ and the weak band at ~1603 cm^{-1} is possibly due to the presence of coke or adsorbed organic products which was reported previously for the IR spectrum of the spent catalyst excluding the water co-feed and including the EtOH (Fig. 6.5).

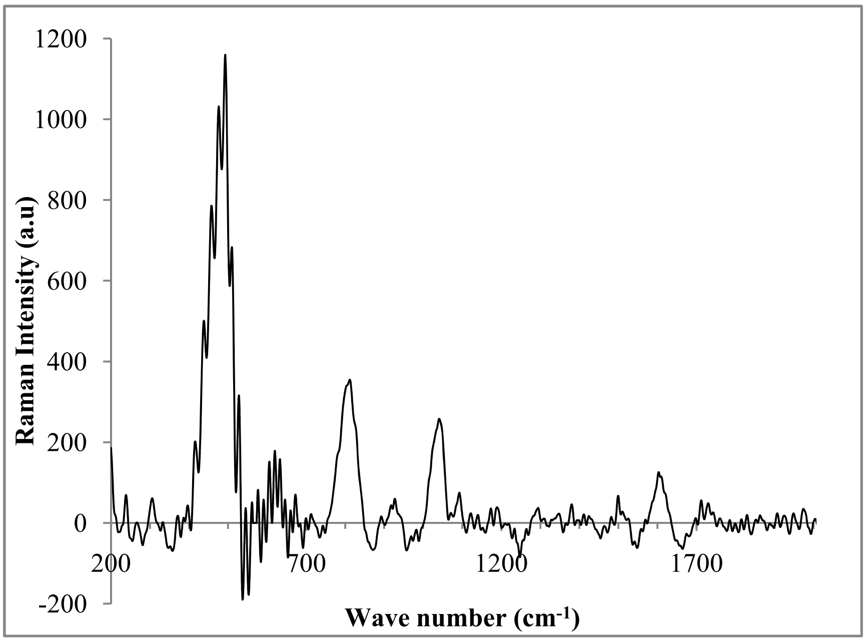

Figure 6.11. Raman spectrum of the spent catalyst (EIB and EtOH co-feed, excluding water)

6.8 Summary

Characterization of the spent catalyst had provided an understanding of changes of the catalyst when subjected to varying reactor conditions within the reactor bed. Several properties were considered which included the change in surface area, surface morphology and phases during the testing process.

The surface area and pore volume measurements of the spent catalysts were compared to the original fresh catalyst. Conditions which were considered included the use of the water co-feed. It was found that for the reactions including the water co-feed, the surface area and pore volume measurements were comparable to those of the fresh catalyst and the reactions excluding the water co-feed showed a slight decrease in both of these properties. The former results could be due to the effect of water in favouring the desorption of products and suppressing the formation of carbon deposits on the surface, hence surface area and pore volume were minimally affected. The decrease in surface area of the spent catalyst when no water was present with the feed was considered to be due the presence of coke on the surface of the catalyst. The results for the spent catalyst after the use of combined co-feeds which included EtOH and water were also considered and they showed that relative to the reaction excluding the water co-feed, these results showed slightly higher surface areas and pore volumes which were correlated with the beneficial effects of water.

The correlation between the XRD, Mössbauer results and IR spectra showed the variation in phase formation under catalytic conditions and the dependence of it on the use of water as a co-feed. Initially, the diffractogram of the spent catalyst which excluded any co-feeds was investigated. It was found that the dominant phase present was the active α-phase and based on this it was decided to observe the phase variation with change in co-feeds. Three reaction conditions were considered, namely, reactions including EtOH as a co-feed (excluding water), reactions including water as a co-feed and reactions including a combined EtOH and water co-feed. XRD results showed that under all three reaction conditions, the α-phase and $Fe_2P_2O_7$ dominated in the diffractograms and a similar trend was observed in the case of the IR spectra.

Mössbauer results provided a more in-depth understanding of phase allocation relative to the reaction conditions. The results showed that both the α-phase and $Fe_2P_2O_7$ were present in all three catalysts and this was very beneficial seeing that these two phases favour the ODH process. The reactions excluding the water co-feed (including the EtOH co-feed), showed the formation of the unwanted β-phase. However, it was found that for the reactions including a water co-feed only, this phase was not observed and, in addition, for the reactions including the water and EtOH co-feed, this unwanted β-phase was not observed. It was postulated that water plays a role in reducing the formation of the β-phase. The addition of water was also shown to enhance the formation of the α-phase, seeing that the site fraction allocated to the α-phase increased with the addition of the water co-feed.

The Raman spectrum of the spent catalyst including the EtOH co-feed was compared to a representative spectrum consisting of the α-phase as well as $Fe_2P_2O_7$. The bands attributed to both the α-phase and $Fe_2P_2O_7$ were observed, however, the occurrence of a minor peak in the region ~1603 cm^{-1} was also noted. This band was considered to be the result of coke formation or adsorbed organic product on the surface of the spent catalyst. The presence of coke or adsorbed organic products was also verified by the reduction in the surface area and pore volume of catalysts after these types of reactions and a similar band in the IR spectrum at approximately 1590 cm^{-1} was observed.

In terms of SEM analysis, the surface morphology of the spent catalysts under the varying reaction conditions showed an uneven distribution of iron phosphate on the surface of the catalyst which was similar to that of the reduced catalyst A, mentioned in Chapter 4. TEM analysis proved quite difficult for the spent catalysts. Particle size of the silica support was consistent for both the spent, as well as the fresh catalyst; however, in terms of the iron phosphate particles, isolation of individual particles was difficult. The SADP pattern did indicate that the spent catalysts consisted of crystalline regions with no evidence of amorphous regions.

References

[1] J.-M.M. Millet, Catal. Rev. Sci. Eng. 40 (1998) 1-38.

[2] M. Ai, E. Muneyama, A. Kunishige, K. Ohdan, J. Catal. 144 (1993) 632-635.

[3] E. Muneyama, A. Kunishige, K. Ohdan, M. Ai, J. Catal. 158 (1996) 378-384.

[4] E. Muneyama, A. Kunishige, K. Ohdan, M. Ai, J. Mol. Catal. 89 (1994) 371-381.

[5] E. Muneyama, A. Kunishige, K. Ohdan, M. Ai, Catal. Lett. 31 (1995) 209-220.

[6] J.-M.M. Millet, M. Forissier, D. Rouzies, P. Bonnet, J.C. Vedrine, Stud. Surf. Sci. Catal., 101(1996) 1011-1020.

[7] E. Muneyama, A. Kunishige, K. Ohdan, M. Ai, Bull. Chem. Soc. Jpn. 69 (1996) 509.

[8] W.M. Reiff, C.C. Torardi, Hyperfine Interact. 53 (1990) 403-407.

[9] P. Bonnet, J.M.M. Millet, C. Leclercq, J.C. Védrine, J. Catal. 158 (1996) 128-141.

[10] M. Ai, K. Ohdan, Appl. Catal., A. 180 (1999) 47-52.

[11] J. Millet, C. Virely, M. Forissier, P. Bussière, J. Vedrine, Hyperfine Interact. 46 (1989) 619-621.

[12] R. A. Nyquist, R.O. Kagel, Infrared spectra of Inorganic Compounds Academic press, New York and London, 1971.

[13] J.L.G. Fierro, Spectroscopic Characterisation of Heterogenous Catalysts: Chemisorption of Probe Molecules, Studies in Surface Science and Catalysis, 57 Part B, Elsevier Science Publishers, New York, 133.

[14] J.J. Spivey, Catalysis, Royal Society of Chemistry, 2004.

CHAPTER 7

INVESTIGATION OF CESIUM PROMOTED IRON PHOSPHATE CATALYSTS

The use of promoters for $FePO_4$ catalysts has been studied for ODH reactions involving the conversion of IBA to MAA [1]. In this reported study, the use of lead (Pb) showed the best promotional effect with optimal P/Pb/Fe molar ratios within the range of 1.2-1.3/0.15/1 and 1.3-1.4/0.3/1. It was found that the Pb^{2+} ion exists in the form of $Pb_2P_2O_7$ and plays a role in suppressing the consecutive oxidation of MAA to COx.

Although it was concluded that lead showed the most promising results, it was also reported that ODH catalysts containing alkaline elements, such as K, Rb and Cs, showed enhanced selectivities and activities [2, 3]. The effect of cesium was further studied and it was observed that the presence of cesium ions during the preparation of the $FePO_4$ catalyst favoured the formation of the tridymite-like $FePO_4$ phase over the stable quartz type $FePO_4$ structure, provided that an excess of phosphorous was used during the synthetic procedure [4]. It was reported that preparation of the tridymite-like $FePO_4$ phase was possible in an almost pure state (95 %) by using a P/Fe ratio up to an optimum of 1.32 [4]

It was also found that cesium exists in the form of $CsFeP_2O_7$ which showed poor catalytic selectivity independently in the ODH of IBA to MAA, however, mixtures of $CsFeP_2O_7$ and $Fe_2P_2O_7$ did exhibit a synergistic effect at low $CsFeP_2O_7$ content [4].

Based on these findings it was decided to synthesize a promoted $FePO_4$ catalyst for the ODH of EIB to EMA with the following ratios, P/Cs/Fe ~ 1.2-1.3/0.05-0.30/1, in increments of 0.05 for the cesium ions.

7.1 Characterization of the cesium promoted $FePO_4$ catalysts

7.1.1 Room temperature X-ray Diffraction (XRD)

The effect of cesium as a suitable promoter to enhance structure stability with respect to the tridymite-like $FePO_4$ phase was firmly established in Chapter 2, Section 2.6. Several cesium promoted $FePO_4$ catalysts were synthesized with varying Cs ratios within the range of 0.05-0.30 as outlined in the procedure found in Chapter 3, Section 3.2.

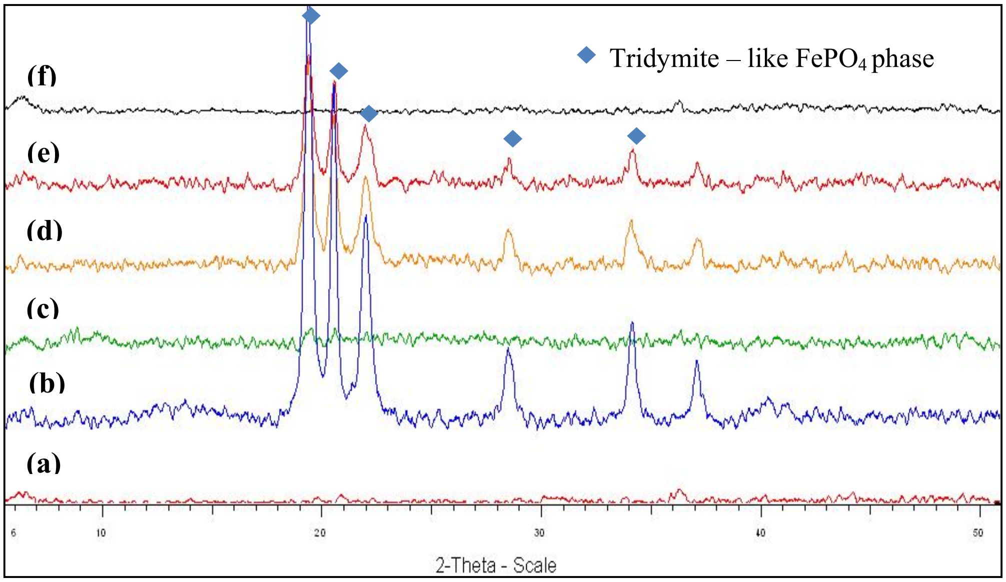

Figure 7.1 XRD of the $FePO_4$ catalysts promoted with varying Cs ratios of 0.05 (a), 0.10 (b), 0.15 (c), 0.20 (d), 0.25 (e) and 0.30 (f)

Figure 7.1 shows the diffractograms of the iron phosphate catalysts promoted with Cs at the varying loadings. The XRD data showed that the major peaks attributed to the tridymite-like $FePO_4$ phase ($2\theta = 19.8$ °, 20.8 °, 22.4 °, 28.9° and 35.2 °) were clearly present for the cesium promoted $FePO_4$ catalysts having a P/Fe ratio of ~ 1.26 and Cs/Fe ratios of 0.10. 0.20 and 0.25 respectively. However, minor reflections at $2\theta = 37.3$ ° and 41.0 ° were also found. It was thought that these peaks were possibly due to the formation of the quartz type $FePO_4$ phase, although the major reflection for the quartz type $FePO_4$ phase at $2\theta = 25.8$ ° was not observed and, in addition, the peaks at $2\theta = 19.8$ ° and 20.8 ° for the tridymite-like $FePO_4$ phase would overlap with the peak at $2\theta = 20.4$ ° for the quartz type $FePO_4$ phase.

The results obtained from the XRD data outlined the parameters for the scope of work with respect to both the characterization as well as the catalytic testing.

7.1.2 Inductively Coupled Plasma-Optical Emission Spectroscopy (ICP-OES) and Brunauer-Emmett-Teller (BET) surface area and pore volume

The results obtained from ICP analysis showed that the P/Fe ratio is slightly higher than the unpromoted $FePO_4$ catalyst which was mentioned in Chapter 4, Section 4.1 as being within the range of 1.14-1.15 and the cesium content is consistent with the experimental ratios considered. A slightly higher P/Fe ratio was considered during the synthesis due to the presence of cesium. It was observed that the tridymite-like $FePO_4$ phase can be stabilised with a high content of phosphorous, such that under catalytic conditions only the active α-phase and the $CsFeP_2O_7$ phase result [3]. The cesium promoted $FePO_4$ catalysts showed higher surface areas in comparison to the unpromoted $FePO_4$ catalyst (Chapter 4, Table 4.2). This could be attributed to the effect of the cesium existing on the surface of the catalyst and thus enhancing the surface area as opposed to blockage of the pores. As the cesium loading increased, the surface area increased until the Cs/Fe ratio of 0.20. A further increase in cesium loading showed a decrease in the surface area. This could be the result of the formation of cesium layers on the iron phosphate catalyst, which is further supported by the decrease in the pore volume relative to the cesium promoted $FePO_4$ catalyst with the Cs/Fe ratio of 0.20

Table 7.1. ICP-OES and BET surface area analysis of the cesium promoted $FePO_4$ catalysts

Catalyst	**P/Fe**	**Cs/Fe**	**Surface area (m^2/g)**	**Pore volume (cc/g)**
Cs-0.10	1.27	0.09	15.3	0.063
Cs-0.20	1.26	0.19	17.2	0.071
Cs-0.25	1.26	0.28	16.1	0.066

7.1.3 Infrared Spectroscopy (IR)

The reflections observed on the diffractograms from XRD showed the occurrence of the tridymite-like $FePO_4$ phase as the major phase. Based on these results, it would be reasonable to anticipate the occurrence of the PO_4^{3-} (orthophosphate) group as the major peak in the infrared spectra. Figure 7.2 shows the results obtained from the IR analyses of the calcined cesium promoted $FePO_4$ catalysts. An intense peak was found within the region of ~ 1000 cm^{-1} and a medium intensity peak with a shoulder was observed between 550-660 cm^{-1}. The common frequencies for the PO_4^{3-} ion are generally characterized by a strong peak between 940-1120 cm^{-1} and medium intensity peaks, often occurring as doublets, between 540-650 cm^{-1} [5].

The intensity of the band characteristic of the orthophosphate ion (~ 1000 cm^{-1} and between 550-660 cm^{-1}) showed a slight increase in intensity with an increase in cesium loading. It was also found in literature that, during the characterisation of cesium loaded iron phosphate glasses, the infrared spectra showed an increase in intensity of the band within the region of 1050 cm^{-1} with an increase in cesium content, which was attributed to the asymmetrical stretching mode of the orthophosphate ion [6].

A comparison of the promoted catalysts before and after calcination showed a substantial change in three peaks, namely the peaks at ~ 3000 cm^{-1}, ~ 1600 cm^{-1} and ~ 1300 cm^{-1}, all of which are peaks characteristic of water [7, 8]. Reduction in the intensity of these peaks would be expected in line with the effect of calcination. The infrared spectra obtained for the uncalcined promoted $FePO_4$ catalysts are found in Appendix D, Figure D.1.

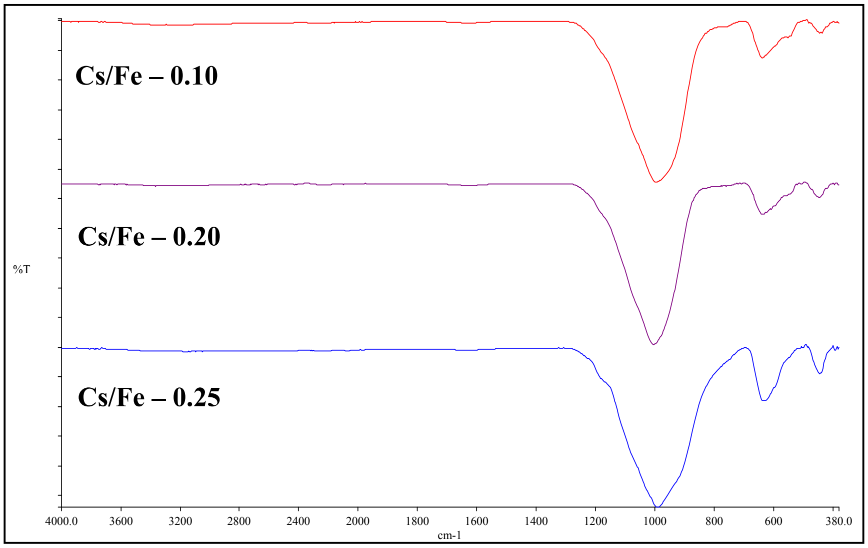

Figure 7.2 Infrared spectra of the cesium promoted $FePO_4$ catalysts

7.1.4 Scanning Electron Microscopy (SEM)

SEM images showing the surface morphology of the calcined cesium promoted $FePO_4$ catalysts are found in Figure 7.3. The appearance of the catalyst is similar to the unpromoted $FePO_4$ catalyst where bead-like structures were observed, showing an even distribution of $FePO_4$ on the surface of the silica support. It was, however, noted that there was a significant change in the structure of the particles as the cesium loading increased. This could be attributed to the effect of the increasing cesium loading which is considered to form layers on the surface of the $FePO_4$. This was also shown by EDX mapping of the SEM images of the various promoted catalysts, which showed regions of high cesium content with increase in cesium loading (Appendix D, Fig. D.2-D.4). Further evidence to support this is based on the decrease in the surface area of the promoted $FePO_4$ catalyst with the Cs/Fe ratio of 0.25. The ratios of P/Fe and Cs/Fe obtained from the EDX analysis was slightly lower than the values obtained from ICP analysis reported in Table 7.1. This could be explained by the parameters of the analysis where EDX is localised to the area being analysed, while ICP determines the ratio in the bulk.

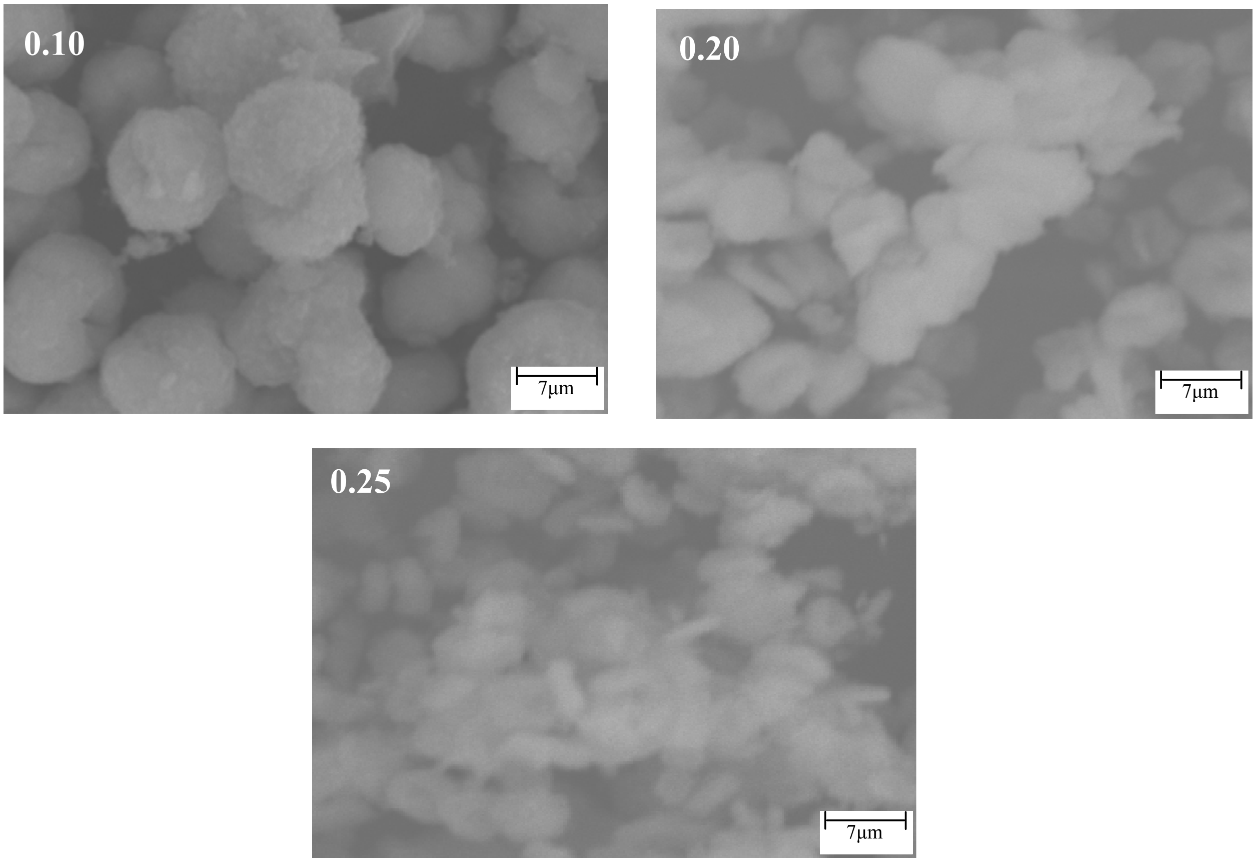

Figure 7.3 SEM micrographs (scale = 7 µm) of the cesium promoted $FePO_4$ catalysts with varying Cs/Fe ratios

Table 7.2. SEM-EDX analysis of cesium promoted $FePO_4$ catalysts

Catalyst	P/Fe	Cs/Fe
Cs-0.10	1.25	0.07
Cs-0.20	1.24	0.18
Cs-0.25	1.25	0.23

7.1.5 Temperature programmed reduction (TPR)

The TPR profiles (Fig. 7.4) of the cesium promoted $FePO_4$ catalysts showed that the reducibility of the catalysts increased with an increase in the cesium loading. At lower cesium loadings reduction occurs via three reducing steps, however, with an increase in cesium loading it was found that reduction occurs via two steps including a shoulder at around 750 °C. This could be attributed to the property of cesium which inhibits the reduction of $FePO_4$ with an increase in cesium loading.

It was found that the presence of even the lowest cesium loading resulted in a significant shift of the reduction band at higher temperatures, with minimal effect on the low and medium bands for a cesium promoted copper catalyst [9]. In addition, increasing cesium loading resulted in a decrease in the intensity of the bands, as well as coalescence of medium and high temperature bands [9]. A similar trend is observed in the case of this synthesized catalyst.

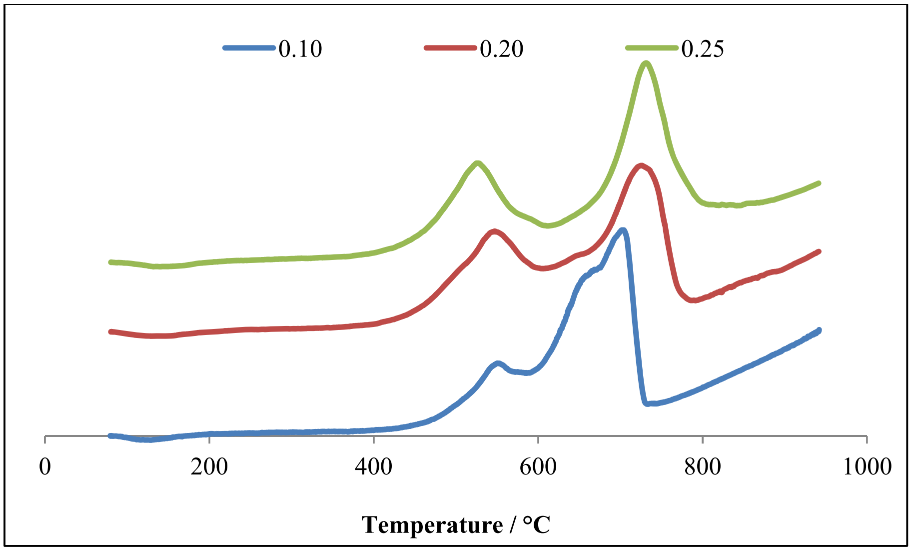

Figure 7.4 TPR profile of the cesium promoted $FePO_4$ catalysts

Variable temperature TPR was carried out for the samples, and after each of the reducing steps the samples were removed and XRD was conducted (Fig. 7.5). It is important to note that due to the quantity of sample removed, interference by an operating parameter resulted in the formation of additional peaks which have been included in Appendix D, Figure D.5. Based on this, isolation of exact phases which formed during the reduction was difficult. However, the 2θ data for the catalyst with the lowest cesium loading supports the formation of the $Fe_2P_2O_7$ phase as well as the intermediate phase, $Fe_3(P_2O_7)_2$. The diffractograms of the catalysts with the higher cesium loadings (Appendix D, Fig. D.6-D.7) showed that the final reduction step resulted in the formation of $Fe_2P_2O_7$ and the intermediate phase was not seen. It has been mentioned in literature that under catalytic conditions, i.e. ODH of IBA to MAA, catalysts synthesized with a higher P/Fe ratio are reduced to the intermediate phase and not to $Fe_2P_2O_7$ [10]. This suggests that the (constant) P/Fe ratio, although higher than for the unpromoted catalyst, was suitable for the lowest cesium loading, however, with an increase in cesium loading, the P/Fe ratio was insufficient thus explaining the phase distribution.

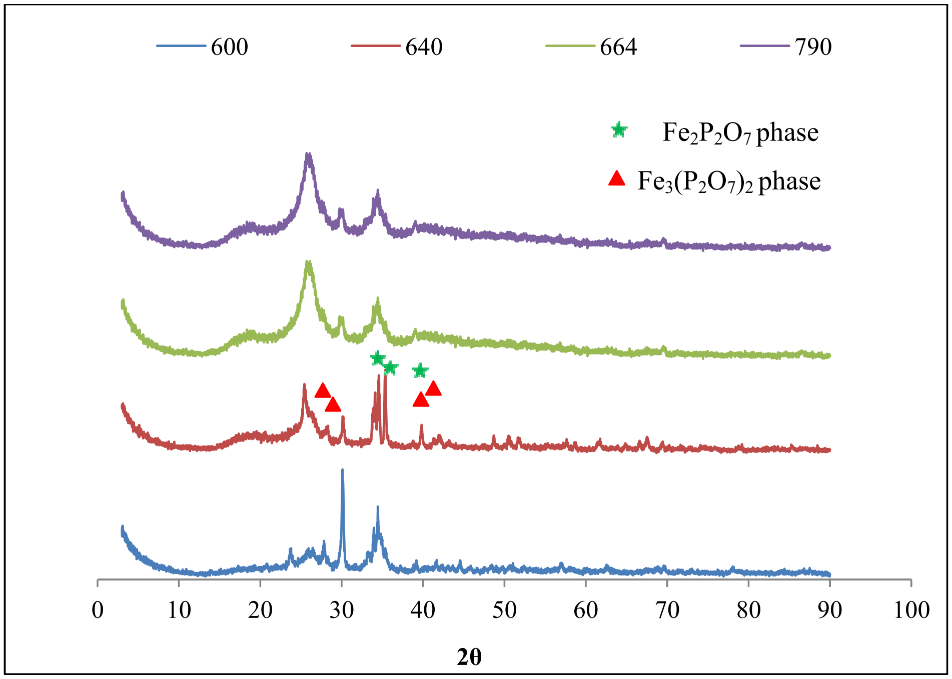

Figure 7.5 XRD of the reduced cesium promoted $FePO_4$ catalyst (Cs/Fe -0.10) catalyst at varying temperatures

7.1.6 Temperature programmed oxidation (TPO)

Figure 7.6 shows the TPO profiles of the cesium promoted $FePO_4$ catalysts. The combined TPR and TPO profiles for all the cesium promoted catalysts are found in Appendix D, Figures D.8-D.10. A similar trend was observed for the reduction process. It was found that the bands shift to higher temperatures with an increase in cesium loading. In the case of the unpromoted $FePO_4$ catalyst the initial reoxidation step was at an onset temperature of 510 °C and the latter at 715 °C, however in the case of the promoted catalysts the onset temperature for the initial reoxidation step was between 660-750 °C and the latter step at ~ 950 °C. The diffractograms obtained for the samples after the reoxidation steps (Fig. 7.7 and

Appendix D, Fig. D.11-D.12) were similar to diffractograms from the TPR/TPO profile of the catalyst consisting of the quartz type $FePO_4$ phase as the precursor. The phase observed at the lower temperature was the active α-phase, while the phase at the higher temperature showed the formation of the quartz type $FePO_4$ phase. These findings suggest the presence of the quartz type $FePO_4$ phase in the freshly calcined catalyst, however, these peaks were of weak intensity in the diffractograms of the calcined precursor.

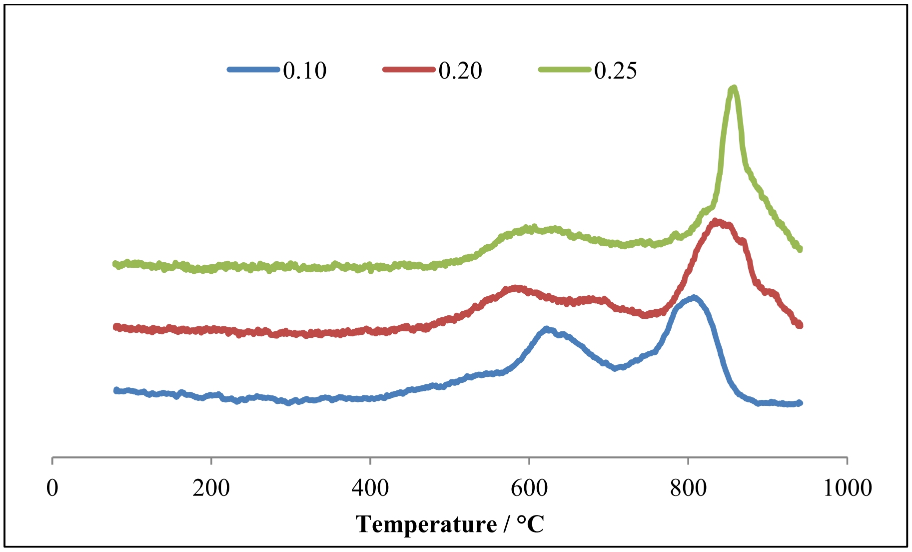

Figure 7.6 TPO profiles of the cesium promoted $FePO_4$ catalysts

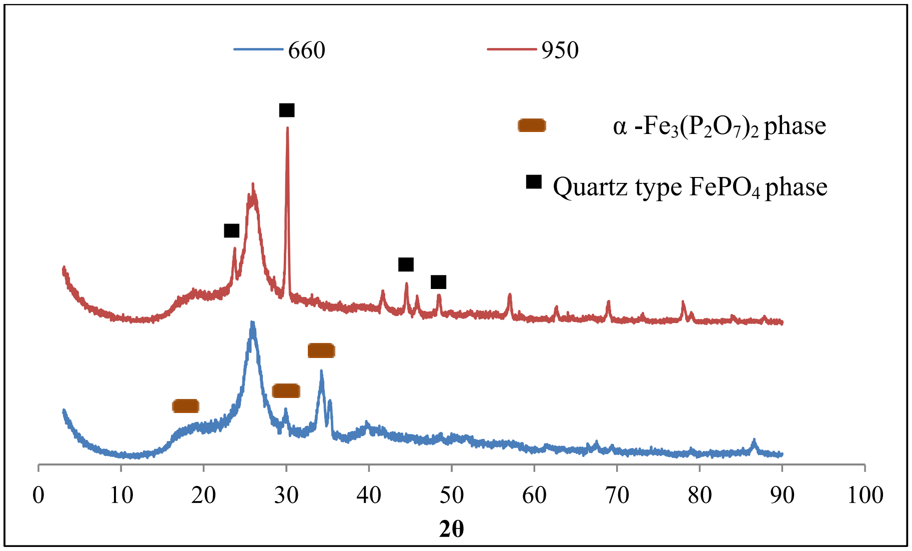

Figure 7.7 XRD of the reoxidised Cs-0.10 catalyst at varying temperatures

7.1.7 Temperature programmed desorption (TPD) and acidic site determination

The TPD profiles of the cesium promoted $FePO_4$ catalysts are shown in Figure 7.8. All promoted catalysts showed a strong desorption peak at a temperature below 350 °C and the area of the peak increases with an increase in cesium loading. The peak observed between the temperatures of 550-650 °C, which is due to the strong acidic nature of the catalyst, is much lower in comparison to the desorption peak at the lower temperature. As the cesium loading increases, the weak acidic sites on the $FePO_4$ catalyst increase and the strong acidic sites on the $FePO_4$ catalyst diminish. Hence, the basic nature of cesium seems to influence the acidic character of the $FePO_4$ catalyst.

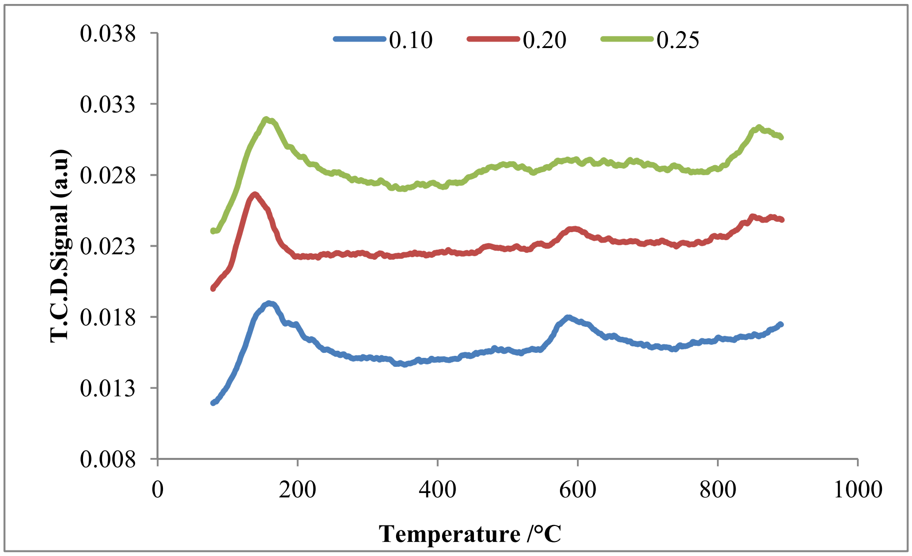

Figure 7.8 TPD profile of the cesium promoted $FePO_4$ catalysts

Table 7.3. Acidic site distribution of the cesium promoted $FePO_4$ catalysts

Catalyst	**Weak acidity (mmol/g)**	**Strong acidity (mmol/g)**	**Total acidiy (mmol/g)**
Cs-0.10	0.438	0.418	0.856
Cs-0.20	0.541	0.204	0.745
Cs-0.25	0.612	0.080	0.692

Table 7.3 shows the acidic site distribution on the surface of the catalysts. Total acidity of the catalysts decreases with an increase in cesium loading.

7.1.8 Transmission Electron Microscopy (TEM) and Selected Area Diffraction Pattern (SADP)

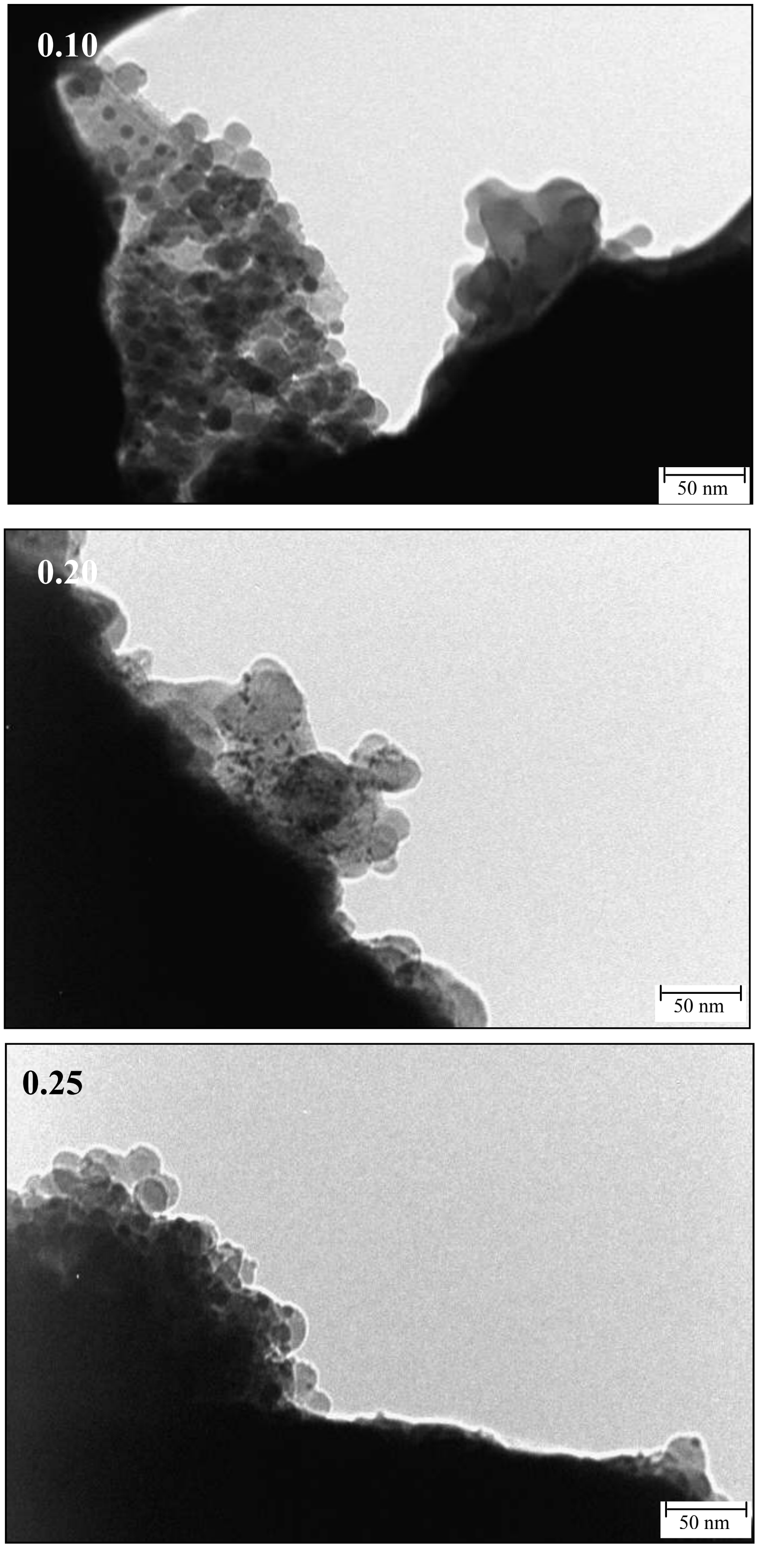

Figure 7.9 TEM micrographs (scale = 50 nm) of the cesium promoted $FePO_4$ catalysts

TEM micrographs of the cesium promoted $FePO_4$ catalysts showed isolation of the $FePO_4$ particles from the silica support (Fig. 7.9). The appearance of the catalyst is also in correlation with the SEM micrographs which showed discrete round particles. The average size of the silica support is still within the region of 35-37 nm, however, there seems to be a correlation in terms of the $FePO_4$ particle size for the lowest and highest cesium loadings, whilst the catalyst with the Cs/Fe ratio of 0.20 showed a decrease in particle size. The SADP images of the promoted catalysts showed evidence of their polycrystalline nature.

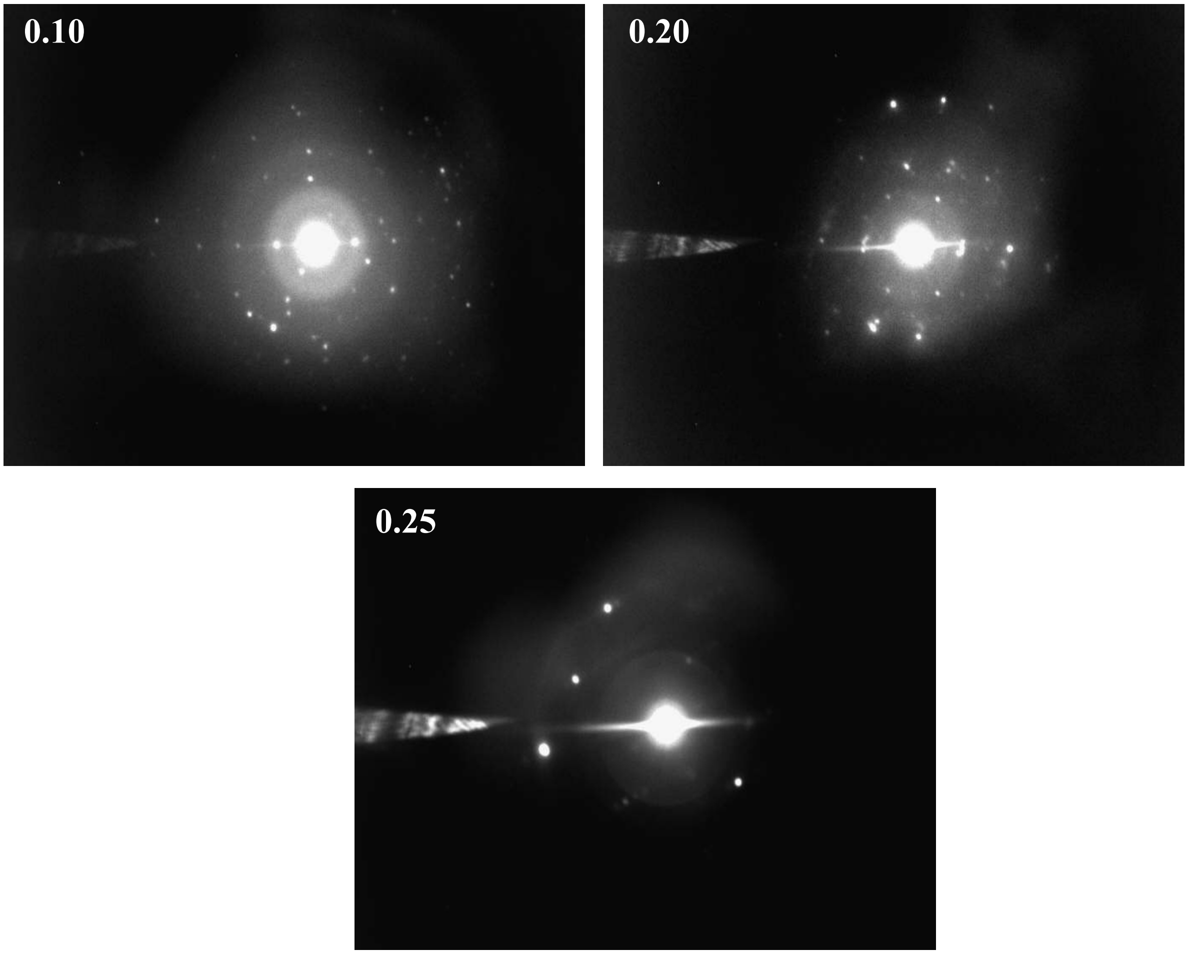

Figure 7.10 SADP of the cesium promoted $FePO_4$ catalysts

7.1.9 Mössbauer spectroscopy

Although the tridymite-like $FePO_4$ phase was the dominant phase based on the results obtained from XRD data, minor peaks were also observed. It was therefore decided to correlate the results from XRD with those obtained from Mössbauer spectroscopy for each of the cesium promoted catalysts.

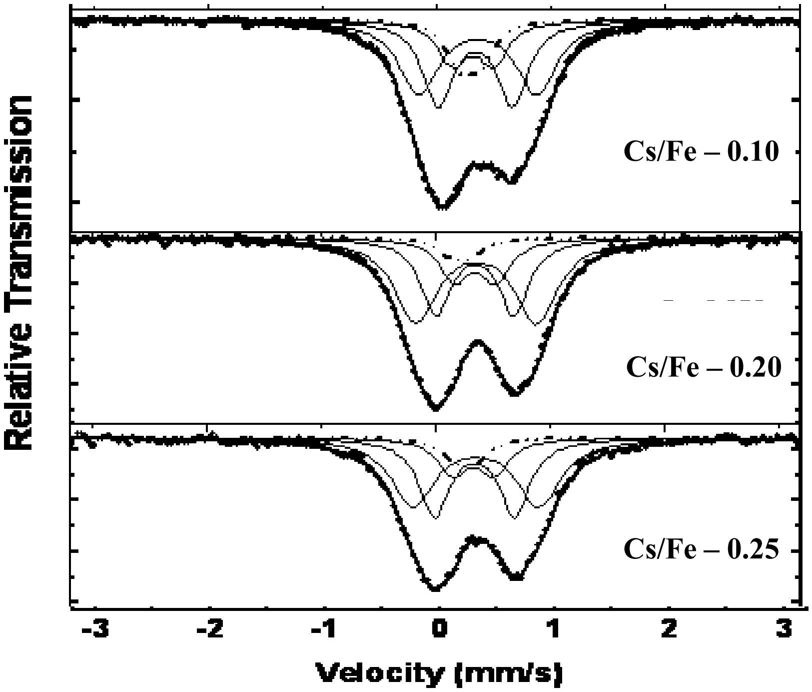

Figure 7.11 Mossbauer spectra of the cesium promoted $FePO_4$ catalysts

The isomer shift (IS/δ) and quadrupolar splitting (QS/Δ) values obtained for the cesium promoted $FePO_4$ catalysts showed the existence of both the tridymite-like $FePO_4$ phase as well as the quartz type $FePO_4$ phase. The IS values of the promoted catalysts with increasing cesium loading were 0.32, 0.35 and 0.34 mm/s and consistent QS values of 0.36 mm/s, respectively, were characteristic of the ferric species of the tridymite-like $FePO_4$ phase. The ferric species corresponding to the quartz type $FePO_4$ phase were identified by the consistent IS values of 0.35 mm/s and QS values of 0.65, 0.68 and 0.70 mm/s respectively. Interestingly, the site fractions for both these phases were very similar for each of the promoted catalysts. This could be related to the fact that although the cesium loading was increasing, there was a marginal variation in the P/Fe ratios as shown by the ICP data in Section 7.1.2. It was, however, noted that the contribution by an unidentified ferric species with IS and QS values within the region of 0.36 mm/s and 1.05 mm/s respectively showed an increase with increase in cesium loading. As mentioned previously, (Chapter 2, Section 2.7.3), in the presence of cesium the tridymite-like $FePO_4$ phase could be stabilised in a 95 % pure form for a P/Fe ratio of 1.32, thus the lower P/Fe ratio did not allow for the structure stability of the tridymite-like $FePO_4$ phase with the increased cesium loadings. Formation of the $CsFeP_2O_7$ phase was also observed, showing the highest concentration for the lowest cesium loading, which was also attributed to the lower P/Fe ratio. The slightly higher P/Fe ratio relative to the unpromoted $FePO_4$ catalyst resulted in the mixture of phases being formed, with the addition of an unidentified phase.

Table 7.4. Mössbauer parameters, isomer shift (IS), electric quadrupole splitting (QS) site fractions (*f*) and phase assignments and the attributed phases, determined from the spectra of cesium promoted iron phosphate catalyst

Sample	**IS (mm/s)**	**QS (mm/s)**	***f***	**Relative Intensity (%)**	**Attributed Phase**
Cs-0.10	0.29(3)	0.18	Fe^{3+}	14(3)	$CsFeP_2O_7$
	0.32(2)	0.36	Fe^{3+}	16(2)	$FePO_4$-tdm
	0.35(2)	0.65(3)	Fe^{3+}	33(2)	$FePO_4$ –quartz
	0.36(2)	1.03(3)	Fe	37(3)	X*
Cs-0.20	0.22(3)	0.18	Fe^{3+}	6(2)	$CsFeP_2O_7$
	0.35(2)	0.36	Fe^{3+}	16(2)	$FePO_4$-tdm
	0.35(2)	0.68(3)	Fe^{3+}	31(2)	$FePO_4$ –quartz
	0.36(2)	1.05(3)	Fe	47(3)	X*
Cs-0.25	0.27(3)	0.18	Fe^{3+}	8(3)	$CsFeP_2O_7$
	0.34(2)	0.36	Fe^{3+}	15(2)	$FePO_4$-tdm
	0.35(2)	0.70(3)	Fe^{3+}	34(2)	$FePO_4$ –quartz
	0.36(2)	1.10(3)	Fe	43(3)	X*

* *unidentified phase*

7.1.10 Raman spectroscopy

Figure 7.12 shows the Raman spectra of the cesium promoted $FePO_4$ catalysts. The intense band in the region of ~ 1000 cm^{-1} is representative of isolated PO_4^{3-} groups, thus correlating with the presence of the both the tridymite-like $FePO_4$ phase as well as the quartz type $FePO_4$ phase determined using Mössbauer spectroscopy. It was observed that an increase in cesium loading resulted in a slight shift of the bands to lower wavenumbers.

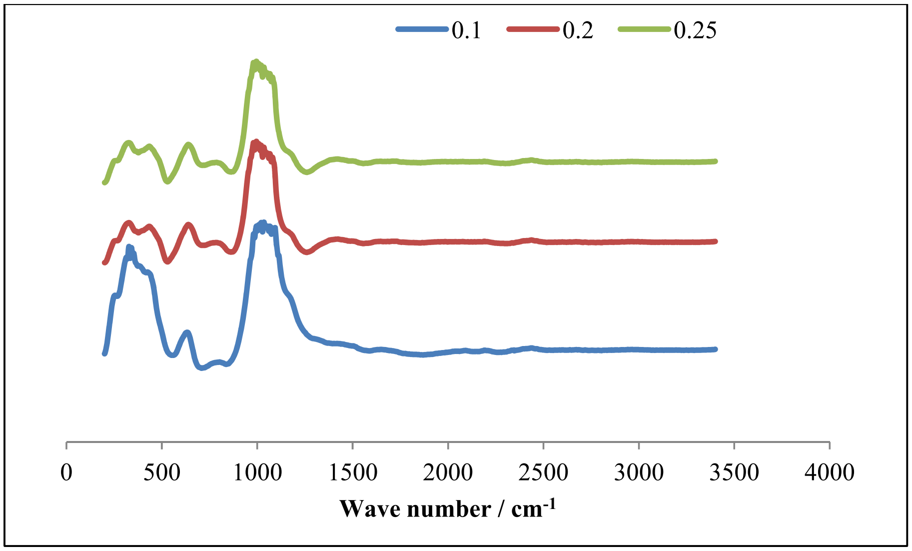

Figure 7.12 Raman spectra of the cesium promoted $FePO_4$ catalysts

7.2 Catalytic testing

7.2.1 Effect of cesium loading on EIB conversion

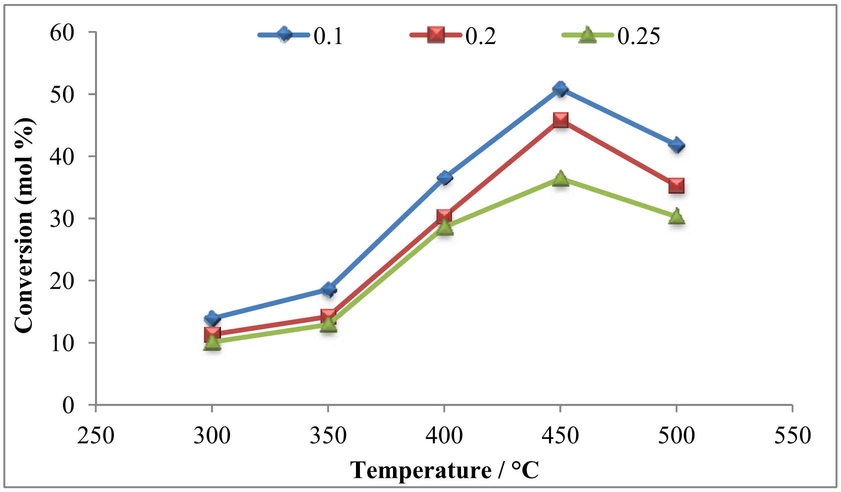

Figure 7.13 Effect of cesium loading on EIB conversion with increase in temperature

Figure 7.13 showed the effect of increasing cesium loading on the conversion of EIB. It was observed that as the cesium loading increased there was a corresponding decrease in the conversion. The temperature programmed experiments showed that the reduction of the promoted $FePO_4$ catalysts shifted to higher temperatures with an increase in cesium loading hence explaining the decrease in conversion with increase in cesium content. However, a decrease in conversion was also observed at higher temperatures (i.e. 500 °C) and it was considered to be the result of coke formation on the surface of the catalysts. In addition, characterization of the acidic properties of the catalysts showed that with an increase in cesium content, there was a significant decrease in total acidity of the promoted catalysts which further influenced EIB conversion (Table 7.3).

7.2.2 Effect of cesium loading on EMA selectivity

The selectivity towards EMA increased with a decrease in the cesium loading, as observed in Figure 7.14. The product profile obtained after catalytic testing for the various cesium loadings is found in Appendix D, Tables D.1-D.3. The results obtained from Mössbauer spectroscopy showed the existence of both the tridymite-like and quartz type $FePO_4$ phases, which was further supported by the corresponding XRD data. However, the presence of the $CsFeP_2O_7$ phase was also noted for all the promoted catalysts, with the highest site fraction observed for the catalyst having the lowest cesium loading i.e. Cs/Fe = 0.10. The existence of the $CsFeP_2O_7$ phase could correlate with the higher selectivity towards the major ODH product, EMA. In addition, the reduction in total acidity negatively affected the conversion and it is likely that this effect is also observed in terms of the EMA selectivity.

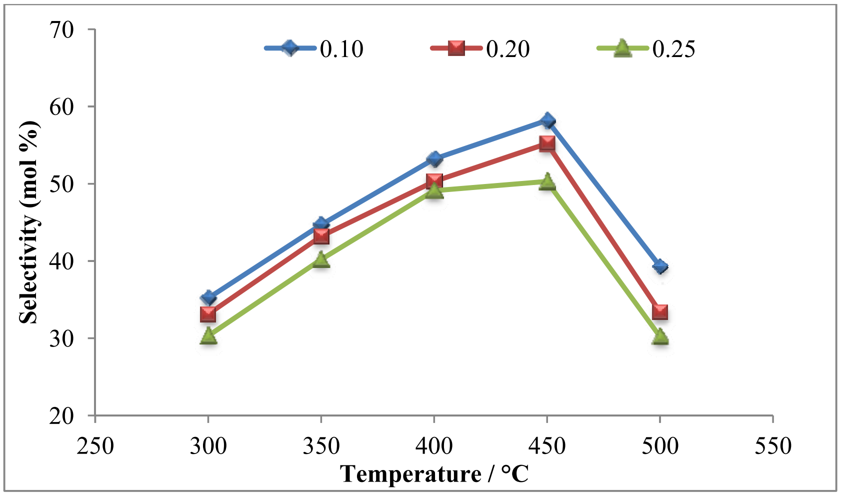

Figure 7.14 Effect of cesium loading on EMA selectivity with increase in temperature

7.2.3 Product profile at iso-conversion

Figure 7.15 shows the product profile at an iso-conversion of 45 % and at the temperature of 450 °C at varying cesium loadings. The highest selectivity towards EMA was observed for the lowest cesium loading. This can be attributed to the highest presence of $CsFeP_2O_7$ [Table 7.4], which has been known to exhibit a small synergy effect in the presence of the $Fe_2P_2O_7$ phase and the active α-phase, which favours ODH reactions [4].

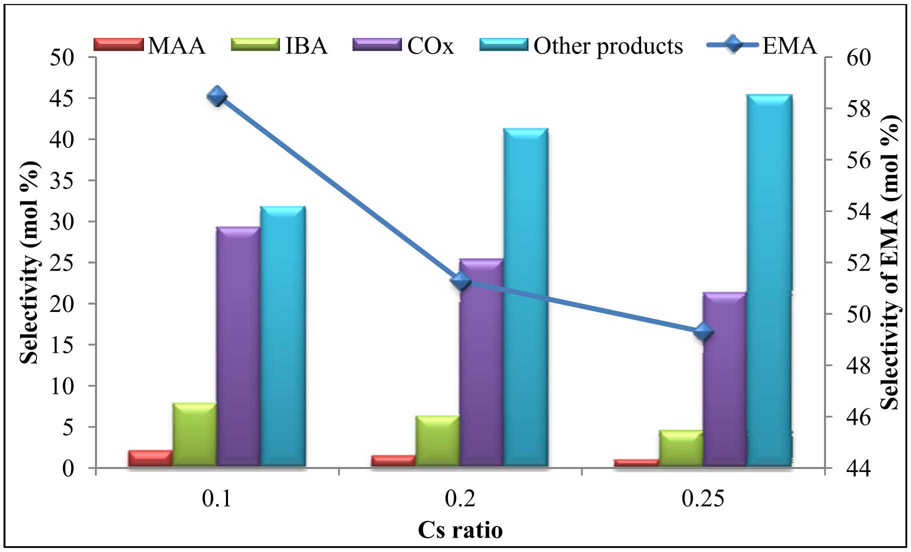

Figure 7.15 Effect of cesium loading on the product profile at iso-conversion of 45 %, Temperature = 450 °C

It was considered that the formation of the $CsFeP_2O_7$ phase was hindered at higher loading seeing that a higher phosphorous content was necessary to favour formation of the $CsFeP_2O_7$ phase [4]. Thus, although a higher content of cesium was included during the synthetic procedure, the constant P/Fe ratio did not favour formation of the $CsFeP_2O_7$ phase and the results obtained from Mössbauer spectroscopy showed the formation of a large quantity of an unidentified phase (also observed in the unpromoted catalyst - Chapter 4, Table 4.8), which generally forms in the presence of the quartz type $FePO_4$ phase, in increasing content with increasing cesium loading.

The increase in the EMA selectivity at the lower cesium loadings could also be attributed to the greater total acidity of the promoted $FePO_4$ catalyst which enhances the ODH of EIB to EMA.

At the higher cesium loading i.e. 0.20 and 0.25, it was observed that there was a decrease in EMA selectivity as well as COx selectivity and an increase in selectivity towards other products such as propene and acetone.

7.3 Summary

Cesium promoted $FePO_4$ catalysts have been shown to favour stabilization of the tridymite-like structure of the iron phosphate catalyst with a P/Fe ratio of 1.32. Based on this evidence from literature it was decided to synthesize a cesium promoted $FePO_4$ catalyst within the following limits, P/Fe/Cs ~ 1.2-1.3/1/0.05-0.30, in increments of 0.05 for the cesium ions. The aim was to maintain a close P/Fe ratio for comparative purposes in terms of the unpromoted catalyst while allowing for phase stability with respect to the precursor and hence minimal unwanted phase transformation during the catalytic process.

The XRD results for the various cesium promoted catalysts showed that the catalysts consisting of the P/Fe ratio of ~ 1.26 and Cs/Fe ratios of 0.10. 0.20 and 0.25 consisted of the tridymite-like $FePO_4$ phase with evidence of additional peaks attributed to the quartz type $FePO_4$ phase, although not conclusive due to peak overlap of the most intense peak for the quartz type phase. Infrared and Raman spectroscopy confirmed the existence of the orthophosphate ion for the promoted catalysts. The Mössbauer results provided more depth in terms of phase assignment. It was found that all three promoted catalysts consisted of almost equivalent amounts of both the tridymite-like $FePO_4$ phase as well as the quartz type $FePO_4$ phase, with a higher relative intensity towards the quartz type phase. The presence of the $CsFeP_2O_7$ phase was also observed with the highest relative intensity for the promoted catalyst with the Cs/Fe ratio of 0.10. It has been reported in literature that $CsFeP_2O_7$ exhibits a small synergy effect in the presence of the $Fe_2P_2O_7$ phase and the active α-phase, which favours ODH reactions. An unidentified phase with IS and QS values within the region of 0.36 mm/s and 1.05 mm/s respectively showed an increase in relative intensity with increase in cesium loading. This phase was also observed previously, (Chapter 4, Table 4.8), and was found to form in the presence of the quartz type $FePO_4$ phase.

The ICP analysis showed that the promoted catalysts were synthesized within the limits defined during the experimental procedure. A slightly higher P/Fe ratio of ~ 1.26 was observed and the Cs/Fe ratios were 0.09, 0.19 and 0.28 respectively. The increase in surface area with increase in cesium loading up to the Cs/Fe ratio of 0.20, was due to the presence of cesium on the surface of the catalyst and thus enhancing the surface area as opposed to cesium blocking the pores and decreasing surface area. However, the higher Cs/Fe ratio of 0.25 showed a decrease in surface area and pore volume and this was considered to be the results of the formation of cesium layers on the surface of the catalyst. The effect of cesium loading was further outlined by the SEM images obtained and the cesium distribution was depicted by the EDX mapping of the SEM images.

The temperature programmed techniques showed that during the reduction process, the reducibility of the catalyst increased with an increase in cesium loading. The effect of increasing cesium loading resulted in a shift of the reduction band to higher temperatures thus indicating that cesium inhibits the reduction of $FePO_4$ and in addition there was a coalescence of medium and high temperature bands. The diffractograms of the catalysts after variable temperature TPR showed that in the case of the lowest cesium loading the $Fe_2P_2O_7$ phase as well as the intermediate phase, $Fe_3(P_2O_7)_2$ was observed, however, with an increase in cesium loading it was found that after the final reduction step the $Fe_2P_2O_7$ phase was observed and the intermediate phase was not seen. This was considered to be the effect of varying Cs/Fe ratios and consistent P/Fe ratios. The shift of bands to higher temperatures was also observed for the temperature programmed oxidation process. It was found that the phases formed during the reoxidation process was similar to the catalyst synthesized previously which consisted of the quartz type $FePO_4$ phase as the precursor. At the lower temperature the active α-phase was observed and at higher temperatures saw the formation of the quartz type $FePO_4$ phase. The desorption profiles for the promoted catalysts showed that the basic nature of cesium influenced the acidic character of the $FePO_4$ catalyst where a reduction of the strong acidic peak between the temperatures of 550-650 °C was observed.

The catalytic testing was carried out at optimal reaction conditions observed for the unpromoted catalyst. The reaction conditions included an EIB:EtOH ratio of 1:5 to enhance EMA selectivity. The EIB conversion was monitored over a temperature range of 300-500 °C. It was found that there was an increase in EIB conversion as well as EMA selectivity with a decrease in cesium loading. The product profile at an iso-conversion of 45 % and at the temperature of 450 °C for the varying cesium loadings showed that the highest selectivity towards EMA was observed for the lowest cesium loading. The existence of a larger quantity of the $CsFeP_2O_7$ phase for the lower cesium loading which exhibits a small synergy effect in the presence of the $Fe_2P_2O_7$ phase and the active α-phase, thus favouring ODH reactions and a smaller relative intensity of the unwanted phase could correlate with the higher selectivity towards the major ODH product, EMA seeing that the site fractions for the tridymite-like $FePO_4$ phase and the quartz type $FePO_4$ phase were relatively consistent for all the catalysts thus having minimal influence on the results for the varying cesium ratios.

The results obtained for the unpromoted catalyst showed a higher selectivity towards the target product EMA relative to the promoted catalyst with the lowest cesium loading (Cs/Fe ratio = 0.10). The reduced selectivity towards EMA was considered to be the result of the reducibility of the promoted catalyst since it was observed that cesium inhibits the reduction of $FePO_4$ and also reoxidation occurs at higher temperatures. In addition, phase stability was not enhanced during the synthesis and thus the mixture of phases formed negatively influenced the reaction. The influence of cesium on the acidic character of the $FePO_4$ catalyst could also contribute to the reduced selectivity towards the target product.

References

[1] M. Ai, E. Muneyama, A. Kunishige, K. Ohdan, Appl. Catal., A. 109 (1994) 135-146.

[2] C. Daniel, in: I. Ashland Oil (Ed.), Ashland Oil, Inc., 1983.

[3] D. Chelliah, P.L. Brusky, in: A.O. Inc (Ed.), United Kingdom, 1982.

[4] J.-M.M. Millet, J.C. Vedrine, Appl. Catal., A. 76 (1991) 209-219.

[5] R. A. Nyquist, R.O. Kagel, Infrared spectra of Inorganic Compounds Academic press, New York and London, 1971.

[6] K. Joseph, M. Premila, G. Amarendra, K.V. Govindan Kutty, C.S. Sundar, P.R. Vasudeva Rao, J. Nucl. Mater. 420 (2012) 49-53.

[7] P. Bonnet, J.M.M. Millet, C. Leclercq, J.C. Védrine, J. Catal. 158 (1996) 128-141.

[8] S. Scaccia, M. Carewska, A.D. Bartolomeo, P.P. Prosini, Thermochim. Acta. 383 (2002) 145-152.

[9] P. Kowalik, W. Próchniak, M. Konkol, T. Borowiecki, Appl. Catal., A. 423–424 (2012) 15-20.

[10] E. Muneyama, A. Kunishige, K. Ohdan, M. Ai., J. Catal., 158 (1996) 378-384.

CHAPTER 8

SUMMARY AND CONCLUSION

The characterization results obtained for the synthesized iron phosphate catalyst showed isolation of the tridymite-like $FePO_4$ phase *via* the specified synthetic procedure. This was confirmed by several techniques.

Room temperature XRD showed that the tridymite-like $FePO_4$ phase was isolated as the major phase and reflections which were consistent with the unwanted quartz type $FePO_4$ phase were not evident. The infrared spectra showed the presence of bands within the region of 600-1050 cm^{-1} pre and post calcination which served as evidence of the orthophosphate group.

The TPR/TPO profile of the catalyst was correlated with room temperature XRD as well as the infrared spectra obtained for the sample at each reduction and oxidation step respectively. It was observed that the tridymite-like $FePO_4$ phase was reduced *via* an intermediate phase, $Fe_3(P_2O_7)_2$, to form $Fe_2P_2O_7$. Upon reoxidation of the reduced catalyst, the active α-phase was observed at the lower temperature and formation of the quartz type $FePO_4$ phase at the higher temperature. The TPD experiments determined the number and strength of acidic sites. It was evident that the catalyst contains medium to strong acidic sites, seeing that a major peak was observed in the region of 580 °C.

In situ variable temperature XRD data showed the phase transformations which had occurred during the calcination, reduction and reoxidation process. Reflections of the tridymite-like $FePO_4$ phase were observed up to the elevated temperature of 550 °C with no evidence of the unwanted quartz type $FePO_4$ phase, thus showing isolation of the tridymite-like $FePO_4$ phase up to 550 °C. Calcination for longer periods at each temperature interval resulted in the emergence of the quartz type $FePO_4$ phase from 548 °C, thus indicating that longer exposure of the catalyst at each temperature interval influenced phase formation. In the reducing atmosphere, no evidence of the intermediate phase was observed after complete reduction at elevated temperatures and during reoxidation only the active α-phase emerged.

Looking at the surface morphology of the calcined catalyst *via* SEM image analysis showed that post calcination there was an even distribution of phosphorous and iron over the surface of the catalyst while in the case of the reduced and reoxidized catalyst there was evidence of agglomeration or sintering, which was further depicted by the EDX map of the surface.

It was seen from the results obtained from Mössbauer spectroscopy that there was a direct correlation with the XRD data as well as the TPR/TPO results in terms of the phase changes and oxidation state of the calcined, uncalcined, reduced and reoxidized catalyst. Mössbauer spectroscopy also allowed for a percentage allocation of the phases present. The Raman data obtained supported the assignment of the phase changes of the uncalcined catalyst, as well as the phase changes of the calcined catalyst found during reduction and reoxidation using *in situ* XRD and TPR/TPO.

The TGA-DSC profile for the uncalcined catalyst showed weight loss within the temperature range of 100-300 °C which was attributed to the loss of water at the lower temperature and it was postulated that the weight loss which had occurred at the higher temperature was linked to the onset for the formation of the tridymite-like $FePO_4$ phase.

TEM particle size analysis had allowed for differentiation of the silica particles and the iron phosphate particles, with silica within the range of 30-35 nm and iron phosphate particles within the range of 7-11 nm. The SADP pattern of the calcined catalyst suggested that the catalyst was polycrystalline.

The catalytic testing carried out demonstrated the effect of various reaction conditions on the performance of the tridymite-like $FePO_4$ catalyst precursor for the formation of the target product EMA. Initial testing involved the use of the EIB feed only in the presence of an oxidizing atmosphere at varying contact times and during the investigation it was observed that the optimal conversion was obtained at a temperature of 450 °C at each of the contact times. The selectivity and yield data for EMA at the optimal operating temperature over the varying contact times showed that the contact time of 0.8 seconds produced the greatest yield of EMA, which was ~ 17 mol % with a ~ 30 % selectivity. To confirm the assumption made in choosing a suitable catalyst precursor, which was that the tridymite-like $FePO_4$ catalyst was better than the quartz type $FePO_4$ catalyst for ODH reactions, the quartz type phase was tested at the optimal contact time of 0.8 seconds. In the case of the quartz $FePO_4$ type phase, optimal results were obtained at a similar temperature of 450 °C with a maximum EMA yield of ~ 14 mol % and a selectivity of ~ 27 %.

The investigations including a water co-feed over the varying contact times also showed optimal results at 0.8 seconds; however the temperature of optimal efficiency shifted to a lower temperature of 400 °C, which was postulated to be related to the effect of water in favouring the formation of the hydroxylated form of the active α-phase. The presence of water during the catalytic testing showed an increase in the conversion of EIB however, the selectivity towards EMA was lower, whilst that of hydrolysis products increased. In addition, the selectivity towards carbon oxides also decreased in the presence of the water co-feed.

Although the conversion was found to increase with the addition of the water co-feed, the effect of hydrolysis reduced the selectivity towards EMA. The use of ethanol was considered during the catalytic testing to shift the equilibrium towards EMA. Initial testing involved the exclusion of the water co-feed to eliminate the effect of hydrolysis. The reactions were carried out at varying ratios and at a contact time of 0.8 seconds. Optimal conversion was obtained at 450 °C and the product profile for the varying fuel(EIB):EtOH ratios evidenced that addition of the alcohol reduced hydrolysis and enhanced selectivity towards EMA. Optimal results were obtained at a ratio of 1:5 fuel:EtOH with a yield of ~ 34 mol % EMA at a EIB conversion of ~ 57 %.

It was considered that since the addition of ethanol enhances EMA selectivity and reduces the formation of hydrolysis products, the addition of water would benefit this study by influencing the conversion. The catalytic tests were carried out at varying fuel:EtOH ratios, which were in line with the reactions excluding the water co-feed and the fuel(EIB):water ratio was maintained at 1:15. The reaction with the fuel(EIB):EtOH:water ratio of 1:5:15 showed optimal selectivity (31 %) at 400 °C towards EMA at a conversion of 70 %.

The lifetime and regeneration studies were carried out to observe the efficacy of the catalyst with time on stream and whether water served as an effective regeneration medium during this process. The investigation of the varying regeneration techniques showed that the tridymite-like $FePO_4$ catalyst was significantly more active over a 25 hour period on stream and the use of heat and steam enhanced the conversion and selectivity towards the target product EMA.

Spent catalyst characterization provided an understanding of changes of the catalyst when subjected to varying reactor conditions within the reactor bed. Several properties were considered which included the change in surface area, surface morphology and phases during the testing process. Three reaction conditions were considered, namely, reactions including

EtOH as a co-feed (excluding water), reactions including water as a co-feed and reactions including a combined EtOH and water co-feed. XRD results showed that under all three reaction conditions, the α-phase and $Fe_2P_2O_7$ dominated in the diffractograms and a similar trend was observed in the case of the IR spectra.

Mössbauer results evidenced that both the α-phase and $Fe_2P_2O_7$ were present in all three catalysts under the three different reaction conditions and this was very beneficial seeing that these two phases favour the ODH process. The reactions excluding the water co-feed (including the EtOH co-feed), also showed the formation of the unwanted β-phase. However, it was found that for the reactions including a water co-feed only, this phase was not observed and, in addition, for the reactions including the water and EtOH co-feed, this unwanted β-phase was not observed. It was postulated that water plays a role in reducing the formation of the β-phase. The addition of water was also shown to enhance the formation of the α-phase, seeing that the site fraction allocated to the α-phase increased with the addition of the water co-feed.

Cesium promoted $FePO_4$ catalysts have been shown to favour stabilization of the tridymite-like structure of the iron phosphate catalyst with a P/Fe ratio of 1.32. Based on this evidence from literature it was decided to synthesize a cesium promoted $FePO_4$ catalyst. The Mössbauer results provided an in depth understanding of phase assignment. It was found that all three promoted catalysts consisted of almost equivalent amounts of both the tridymite-like $FePO_4$ phase as well as the quartz type $FePO_4$ phase, with a higher relative intensity towards the latter. The presence of the $CsFeP_2O_7$ phase was also observed with the highest relative intensity for the promoted catalyst with the Cs/Fe ratio of 0.10. It has been reported in literature that $CsFeP_2O_7$ exhibits a small synergy effect in the presence of the $Fe_2P_2O_7$ phase and the active α-phase, which favours ODH reactions.

The results obtained for the unpromoted catalyst showed a higher selectivity towards the target product EMA relative to the promoted catalyst with the lowest cesium loading (Cs/Fe ratio = 0.10). The reduced selectivity towards EMA was considered to be the result of the reducibility of the promoted catalyst, since it was observed that cesium inhibits the reduction of $FePO_4$ and also reoxidation occurs at higher temperatures. In addition, phase stability was not enhanced during the synthesis and thus the mixture of phases formed negatively influenced the reaction. The influence of cesium on the acidic character of the $FePO_4$ catalyst could also contribute to the reduced selectivity towards the target product.

APPENDIX A1

A1.1 Reactor Design

Figure A1.1 Overall reactor setup

Figure A1.2 Gas inlet controls (rotameters) and heating gauges

Figure A1.3 Chiller for product outlet line

Figure A1.4 HPLC feed pumps and weighing balances

Figure A1.5 Reactors attached to catchpots

Figure A1.6 Catchpots for product streams

Figure A1.7 Reactors, pressure gauges and housing

Figure A1.8 Ritter Wetgas flowmeters for off gas streams

APPENDIX A2

The stepwise process for the calculation of conversion, yield and selectivity based on one example using an EIB feed at a contact time of 0.8 s and at 450 °C is shown below.

Table A2.1 Conversion

Reaction No.	11
Temperature	450 °C
Mass of EIB initial (g)	534.97
Mass of EIB final (g)	502.54
Mass of EIB entering reactor (g)	32.43
Moles of EIB entering reactor(g)	0.2792
Total mass of product formed (g)	24.65
Total out gas flow (mL/min)	66724
Mass of organic phase (g)	18.83
Mass of aqueous phase (g)	5.82
Karl Fischer (%) of organic phase	6.31
Karl Fischer (%) of aqueous phase	85.97
Actual mass of organic phase (g)	17.64
Actual mass of aqueous phase (g)	0.82
Conversion of EIB (%)	57.35
Carbon balance (%)	99.46

Table A2.2 Organic phase - FID

	Molar mass(g/mol)	RRF	Area (%)	Corrected area(%)	Normalised area(%)	Mass of component(g)	No. of moles(mol)
ACE	58.08	0.9	1.01	1.12	0.99	0.1751	0.0030
IBA	88.11	1	2.37	2.37	2.09	0.2437	0.0042
MAA	86.09	1	5.11	5.11	4.52	0.5379	0.0092
EIB	116.19	0.9	64.18	71.31	63.08	5.5633	0.0958
ETHACE	88.11	1.1	0.18	0.16	0.14	0.0168	0.0003
ACETALD	44.05	1.2	0.12	0.1	0.08	0.0205	0.0004
ACETIC	60.05	2	0.17	0.09	0.75	0.0128	0.0002
EtOH	46.03	1	1.48	1.48	1.30	0.2913	0.0050
EMA	114.15	0.8	25.04	31.3	27.69	2.4848	0.0427

Table A2.3 Aqueous phase - FID

	Molar mass(g/mol)	RRF	Area (%)	Corrected area(%)	Normalised area(%)	Mass of component(g)	No. of moles(mol)
ACE	58.08	0.9	14.50	16.11	15.86	0.1295	0.0022
IBA	88.11	1	5.71	5.71	5.62	0.0302	0.0005
MAA	86.09	1	8.13	8.13	8.00	0.0441	0.0008
EIB	116.19	0.9	11.69	12.99	12.79	0.0522	0.0009
ETHACE	88.11	1.1	0.00	0.00	0.00	0.00	0.00
ACETALD	44.05	1.2	0.00	0.00	0.00	0.00	0.00
ACETIC	60.05	2	4.65	2.33	2.29	0.0180	0.0003
EtOH	46.03	1	51.31	51.31	50.52	0.5206	0.0089
EMA	114.15	0.8	3.99	4.99	4.91	0.0204	0.0003

$$\text{Corrected Area (\%)} = \frac{\text{Percentage Area of Component}}{\text{Relative response factor}}$$

$$\text{Normalized Area (\%)} = \frac{\text{Corrected Area}}{\text{Sum of all corrected areas}} \text{ x } 100$$

$$\text{Mass component out (g)} = \frac{\text{Normalized Area}}{100} \text{ x Actual mass of organic layer}$$

$$\text{Moles component out (mol)} = \frac{\text{Mass component out}}{\text{Molar mass of the component}}$$

Table A2.4 Gaseous phase - FID

	Calibration curve slope	Area	Moles in injection volume	No. of Moles in outgas flow(mol)
ACE	3.21E+11	24945.87	7.77E-08	0.01371
IBA	4.47E+11	0.00	0.00	0.00
MAA	4.41E+11	0.00	0.00	0.00
EIB	6.9E+11	115795.30	1.67E-07	0.02239
ETHACE	3.92E+11	1571.46	4.1E-09	0.00054
ACETALD	1.48E+11	12892.35	7.1E-08	0.00935
ACETIC	1.52E+11	0.00	0.00	0.00
EtOH	2.35E+11	8839.46	3.76E-08	0.00502
EMA	6.99E+11	26323.37	3.77E-08	0.00502

Table A2.5 Gaseous phase - TCD

	Calibration curve slope	Area	Moles in injection volume	No. of Moles in outgas flow(mol)
CO	6.79E+06	28.65	4.11E-06	0.1830
CO_2	8.43E+06	29.47	3.53E-06	0.1572
Propane	3.45E+11	0.00	0.00	0.00
Propene	3.34E+11	59260.10	1.77E-07	0.0078
Methane	1.15E+11	972.62	8.46E-09	0.0003
Ethane	1.75E+11	560.36	4.87E-09	0.0002
Butane	3.43E+11	0.00	0.00	0.00
Ethene	1.85E+11	271414.28	1.47E-06	0.0652

$$\text{Moles in injection volume} = \frac{\text{Area}}{\text{Slope of Calibration Curve}}$$

$$\text{Moles in outgas flow (mol)} = \frac{\text{Moles in injection volume x outgas flow}}{\text{injection volume}}$$

Table A2.6 Yield and Selectivity

	Total no. of moles (mol)	Yield (mol %)	Selectivity (mol %)
ACE	0.01561	2.80	4.89
IBA	0.00471	1.13	1.97
MAA	0.01002	2.41	4.19
ETHACE	0.00082	0.20	0.35
ACETALD	0.00970	1.15	2.00
ACETIC	0.00053	0.06	0.11
EtOH	0.01900	2.25	3.92
EMA	0.04816	17.25	30.08
CO	0.1830	11.13	19.41
CO_2	0.1572	9.57	16.70
Propane	0.00	0.00	0.00
Propene	0.0078	1.41	2.47
Methane	0.0003	0.02	0.40
Ethane	0.0002	0.03	0.05
Butane	0.00	0.00	0.00
Ethene	0.0652	7.71	13.45

APPENDIX B

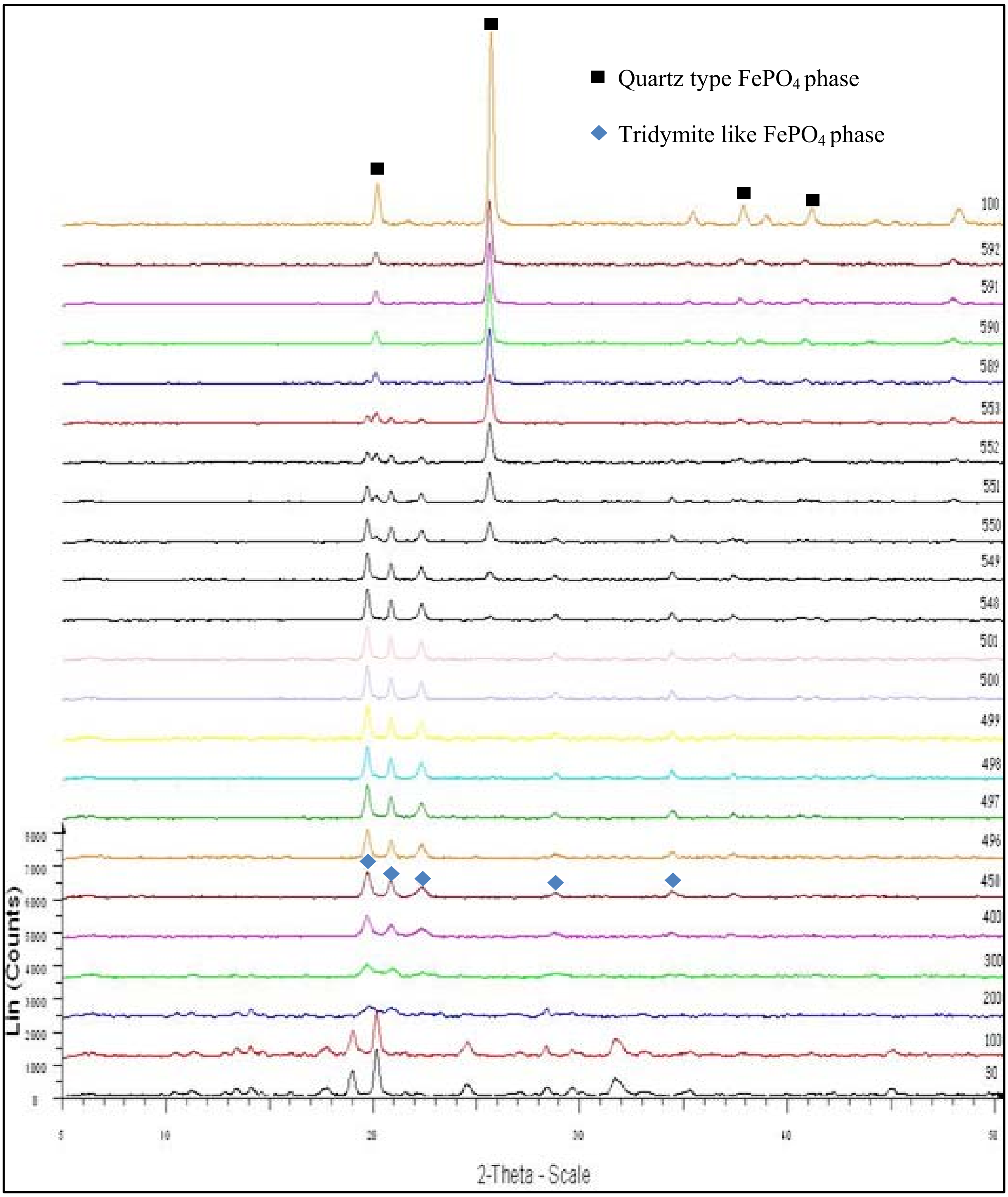

Figure B.1 High temperature and extended period calcination of the tridymite-like $FePO_4$ phase to form the quartz type $FePO_4$ phase

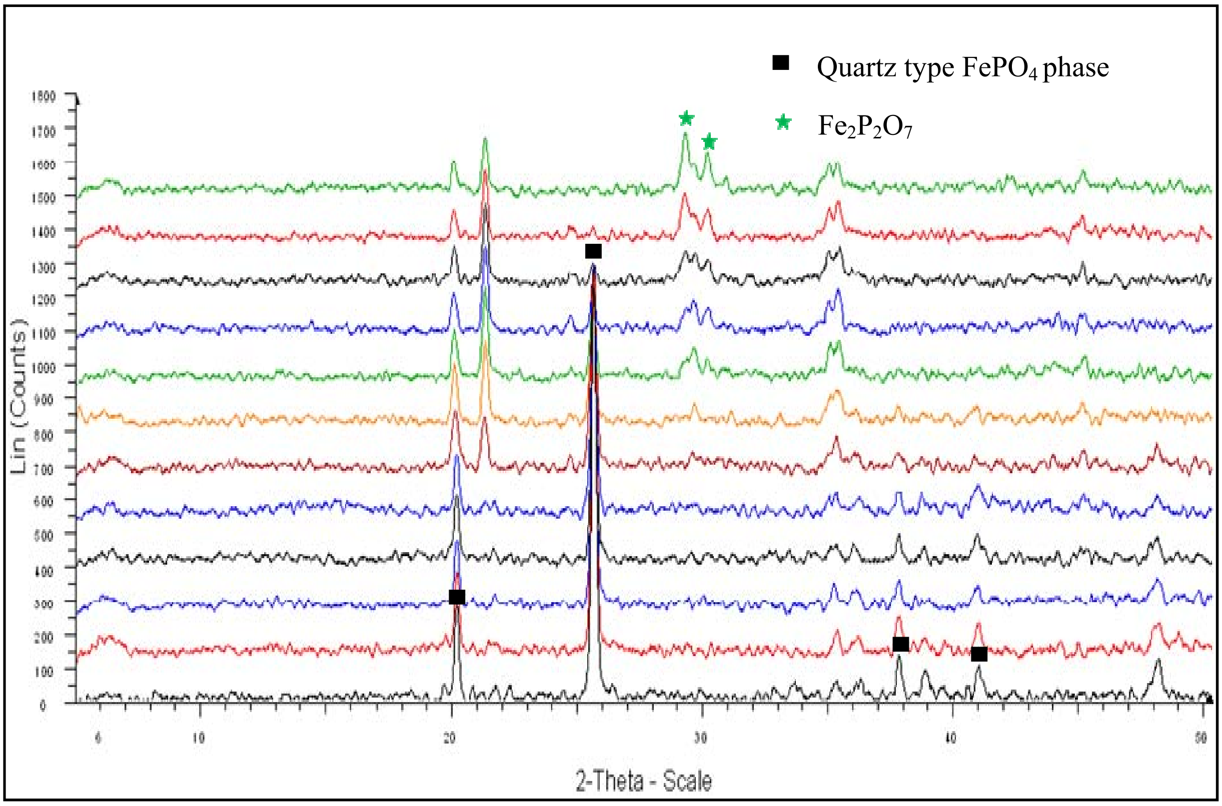

Figure B.2 Reduction of the quartz type $FePO_4$ phase to form the $Fe_2P_2O_7$ phase

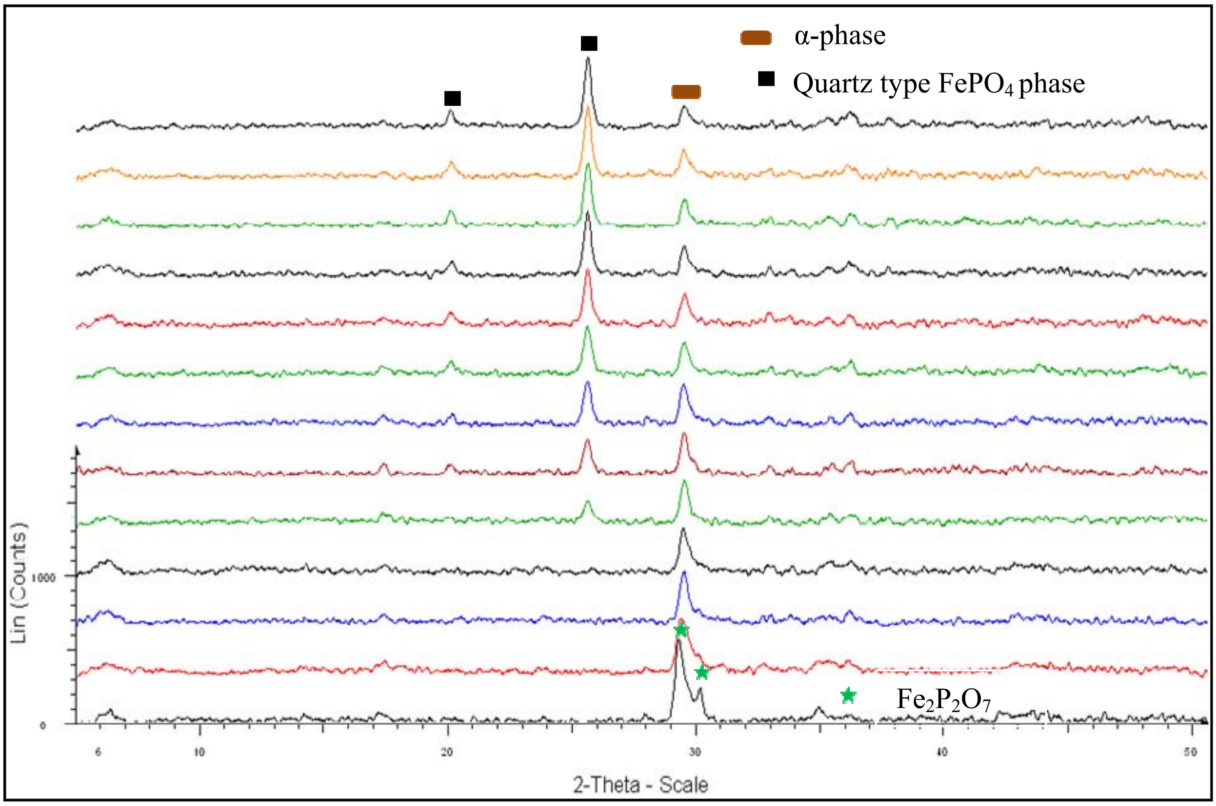

Figure B.3 Oxidation of the $Fe_2P_2O_7$ phase to form the α-phase as well as the quartz type $FePO_4$ phase

APPENDIX C1

C1.1 Non-catalytic reaction conditions

Table C1.1 Conditions: EIB - empty reactor

	EIB	**O_2**	**Nitrogen**
mmol/hr	8.99	7.47	171.91

Table C1.2 Conditions: EIB - carborundum packed reactor

	EIB	**O_2**	**Nitrogen**
mmol/hr	8.99	7.90	171.91

Table C1.3 Conditions: Ethanol - empty reactor

	Ethanol	**O_2**	**Nitrogen**
Mmol/hr	10.29	8.51	154.17

Table C1.4 Conditions: Ethanol - carborundum packed reactor

	Ethanol	**O_2**	**Nitrogen**
Mmol/hr	10.29	7.90	158.80

APPENDIX C2

C2.1 Catalytic reaction conditions: EIB in air over varying contact times

Table C2.1 Conditions: EIB in air at a contact time of 1.2 seconds

	EIB	**O_2**	**Nitrogen**
mmol/hr	17.98	14.67	93.09

Table C2.2 Conditions: EIB in air at a contact time of 1.0 seconds

	EIB	**O_2**	**Nitrogen**
mmol/hr	22.47	19.47	99.24

Table C2.3 Conditions: EIB in air at a contact time of 0.8 seconds – Tridymite-like $FePO_4$ phase

	EIB	**O_2**	**Nitrogen**
mmol/hr	17.98	14.78	136.99

Table C2.4 Conditions: EIB in air at a contact time of 0.6 seconds

	EIB	**O_2**	**Nitrogen**
mmol/hr	22.47	19.89	203.23

Table C2.5 Conditions: EIB in air at a contact time of 0.4 seconds

	EIB	**O_2**	**Nitrogen**
mmol/hr	26.96	19.89	369.51

Table C2.6 Conditions: EIB in air at a contact time of 0.8 seconds – Quartz-type $FePO_4$ phase

	EIB	**O_2**	**Nitrogen**
mmol/hr	17.98	14.78	136.99

APPENDIX C2

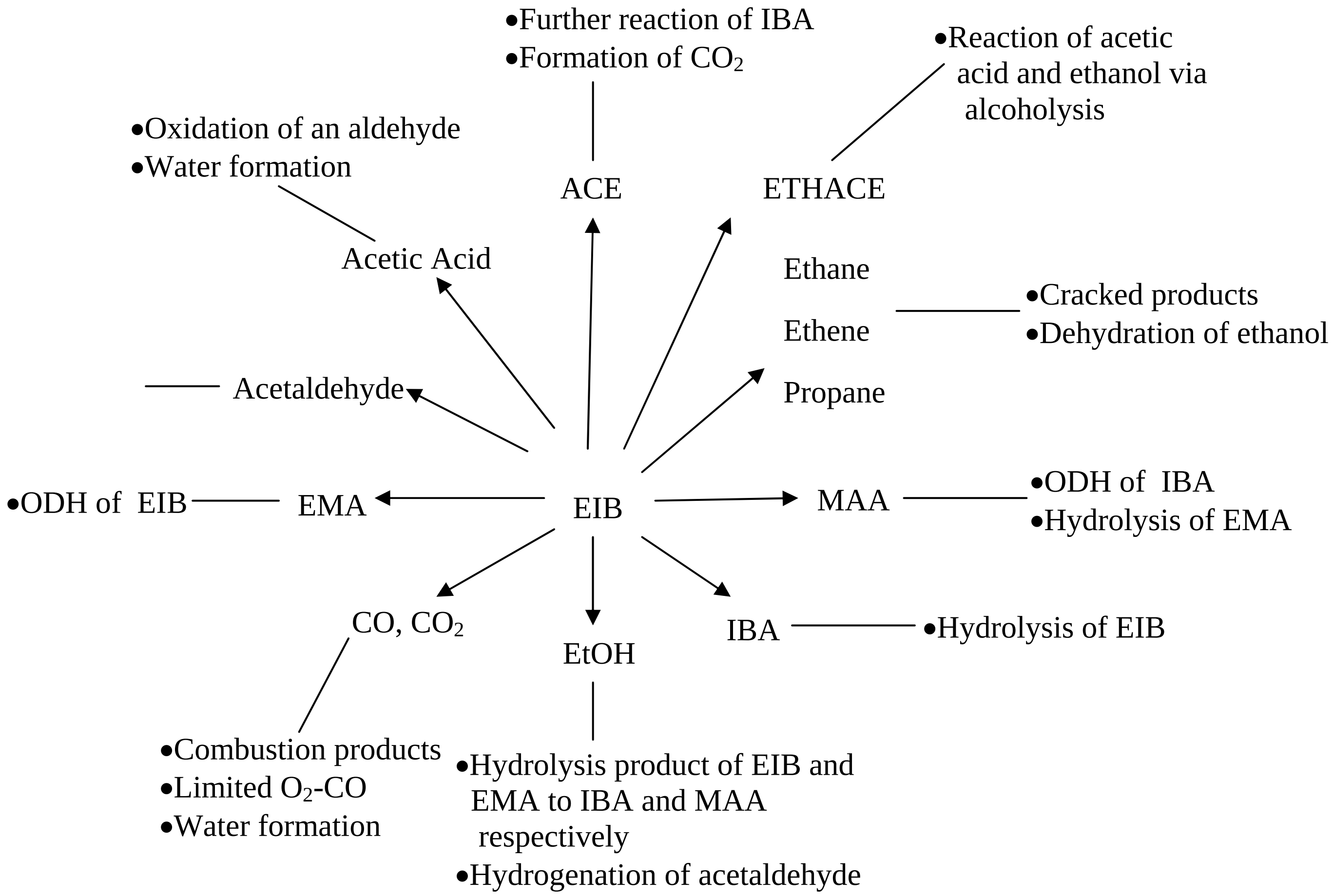

Figure C2.1 ODH products from EIB

List of Abbreviations	
Other Products	Methane, Acetaldehyde, Acetic Acid, Ethanol (EtOH), Ethane, Ethene, Acetone (ACE), Propene, Propane, Ethyl Acetate (ETHACE), and Unidentified products
COx	CO and CO_2
MAA	Methacrylic Acid
IBA	Isobutyric Acid
EMA	Ethyl Methacrylate

APPENDIX C3

C3.1 Catalytic reaction results: EIB in air at varying contact times

Table C3.1 EIB in air at a contact time of 1.2 seconds

Temperature T/^oC	Conversion X/(mol%)	Selectivity (mol %)	Yield (mol)	Selectivity (mol %)			
		EMA	EMA	MAA	IBA	COx	Other Products
300.0	12.0	5.5	0.7	1.2	19.0	24.1	50.2
350.0	25.8	7.8	2.0	2.2	11.3	34.9	43.8
400.0	39.1	17.0	6.6	1.5	6.1	37.3	38.1
450.0	63.0	24.5	15.5	4.7	2.3	44.0	24.5
500.0	58.2	10.6	6.2	3.7	5.1	50.3	30.3

Table C3.2 EIB in air at a contact time of 1.0 seconds

Temperature T/^oC	Conversion X/(mol%)	Selectivity (mol %)	Yield (mol)	Selectivity (mol %)			
		EMA	EMA	MAA	IBA	COx	Other Products
300.0	15.9	9.8	1.6	2.4	13.1	16.7	58.0
350.0	20.7	17.0	3.5	4.3	8.5	21.1	49.1
400.0	35.3	17.4	6.2	5.9	6.5	32.8	37.4
450.0	59.2	26.3	15.6	2.7	1.6	40.9	28.5
500.0	57.7	10.3	5.9	3.6	4.9	50.8	30.4

Table C3.3 EIB in air at a contact time of 0.8 seconds – Tridymite-like $FePO_4$ phase

Temperature T/^{o}C	Conversion X/(mol%)	Selectivity (mol %)	Yield (mol)	Selectivity (mol %)			
		EMA	EMA	MAA	IBA	COx	Other Products
300.0	11.0	7.4	0.8	1.7	11.0	21.8	58.1
350.0	24.4	11.5	2.8	2.3	7.1	24.2	54.9
400.0	37.0	22.4	8.3	2.8	5.2	26.8	42.8
450.0	57.4	30.1	17.3	4.2	2.0	36.1	27.6
500.0	50.4	14.5	7.3	3.4	4.5	42.0	35.6
550.0	50.1	11.7	5.8	3.8	4.1	45.9	34.5

Table C3.4 EIB in air at a contact time of 0.6 seconds

Temperature T/^{o}C	Conversion X/(mol%)	Selectivity (mol %)	Yield (mol)	Selectivity (mol %)			
		EMA	EMA	MAA	IBA	COx	Other Products
300.0	10.0	6.2	0.6	1.4	11.8	21.4	59.2
350.0	21.5	7.9	1.7	2.1	11.9	39.6	38.5
400.0	25.1	18.8	4.7	1.5	5.2	38.0	36.5
450.0	57.1	27.8	15.9	3.2	1.4	40.9	26.7
500.0	56.0	17.2	9.6	10.2	2.5	43.3	27.0

Table C3.5 EIB in air at a contact time of 0.4 seconds

Temperature T/^{o}C	**Conversion X/(mol%)**	**Selectivity (mol %)**	**Yield (mol)**	**Selectivity (mol %)**			
		EMA	**EMA**	**MAA**	**IBA**	**COx**	**Other Products**
300.0	3.2	6.7	0.2	1.8	19.3	13.4	58.8
350.0	6.6	11.0	0.7	3.8	18.9	14.3	52.0
400.0	13.2	21.2	2.8	3.7	6.4	24.0	44.7
450.0	49.6	23.0	11.4	6.8	1.9	26.4	41.9
500.0	48.8	10.1	4.9	11.8	7.2	31.4	40.5

Table C3.6 EIB in air at a contact time of 0.8 seconds – Quartz type $FePO_4$ phase

Temperature T/^{o}C	**Conversion X/(mol%)**	**Selectivity (mol %)**	**Yield (mol)**	**Selectivity (mol %)**			
		EMA	**EMA**	**MAA**	**IBA**	**COx**	**Other Products**
300.0	8.1	10.3	0.8	2.3	15.2	15.9	56.3
350.0	17.4	15.2	2.6	3.4	10.0	25.6	45.8
400.0	40.3	25.3	10.2	3.2	5.9	30.7	34.9
450.0	53.3	26.6	14.1	3.7	1.7	38.9	29.1
500.0	55.0	24.9	13.7	4.1	1.3	41.1	28.6
550.0	46.7	11.8	5.5	2.9	4.8	44.8	35.7

APPENDIX C4

C4.1 Catalytic reaction results: EIB and a water co-feed in air at varying contact times

Table C4.1 EIB and a water co-feed at a contact time of 1.2 seconds

Temperature T/^{o}C	Conversion X/(mol%)	Selectivity (mol %)	Yield (mol)	Selectivity (mol %)			
		EMA	EMA	MAA	IBA	COx	Other Products
300.0	13.6	1.9	0.3	1.8	30.6	25.1	40.6
350.0	39.8	5.2	2.1	7.1	20.5	28.8	38.4
400.0	60.0	10.6	6.4	13.2	15.9	30.5	29.8
450.0	79.0	7.9	6.3	11.0	19.4	31.8	29.9
500.0	91.8	1.0	0.9	10.0	14.8	38.2	36.0

Table C4.2 EIB and a water co-feed at a contact time of 1.0 seconds

Temperature T/^{o}C	Conversion X/(mol%)	Selectivity (mol %)	Yield (mol)	Selectivity (mol %)			
		EMA	EMA	MAA	IBA	COx	Other Products
300.0	11.5	2.3	0.3	2.1	35.9	21.3	38.4
350.0	36.0	6.3	2.3	6.7	15.7	29.6	41.7
400.0	60.3	8.6	5.2	11.6	18.1	32.2	29.5
450.0	68.9	5.4	3.7	6.4	12.9	36.6	38.7
500.0	71.1	5.1	3.7	9.2	13.7	41.1	30.9

Table C4.3 EIB and a water co-feed at a contact time of 0.8 seconds

Temperature T/^{o}C	**Conversion X/(mol%)**	**Selectivity (mol %)**	**Yield (mol)**	**Selectivity (mol %)**			
		EMA	**EMA**	**MAA**	**IBA**	**COx**	**Other Products**
300.0	12.3	2.6	0.3	4.5	41.9	6.8	44.2
350.0	43.1	7.1	3.1	16.5	19.0	7.8	49.8
400.0	58.7	12.9	7.6	22.1	17.2	11.8	36.0
450.0	78.4	2.5	2.0	11.2	21.2	23.5	41.6
500.0	79.1	1.5	1.2	5.4	10.8	26.8	56.2

Table C4.4 EIB and a water co-feed at a contact time of 0.6 seconds

Temperature T/^{o}C	**Conversion X/(mol%)**	**Selectivity (mol %)**	**Yield (mol)**	**Selectivity (mol %)**			
		EMA	**EMA**	**MAA**	**IBA**	**COx**	**Other Products**
300.0	9.8	2.8	0.3	4.6	46.6	8.6	37.9
350.0	34.2	6.0	2.0	9.5	15.1	26.0	43.4
400.0	53.0	8.9	4.7	13.5	12.2	32.4	33.4
450.0	73.8	4.3	3.2	7.6	10.5	34.0	43.6
500.0	77.8	2.1	1.6	7.8	13.6	34.2	42.3

Table C4.5 EIB and a water co-feed at a contact time of 0.4 seconds

Temperature T/°C	Conversion X/(mol%)	Selectivity (mol %)	Yield (mol)	Selectivity (mol %)			
		EMA	EMA	MAA	IBA	COx	Other Products
300.0	8.9	3.0	0.3	2.3	38.8	3.6	52.8
350.0	33.5	7.3	2.5	10.8	29.0	7.7	45.2
400.0	54.0	7.8	4.2	18.0	18.2	13.0	43.0
450.0	62.6	6.0	3.8	19.7	22.0	14.8	37.5
500.0	67.2	3.2	2.2	16.5	28.2	16.2	35.9

APPENDIX C5

C5.1 Catalytic reaction results: EIB and ethanol in air at varying ratios and a constant contact time of 0.8 seconds

Table C5.1 EIB and EtOH in air - a ratio of 1:1

Temperature T/^oC	Conversion X/(mol%)	Selectivity (mol %)	Yield (mol)	Selectivity (mol %)			
		EMA	EMA	MAA	IBA	COx	Other Products
300.0	7.4	29.7	2.2	0.9	3.4	14.1	51.9
350.0	11.0	36.4	4.0	1.1	2.9	16.3	43.3
400.0	18.7	42.8	8.0	2.5	3.5	20.5	30.7
450.0	44.9	53.2	23.9	3.1	3.0	26.5	14.2
500.0	35.8	25.4	9.1	3.2	2.5	49.9	19.0

Table C5.2 EIB and EtOH in air - a ratio of 1:2

Temperature T/^oC	Conversion X/(mol%)	Selectivity (mol %)	Yield (mol)	Selectivity (mol %)			
		EMA	EMA	MAA	IBA	COx	Other products
300.0	13.3	38.3	5.1	0.2	1.1	12.7	47.7
350.0	18.1	40.3	7.3	0.9	2.4	19.9	36.5
400.0	43.9	52.6	23.1	1.9	2.0	22.1	21.4
450.0	52.3	56.2	29.4	2.0	2.5	28.2	11.1
500.0	36.7	32.7	12.0	2.5	2.0	52.7	10.1

Table C5.3 EIB and EtOH in air - a ratio of 1:5

Temperature T/^{o}C	Conversion X/(mol%)	Selectivity (mol %)	Yield (mol)	Selectivity (mol %)			
		EMA	EMA	MAA	IBA	COx	Other Products
300.0	14.2	39.4	5.6	0.0	0.5	9.4	50.7
350.0	19.9	50.8	10.1	0.0	1.2	15.4	32.6
400.0	39.1	57.5	22.5	1.4	1.7	23.8	15.6
450.0	56.9	59.8	34.0	1.7	2.8	27.1	8.6
500.0	48.3	37.1	17.9	2.4	3.3	47.1	10.1

Table C5.4 EIB and EtOH - a ratio of 1:7

Temperature T/^{o}C	Conversion X/(mol%)	Selectivity (mol %)	Yield (mol)	Selectivity (mol %)			
		EMA	EMA	MAA	IBA	COx	Other Products
300.0	4.2	2.4	0.1	0.0	7.3	2.9	87.4
350.0	9.9	7.7	0.8	3.0	3.9	6.2	79.2
400.0	26.5	17.0	4.5	1.9	2.0	11.4	67.7
450.0	54.5	24.6	13.4	6.4	2.3	14.2	52.5
500.0	42.8	6.7	2.8	1.5	4.2	19.6	68.1

Table C5.5 EIB and EtOH - a ratio of 1:10

Temperature T/^{o}C	**Conversion X/(mol%)**	**Selectivity (mol %)**	**Yield (mol)**	**Selectivity (mol %)**			
		EMA	**EMA**	**MAA**	**IBA**	**COx**	**Other Products**
300.0	11.8	0.0	0.0	0.0	0.3	5.0	94.6
350.0	21.3	4.2	0.9	0.0	1.0	8.6	86.2
400.0	44.5	8.2	3.6	1.1	1.4	12.6	76.7
450.0	58.3	9.6	5.6	2.5	2.4	19.0	66.5
500.0	55.4	1.6	0.9	0.8	8.5	25.0	64.1

APPENDIX C6

C6.1 Catalytic reaction results: EIB, ethanol and water in air at varying ratios and a constant contact time of 0.8 seconds

Table C6.1 EIB, ethanol and water - a ratio of 1:1:15

Temperature T/°C	Conversion X/(mol%)	Selectivity (mol %)	Yield (mol)	Selectivity (mol %)			
		EMA	EMA	MAA	IBA	COx	Other Products
300.0	20.2	0.61	0.1	2.1	23.2	5.8	68.3
350.0	41.2	6.87	2.8	11.4	11.3	8.2	62.2
400.0	73.3	10.8	7.9	30.5	12.1	13.5	33.1
450.0	75.8	9.3	7.0	27.4	9.4	13.4	40.5
500.0	70.4	6.6	4.7	19.7	10.5	17.6	45.6

Table C6.2 EIB, ethanol and water - a ratio of 1:2:15

Temperature T/°C	Conversion X/(mol%)	Selectivity (mol %)	Yield (mol)	Selectivity (mol %)			
		EMA	EMA	MAA	IBA	COx	Other Products
300.0	21.0	0.8	0.2	0.2	12.0	3.6	83.5
350.0	28.8	6.0	1.7	4.4	16.1	8.4	65.1
400.0	81.0	9.4	7.6	17.7	8.2	10.3	54.4
450.0	98.3	6.9	6.8	18.3	0.6	14.2	60.0
500.0	97.6	2.8	2.8	18.4	1.6	20.3	56.8

Table C6.3 EIB, ethanol and water - a ratio of 1:5:15

Temperature T/^{o}C	**Conversion X/(mol%)**	**Selectivity (mol %)**	**Yield (mol)**	**Selectivity (mol %)**			
		EMA	**EMA**	**MAA**	**IBA**	**COx**	**Other Products**
300.0	7.7	3.1	0.2	2.1	16.7	4.9	73.1
350.0	32.9	11.8	3.9	8.8	6.1	8.8	64.4
400.0	69.8	30.2	21.1	14.7	1.3	13.3	40.4
450.0	83.8	16.8	14.0	22.6	4.4	16.6	37.8
500.0	91.3	5.5	5.1	18.1	5.8	22.5	45.4

Table C6.4 EIB, ethanol and water - a ratio of 1:7:15

Temperature T/^{o}C	**Conversion X/(mol%)**	**Selectivity (mol %)**	**Yield (mol)**	**Selectivity (mol %)**			
		EMA	**EMA**	**MAA**	**IBA**	**COx**	**Other Products**
300.0	8.6	3.0	0.3	0.0	13.7	3.7	79.7
350.0	19.3	8.2	1.6	4.0	14.1	5.3	68.4
400.0	54.3	16.8	9.1	8.6	6.3	6.3	62.0
450.0	62.1	10.9	6.8	16.5	6.1	10.5	56.0
500.0	68.1	3.5	2.4	3.4	10.2	17.9	65.0

Table C6.5 EIB, ethanol and water - a ratio of 1:10:15

Temperature $T/^{o}C$	Conversion X/(mol%)	Selectivity (mol %)	Yield (mol)	Selectivity (mol %)			
		EMA	EMA	MAA	IBA	COx	Other Products
300.0	11.9	1.1	0.1	0.4	7.5	1.8	89.2
350.0	20.8	7.4	1.5	3.7	12.8	4.9	71.2
400.0	57.0	15.0	8.5	7.7	10.4	10.7	56.2
450.0	61.3	10.2	6.3	6.1	9.9	13.2	60.6
500.0	69.4	8.4	5.8	5.8	9.5	17.6	59.1

APPENDIX C7

C7.1 Postulated mechanisms for product formation

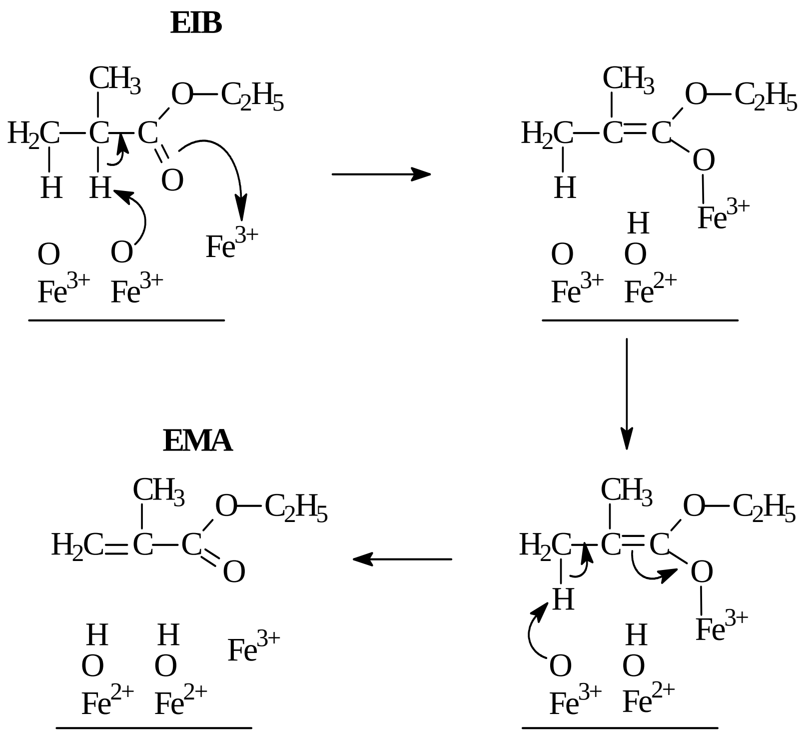

Scheme C7.1 Mars-Van Krevelen mechanism showing the formation of EMA from EIB

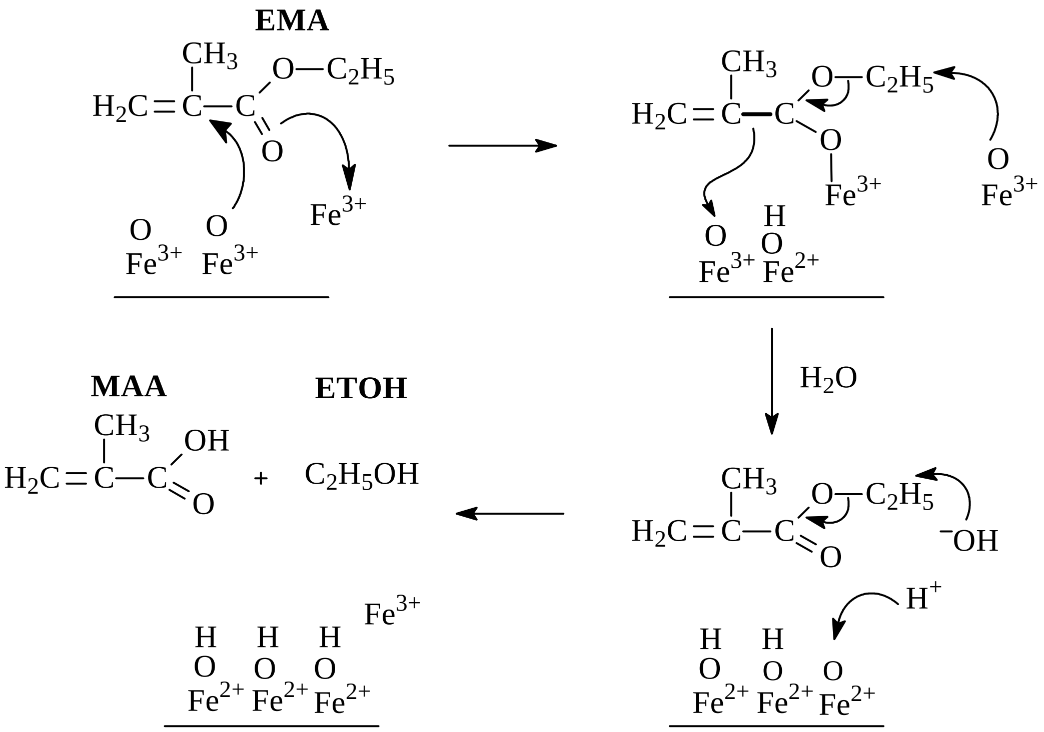

Scheme C7.2 Hydrolysis of EMA to form MAA and ethanol

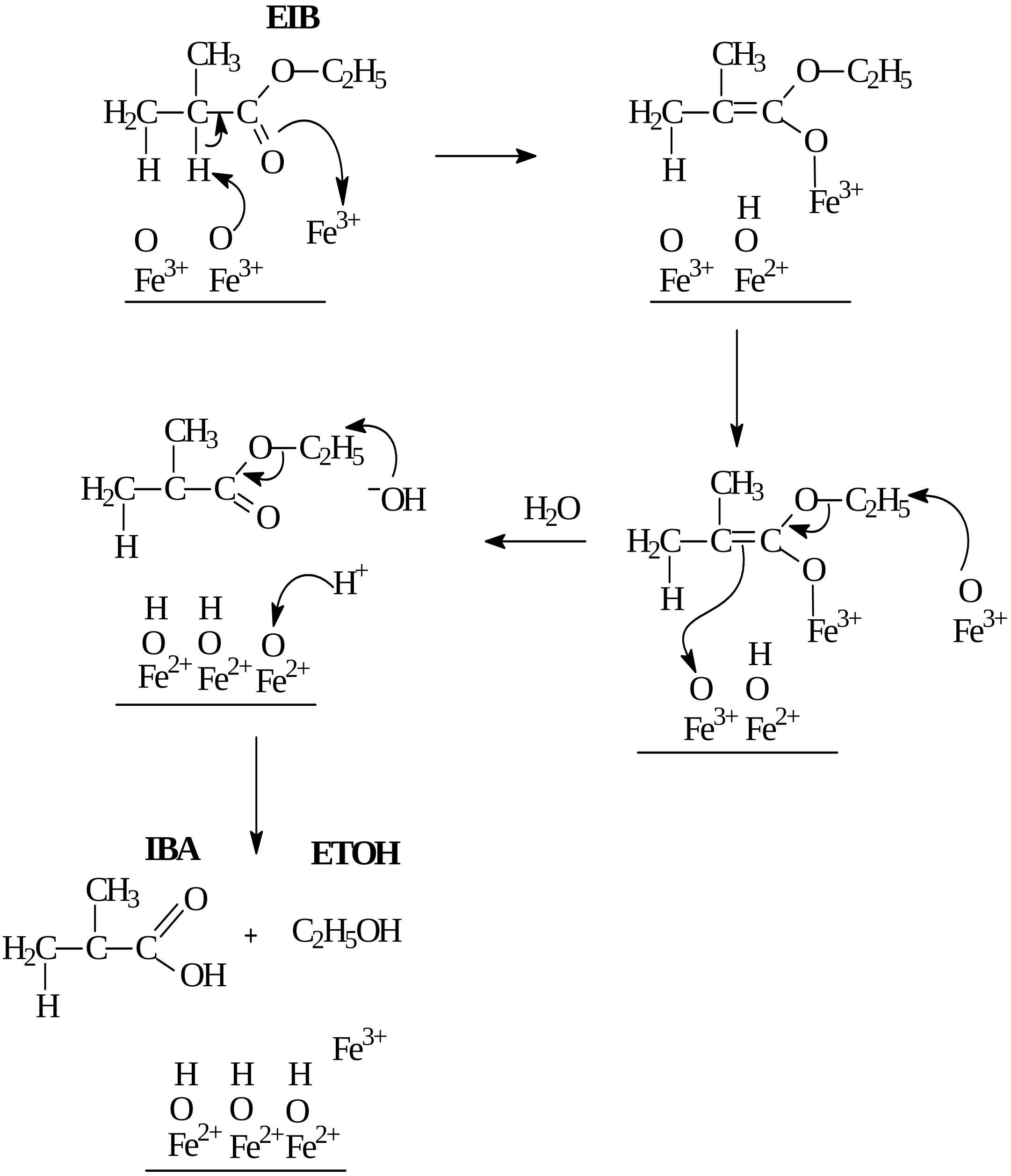

Scheme C7.3 Hydrolysis of EIB to form IBA and ethanol

APPENDIX D

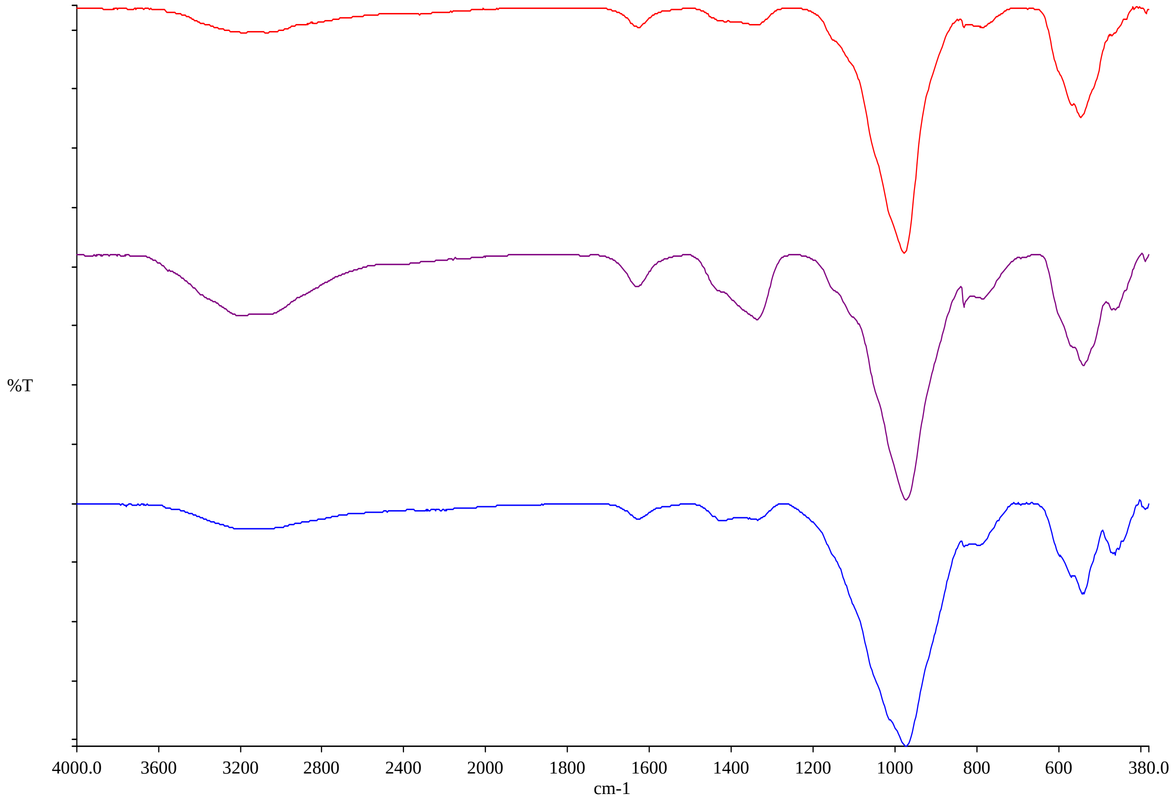

Figure D.1 Infrared spectra of the uncalcined cesium promoted iron phosphate catalysts

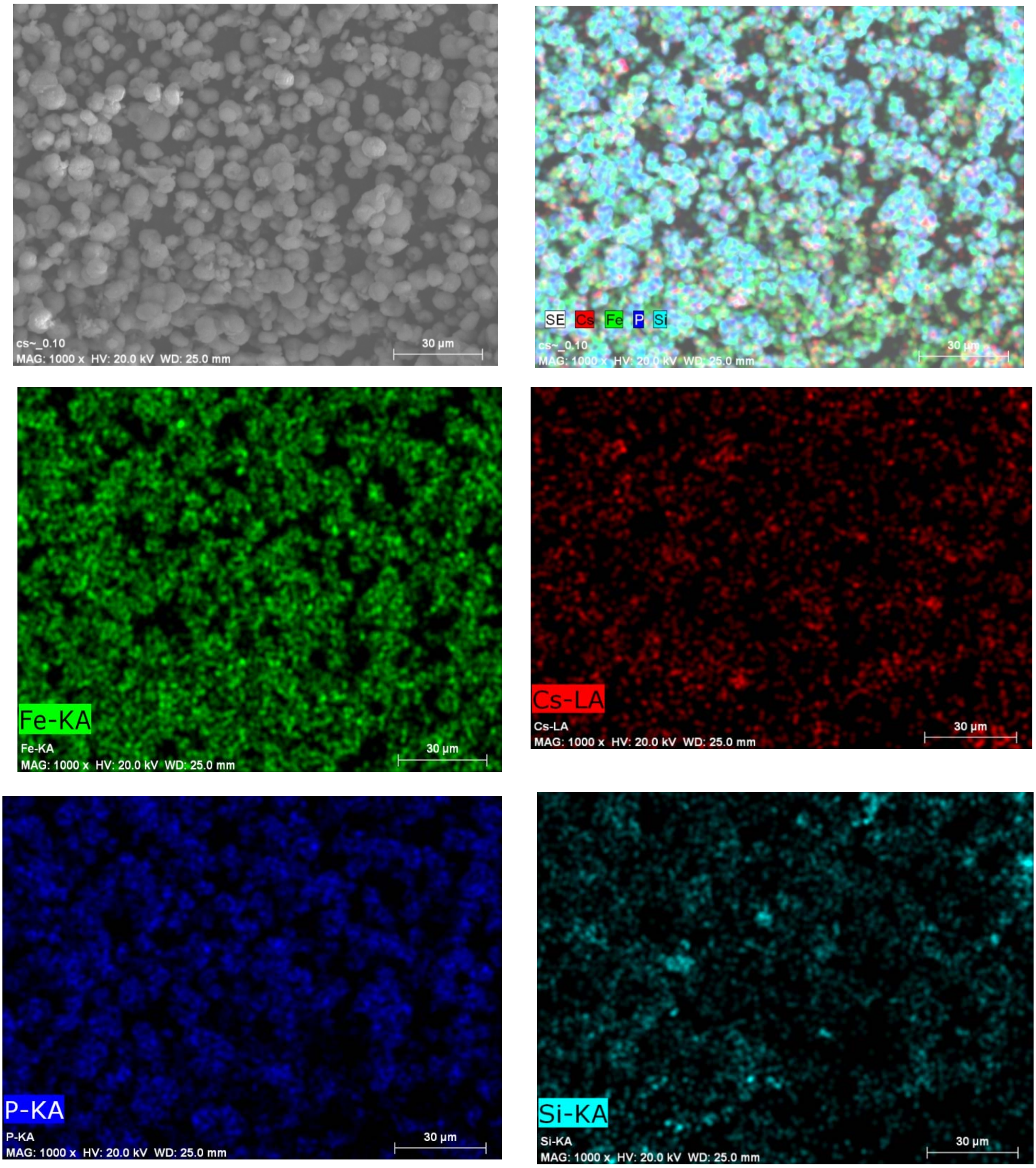

Figure D.2 SEM-EDX mapping images of the cesium promoted catalyst with Cs/Fe - 0.10

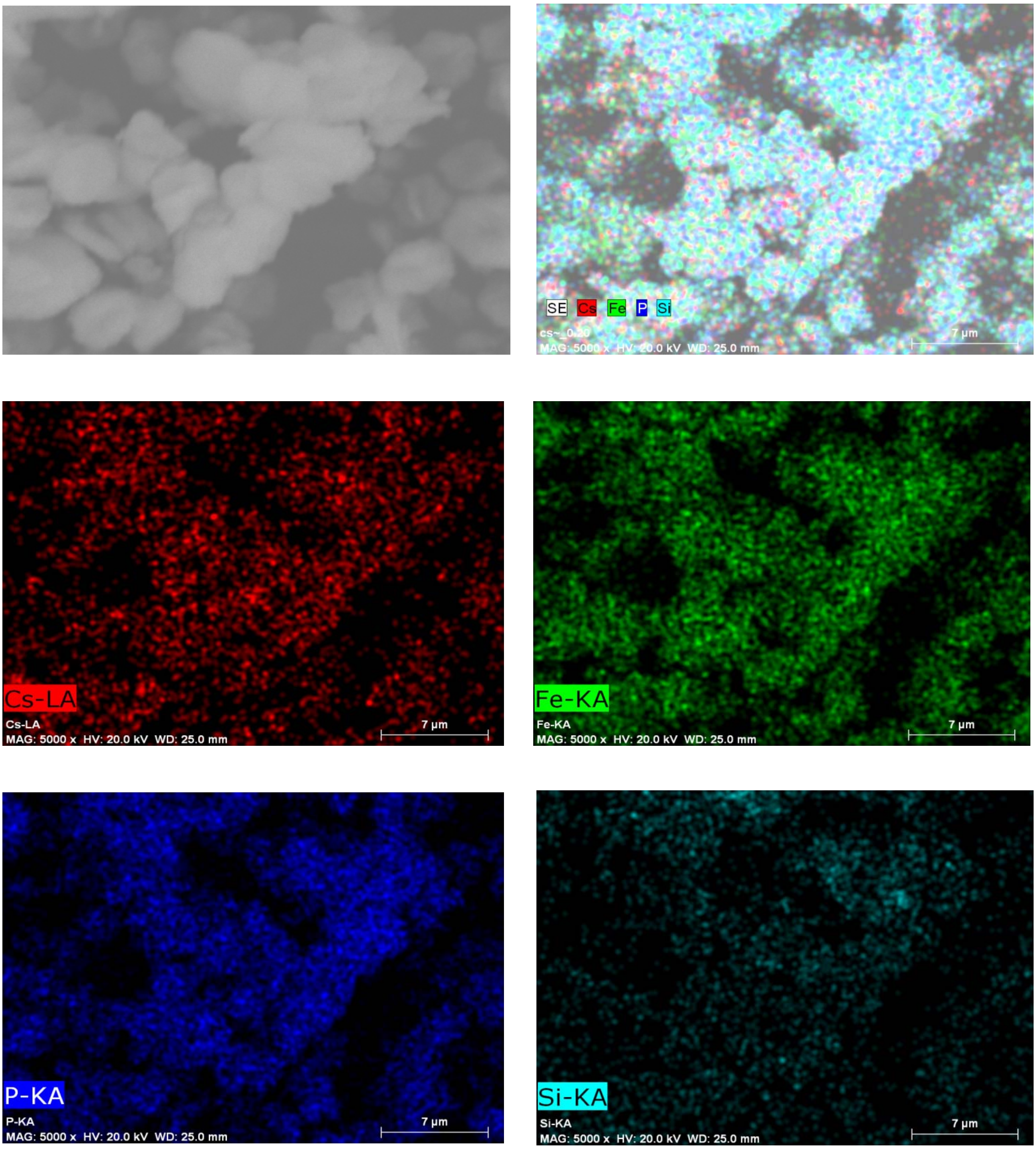

Figure D.3 SEM-EDX mapping images of the cesium promoted catalyst with Cs/Fe - 0.20

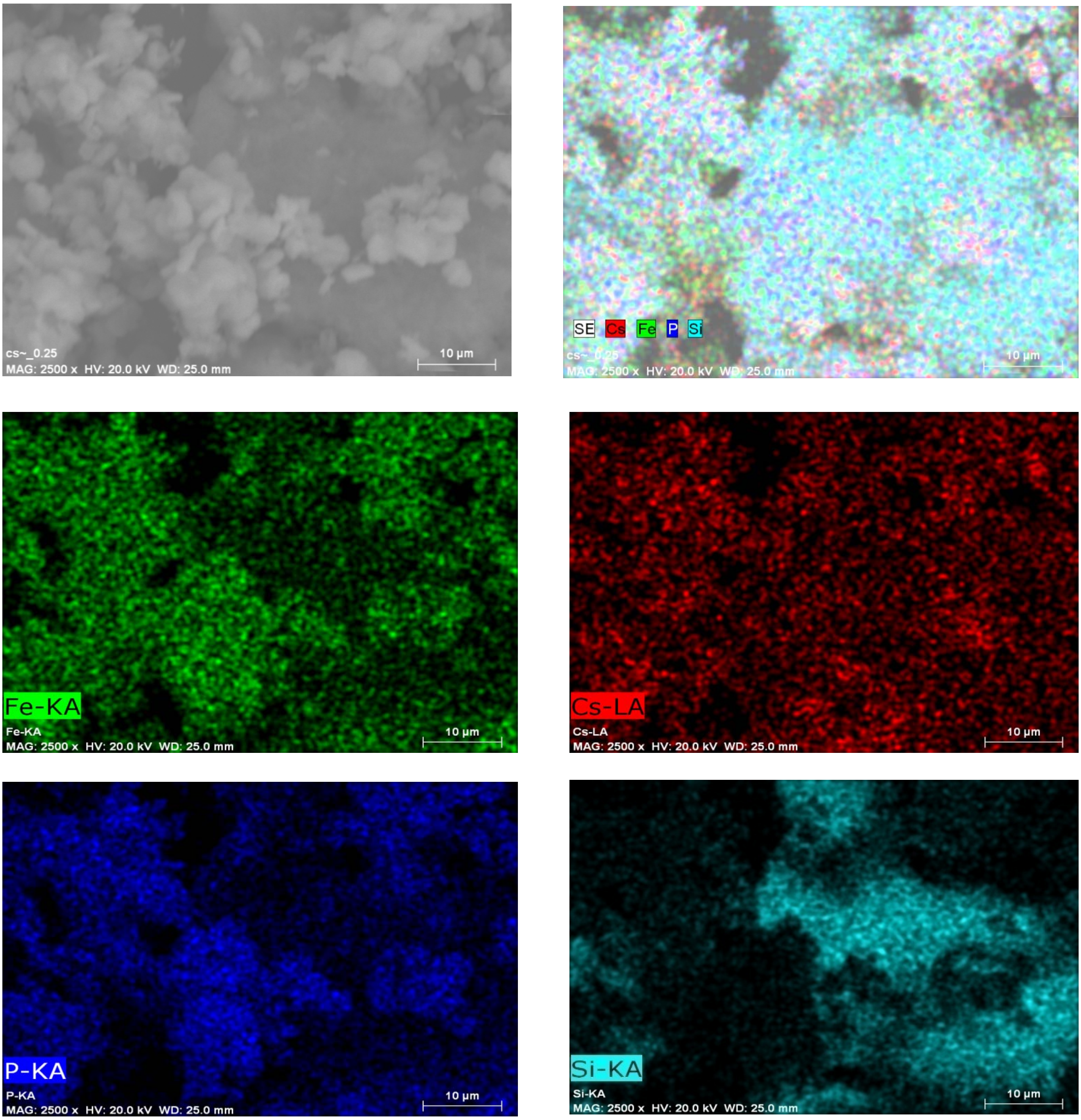

Figure D.4 SEM-EDX mapping images of the cesium promoted catalyst with Cs/Fe - 0.25

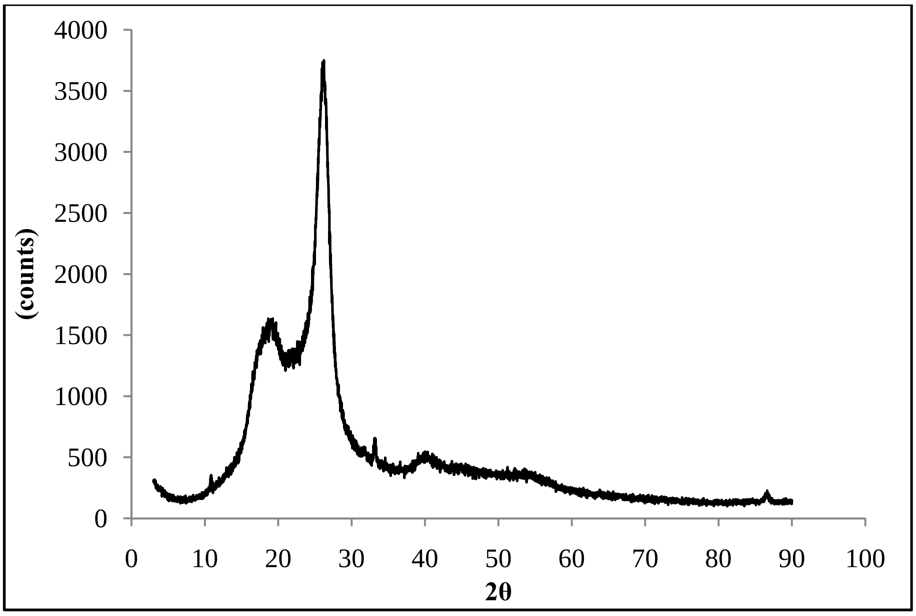

Figure D.5 XRD of the tape used during the XRD analysis

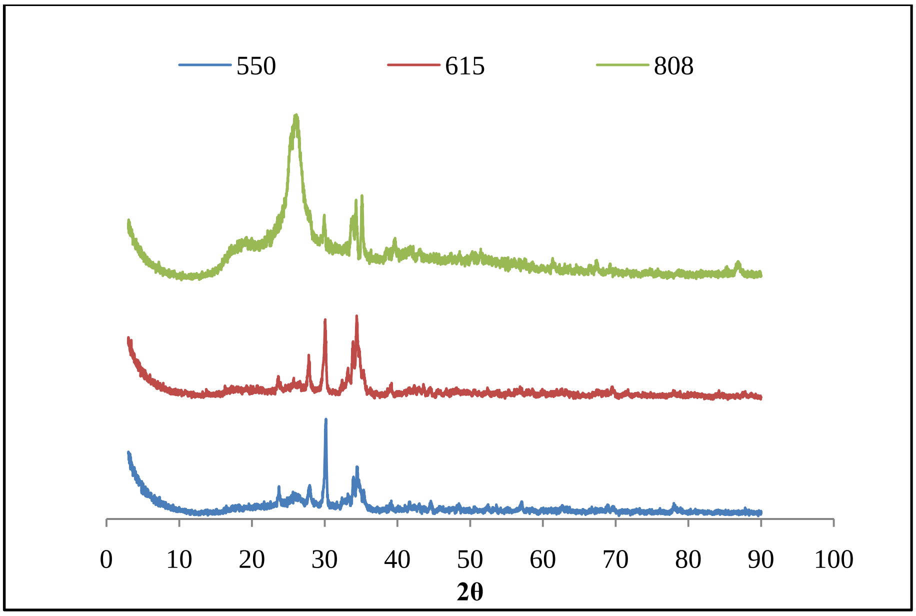

Figure D.6 XRD of the cesium promoted catalyst with Cs/Fe - 0.20 at variable temperature TPR

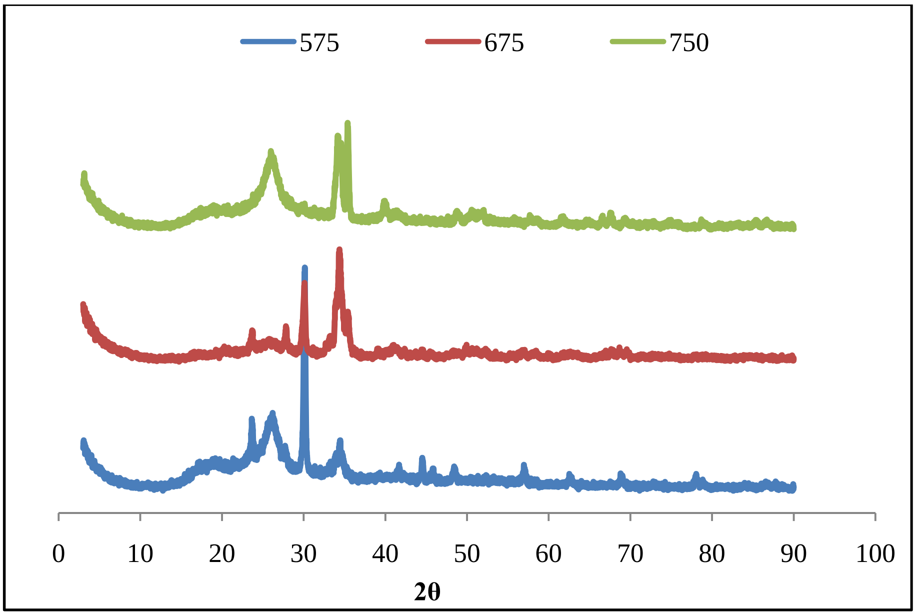

Figure D.7 XRD of the cesium promoted catalyst with Cs/Fe - 0.25 at variable temperature TPR

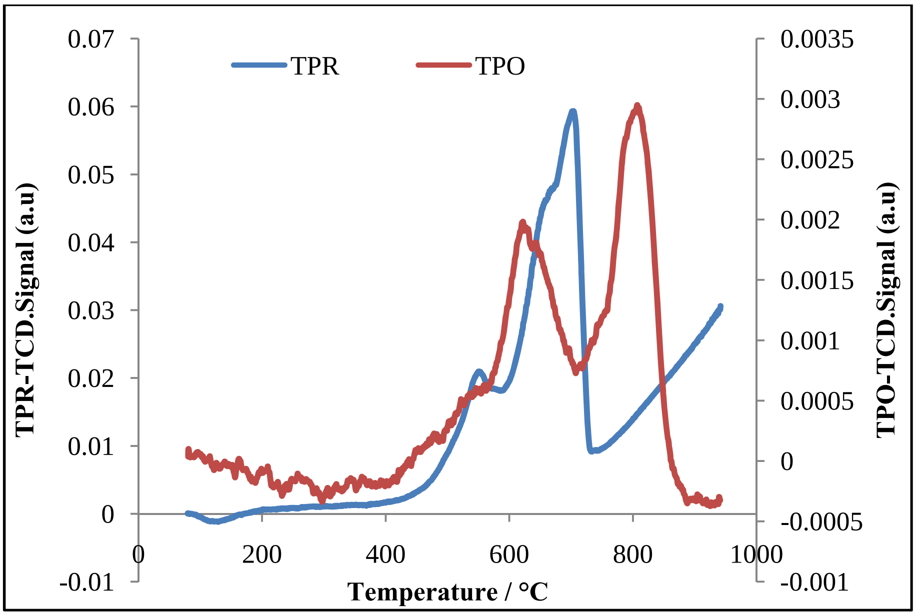

Figure D.8 TPR-TPO analysis of the cesium promoted catalyst with Cs/Fe - 0.10

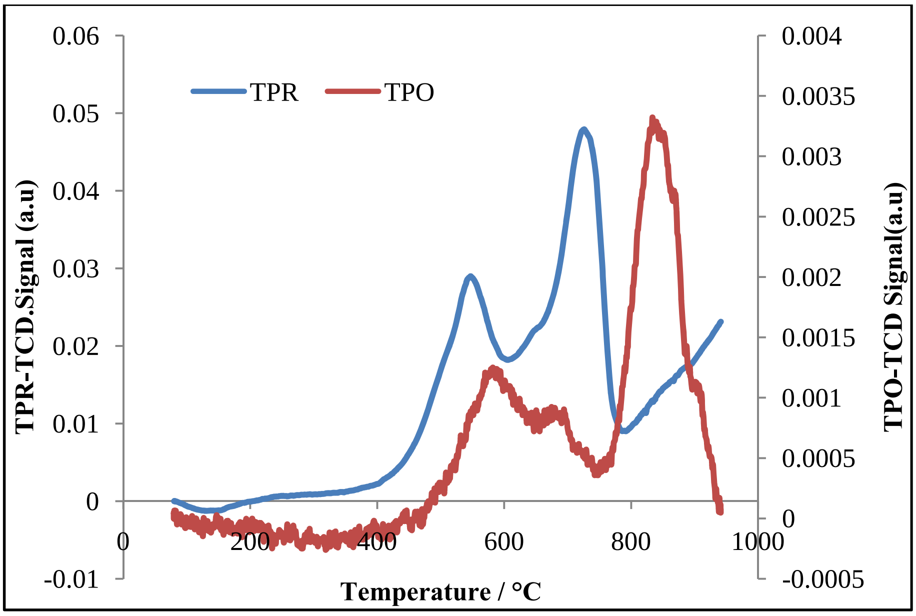

Figure D.9 TPR-TPO analysis of the cesium promoted catalyst with Cs/Fe - 0.20

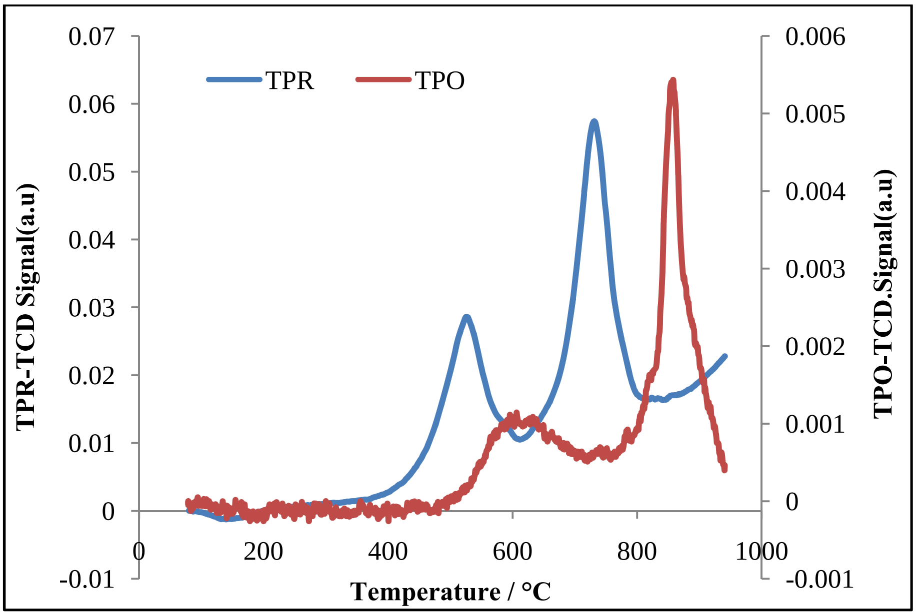

Figure D.10 TPR-TPO analysis of the cesium promoted catalyst with Cs/Fe - 0.25

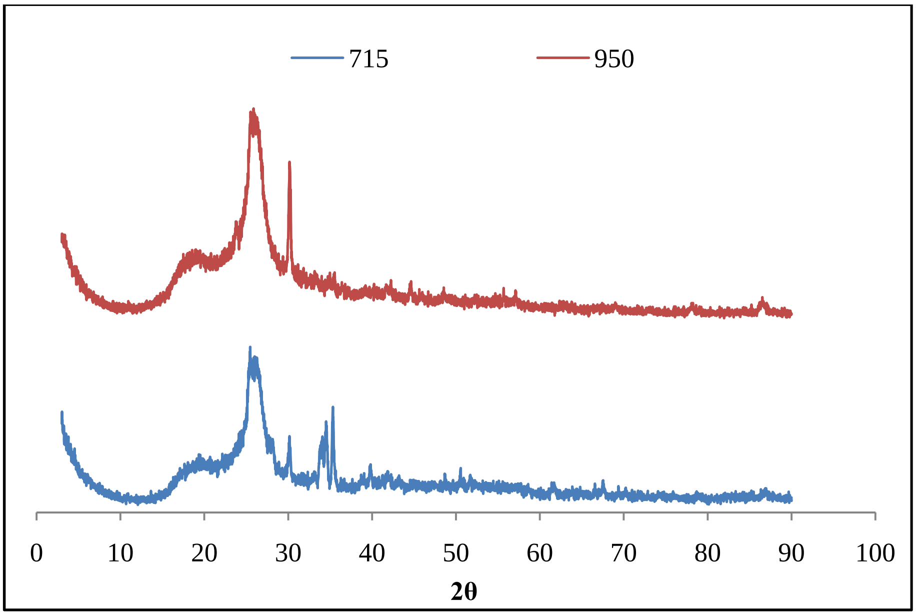

Figure D.11 XRD of the cesium promoted catalyst with Cs/Fe - 0.20 at variable temperature TPO

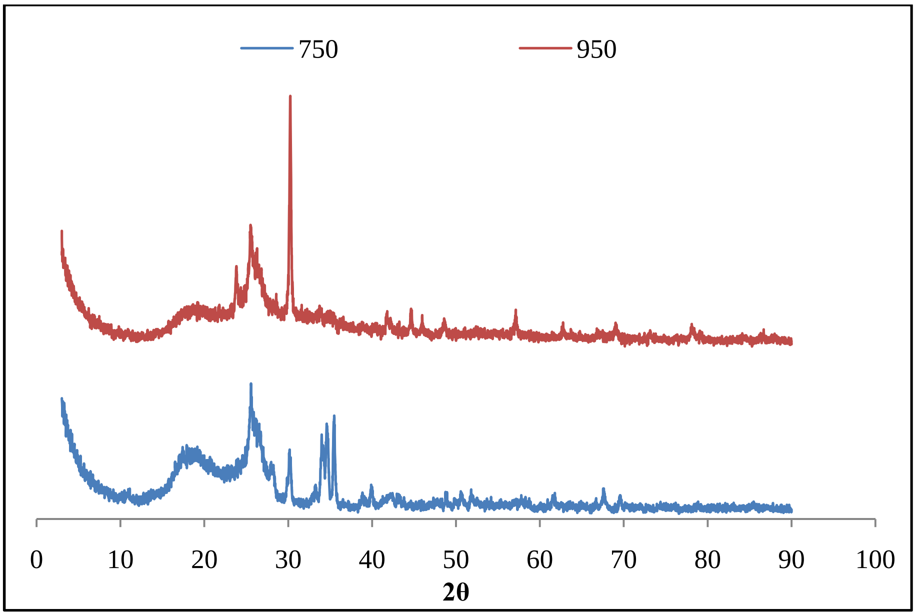

Figure D.12 XRD of the cesium promoted catalyst with Cs/Fe - 0.25 at variable temperature TPO

Table D.1 EIB and ethanol co-feed (ratio of 1:5) at a contact time of 0.8 seconds – with promoted catalyst having a Cs/Fe – 0.10

Temperature T/^{o}C	**Conversion X/(mol%)**	**Selectivity (mol %)**	**Yield (mol)**	**Selectivity (mol %)**			
		EMA	**EMA**	**MAA**	**IBA**	**COx**	**Other Products**
300	13.87	35.2	4.9	0.0	2.1	18.1	44.6
350	18.55	44.7	8.3	0.0	3.2	21.2	30.9
400	36.51	53.2	19.4	1.2	5.3	26.3	14.0
450	50.83	58.2	29.6	1.5	7.2	29.2	3.9
500	41.80	39.3	16.4	2.5	7.7	30.4	20.1

Table D.2 EIB and ethanol co-feed (ratio of 1:5) at a contact time of 0.8 seconds – with promoted catalyst having a Cs/Fe – 0.20

Temperature T/^{o}C	**Conversion X/(mol%)**	**Selectivity (mol %)**	**Yield (mol)**	**Selectivity (mol %)**			
		EMA	**EMA**	**MAA**	**IBA**	**COx**	**Other Products**
300	11.3	33.1	3.7	0.0	1.8	20.3	44.8
350	14.2	43.2	6.1	0.0	2.6	23.6	30.6
400	30.3	50.3	15.2	1.0	4.5	25.2	19.0
450	45.8	55.2	25.3	1.1	6.7	25.3	11.7
500	35.3	33.4	11.8	1.9	7.4	39.3	18.0

Table D.3 EIB and ethanol co-feed (ratio of 1:5) at a contact time of 0.8 seconds – with promoted catalyst having a Cs/Fe – 0.25

Temperature T/^oC	**Conversion X/(mol%)**	**Selectivity (mol %)**	**Yield (mol)**	**Selectivity (mol %)**			
		EMA	**EMA**	**MAA**	**IBA**	**COx**	**Other Products**
300	10.1	30.3	3.1	0.0	1.9	19.8	48.0
350	12.9	40.2	5.2	0.0	2.3	22.3	35.2
400	28.6	49.1	14.0	0.6	3.6	24.1	22.6
450	36.4	50.3	18.3	0.9	4.1	31.3	13.4
500	30.3	30.2	9.2	1.2	5.9	42.4	20.3